

**Micro-mechanical characteristics and dimensional
change of Cu-Sn interconnects due to growth of
interfacial intermetallic compounds**

by

Zhiwen Chen

A Doctoral Thesis

Submitted in partial fulfilment of the requirements
for the award of
Doctor of Philosophy of Loughborough University

December 2014

© by Zhiwen Chen, 2014

CERTIFICATE OF ORIGINALITY

This is to certify that I am responsible for the work submitted in this thesis, that the original work is my own except as specified in acknowledgments or in footnotes, and that neither the thesis nor the original work contained therein has been submitted to this or any other institution for a degree.

..... (Signed)

..... (Date)

Abstract

Sn-based solder alloys are extensively used in electronic devices to form interconnects between different components to provide mechanical support and electrical path. The formation of a reliable solder interconnects fundamentally relies on the metallurgic reaction between the molten solder and solid pad metallization in reflowing. The resultant IMC layer at the solder/pad metallization interface can grow continuously during service or aging at an elevated temperature, uplifting the proportion of IMCs in the entire solder joint. However, the essential mechanical properties of interfacial IMC (i.e. Cu_6Sn_5 , Cu_3Sn) layers, such as Young's modulus and hardness, are drastically different in comparison with Sn-based solder and substrate. Therefore, the increasing fraction of interfacial IMCs in the solder joint can lead to significant deformation incompatibility under exterior load, which becomes an important reliability concern in the uses of solder joints for electronic interconnects.

In the past decades, extensive research works were implemented and reported regarding the growth of interfacial IMC layers and its effect on the mechanical integrity of solder joints. But, the following fundamental issues in terms of mechanical and microstructural evolution in the uses of solder joints still remain unclear, demanding further research to elaborate:

(1) The protrusion of IMCs: Though the growth of interfacial IMC layers along the diffusion direction in solder joints were studied extensively, the growth of IMCs perpendicular to the diffusion direction were reported in only a few papers without any further detailed investigation. This phenomena can crucially govern the long-term reliability of solder interconnects, in particular, in the applications that require a robust microstructural integrity from a solder joint.

(2) Fracture behaviour of interfacial IMC layers: The fracture behaviour of interfacial IMC layers is a vital factor in determining the failure mechanism of solder joints, but this was scarcely investigated due to numerous challenges to enable a potential *in-situ* micro-scale tests. It is therefore highly imperative to carry out such study in order to reveal the fracture behaviour of interfacial IMC layers which can eventually provide better understanding of the influence of interfacial IMC layers on the mechanical integrity of solder joints.

(3) Volume shrinkage: The volume shrinkage (or solder joint collapse) induced by the growth of interfacial IMC layers was frequently ascribed as one of the main causes of the degradation of mechanical reliability during aging due to the potentially resulted voids and residual stress at the solder/substrate interface. However, very few experimental works on the characterisation of such type of volume shrinkage can be found in literatures, primarily due to the difficulties of observing the small dimensional changes that can be encountered in the course of IMCs growth.

(4) Residual stress: The residual stress within solder joints is another key factor that contributes to the failure of solder joints under external loads. However, the stress evolution in solder joints as aging progresses and the potential correlation between the residual stress and the growth of interfacial IMC layers is yet to be fully understood, as stress/strain status can fundamentally alter the course of total failure of a solder joint.

(5) Crack initiation and propagation in solder joints: Modelling on the mechanical behaviour of solder joints is often undertaken primarily on the stress distribution within solder joints, for instance, under a given external loading. But there is lack of utilising numerical analysis to simulate the crack initiation and propagation within solder joints, thus the effect of interfacial IMC layers on the fracture behaviour of the solder joints can be elaborated in further details.

In this thesis, the growth of interfacial IMCs in parallel and perpendicular to the interdiffusion direction in the Sn99Cu1/Cu solder joints after aging was investigated and followed by observation with SEM, with an intention of correlating the growth of IMCs along these two directions with aging durations based on the measured thickness of IMC layer and height of perpendicular IMCs. The mechanism of the protrusion of IMCs and the mutual effect between the growth of IMCs along these two directions was also discussed.

The tensile fracture behaviour of interfacial Cu_6Sn_5 and Cu_3Sn layers at the Sn99Cu1/Cu interface was characterised by implementing cantilever bending tests on micro Cu_6Sn_5 and Cu_3Sn pillars prepared by focused ion beam (FIB). The fracture stress and strain were evaluated by finite element modelling using Abaqus. The tensile fracture mechanism of both Cu_6Sn_5 and Cu_3Sn can then be proposed and discussed based on the observed fracture surface of the micro IMC pillars.

The volume shrinkage of solder joints induced by the growth of interfacial IMC layers in parallel to the interdiffusion direction in solder joint was also studied by specifically designed specimens, to enable the collapse of the solder joint to be estimated by surface profiling with Zygo Newview after increased durations of aging. Finite element modelling was also carried out to understand the residual stress potentially induced due to the volume shrinkage.

The volume shrinkage in solder joints is likely to be subjected to the constraint from both the attached solder and substrate, which can lead to the build-up of residual stress at the solder/Cu interface. Depth-controlled nanoindentation tests were therefore carried out in the Sn99Cu1 solder, interfacial Cu_6Sn_5 layer, Cu_3Sn layer and Cu with Vickers indenter after aging. The residual stress was then evaluated in the correlation with aging durations, different interlayers and the locations in the solder joint.

Finally, finite element models incorporated with factors that may contribute to the failure of solder joints, including microstructure of solder joints, residual stress and the fracture of interfacial IMC, were built using Abaqus to reveal the effect of these factors on the fracture behaviour of solder joints under applied load. The effect of growth of IMC layer during aging on the fracture behaviour was then discussed to provide a better understanding of the degradation of mechanical integrity of solder joints due to aging.

The results from this thesis can facilitate the understanding of the influence of interfacial IMC layers on the mechanical behaviour of solder joints due to long-term exposure to high temperatures.

Keywords: Growth of IMCs, micro cantilever bending, collapse of solder joint, residual stress, nanoindentation, finite element modelling.

List of Publications

1. Zhiwen Chen, Bing An, Yiping Wu, Changqing Liu, Parkin, R., Dimensional change in micro-scale solder joint induced by evolution of IMCs, Proceedings of the 13th International Conference on Electronic Packaging Technology and High Density Packaging (ICEPT-HDP), Guilin China, 13-16 August 2012, 1234-1239;
(the content is related to chapter 5)
2. Zhiwen Chen, Bing An, Yiping Wu, Changqing Liu, Parkin, R., Influence of IMCs volume ratio in micro-scale solder joints on their mechanical integrity, Proceedings of the 62nd Electronic Components and Technology Conference, San Diego USA, 29th May – 1st June 2012, 710-716;
(It is from a previous project, not included in the thesis)
3. Zhiwen Chen, Bing An, Yiping Wu, Changqing Liu, Parkin, R., An investigation of the influence of intermetallic compounds on compressive creep of SAC305/copper solder joints by modelling, 2011 International Symposium on Advanced Packaging Materials (APM), Xiamen China, 25 - 28 October 2011, 322-329;
(It is from a previous project, not included in the thesis)
4. Zhiwen Chen, Changqing Liu, Yiping Wu, Bing An, Longzao Zhou, A study on the collapse of Sn99Cu1/Cu solder joints due to isothermal aging, Journal of Electronic Materials, *Minor revision*.
(the content is related to chapter 5)
5. Zhiwen Chen, Changqing Liu, Yiping Wu, Bing An, Longzao Zhou, Fracture characteristics of Cu-Sn intermetallic compounds in Sn99Cu1/Cu solder joints by micro cantilever bending, *Will be submitted to Intermetallics*.
(the content is related to chapter 4)
6. Zhiwen Chen, Changqing Liu, Yiping Wu, Bing An, Perpendicular growth characteristics of Cu-Sn intermetallic compounds at the surface of Sn99Cu1/Cu solder interconnects, *submitted to Journal of Electronic Materials*
(the content is related to chapter 3)
7. Liping Mo, Zhiwen Chen, Fengshun Wu, Changqing Liu, An investigation of Cu-Sn intermetallic joints on isothermal evolution of microstructure and mechanical property, Intermetallics, *Accepted*.

Acknowledgement

The research is funded by the joint PhD programme between Loughborough University (UK) and Huazhong University of Science and Technology (China). This research was also supported by a Marie Curie International Research Staff Exchange Scheme Project within the 7th European Community Framework Programme, No. PIRSES-GA-2010-269113, entitled “Micro-Multi-Material Manufacture to Enable Multifunctional Miniaturised Devices (M6)”.

It is a long and challenging journey from the start of the PhD study to deliver this thesis. I would like to take this opportunity to express my sincere thanks to the people who have helped me in the process of my research.

I owe my deepest gratitude and appreciation to my supervisors, Prof. Changqing Liu in Loughborough University and Prof. Yiping Wu in Huazhong University of Science and Technology, for providing me the opportunity to work in this joint project. Their expertise, continuous support and patience have guided me in the way of my research. Without their help, everything presented in this thesis would be impossible. I also wish to thank Dr. Bing An (HUST) and Professor Rob Parkin (LU) who are my secondary supervisors for their suggestions and helpful ideas on the PhD study.

I would also like to thank immensely Dr. Geoff West and Dr. Keith Yendall in Department of Materials and Engineering, Loughborough University, for their kind help, training and assistance on material characterizations using focused ion beam and scanning electron microscopy. The training and support from Dr. Javad Falsafi, Dr. Simin Li and Andrew Bird on nanoindentation tests are also much appreciated. My thanks are also due to Dr. David Hutt, Andrew Sandaver and Jagpal Singh for their support on sample preparation and surface profiling. The kind suggestions and help from Prof. Fengshun Wu and Dr. Longzao Zhou are also gratefully acknowledged.

Besides, special thanks to my friends in both Loughborough and Wuhan. Without your help and company all these years, my life in PhD study would be rather dull and miserable.

Finally, I wish to express my sincere gratitude to my family, my girlfriend Li Liu and her family for their patience, encouragement, deep understanding and support. Their love is essential for me to finish this long journey and get ready for the new period of life.

Wuhan, China

Zhiwen Chen

Table of Contents

Abstract	I
List of Publications	III
Acknowledgement	IV
List of Figures	IX
List of Tables	XVII
List of Abbreviations	XIX
Chapter 1 Introduction	1
1.1 Context and problem definition	1
1.2 Scope of the research.....	3
1.3 Aims and objectives.....	4
1.4 Structure of the thesis	5
Chapter 2 Literature review	7
2.1 Growth of IMC layers	7
2.1.1 Formation of planar interfacial IMC layers in reflowing.....	8
2.1.2 Planar Growth of IMC layers	9
2.1.3 Perpendicular growth of IMCs	11
2.2 Mechanical properties of interfacial IMC layers	12
2.3 Volume shrinkage induced by the growth of IMCs.....	15
2.4 Measurement of residual stress in solder joints	16
2.5 Modelling on the fracture behaviour of solder joints.....	19
2.6 Summary	20
Chapter 3 Growth of interfacial intermetallic compounds in Sn99Cu1/Cu solder joints in aging	22
3.1 Introduction	22
3.2 Planar growth of IMC layers.....	22
3.2.1 Experimental details	22
3.2.2 Planar growth of interfacial IMC layers.....	23
3.2.3 Morphological evolution of planar interfacial IMC layers	25
3.3 Perpendicular growth of IMCs.....	28
3.3.1 Experimental details	28
3.3.2 Results & discussions	29
3.4 Comparisons and general discussions	34

3.4.1 Rate-controlling process in the growth of IMCs.....	34
3.4.2 Formation sequence of Cu_6Sn_5 and Cu_3Sn	35
3.4.3 Growth rates of perpendicular and planar IMCs.....	36
3.5 Summary	36
Chapter 4 Tensile fracture behaviour of Cu-Sn intermetallic compounds	38
4.1 Introduction	38
4.2 Experimental and modelling details	38
4.2.1 Methodology.....	38
4.2.2 Experimental procedures	41
4.2.3 Numerical modelling.....	46
4.3 Fracture behaviour of Cu_6Sn_5	48
4.3.1 Experimental results of micro cantilever bending tests	48
4.3.2 Modelling results	52
4.3.3 Discussion.....	54
4.4 Fracture behaviour of Cu_3Sn	57
4.4.1 Experimental results.....	57
4.4.2 Modelling results	60
4.4.3 Discussions	61
4.5 General discussions	62
4.5.1 Modelling and flexural formula	62
4.5.2 Effects of aging on the fracture strength of solder joints	63
4.6 Summary	64
Chapter 5 Collapse of Sn99Cu1/Cu solder joints due to isothermal aging	66
5.1 Introduction	66
5.2 Collapse of solder joints.....	66
5.2.1 Experiment procedures	66
5.2.2 Collapse of solder joints induced by growth of IMCs.....	69
5.2.3 Comparison with numerical analysis	73
5.2.4 Effect of oxidation.....	75
5.3 The effect of collapse of solder joints.....	77
5.3.1 Modelling and experimental approaches.....	77
5.3.2 Internal stress induced by the collapse of solder joint	79
5.3.3 Grain redistribution in Cu substrate	81
5.4 Summary	83

Chapter 6 Residual stress induced by the growth of interfacial IMC layers ..	84
6.1 Introduction	84
6.2 Theoretical attributes and methodology	84
6.3 Experimental details	88
6.4 Experimental results	90
6.4.1 Projected contact area of nano indents	90
6.4.2 Residual stress in Cu and Sn99Cu1 solder	91
6.4.3 Stress evolution in Cu_6Sn_5 and Cu_3Sn layers	97
6.5 Discussions	102
6.5.1 Correlation of evolution of residual stress	102
6.5.2 Factors contributing to the evolution of residual stress	104
6.5.3 Deviations in experimental results	106
6.6 Summary	106
Chapter 7 Modelling on the fracture behaviour of solder joints	107
7.1 Introduction	107
7.2 Numerical simulation and geometries of the models	107
7.2.1 Methodology	107
7.2.2 The original finite element models	108
7.2.3 Finite element models with residual stress field	110
7.2.4 Finite element models with grain boundaries	113
7.2.5 Finite element models with both residual stress and microstructure ...	116
7.3 Major parameters and settings in the simulations	117
7.3.1 Fracture parameters of bulk solder	117
7.3.2 Fracture parameters of Cu_6Sn_5 and Cu_3Sn	119
7.3.3 Other settings and parameters	121
7.4 Modelling results	122
7.4.1 Crack initiation and propagation in original models	122
7.4.2 Effect of residual stress on the fracture behaviour	123
7.4.3 Effect of microstructure on the fracture behaviour	124
7.4.4 The combined effect of microstructure and residual stress	125
7.5 Discussions	126
7.6 Summary	128
Chapter 8 Conclusions and future work	129
8.1 Main conclusions	129

8.1.1 Growth of IMCs at Sn99Cu1/Cu interface	129
8.1.2 Mechanical properties of Cu-Sn IMCs.....	129
8.1.3 Collapse of solder joints	130
8.1.4 Residual stress.....	130
8.1.5 Modelling on fracture behaviour of solder joints	131
8.2 Contribution of the work.....	131
8.3 Future work.....	132
8.2.1 Growth of IMCs	132
8.2.2 Mechanical properties of IMCs.....	133
8.2.3 Collapse of solder joints	133
8.2.4 Residual stress in solder joints.....	133
8.2.5 Modelling on the fracture behaviour of solder joints	134
References	135
Appendices 1- Code for post-processing	155
Appendices 2- Code for creating grain boundaries	157
Appendices 3- Code for importing grain boundaries	158

List of Figures

Fig. 1.1 Schematics of different layers in a solder joint between chip and substrate: (a) solder joints serve as interconnects between a chip and substrate; (b) initial interfacial IMC layers formed in reflow; (c) increased fraction of IMC layer after long-term service or aging. 2

Fig. 1.2 Schematic of the structure of the thesis. 5

Fig. 2.1 Schematic of the planar and perpendicular growth of interfacial IMCs at the Sn/Cu interface in aging. 11

Fig. 2.2 Schematics of the test methodologies for the (a) compression tests [19] and (b) shear tests [74] on Cu_6Sn_5 at the solder/substrate interface by nanoindentation tests. 14

Fig. 2.3 Schematic of the design of the specimen for the direct measurement of volume shrinkage of Ni/Sn/Ni solder joints induced by the growth of Ni_3Sn_4 in aging [80, 81]. 16

Fig. 3.1 The growth of IMCs parallel and perpendicular to the interdiffusion direction. 22

Fig. 3.2 Preparation of specimens: (a) Reflow profile; (b) the schematic of specimens for the investigation of planar growth of IMCs. 23

Fig. 3.3 The measurement of the thickness of planar Cu_6Sn_5 and Cu_3Sn layers. 23

Fig. 3.4 The thickness of interfacial IMC layers at the Sn99Cu1 solder/Cu interface (a) before aging and (b) after aging at 175°C for 1006.5 hours. 24

Fig. 3.5 The correlation between the growth of interfacial IMC layers and aging durations at 175°C. 24

Fig. 3.6 Morphological evolution of the interfacial IMC layers after aging at 175°C for (a) 0 hours; (b) 168 hours; (c) 672 hours; (d) 840 hours and (e) 1006.5 hours. 26

Fig. 3.7 Different parts in molten solder/ Cu_6Sn_5 system in reflowing. 26

Fig. 3.8 Comparison of diffusion distances at the peaks and valleys in the (a) dendritic and (b) layer-type interfacial IMC layers in aging. 27

Fig. 3.9 Curvature effect in morphological evolution: (a) the Cu atoms move from positions with higher curvature to those less curved; (b) the curvature of IMCs becomes more homogeneous as the aging prolongs. 27

Fig. 3.10 Schematic of specimen used for measuring the perpendicular IMCs. 28

Fig. 3.11 The illustration of (a) Zygo Newview used in this work and (b) the mechanism of the measurement. 29

Fig. 3.12 The growth of perpendicular IMCs: (a), (c), (e) are the SEM images of the perpendicular IMCs after aging at 175 °C for 0h, 168 hours and 1006.5 hours and (b), (d) and (f) are the example of surface profile of the corresponding specimens. 30

Fig. 3.13 Estimation of the heights of perpendicular IMCs: (a) an example of series of profiles derived from the scanned area. The red line is the average profile of the scanned

area and the grey area is the overlapped surface profiles; (b) the obtained average height of perpendicular IMC versus square root of aging durations.	31
Fig. 3.14 The perpendicular IMCs at the Sn99Cu1 solder/Cu interface after aging at 175°C for 1006.5 hours. The Pt on the top of the cross section was deposited before the milling with ion beam to protect the sample beneath it during milling.	31
Fig. 3.15 Growth of perpendicular IMCs: (a), (c), (e), (g) and (i) illustrate the different stages of the growth of perpendicular IMCs; (b), (d), (f) and (j) show the observed evolution of perpendicular IMCs with SEM after aging at 175°C for 0 week, 1 week, 4 weeks, 5 weeks and 6 weeks.	33
Fig. 3.16 Shift of the Cu_3Sn/Cu_6Sn_5 and Cu/Cu_3Sn interfaces in the region close to the surface of Sn99Cu1/Cu solder joint. The Pt on the top was deposited to protect the sample beneath it during milling.	34
Fig. 4.1 The cylindrical Cu_6Sn_5 pillar fabricated with FIB in perpendicular to the solder/Cu interface [9, 73].	39
Fig. 4.2 The micro (a) Cu_6Sn_5 and (b) Cu_3Sn pillars parallel to the solder/Cu interface at the corner of the solder joint; (c) A brief procedures of the work.	40
Fig. 4.3 The reflow profile obtained with the thermal couple attached to the sample during reflowing.	41
Fig. 4.4 The Nano flat indenter used in the work: (a) the shape of the indenter; (b) an enlarged image of the tip of the indenter.	41
Fig. 4.5 Calibration of the positioning accuracy of the nanoindentation instrument: (a) a reference indent; (b) the new indent overlapped perfectly on the reference indent.	42
Fig. 4.6 Schematic of the milling with FIB.	43
Fig. 4.7 (A)~(G) the SEM images of an IMC pillar at the Sn99Cu1 solder/Cu interface during the preparation with FIB, (a)~(f) schematics to illustrate the direction and position of the specimen during milling; (1)~(7) the explanations of the corresponding procesudres.	46
Fig. 4.8 Finite element models of micro Cu_6Sn_5 and Cu_3Sn pillars built in Abaqus: (a) and (c) The regions included in the finite element models; (b) and (d) the geometry of the built models with Abaqus. The red surfaces of the support of the IMC pillar were fixed along all the three directions. The red surfaces of the indenter was only constrained along x and y direction.	46
Fig. 4.9 Comparison between (a) linear (C3D8) and (b) quadratic (C3D20) element. The black dots denote the nodes in the element.	47
Fig. 4.10 An example of the model after meshing.	47
Fig. 4.11 An example of micro Cu_6Sn_5 pillar fabricated by FIB in this work: (a) an example of the Cu_6Sn_5 pillar; (b) the EDX spectrum of the IMC pillar.	48

Fig. 4.12 Cantilever bending test on a micro Cu_6Sn_5 pillar: optical images of the specimen (a) before the test and (b) after the test; (c) the obtained load-displacement curve from the test.	49
Fig. 4.13 The load-deflection curves from the cantilever bending tests on three micro Cu_6Sn_5 pillars. The cross at the end of the curves denotes the fracture points of the pillars.	50
Fig. 4.14 Observation and composition analysis of the fracture surface of micro Cu_6Sn_5 pillar after cantilever bending test: (a) the Cu_6Sn_5 pillar after cantilever bending test; (b) and (c) two types of fracture surface observed from the tested Cu_6Sn_5 micro pillars; (d) the EDX spectrum of the fracture surface.	51
Fig. 4.15 Rectangular cross section of a cuboid pillar.....	52
Fig. 4.16 An example of the comparison of load-deflection curves from experiment and modelling.....	53
Fig. 4.17 The selected region where the stress is independent of mesh size for the evaluation of tensile fracture strength of Cu_6Sn_5	53
Fig. 4.18 The Cu_6Sn_5 grains at the solder/Cu interface in Sn99Cu1/Cu solder joint after aging at 175 °C for 1132.5 hours: (a) the region on the specimen for the scanning with EBSD; (b) grain orientations of Cu_6Sn_5 grains at the interface.	54
Fig. 4.19 Two different fracture modes of micro Cu_6Sn_5 pillars after cantilever bending test; (a) and (c) illustrate the two possible locations of the bottom of micro Cu_6Sn_5 pillar in the Cu_6Sn_5 layer; (b) and (d) are the SEM images of the two corresponding fracture surfaces after cantilever bending tests.	55
Fig. 4.20 The compression test on micro Cu_6Sn_5 pillar in reference [73]: (a) the indenter was parallel to the top surface of the Cu_6Sn_5 pillar in ideal case; (b) the indenter was not parallel to the top surface of micro Cu_6Sn_5 pillar in real case.	56
Fig. 4.21 An example of the micro Cu_3Sn pillars fabricated with FIB: (a) the dimensions of the Cu_3Sn pillar; (b) the EDX spectrum of the fabricated pillar.	57
Fig. 4.22 Cantilever bending test on Cu_3Sn pillar: images of the micro Cu_3Sn pillar (a) before test, (b) after test, and (c) the load-displacement curve from the test.....	58
Fig. 4.23 Load-deflection curves of the micro Cu_3Sn pillars from cantilever bending tests.	58
Fig. 4.24 The micro Cu_3Sn pillar after cantilever bending tests: (a) the fractured micro Cu_3Sn pillar; (b) The enlarged view of the fracture surface of micro Cu_3Sn pillar; (c) the EDX spectrum of the fracture surface of the test pillar.....	59
Fig. 4.25 Comparison between the load-deflection curves from the experiment and modelling.....	60
Fig. 4.26 The stress at the selected region was independent of mesh size.....	61

Fig. 4.27 The contrast of grain orientations in the interfacial Cu_3Sn layer by the ion beam in FIB.....	62
Fig. 4.28 Schematic of the comparison between the strain distribution across the bottom of micro Cu_6Sn_5 pillar in finite element model with Cu_6Sn_5 support and the model with ideally rigid support.	63
Fig. 5.1 A schematic view of the test specimens (the interfacial IMC layer is exaggerated): (a) the geometry and dimensions; (b) cross-sectional view before aging test: the Cu and solder are at the same height; (c) cross-sectional view after aging: the solder collapses due to the further growth of IMC layers at the interface.	67
Fig. 5.2 An example of the surface morphology obtained by Zygo Newview 5000: (a) the original data from the measurement with Zygo; (b) the surface morphology after the levelling with the Cu surface.	69
Fig. 5.3 An example of series of surface profiles derived from the measurement with Zygo; (a) The height-distance curves of the scanned region across the Sn99Cu1 solder/Cu interface; (b) the derived average surface profile of the region.....	70
Fig. 5.4 Zygo surface profiling across the Cu/solder boundaries to evaluate the height reduction due to the collapse of solder joints after aging: (a) A series of average surface profiles from one specimen aged at 175°C for 0, 97.5, 630.5 and 1132.5 hours; (b) The plot of decrease in solder height of one specimen vs aging time showing parabolic relationship.....	71
Fig. 5.5 Cross-sectional views of Cu/Sn99Cu1 samples prepared by FIB: (a) before, and (b) after aging at 175 °C for 1132.5 hours. The Pt on the top was deposited to protect the sample beneath it during milling.....	71
Fig. 5.6 The average reduction of joint height of four specimens vs aging durations at 175°C.	72
Fig. 5.7 The colour of the Cu part in the Sn99Cu1/Cu solder joints after aging at 175°C for (a) 0 hour, (b) 168 hours and (c) 1132.5 hours.	76
Fig. 5.8 Evaluation of the oxide layer on Cu and Sn after aging at 175°C for 1132.5 hours: (a) copper oxide layer (~ 0.36 μm); (b) tin oxide layer (~0.07 μm). The Pt on the top was deposited to protect the sample beneath it during milling.	76
Fig. 5.9 The geometry and the boundary conditions of the finite element model. The three edges with triangles were fixed in both X and Y directions.	78
Fig. 5.10 The schematic and dimensions of the Cu specimen for the comparison with Sn99Cu1/Cu solder joints.	79
Fig. 5.11 Redistribution of stress within solder joint due to the collapse of solder joint: (a) The overall distribution of internal stress due to the growth of interfacial IMC layers; (b) The distribution of von Misses stress along the dash path in (a).	80

Fig. 5.12 Stress distribution in (a) solder and (c) Cu substrate; (b) and (d) illustrates the stress distribution along path in solder and Cu, respectively. The dash lines in (a) and (c) represent the path for the stress distribution in (b) and (d).	81
Fig. 5.13 Grain boundaries in Cu revealed by oxidation: (a)The grains in the Cu part of Sn99Cu1/Cu solder joints and (b) the grains in the machined Cu specimen after aging at 175 °C for one week.....	81
Fig. 5.14 The comparison of the size of Cu grains close to the solder/Cu interface after aging at 175°C for (a) 168 hours and (b) 672 hours.	82
Fig. 6.1 Schematics of the effect of residual stress on nanoindentation tests: (a) the indentation on specimens without any residual stress; (b) and (c) the effect of compression and tension stress on the nanoindentation tests; (d) the comparison of load-depth curves from nanoindentation tests on specimens in different stress states.....	85
Fig. 6.2 Projected contact area vs plastic depth of the Nanotest platform 3 in this work. ..	86
Fig. 6.3 Schematic for the estimation of the initial unloading stiffness S by deriving the slope of the beginning of the unloading curve after nanoindentation tests.	87
Fig. 6.4 Procedures for the estimation of residual stress within solder joints by nanoindentation tests.	87
Fig. 6.5 Planned locations of the nanoindents in the entire solder joint.	88
Fig. 6.6 Representative surface profiles of nano indents made within (a) solder, (b) Cu, (c) interfacial Cu_6Sn_5 layer and (d) interfacial Cu_3Sn layers.....	90
Fig. 6.7 An example of the comparison between the measured contact area and the calculated contact area based on equation (6.4) for the nano indents in the interfacial Cu_3Sn layer.	91
Fig. 6.8 The nano indents in reference solder and Cu specimen: (a) and (c) are the indents in reference Cu and solder specimens, respectively; (b) and (d) illustrate the corresponding load-displacement curves from the nano indents.....	92
Fig. 6.9 Nano indents in the Cu substrate: (a) and (c) illustrate the overall location of the nano indents at the centre and at the edge of the solder joints respectively; (b) and (d) show the examples of nano indents at the corresponding locations.....	92
Fig. 6.10 Evolution of maximum forces of the nano indents (a) at the centre and (b) at the edge of Cu substrate after prolonged aging.....	93
Fig. 6.11 Projected contact areas of the nano indents at the center and at the edge of Cu substrate with prolonged aging.	93
Fig. 6.12 Residual stress (a) at the centre and (b) at the edge of Cu substrate after progressively increasing aging durations.	94

Fig. 6.13 Nano indents in the Sn99Cu1 solder matrix close to the solder/ Cu_6Sn_5 interface: (a) and (c) illustrates the overall location of the indents in the Sn99Cu1 solder joints; (b) and (d) show the indents made at the corresponding locations in the solder.	95
Fig. 6.14 Maximum forces of the nano indents (a) at the centre and (b) at the edge of the Sn99Cu1 solder joints close to the solder/ Cu_6Sn_5 interface after aging.....	96
Fig. 6.15 Calculated projected contact areas of nano indents in solder matrix close to the solder/ Cu_6Sn_5 interface at the centre and at the edge of Sn99Cu1 solder joints.....	96
Fig. 6.16 The residual stress within solder matrix (a) at the centre and (b) at the edge of the Sn99Cu1/Cu solder joints.	97
Fig. 6.17 Nanoindents within the interfacial Cu_6Sn_5 layer: (a) and (c) the overall locations of the indents in the entire solder joints; (b) and (d) examples of the indents at the corresponding locations, which are indicated by the arrows.....	98
Fig. 6.18 Maximum forces of the nanoindents (a) at the centre and (b) at the edge in the interfacial Cu_6Sn_5 layer in Sn99Cu1 solder joints.	98
Fig. 6.19 Projected contact areas of the nano indents made at the center and at the edge of the interfacial Cu_6Sn_5 layer after aging for 0h - 500h.	99
Fig. 6.20 Evolution of compression stress (a) at the centre and (b) at the edge of the interfacial Cu_6Sn_5 layer in the progressively prolonged aging.....	99
Fig. 6.21 Nano indents in the interfacial Cu_3Sn layer for the evaluation of residual stress: (a) and (c) the location of the indents at the centre and at the edge of interfacial Cu_3Sn layer; (b) and (d) examples of the nano indents made at the corresponding locations.	100
Fig. 6.22 Summary of the maximum force of the nano indents (a) at the centre and (b) at the edge of the interfacial Cu_3Sn layer in Sn99Cu1/Cu solder joints after aging.	101
Fig. 6.23 Projected contact area of the nano indents in interfacial Cu_3Sn layer after aging at 175°C for 0 ~ 500 h.....	101
Fig. 6.24 The evolution of residual stress (a) at the centre and (b) at the edge of the interfacial Cu_3Sn layer in Sn99Cu1/Cu solder joints after aging. The negative values of the stress represent the tension stress within the Cu_3Sn layer.	102
Fig. 6.25 The comparison of the evolution of residual stress within two adjacent parts in Sn99Cu1/Cu solder joints in aging: (a), (c) and (e) illustrate the evolution of stress close to the Sn99Cu1 solder/ Cu_6Sn_5 , Cu_6Sn_5/Cu_3Sn and Cu_3Sn/Cu interfaces at the centre of the solder joint; and (b), (d) and (f) are the stress within the same parts at the edge.....	104
Fig. 6.26 Growth of Sn whiskers within a void in Sn99Cu1 solder next to the Sn99Cu1 solder/Cu interface.	105
Fig. 7.1 Methodology of the modelling on the effect of residual stress, microstructure and interfacial IMC layers on the fracture behaviour of solder joints.	108

Fig. 7.2 Interfacial IMC layers (a) before aging and (b) after aging at 175 °C for 1006.5 hours in Sn99Cu1/Cu solder joints.....	109
Fig. 7.3 Geometries of the original finite element models for (a) the solder joints before aging and (b) the solder joint after aging for 1006.5 hours.	109
Fig. 7.4 Boundary conditions for the simulation on the tensile fracture of solder joints (a) before aging and (b) after aging.....	110
Fig. 7.5 Procedures for simulating the residual stress within solder joints in finite element modelling.....	111
Fig. 7.6 Boundary conditions and settings in the models of solder joints (a) before aging and (b) after aging for 1006.5 hours in the modelling on residual stress.	112
Fig. 7.7 Stress distribution within solder joints: the overall distribution of residual stress in the (a) solder joint with thin interfacial IMC layer and (c) solder joint with thick interfacial IMC layer; (b) and (d) are the detailed stress distribution within the solder matrix in corresponding models.....	113
Fig. 7.8 Generated grain boundaries in finite element models: (a) general procedures for producing the grain boundaries; (b) the Voronoi diagram generated in Matlab; (c) the original finite element model of solder matrix before introducing grain boundaries; (d) the finite element model with grain boundaries.....	115
Fig. 7.9 The finite element models incorporated with grain boundaries: (a) the model of solder joint before aging and (b) after aging for 1006.5 hours.	115
Fig. 7.10 The model of solder joint (a) before aging and (c) after aging with combined residual stress and grain boundaries; (b) and (d) illustrates the detailed stress distribution within the bulk solder.....	116
Fig. 7.11 The steps in the modelling for investigating the combined effects of residual stress and grain boundaries on the fracture behaviour of solder joints.....	117
Fig. 7.12 (a) nominal stress-strain curve [233] and (b) the derived true stress-strain curve of lead-free solder at the stain rate of 0.01.	118
Fig. 7.13 The post-failure behaviour of interfacial Cu_6Sn_5 and Cu_3Sn	120
Fig. 7.14 Power law form of the shear retention model [279].....	120
Fig. 7.15 Crack propagation within the original models of Cu/solder/Cu solder joints (a) with thin interfacial IMC layer and (b) with thick interfacial IMC layers.....	122
Fig. 7.16 Effect of residual stress on the crack initiation and propagation in solder joints with thin interfacial IMC layer: (a) the distribution of residual stress in solder matrix before tension; (b) the initiation of cracks within the solder joint in the beginning of tension; (c) the failure of the solder joints after tension.	123

Fig. 7.17 The crack propagation path in the stressed Sn99Cu1/Cu solder joint with thick interfacial IMC layers: (a) the stress distribution within the solder matrix before tension; (b) the failure of the solder joint after tension. 124

Fig. 7.18 Crack propagation path within the models for the solder joint (a) with thin and (b) thick interfacial IMC layers. 125

Fig. 7.19 The crack initiation and propagation in the models of solder joint with both residual stress and grain boundaries: (a) the model of solder joint with thin interfacial IMC layer; (b) the model with thick IMC layer. 126

List of Tables

Table 2.1 Mechanical properties of difference parts in Sn-based solder/Cu solder joints. ..	7
Table 2.2 Summary of the elastic properties of Ag_3Sn , Cu_6Sn_5 and Cu_3Sn based on calculation [65-67].	12
Table 2.3 Young's moduli and hardnesses of various types of IMCs.	13
Table 2.4 Young's moduli and hardness of Cu_6Sn_5 , Cu_3Sn , and Ni_3Sn_4 IMCs from nanoindentation tests along two perpendicular directions [71].	14
Table 2.5 Densities and relative atomic masses of the involved reagents (Sn and Cu) and products (Cu_6Sn_5 and Cu_3Sn) in solid-state reactions [16, 75-77].	15
Table 2.6 Calculated volume shrinkage induced by the growth of Ni_3Sn_4 , Cu_6Sn_5 and Cu_3Sn in aging.	15
Table 2.7 Summary of common techniques for the measurement of residual stress [98].	17
Table 4.1 Parameters and settings for cantilever bending tests on micro Cu_6Sn_5 and Cu_3Sn pillar.....	42
Table 4.2 Parameters and settings in the finite element modelling.....	47
Table 4.3 The tensile fracture strength of Cu_6Sn_5 based on modelling.....	54
Table 4.4 Tensile fracture strength of Cu_3Sn from modelling.....	61
Table 4.5 Comparison of tensile strengths of Cu_6Sn_5 and Cu_3Sn estimated by modelling and flexural formula.....	62
Table 5.1 The colour of Cu oxide films and its corresponding thickness [219].	68
Table 5.2 Densities and relative atomic masses of reagents (Sn, Cu) and products (Cu_6Sn_5 , Cu_3Sn) in the reactions in the aging of Sn99Cu1/Cu solder joints [16, 75-77]......	74
Table 5.3 Densities and relative atomic masses of the reagents (Sn and Cu) and the products (Cu_2O and SnO) in the oxidation of Sn99Cu1/Cu solder joints.	77
Table 5.4 Major parameters and settings of the involved materials in a solder joint in modelling [16]......	78
Table 6.1 Values of constants, C_1 - C_8 , in Equation (4) derived by fitting the contact area-plastic depth curve in Fig. 6.2.	86
Table 6.2 Correction factor ϵ for different indenter geometries [252].	87
Table 6.3 Parameters and settings of the nanoindentation tests.	89
Table 6.4 Parameters and settings used for the analysis of the load-displacement curves from nanoindentation tests.	89
Table 6.5 Coefficients of thermal expansion of solder, Cu_6Sn_5 , Cu_3Sn and Cu in Sn99Cu1/Cu solder joints [16].	105
Table 7.1 Dimensions of the interfacial IMC layers in the original finite element models.	109

Table 7.2 Parameters for the modelling on the distribution of residual stress within solder joints after aging.....	111
Table 7.3 Parameters for the fracture of bulk solder in solder joints.....	119
Table 7.4 Brittle cracking of Cu_6Sn_5 and Cu_3Sn	121
Table 7.5 Settings and parameters for the major mechanical properties of the involved materials in modelling.	121
Table 7.6 Summary of the fracture path in different finite element models and the comparison with experimental observation	127

List of Abbreviations

ATLAS	Argonne Tandem Linac Accelerator System
at.%	Atomic Percentage
BGA	Ball Grid Array
μ BGA	Micro Ball Grid Array
CTE	Coefficient of Thermal Expansion
CDM	Continuum Damage Mechanics
EBSD	Electron Backscatter Diffraction
EDX	Energy Dispersive X-ray Spectrometer
FC	Flip Chip
FCOB	Flip Chip on Board
FEA	Finite Element Analysis
FEM	Finite Element Model
FIB	Focused Ion Beam
IMC	Intermetallic Compound
SEM	Scanning Electron Microscopy
SLID	Solid-Liquid Inter Diffusion
TEM	Transmission Electron Microscopy
UBM	Under Bump Metallization
vol.%	Volume Percentage
wt.%	Weight Percentage

WLI	White Light Interferometer
X-FEM	Extended Finite-element Model
XRD	X-ray Diffraction

Chapter 1 Introduction

1.1 Context and problem definition

Electronic devices are extensively involved in our daily life and various industry sectors. The manufacturing process of electronic devices normally consists different levels of packaging, including zero level packaging (chip/wafer level), first level packaging (single/multi-chip module), second level packaging (PCB or card) and third level packaging (mother board) [1]. Among these different levels of packaging, solder joints are widely used to interconnect forming electrical path and provide mechanical support between components in the device (Fig. 1.1 a)) [2].

The solder joints in electronic devices are normally formed by reflowing, during which the molten solder is in contact with solid substrate. The metallurgical reactions between them can produce different layers of IMCs at the solder/pad interface, which provides the metallurgical bonding between the solder and substrate. The quality and reliability of the solder interconnects are fundamentally governed by the these IMCs [3]. For instance, the formation of a reliable Sn-based solder/Cu interconnect relies on the formation of interfacial Cu_6Sn_5 layer at the solder/Cu interface in reflowing process, which is also the key to maintain the reliability of the mechanical structure and the electrical path between the solder and Cu after reflowing.

However, after reflowing, the proportion of interfacial IMC layers in the entire solder joint can grow continuously during the service of the electronic devices (Fig. 1.1 b) and c)), particularly when the devices are exposed to an elevated temperature [4]. Furthermore, in order to achieve higher packaging density, the diameter of solder joints shrinks dramatically, from 760 μm in Ball Grid Array (BGA) to 75 μm in Flip Chip (FC), and the height decreases from 220 μm in μBGA to 60 μm in Flip Chip on Board (FCOB) [5]. In some specific applications, the interconnection height is even lower, such as the solder joints with a height of 8 μm in Argonne Tandem Linac Accelerator System (ATLAS) pixel detector [6, 7]. The miniaturization of solder interconnects in electronic devices leads to an even higher proportion of interfacial IMC layers in the solder joint.

Due to the notable difference between the mechanical properties of IMCs and solder alloys [8-10], the increasing proportion of interfacial IMC layers can lead to significant incompatible deformation between the solder and IMCs when the solder interconnect is subject to external load, such as impact or vibration. The deformation incompatibility within solder joint can pose a dramatic effect on the reliability of the entire solder joint.



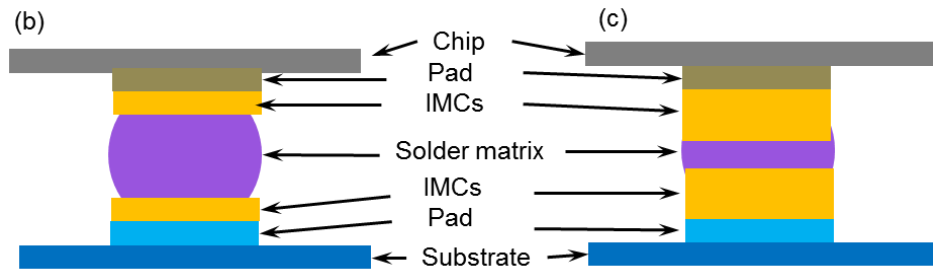


Fig. 1.1 Schematics of different layers in a solder joint between chip and substrate: (a) solder joints serve as interconnects between a chip and substrate; (b) initial interfacial IMC layers formed in reflow; (c) increased fraction of IMC layer after long-term service or aging.

Consequently, the growth of interfacial IMC layers in solder joints after aging and its effect on the reliability of solder joints were extensively investigated in the past decades. However, based on the literatures, as the size of solder joints continues to reduce, the following fundamental aspects regarding the growth of IMCs and its effect on the mechanical integrity of solder joints are identified, which demands further investigations :

(1) The protrusion of IMCs: Though the growth of interfacial IMC layers along the diffusion direction in solder joints both during reflowing and aging was studied extensively, the growth of IMCs perpendicular to the diffusion direction has rarely been reported in literatures. The protrusion of IMCs at the solder/pad interface is potentially correlated with the bulk diffusion and surface diffusion near the surface and the stress state of interfacial IMC layers in solder joints. Furthermore, the protruded IMCs could potentially alter the course of the growth of interfacial IMC layers parallel to the interdiffusion direction. This phenomena can crucially govern the long-term reliability of solder interconnects, in particular, in the applications that require a robust microstructural integrity from a solder joint.

(2) Fracture behaviour of interfacial IMC layers: The interfacial IMC layers are generally believed to be the origin of the degradation of the mechanical reliability of solder joints. It has been frequently reported that the fracture path within solder joints shifted from the solder matrix to the interfacial IMC layers due to the growth of interfacial IMCs after prolonged aging. The corresponding fracture mechanism is therefore expected to change from ductile fracture to brittle fracture. Hence, the fracture behaviour of interfacial IMC layers becomes a vital factor in determining the failure mechanism of solder joints, but this has been hardly concerned and investigated due to numerous challenges to enable a potential *in-situ* micro-scale test on the interfacial IMCs. It is therefore highly imperative to carry out such study in order to reveal the fracture behaviour of interfacial IMC layers which can eventually provide better understanding of the influence of interfacial IMC layers on the mechanical integrity of solder joints.

(3) Volume shrinkage: During the growth of interfacial IMC layers in aging, the total volume could decrease due to the increase in densities from the reagents (i.e. Cu and Sn) to the products (i.e. Cu_6Sn_5 and Cu_3Sn) in the solid-state reactions between solder and pad metallization. The volume shrinkage (or solder joint collapse) has frequently been ascribed as one of the main causes of the degradation of mechanical reliability during aging due to the potentially resulted voids and

residual stress at the solder/substrate interface. However, very few experimental works on the characterisation of such type of volume shrinkage can be found in the literatures, primarily due to the difficulties of observing the small dimensional changes that can be encountered in the course of IMCs growth.

(4) Residual stress: The residual stress within solder joints is another key factor that contributes to the failure of solder joints under external loading. It was reported that the fracture strength of solder joints decreased with prolonged aging durations, which could possibly be resulted from the increase of residual stress within solder joints. However, the stress evolution in solder joints as aging progresses and the potential correlation between the residual stress and the growth of interfacial IMC layers is yet to be fully understood, as stress/strain status can fundamentally alter the course of the failure of a solder joint.

(5) Crack initiation and propagation in solder joints: It has been frequently recognised that the growth of interfacial IMC layers can affect the initiation and propagation of cracks in solder joint under an exerted load. However, the direct observation of the crack initiation and propagation potentially requires an *in-situ* test with an instrument of high resolution observation, leaving the modelling a more versatile and promising approach to understand the mechanism. However, modelling on the fracture behaviour of solder joints was often undertaken primarily on the stress distribution within solder joints, for instance, under a given external loading condition. There is a lack of practice in utilising numerical analysis to simulate the crack initiation and propagation within solder joints, thus the effect of interfacial IMC layers, microstructure and residual stress on the fracture behaviour of the solder joints can be elaborated in further details.

1.2 Scope of the research

In the thesis, lead-free Sn99Cu1/Cu solder joint was the focus in the experimental work. The growth of IMCs both along and perpendicular to the interdiffusion direction were investigated. Due to the thin interfacial Cu_6Sn_5 and Cu_3Sn layers at the Sn99Cu1/Cu interface, the fracture behaviour of Cu-Sn IMCs were studied by micro cantilever bending with the combination of FIB and nanoindentation. Hence, the micro pillars could be fractured by the tensile stress at the bottom of the pillar. Due to the increase in the densities during the phase transformation in the growth of IMCs, the resultant collapse of solder joint is a three-dimensional phenomenon. But it was characterised by the reduction of joint height after aging, since it was difficult to maintain the quality and integrity of all the involved sample surfaces for the precise measurement during experiments. Because of the thin IMC layer, the residual stress induced by its growth could also be more prominent at the Sn99Cu1 solder/Cu interface. Therefore, the residual stress in solder joint was studied at the interfacial Cu_6Sn_5 and Cu_3Sn layers and the adjacent solder and Cu at both the centre and the edge of solder joints after progressively extended aging. For crack initiation and crack propagation in solder joints, it is challenging to capture in experiments. Therefore, FEA was employed to investigate the effects of IMC layers, grain boundaries and residual stress on the path of crack propagation in solder joints under tensile load.

1.3 Aims and objectives

The primary aim of this thesis is to investigate the influence of the growth of interfacial IMCs on the mechanical integrity of solder joints based on the fracture behaviour of interfacial IMC layers and the residual stresses within a solder joint. Against such an overall aim, following objectives of the research can therefore be identified:

1. **Characterisation of the perpendicular growth of IMCs:** The morphology of the perpendicular IMCs at Sn99Cu1 solder/Cu interface will be revealed after progressively prolonged aging and followed by detailed measurement of its height. The correlation between the growth of perpendicular IMCs and aging durations can then be proposed, based on which the potential dominant growth mechanism can be proposed. Due to the potential mutual effect between the planar growth and perpendicular growth of IMCs, the comparison between them regarding growth rates, dominant growth mechanism will thereby be elaborated.
2. **Fracture characteristics of Cu_6Sn_5 and Cu_3Sn :** Due to the micro-scale thickness of interfacial Cu_6Sn_5 and Cu_3Sn layers at the solder/Cu interface, micro-pillar Cu_6Sn_5 and Cu_3Sn specimens need to be designed and prepared to enable mechanical tests on them individually without involving interferences of any adjacent materials in the solder joints. The probable fracture mechanisms of Cu_6Sn_5 and Cu_3Sn can then be proposed based on the examination of the fracture morphology of Cu_6Sn_5 and Cu_3Sn micro specimens after the tests. At the same time, the fracture strength and strain of these two IMCs should also be derived.
3. **Collapse of solder joints induced by the growth of interfacial IMC layers:** Due to the challenge in determining the involved volume of Sn and Cu in the solid-state reactions, the volume shrinkage should be characterised by evaluating the height reduction of the solder joint after aging. Its dependence on the aging durations can therefore be considered. Because both Cu_6Sn_5 and Cu_3Sn are produced during aging, the contribution of the growth of each type of IMCs to the overall reduction of joint height should be calculated and discussed.
4. **Evolution of residual stress within solder joints:** The volume shrinkage induced by the growth of interfacial IMC layers is constrained by the attached solder and Cu, which could lead to residual stress at the solder/Cu interface. Therefore, the resultant residual stress within interfacial Cu_6Sn_5 and Cu_3Sn layers, the adjacent solder matrix and Cu substrate should be estimated at both the centre and edge of the solder joints. The effect of the growth of interfacial IMC layers on the stress evolution in aging can thereby be understood, as such the mechanisms that can contribute to the evolution of residual stress within solder joint may be proposed.
5. **Modelling on the fracture behaviour of solder joint:** Finite element models as a powerful simulation method can enable further understanding of fracture behaviour of solder joints by building various factors into the models. These factors may contribute to the failure of solder joints, including the microstructure of solder joints, residual stress and the crack within interfacial IMCs. The effect of these factors on the crack initiation and propagation in solder

joints under tension should be investigated separately, so that a clearer understanding of various factors that are induced by the growth of IMC layers on the failure of solder joint can be provided.

1.4 Structure of the thesis

The thesis consists of eight chapters as illustrated in Fig. 1.2. Chapter 1 provides a general background of the work in the thesis and presents the identified problems and challenges based on main findings from the literatures, and the aims and objectives of this thesis are also described.

In chapter 2, a number of literatures about the growth of interfacial IMC layers in solder joints and its effect on the reliability of solder joints were reviewed to provide the foundation of relevant knowledge and the state of art technologies towards the identified objectives. It covers primarily the microstructural evolution of solder joints, mechanical properties of interfacial IMCs, volume shrinkage in solder joints, the measurement of residual stress in solder joints and the modelling on the reliability of solder joints.

The investigation on the planar and perpendicular growth of interfacial IMCs in Sn99Cu1/Cu solder joints is presented in chapter 3. The planar growth of interfacial IMC layers in Sn99Cu1/Cu solder joints was studied by polishing and etching to reveal cross sectional view of solder joints after aging. The protrusion of IMCs was observed by specific designed specimens which can enable the measurement of the height of IMCs by white light interferometer (WLI). The comparison between the growth characteristics of interfacial IMCs along these two directions were then made accordingly.

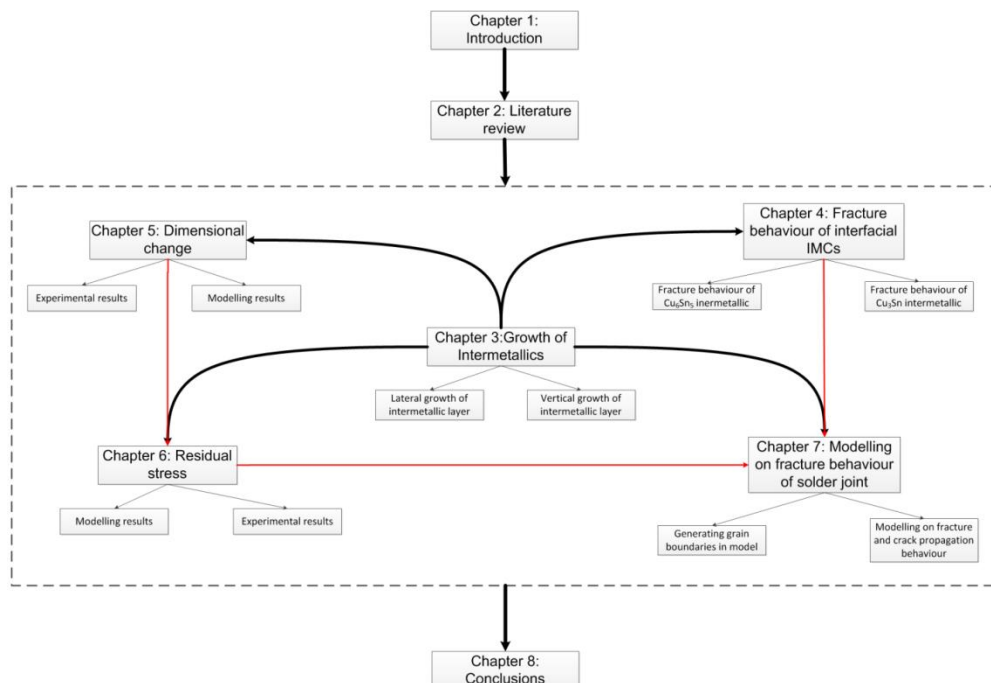


Fig. 1.2 Schematic of the structure of the thesis.

Chapter 4 focuses on the characterisation of the fracture behaviour of interfacial Cu_6Sn_5 and Cu_3Sn that commonly formed at the Sn-based solder/Cu interface. The micrometres thick interfacial

Cu_6Sn_5 and Cu_3Sn layers were machined by Focused Ion Beam (FIB) into micro pillars for the followed cantilever bending tests. Both Scanning Electron Microscope (SEM) and Energy-dispersive X-ray spectroscopy (EDX) were then utilised to examine the fracture surface of tested IMC pillars for the analysis of possible fracture mechanisms. The tensile fracture strength and strain of the investigated Cu_6Sn_5 and Cu_3Sn were then evaluated by finite element modelling.

Chapter 5 describes the measurement of the minimal amount of the shrinkage of the specifically designed solder interconnect specimens after aging. The correlation between the volume shrinkage and the aging duration was found based on surface profiles by the measurement of Zygo (a white light surface profiler). A preliminary investigation on the effect of the volume shrinkage on the solder joint was also implemented.

The volume shrinkage of solder joints is subject to the constraints between the solder and Cu substrate, causing the internal residual stresses. In chapter 6, the measurements of the residual stress at the solder/Cu interface are presented. In such case, the nano Vickers indenter was used to make series of nano indents at the solder, interfacial Cu_6Sn_5 layer, Cu_3Sn layer and Cu substrate in Sn99Cu1/Cu solder joints after aging. The comparison of the evolution of residual stress within different interlayers with progressively prolonged aging time was therefore possible.

Modelling on the fracture behaviour of solder joints was conducted and the results are discussed in chapter 7. The major factors that may affect the fracture behaviour of solder joints, including the thickness of IMCs, residual stresses, and microstructure, were incorporated in the finite element models step by step to reveal the influence of individual factors on the fracture propagation path within solder joints under the tension.

Based on the presented work and discussions in the previous chapters, chapter 8 summarises the major findings in each chapters for the entire thesis, and based on the current work and main results, a number of recommendations and suggestions for further work were also provided in this chapter.

Chapter 2 Literature review

In this chapter, the literatures regarding the growth of interfacial IMC layers in solder joints, mechanical properties of IMCs and the subsequent effect on the volume change, stress state and failure of solder joints are summarised to serve as the foundation of the research in the following chapters. Specifically, papers about the Sn-based solder/Cu solder joints are particularly concerned in this chapter as Sn99Cu1/Cu solder joints were performed as the samples in the experimental work in this thesis.

2.1 Growth of IMC layers

Electronic products, particularly consumable electronic devices, are generally developing towards smaller size but with more powerful functions, leading to the continuous miniaturization of the solder joints in the devices [11]. The volume fraction of the interfacial IMC layers produced during the reflowing process can also increase notably in service. This is particularly true in lead-free solder joints, since a higher growth rate of the IMCs was observed in the lead-free solder joints in comparison to the growth of interfacial IMCs in conventional Sn–Pb solder joints [12].

However, the mechanical properties of interfacial IMC (i.e. Cu_6Sn_5 , Cu_3Sn) layers are dissimilar from the properties of solder and substrate in Sn/Cu solder joints, as listed in Table 2.1. Therefore, the growing proportion of interfacial IMC layers could result in deformation incompatibility within the solder joint under external loads, which could further lead to significant degradation in the mechanical reliability of solder joints [13-15]. Hence, the growth of interfacial IMC layers in solder joints received massive attention of researchers in the past decades.

Table 2.1 Mechanical properties of difference parts in Sn-based solder/Cu solder joints.

	Cu [16]	Solder [16]	Cu_6Sn_5 [17]	Cu_3Sn [17]
Yield strength (MPa)	68.9	24.8	-	-
Ultimate tensile strength (MPa)	220	34.5~48.3	-	-
Young's modulus (GPa)	129.8 [18]	52.73	114.7 [19]	131.9 [20]
Poisson's ratio	0.339	0.36	0.309	0.299
Hardness	37 (Brinell)	14.8 (Brinell)	358 (Brinell) [21]	325 (Brinell) [21]

** Note: The Vickers hardness of Cu_6Sn_5 and Cu_3Sn in reference [21] was converted to Brinell hardness for comparison. The conversion was done at <http://www.tribology-abc.com/calculators/hardness.htm>.

Generally, the planar growth of interfacial IMC layers involves two processes: reflowing (the formation of IMC layer at solder/pad interface) and long-term exposure to an elevated temperature (the growth of interfacial IMC layers due to solid-state reactions). Apart from the planar growth of interfacial IMC layers, the IMCs could also protrude out of the sample surface in perpendicular to

the interdiffusion between solder and substrate during the aging. Therefore, the literatures about the growth of interfacial IMC layers will be divided in to following parts: formation of planar interfacial IMC layers in reflowing, growth of planar IMC layer in aging and the protrusion of IMCs.

2.1.1 Formation of planar interfacial IMC layers in reflowing

During reflowing, two types of IMCs, Cu_6Sn_5 and Cu_3Sn , can be produced due to the reactions between molten Sn-based solder and Cu substrate. This type of IMC layer normally covers the entire solder/Cu contact plane, so it is named as the planar interfacial IMC layers in the thesis.

It is generally accepted that the planar interfacial Cu_6Sn_5 layer is formed in reflowing, which was confirmed by the observation with both SEM and TEM [22, 23]. The interfacial Cu_6Sn_5 layer after reflowing is normally observed to be in scalloped shape [24]. K. N. Tu *et al.* reported that the scalloped shape was thermodynamically stable in molten solder/Cu system in reflowing based on the observation that the layer-type Cu_6Sn_5 layer transformed back to scalloped in multi-reflowing [25]. The growth mechanism of interfacial Cu_6Sn_5 during aging was further suggested by A. M. Gusak and K. N. Tu [26]. From the cross-sectional TEM images of Cu_6Sn_5 scallops after reflowing, the diffusion channels, which serve as rapid diffusion paths for Cu atoms to diffuse into the molten solder for the reaction, were identified between the scalloped Cu_6Sn_5 [26]. The observed channels can be regarded as the direct proof that reveals the growth mechanism of Cu_6Sn_5 in reflowing. But, J. Görlich also argued that those channels can also be interpreted as ordinary grain boundaries separating two grains of Cu_6Sn_5 [27].

In contrast, the existence of interfacial Cu_3Sn layer in solder joint after reflowing remains controversial. The Cu_3Sn layer was reported to be a thin layer with the thickness of about 100 nm or discontinuous scallops on Cu substrate after reflowing [22, 28]. But, other researchers also reported that Cu_3Sn phase was absent in the SEM images of interfacial IMC layers in solder joints after reflowing [29-31].

For solder joints containing Ag, such as Sn3.0Ag0.5Cu solder/Cu solder joints, the precipitate of Ag_3Sn particles during the cooling is also worth of notice [32]. Nano- Ag_3Sn particles were observed on the surfaces of the Cu_6Sn_5 grains after reflowing, and the size of the particles increased with higher soldering temperature, longer reflowing time and lower cooling rate [33-38]. Ochoa *et al.* reported that at very fast cooling rate (24°C/s), a combination of Sn dendrites and a eutectic mixture that consisted of a fine dispersion of Ag_3Sn particles in Sn matrix was formed, but at slower cooling rates (0.1°C/s) a completely eutectic microstructure was formed with the Ag_3Sn forming in needle-like form [39-41]. If the precipitated Ag_3Sn particles congregate along the Sn grain boundaries or the interfacial Cu_6Sn_5 layer, they can serve as the crack initiation sites under exerted loads, which can lead to decrease in mechanical strength of the solder joint [32].

2.1.2 Planar Growth of IMC layers

2.1.2.1 The correlation between the growth of IMC layers and aging duration

In the service of electronic devices, the solder interconnects are normally exposed to elevated temperature, which can promote the planar growth of interfacial IMC layers [42]. In order to

investigate the growth of interfacial IMC layers in experiments, solder joints are normally stored at high temperature, such as temperatures above 100°C, to accelerate the growth of interfacial IMC layers. The cross section of the solder joints can then be exposed and etched for the measurement of the thickness of IMC layer after progressively prolonged aging. The correlation between the thickness of interfacial IMC layers and aging durations is often reported to follow parabolic law [43, 44]

$$H = h_0 + K \times \sqrt{t} \quad (2.1)$$

where H is the thickness of interfacial IMC layers after aging; h_0 is the initial thickness of interfacial IMC layers before aging; K is the diffusion coefficient; t is aging durations. The diffusion coefficient K is the slope of the $H-t^{1/2}$ curve, which can be derived by curve fitting. K is also involved in the Arrhenius equation, which is correlated with the activation energy of the growth of interfacial IMC layers [45]

$$K = A \exp(-E/RT) \quad (2.2)$$

where A is the temperature-independent pre-exponential factor; E is the activation energy of the growth of interfacial IMC layers; R is the ideal gas constant; T is the absolute temperature. This equation can be utilised to derive the activation energy of the growth of interfacial IMC layers in aging.

2.1.2.2 Growth mechanisms of interfacial IMC layers

During the growth and ripening of interfacial IMC layers at the Sn-based solder/Cu interface in aging, Cu and Sn are the two diffusion elements involved in the interdiffusion. The comparison of the diffusion rates of Cu and Sn is one of the fundamental issues for the understanding of the growth mechanism of interfacial Cu_6Sn_5 and Cu_3Sn layers in aging. If Cu is the dominant diffusion element, the growth of interfacial Cu_6Sn_5 and Cu_3Sn layers will mainly rely on the reaction between Cu and Sn at the solder/ Cu_6Sn_5 interface and Cu_6Sn_5/Cu_3Sn interface respectively, leading to the movement of solder/ Cu_6Sn_5 and Cu_6Sn_5/Cu_3Sn interfaces towards the solder. Meanwhile, due to the diffusion and consumption of Cu, the Cu_3Sn/Cu interface will move towards the Cu side. In contrast, if Sn atoms diffuse faster than Cu atoms during aging, the thickening of interfacial IMC layers will primarily depend on the motion of Cu_3Sn/Cu and Cu_6Sn_5/Cu_3Sn interfaces towards the Cu. But the solder/ Cu_6Sn_5 interface can still move towards solder, since the solder is consumed by the solid-state reactions.

However, in literatures, the dominant diffusion species in Sn/Cu solder joint during aging still remains controversial. K. N. Tu *et al.* used porous W thin film as diffusion markers to determine the dominant diffusing species in bimetallic thin Sn/Cu films after aging above 100°C. It was found that Cu was the dominant diffusing species based on the motion of the marker [46]. The Kirkendall voids formed within interfacial Cu_3Sn layer were also interpreted as a type of diffusion marker to analyse the relative fluxes of Cu and Sn by Z. Kejun *et al.*. The reasoning was that an existing void at the Cu_3Sn/Cu interface would remain there if Cu were the only diffusing species. On the other hand, the void would be displaced into the interfacial Cu_3Sn layer when some of the Sn atoms diffused to the Cu_3Sn/Cu interface to react with the Cu behind the void. It was observed that most of the voids

were near the interface while some were in the Cu_3Sn layer, so they concluded that Cu was the dominant diffusing species in Cu_3Sn layer, yet some diffusion of Sn atoms also occurred in the interfacial Cu_3Sn layer [47].

However, Onishi Masami reported a reverse motion direction of molybdenum markers in Sn-Cu diffusion couples after aging at 220°C for 900 hours [48]. Similar movement of markers was also confirmed by H.C. Bhedwar *et al.* in Sn-Cu diffusion couples [49]. Jiunn Chen *et al.* also suggested that Sn atoms were the dominant diffusion species based on the first-principles calculations [50]. Hence, it is also reasonable to argue that the diffusion of Sn is much faster than that of Cu in aging. This appears to contradict the above conclusion that Cu is the dominant diffusion species, which could be primarily attributed to the different temperatures in literatures. According to equation (2.2) in section 2.1.2.1, the diffusion coefficient primarily depends on the aging temperature, which means that atoms can diffuse faster under higher temperature. Onishi Masami's work was carried out at 220°C [48], which is significantly higher than the temperature in the work reported by K. N. Tu *et al.* [46]. The increase in temperature can possibly raise the mobility of Sn atoms much more in comparison to the movement of Cu atoms, since 220°C is close to the melting point of Sn. This can result in changes in the dominant diffusion elements at low and high temperatures in Cu-Sn diffusion couple.

The dominant diffusion element in Sn-Cu diffusion couple primarily governs the growth direction of interfacial IMC layers. Because the dominant diffusion element remains controversial as discussed above, for simplicity, Cu is assumed to be the dominant diffusion species in the interdiffusion between Sn-based solder and Cu in the following discussions in chapter 2.

During aging, the growth of interfacial Cu_6Sn_5 layer relies on the diffusion of Sn and Cu atoms and the followed solid-state reaction, $6Cu+5Sn\rightarrow Cu_6Sn_5$. The adjacent solder matrix can serve as the source of Sn atoms for the reaction, thus Cu atoms need to diffuse through the existed IMC layer to react with Sn atoms near the Cu_6Sn_5 /solder interface. So the solder/ Cu_6Sn_5 interface generally moves towards the solder due to the consumption of solder [47, 51].

For the growth of interfacial Cu_3Sn layer, two solid-state reactions can contribute to its thickening, $3Cu+Sn\rightarrow Cu_3Sn$ and $Cu_6Sn_5+9Cu\rightarrow 5Cu_3Sn$ [51]. For the first reaction, Sn atoms diffuse to the Cu_3Sn /Cu interface to react with Cu atoms, thus the Cu_3Sn layer grows. Hence, the Cu_3Sn /Cu interface retracts during the growth of interfacial Cu_3Sn layer [52].

For the reaction $Cu_6Sn_5+9Cu\rightarrow 5Cu_3Sn$, it involves the decomposition of Cu_6Sn_5 , which happens after the Cu atoms arrive at the interface of Cu_3Sn / Cu_6Sn_5 by diffusion through the grain boundaries of the Cu_3Sn [44]. Because of the consumption of Cu atoms by this reaction, the amount of Cu atoms that can diffuse to the Cu_6Sn_5 /solder interface is greatly reduced, limiting the growth of Cu_6Sn_5 on the solder side. As the result, Cu_3Sn grows rapidly with temperature and time by consuming Cu_6Sn_5 at the interface of Cu_3Sn / Cu_6Sn_5 , which makes the Cu_3Sn / Cu_6Sn_5 interface towards the Cu_6Sn_5 [53, 54].

2.1.2.3 Morphological evolution in aging

During the growth of interfacial Cu_6Sn_5 and Cu_3Sn layers, the morphology of Cu_6Sn_5 layer evolves from dendritic to layer-type after prolonged aging, while the interfacial Cu_3Sn layer remains

layer-type. There are generally two mechanisms that possibly contribute to the morphological evolution of interfacial Cu_6Sn_5 layer, variation in diffusion distance [54] and curvature effect [55].

The evolution of interfacial Cu_6Sn_5 layer fundamentally relies on the interdiffusion and reactions between Sn and Cu atoms in aging. It is assumed that Cu atoms can diffuse through the thin Cu_3Sn layer quickly, but it takes a longer time for them to diffuse through the interfacial Cu_6Sn_5 layer because of the longer diffusion distance [47]. The diffusion distance within the interfacial Cu_6Sn_5 layer further varies with the locations at the peaks and valleys of the Cu_6Sn_5 scallops, longer at the peaks and shorter at the valleys. Consequently, it can be expected that the Cu_6Sn_5 grows faster at the valleys than the growth at the peaks. As a result, Cu_6Sn_5 layer is flattened after extended aging [54].

Curvature effect can also contribute to the morphological evolution of the interfacial Cu_6Sn_5 layer in aging. Different curvature rates at the peaks and the valleys can lead to concentration gradient of Cu atoms between them. Hence, the Cu atoms move from the peaks where the concentration is higher to the valleys with lower concentration, hindering the growth of Cu_6Sn_5 layer at the peaks and accelerating the growth at the valleys [55]. Consequently, the entire Cu_6Sn_5 layer becomes layer-type.

After the morphological transition of the interfacial Cu_6Sn_5 layer, the layer generally keeps growing as a layer with relatively more even thickness.

2.1.3 Perpendicular growth of IMCs

The interfacial IMC layer which grows along the interdiffusion direction between the solder and the substrate was extensively studied. Moreover, due to the interdiffusion in aging, the IMCs could also protrude out of the surface of solder joint, which is perpendicular to the interdiffusion direction, as illustrated in Fig. 2.1.

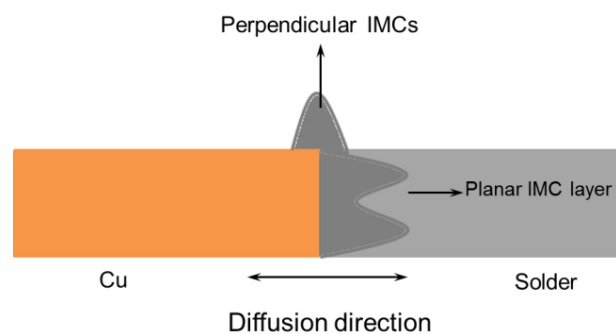


Fig. 2.1 Schematic of the planar and perpendicular growth of interfacial IMCs at the Sn/Cu interface in aging.

The protrusion of IMCs was first reported in electromigration tests, in which a line of IMCs was found protruding out of the polished sample surface after current stressing [56]. But no further details were provided. A more detailed work on the protrusion of IMCs in SnBi/Cu solder joints was reported by P. J. Shang *et al.* [57]. It was suggested that the protrusion of IMCs at the solder/substrate interface can be divided into two stages. In the initial stage of aging, the height of IMC layer on the Cu surface increased very fast, and Cu_6Sn_5 was the dominant phase in the protruded IMCs. Furthermore, the IMC on the Cu surface grew faster and thicker than the planar

growth of interfacial IMC layers in the bulk solder joint at the initial stage of aging. With the extension of aging duration, the growth rate of IMCs on the Cu surface was very slow, even slower than that in the bulk solder joint. The main event happened in the second stage was the Cu_3Sn phase started growing by the consumption of Cu_6Sn_5 phase [57]. During the aging, the protrusion of IMCs was believed to be resulted by the compressive stress at the solder/substrate interface in solder joints [56, 58].

2.2 Mechanical properties of interfacial IMC layers

The excessively thick interfacial IMC layers are often attributed to be one of the major causes that deteriorate the mechanical reliability of solder joints [59]. Furthermore, in solid-liquid inter diffusion (SLID) bonding for die attach in high-temperature applications, the interconnect mainly consists of IMCs [60-64]. Therefore, extensive researches have been reported regarding the characterisation of the mechanical properties of the interfacial IMC layers.

Due to the micro thickness of interfacial IMC layers at the solder/substrate interface, it is challenging to carry out comprehensive experimental studies on the interfacial IMCs in solder joints. Numerical calculation was therefore utilised to evaluate the moduli of common IMCs, such as Ag_3Sn , Cu_6Sn_5 and Cu_3Sn listed in Table 2.2 [65-67]. Among the listed three IMCs, both Ag_3Sn and Cu_3Sn were reported with notable anisotropy based on the calculation [65, 67].

Table 2.2 Summary of the elastic properties of Ag_3Sn , Cu_6Sn_5 and Cu_3Sn based on calculation [65-67].

	Shear modulus (GPa)	Bulk modulus (GPa)	Young's modulus (GPa)	Poisson's ratio	Anisotropy
Ag_3Sn	28.6	84	77	0.347	Yes
Cu_6Sn_5	46	95	119	0.29	Not mentioned
Cu_3Sn	56	132	147	0.315	Yes

However, the mechanical properties of IMCs listed in Table 2.2 are based on ideal crystal structures, which are probably violated in the interfacial IMC layers in real solder joints as they normally contain numerous defects. Therefore, experimental investigation on the mechanical properties of interfacial IMC layers at the solder/substrate interface is still the focus of studies.

Given the micro thickness of interfacial IMC layers in solder joints, the positioning accuracy and the materials involved in the mechanical tests should be in micro scale, which is beyond the capability of traditional tensile and shear test rigs. In order to conduct tests on interfacial IMC layers, both casting and extended annealing above the liquidus temperature were employed to prepare IMCs with large volume, so that ordinary test methods can be applied in macro scale [70]. But, the microstructure of casted IMCs could be significantly different from the microstructure of interfacial IMC layers that produced by solid-state reactions at solder/substrate interface during aging. This can limit the applicability of the obtained results.

Table 2.3 Young's moduli and hardnesses of various IMCs.

Materials	Specimens	Hardness (GPa)	Reduced Modulus, E_r (GPa)	E (GPa)	References
Cu_6Sn_5	Sn-3.5Ag/Cu	6.1±0.5	123±6	125±7	[20]
	Sn-37Pb/Cu	5.6±0.4	116±4	116±4	[20]
	Bulk	6.3±0.3	114±1	115±2	[20]
	Sn-3.8Ag-0.7Cu/Cu	5.7±0.5	-	97±3	[68]
Cu_3Sn	Sn-3.5Ag/Cu	5.7±0.6	132±5	136±6	[20]
	Bulk	5.7±0.3	120±6	122±6	[20]
Ni_3Sn_4	Sn-3.5Ag/Ni	8.1±0.6	140±8	143±9	[20]
	Sn-37Pb/Ni	8.9±0.6	136±6	138±7	[20]
	Sn-3.8Ag-0.7Cu/Ni-Au	7±1	-	160±5	[68]
Cu-Ni-Sn IMC	95.5Sn-3.8Ag-0.7Cu /ENIG	-	-	207±6 (0 h); 165 ± 3(260h); 146 ± 3(500h)	[69]

Therefore, nanoindentation platforms, which are normally equipped with nano indenters and precise positioning system, are extensively used in evaluating the Young's modulus and hardness of interfacial IMC layers in solder joints, such as Cu_6Sn_5 , Cu_3Sn and Ni_3Sn_4 [20, 71]. The tests were normally implemented on the interfacial IMC layers exposed by grinding and polishing the solder joints after aging. Table 2.3 lists the mechanical properties of IMCs in solder joints obtained by nanoindentation tests [20, 68, 69].

The anisotropy of interfacial IMC layers in solder joint has also been investigated by characterizing the Young's modulus along specific directions with nanoindentation. Soud Farhan Choudhury *et al.* utilized the combination of nanoindentation and SEM-EBSD imaging to investigate the effect of crystallographic orientation on the mechanical properties of Cu_6Sn_5 . The results indicated that the hardness of Cu_6Sn_5 grains with different orientation along and normal to the growth axis was statistically indistinguishable [72]. Ping-Feng Yang *et al.* also performed nanoindentation tests along the directions lateral and perpendicular to the IMC layers. The Young's modulus and hardness from the tests are listed in Table 2.4. It shows minimal difference between the Young's moduli and hardness of Cu_6Sn_5 , Cu_3Sn and Ni_3Sn_4 from the tests in two perpendicular directions. This implies that these polycrystalline IMC aggregates are rather isotropic [71].

Table 2.4 Young's moduli and hardness of Cu_6Sn_5 , Cu_3Sn , and Ni_3Sn_4 IMCs from nanoindentation tests along two perpendicular directions [71].

IMC	Young's modulus (GPa)	Hardness (GPa)
Cu_6Sn_5	117 ± 2 (perpendicular)	6.4 ± 0.2 (perpendicular)
	119 ± 2 (lateral)	6.5 ± 0.1 (lateral)
Cu_3Sn	133 ± 4 (perpendicular)	6.3 ± 0.2 (perpendicular)
	132 ± 4 (lateral)	6.3 ± 0.1 (lateral)
Ni_3Sn_4	141 ± 4 (perpendicular)	6.3 ± 0.2 (perpendicular)
	140 ± 4 (lateral)	6.3 ± 0.2 (lateral)

From the Young's moduli of Cu_6Sn_5 and Cu_3Sn listed in Table 2.2, Table 2.3 and Table 2.4, it can be found that the calculated Young's moduli of IMCs are close to the corresponding experimental values obtained by nanoindentation. Furthermore, the Young's moduli of Cu_6Sn_5 , Cu_3Sn , and Ni_3Sn_4 listed in Table 2.4 also agree well with the corresponding values in Table 2.3. But there is a slight variation in the hardnesses of Cu_3Sn and Ni_3Sn_4 in the two tables due to potential differences in sample preparation and specific instruments for the tests in these two works.

Though the measured Young's modulus and hardness of interfacial IMCs can promote the understanding of the influence of interfacial IMC layers on the fracture of solder joints, only a few papers focused on fracture tests which specifically targeted the interfacial IMC layers in solder joint.

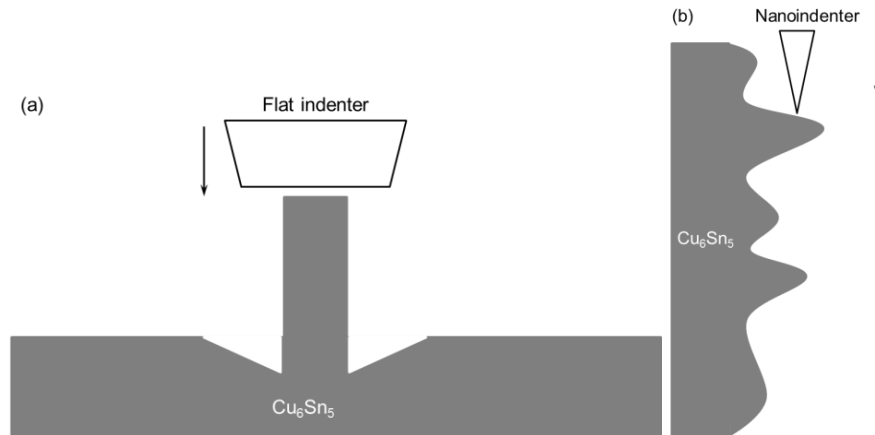


Fig. 2.2 Schematics of the test methodologies for the (a) compression tests [19] and (b) shear tests [74] on Cu_6Sn_5 at the solder/substrate interface by nanoindentation tests.

L. Jiang *et al.* milled micro Cu_6Sn_5 pillars in a thick interfacial Cu_6Sn_5 layer by FIB. The micro Cu_6Sn_5 pillars were then tested by compression load with nanoindentation test platform, as illustrated in Fig. 2.2 a). It was found that the compression strength of Cu_6Sn_5 was about 1.36 GPa and the strain to failure was approximately 1.37% [73]. Furthermore, the effect of grain orientation on the compression strength of Cu_6Sn_5 was also studied. The pillars oriented along the c-axis was found to have higher fracture strength (1724 ± 242 MPa) than those machined normal to the growth axis (1356 ± 64 MPa) [19].

The shear strength of Cu_6Sn_5 in solder joints was investigated by nanoindentation tests on the interfacial Cu_6Sn_5 layer revealed by extended etching (Fig. 2.2 b). The Cu_6Sn_5 dendrites were then

fractured by shear force applied with the nano indenter. The shear fracture strength of Cu_6Sn_5 was estimated to be about 670 MPa [74].

Both the shear test and compression test on Cu_6Sn_5 showed that the applied load increased linearly with the displacement of the nano indenter during the mechanical tests [19, 73, 74], which indicates that the Cu_6Sn_5 remains elastic before its fracture.

2.3 Volume shrinkage induced by the growth of IMCs

During aging, the interfacial IMC layers are produced by solid-state reactions between solder and pad metallization. The densities of the materials involved in the solid-state reactions in Sn-based solder/Cu solder joints are listed in Table 2.5. During the reactions, the densities increased from the reagents (i.e. Sn and Cu) to the products (i.e. Cu_6Sn_5 and Cu_3Sn) in the phase transformation. It can be deduced that the growth of IMCs in aging is accompanied by the decrease in total volume as the total mass in the reactions remains the same.

Table 2.5 Densities and relative atomic masses of reagents (Sn and Cu) and products (Cu_6Sn_5 and Cu_3Sn) in solid-state reactions [16, 75-77].

Materials	Sn	Cu_6Sn_5	Cu_3Sn	Cu
Density (g.cm ⁻³)	7.29	8.28	11.33	8.93
Relative atomic mass	118.7	974.5	309.2	63.5

Based on the available data on the densities and atomic masses, the volume shrinkage induced by the growth of interfacial IMC layers can be deduced numerically. Table 2.6 summarizes the calculated volume shrinkage due to the growth of IMCs in solder joints.

Table 2.6 Calculated volume shrinkage induced by the growth of Ni_3Sn_4 , Cu_6Sn_5 and Cu_3Sn in aging.

	Ni_3Sn_4	Cu_6Sn_5	Cu_3Sn
Volume shrinkage	10.7% [78]	5% [79]	8.5% [79]

However, due to the tiny amount of change in volume, most of the available literatures estimated this volume change numerically without experimental investigation. Up to date, only a few works reported the measurement of volume shrinkage in solder joints after aging [80-82]. The methodology in C. C. Li's work is illustrated in Fig. 2.3 [80, 81]. The Si substrate served as the reference surface to the measurement of the height of the Ni/Sn/Ni interconnects before and after aging at 180 °C. The selected temperature can facilitate the growth of IMCs and ensure the solder was solid during aging. As such, the comparison of surface profiles before and after aging can reveal the decrease in joint height induced by the growth of Ni-Sn IMCs. After aging, 7.3 % reduction of joint height was detected in the Ni-Sn-Ni specimens due to the growth of Ni_3Sn_4 [80, 81].

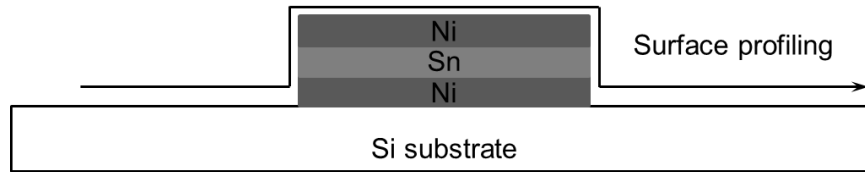


Fig. 2.3 Schematic of the design of the specimen for the direct measurement of volume shrinkage of Ni/Sn/Ni solder joints induced by the growth of Ni_3Sn_4 in aging [80, 81].

In an ordinary solder joint, the volume shrinkage induced by the growth of interfacial IMC layers is likely subject to the constraint from the attached solder and substrate, which hinders the observable reduction in joint height. Hence, the constrained volume shrinkage induced by the growth of IMCs can probably lead to the build-up of residual stress within solder joints during aging [79, 83, 84]. The resultant stress within the solder joint can further contribute to the growth of Sn whisker [85-88] in solder joints. If the volume shrinkage cannot be compensated by microstructural evolution, it will ultimately result in void formation within the interfacial IMC layers at solder/pad interface [89]. This could be ascribed to be one of the main causes that lead to the void formation in solder joints [54, 90], apart from the Kirkendall voids in the interfacial Cu_3Sn layer after aging [47].

The build-up of residual stress and the formation of voids could further facilitate the crack initiation and propagation in interfacial IMC layers under external loads, which deteriorates the mechanical reliability of solder joints [91-93]. Furthermore, if the growth of interfacial IMC layers is accelerated by exterior loads, such as current stressing and thermal cycling, the tensile stress induced by growth of IMCs can become the most significant driving force for crack coalescence during the tests [94-96].

2.4 Measurement of residual stress in solder joints

Residual stresses are those stresses retained within a body when no external force is acting. It is likely caused by misfits between different regions of the material, components or assembly [97]. Generally, the residual stress can be divided into three types according to the scale of its effect: type I which varies continuously over large distances, type II (the grain scale) and type III (the atomic scale) [98]. The accumulation of residual stress at smaller scale can result in the stress at a longer scale [97].

For solder joints, the residual stress could originate from the growth of interfacial IMC layers due to the constrained volume shrinkage in aging [3] and the mismatch of thermal expansion coefficients of different parts at elevated temperature [99]. The resultant residual stress can be categorized as type II. The build-up of residual stress within solder joint has been frequently ascribed to be the direct cause that degrades the mechanical reliability of solder joints [3, 100]. But the evolution of residual stress within solder joint has seldom been characterised experimentally.

There are various ways to estimate the residual stress in stressed materials, including monitoring the change in curvature, hole drilling, X-ray diffraction (XRD), ultrasonic method, magnetic method, Raman and nanoindentation tests. Table 2.7 lists the comparison between various techniques for the measurement of residual stress. Among the listed techniques, curvature

monitoring, ultrasonic methods, magnetic method and nanoindentation can measure the residual stress directly, while hole drilling, XRD, and Raman fundamentally rely on the strain measurement.

Table 2.7 Summary of common techniques for the measurement of residual stress [98].

Method	Penetration	Spatial resolution
Hole drilling	~1.2×hole diameter	50 µm depth
Curvature monitoring	0.1~0.5 of thickness	0.05 of thickness; no lateral resolution
X-ray diffraction	<50 µm (Al); <5 µm (Ti); <1 mm (with layer removal);	1 mm laterally; 20 µm depth
Hard X-ray (the X-ray with energy above 10 keV)	150~50 mm (Al)	20 µm lateral to incident beam; 1 mm parallel to beam
Ultrasonic	>10 cm	5 mm
Magnetic	10 mm	1 mm
Raman	< 1 µm	< 1 µm approximately

Hole drilling is based on the fact that the undisturbed regions of a stressed sample will relax into a different shape, thereby enabling the measurement of strain for the calculation of the residual stress [98]. For ultrasonic method, the ultrasonic speed can be changed when a material is subjected to residual stress, which provides a measure of the stress averaged along the wave path [101]. In stressed magnetostrictive materials, the preferred domain orientations are altered, causing domains most nearly oriented to a tensile stress to grow (positive magnetostriction) or shrink (negative magnetostriction). Stress induced magnetic anisotropy leads to the rotation of an induced magnetic field away from the applied direction [98, 102]. Characteristic Raman luminescence lines shift linearly with variations in the hydrostatic stress, which are useful because spectral shifts can be easily and accurately measured [98]. However, these four methods have seldom been used in studies on solder interconnects.

Curvature monitoring is a straightforward method to determine the stress level within coated layers [103]. It is based on the possibility that the coating of new layer could lead to the residual stress which is strong enough to bend a thin substrate. The residual stress within the coating can then be estimated by Stoney's equation, $P = \frac{4}{3} E \frac{d^2 z}{l^2 t}$, where P is the tension stress in the film; d is the thickness of the substrate; t is the thickness of deposited layer; z is the deflection; l is the length. J.Y. Song *et al.* employed this methodology to investigate the stress evolution induced by the reactive diffusion within deposited thin Sn/Cu films after aging [104]. It was found the initial tension stress within the film evolved to compression stress after prolonged aging.

X-ray diffraction is also widely used in the characterisation of residual stress within materials, which is based on the measurement of the shift of a diffraction peak position recorded for a different

Ψ (the angle between the normal of the sample and the normal of the diffracting plane). It is capable to reveal the change of crystal lattice in crystalized material [105-107].

However, the evaluation of residual stress by curvature monitoring requires a thin film specimen, which is not applicable in common solder joints. For X-ray diffraction, the high sensitivity means that the minimal amount of specimen should be handled carefully without inducing any new stress at the surface of the material [108]. This could also be challenging in sample preparation in some cases. Therefore, nanoindentation was proposed as a nanometer-order local stress-analysis technique. In particular, nanoindentation has been widely applied in characterizing the basic mechanical properties of thin films, such as the Young's Modulus, hardness [109, 110].

Many works have been reported to correlate the nanoindentation results with the residual stress in tested specimens. T. Y. Tsui *et al.* correlated the measured contact area of indents with the applied stress in the specimen [111]. Yun-Hee Lee *et al.* studied the effect of residual stress on the nanoindentation curve to understand the effect of residual stress on the nanoindentation data [112]. Zhi-Hui Xu *et al.* found that both the A_c/A_g (the ratio of the real contact area A_c to the geometrical area A_g) and the h_e/h_{max} (h_e is the elastic recovery, and h_{max} is the maximum penetration depth) followed a linear relationship with the σ_r/σ_y ratio (equi-biaxial residual stress), which may be used for the determination of the residual stress [113]. S. Suresh proposed a theoretical analysis to elucidate the effect of stress on the shape variation of the indentation curves [114],

For tensile residual stress

$$\sigma_r = H(1 - A_0/A) \quad (2.3)$$

For compressive stress

$$\sigma_r = H(1 - A_0/A)f \quad (2.4)$$

where A and A_0 are the contact area of nano indents with and without residual stress, respectively; H is the hardness of the material; $f = \sin\alpha$ is a geometric factor, where α is the indentation angle of an indenter. The theory relies on the fact that the residual stress within the specimen can alter the maximum force of the specimen in nanoindentation tests.

Based on this theory and surface profiling, the residual stress in quenched AISI 1045 steel was evaluated by depth controlled-nanoindentation tests by Li-na Zhu *et al.* [115]. Yun-Hee Lee also utilised similar methodology to evaluate the residual stresses in Diamond-like carbon (DLC)/Si and Au/Si thin films [116].

However, as far as the author can find, there is still lack of reports on the evolution of residual stress induced by the growth of interfacial IMC layers within solder joints after aging. Nanoindentation could be a promising technique to characterise the stress state within solder joint, so that the effect of microstructural evolution in aging on the reliability of solder joints can be clarified.

2.5 Modelling on the fracture behaviour of solder joints

From the literatures, the modelling on solder joints were generally about the stress distribution within solder joint and the life prediction of solder joints subjected to cycling load.

The modelling on the stress distribution within the solder joint normally focused on the effect of external loads, such as the stress state within a double-lap specimen subjected to shear tests [117]. The effect of thermal cycling on the stress within solder joint due to the mismatch of the coefficients of thermal expansion between different parts has also been frequently reported [118, 119].

The prediction of the lifetime of solder joints under cycling load by capturing the failure of solder joint in simulation is also the focus of modelling on solder joints. However, the initiation and propagation of cracks in any structures have always been very complicated phenomenon. In order to cope with this issue, two interrelated approaches were used in the past. The first approach consists of empirical methods, which relies on experimentally measured lifetime (or cycles-to-failure) data as a function of measurable physical quantities. The most widely used embodiment of this approach is the “Coffin-Manson” fatigue law [120]:

$$\Delta \varepsilon N_f^b = C \quad (2.5)$$

where $\Delta \varepsilon$ is the inelastic strain range during the load cycle; N_f is the number of cycles to failure; b and C are material constants measured (fitted) from fatigue tests.

This method does not address the damage mechanisms causing the failure, but focusing on describing the failure response for particular joints if the physical quantity is within the tested range. But, it cannot predict the fatigue failure of solder joints if the thermal–mechanical loads fall beyond the experimentally investigated range. Moreover, its application usually requires different curves for different loading conditions since the equation does not include any damage evolution processes. For instance, different Coffin–Manson equations are needed for the application in high (>1 Hz) and low frequency (<0.01 Hz) loading [121-123]. Despite the insufficiencies of this method, the empirical approach is still the main analytical tool for the design of solder joints [124]. However, the testing required to implement such an approach is a bottle-neck in attempts to shorten the design cycle.

The other approach can be categorized as a mechanistic method, which emphasizes describing the mechanical behaviours and damage evolution that lead to the final failure of solder joints [125, 126]. Constitutive behaviours of solder joints under cycling load are normally derived based on phenomenological [127, 128] or micromechanics-based models [129]. More recently, the concept of continuum damage mechanics (CDM) [130, 131] has been integrated into the unified constitutive relations of solders [132-135]. The accurate description of inelastic deformation and damage mechanics enables the model to predict the lifetime of solder joints as long as the solder material remains the same. However, a large number of material constants are needed to describe the mechanical behaviour and damage evolution in application, such as more than 20 material constants required in Frear *et al*'s model [133, 136]. Deriving these material constants could be challenging and costly.

These models are commonly used together with finite element modelling. The computational cost of a sophisticated constitutive law could also be very high. It is impractical to perform full-scale simulations of solder-connected devices under thermal–mechanical cyclic loading. The empirical method is simple to use once the cyclic stress–number of cycles to failure correlation are known. However, determining these curves could be costly and time-consuming, given the large number of cycles that need to be conducted for each type of loading.

In contrast, the mechanistic method provides potentially better understanding of the

temperature-dependent and rate-dependent deformation and failure mechanisms of solder joints. But, mechanistic models cannot be applied for quick assessment of the life of a solder joint. The cost of determining the numerous material constants for finite element modelling is also very high. Any analytical tools that combine the advantages of both empirical and mechanistic models and can hence provide quick and reasonable lifetime prediction for solder joints are of great value [137].

Furthermore, in the modelling on predicting the fatigue life of solder joints, the effect of the growth of interfacial IMC layers is seldom taken into account. But, the low fracture toughness and the brittleness of interfacial IMC layers [138] mean that the interfacial IMC layers can pose significant effect on the fracture behaviour of solder joints. Moreover, the traditional sample preparation methods, such as mounting, grinding and polishing, can probably induce a second crack during the sample preparation, which cannot be distinguished from the original cracks produced in the mechanical test. Alternatively, focused ion beam or broad ion beam should be employed to reveal the crack and minimise the induced damage during sample preparation. In comparison to the availability of ion milling instrument, finite element modelling could be a more promising and efficient tool to study the microstructural effect on the crack initiation and propagation within solder joints under external loads [139].

Up to date, only K.E. Yazdani reported the modelling about the effect of microstructure on the fracture behaviour and crack propagation within solder joints. A model incorporated with interfacial IMC layers with defects which enables the failure of interfacial IMC layers was built to study the crack propagation path within solder joint [140]. The work reported by Simin Li *et al.* further demonstrated that the associated application of Matlab and Python scripting was an efficient way to incorporate microstructures within the commercial finite element models [141]. Therefore, it is viable to introduce microstructural factors in the finite element to investigate the effect on the fracture behaviour of solder joints.

2.6 Summary

From the reviewed literatures in this chapter, it can be concluded that:

1. Though the planar growth of interfacial IMC layers has been studied extensively, the perpendicular growth of IMCs requires further investigation.
2. Many works on evaluating the Young's modulus and hardness of interfacial IMC layers by both numerical calculation and experiments have been reported. But, the fracture behaviours of IMCs, which determine the fracture mechanism of solder joints under external loads, remain seldom covered.
3. Volume shrinkage induced by the growth of interfacial IMC layers can lead to the void formation and build-up of residual stress within interfacial IMC layers at solder/substrate interface due to the constraint from the attached solder and substrate. Therefore, further study should be carried out to provide more comprehensive understanding of the volume shrinkage in the growth of interfacial IMC layers during aging.
4. The residual stress within solder joint can pose significant threat to the mechanical reliability of solder joints, but it is scarcely covered in literatures. Nanoindentation is a promising

approach to characterise the residual stress at the solder/Cu interface to provide better understanding of the effect of interfacial IMC layers on the reliability of solder joints.

5. The understanding of crack initiation and propagation within solder joint due to the growth of interfacial IMC layers is essential to interpret the effect of microstructure on the reliability of solder joints. Given the difficulty in capturing the crack initiation and propagation within solder joint in mechanical tests, modelling which incorporates the fracture of IMCs, defects within solder joints and growth of IMCs should be implemented to understand the effect of interfacial IMC layers on the fracture behaviour of solder joints.

Chapter 3 Growth of interfacial intermetallic compounds in Sn99Cu1/Cu solder joints in aging

3.1 Introduction

In Sn-based solder/Cu solder joints (i.e. Sn99Cu1/Cu solder joints), the opposing diffusion of Sn and Cu atoms can lead to solid-state reactions and the growth of interfacial IMC layers (i.e. Cu_6Sn_5 and Cu_3Sn) at the solder/substrate interface, which has been extensively investigated [142-146]. Since the growth of IMCs is parallel to the interdiffusion direction and covers the entire solder/Cu interface as illustrated in Fig. 3.1, this interfacial IMC layer is named as planar IMC layer or IMC_{planar} in this chapter. Moreover, the IMCs (i.e. Cu_6Sn_5) can also protrude out of the free surface of solder joints in perpendicular to the diffusion direction as illustrated in Fig. 3.1 [56]. This type of IMCs is named as perpendicular IMCs or $IMC_{perpendicular}$. Unlike the extensively studied planar IMCs, the perpendicular growth of IMCs has seldom been reported in literatures.

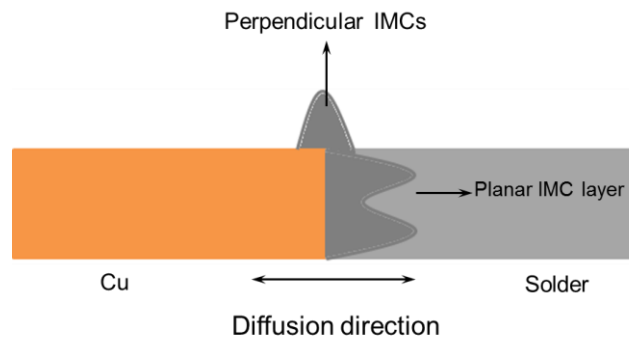


Fig. 3.1 The growth of IMCs in parallel and perpendicular to the interdiffusion direction.

In this chapter, the planar and perpendicular growth of IMCs in Sn99Cu1 solder/Cu solder joint were investigated individually by specifically designed specimens, followed by the comparisons and discussion about the differences between these two.

3.2 Planar growth of IMC layers

3.2.1 Experimental details

Proper amount of Sn99Cu1 solder was reflowed on polished Cu substrate (purity: 99.9%) to form the solder joint for the followed experiments. During the reflowing, a thermal couple was attached to the specimen to monitor the temperature of the specimen. The recorded reflow profile is illustrated in Fig. 3.2 a). The six specimens were then stored in an oven at 175°C to promote the planar growth of IMCs. After aging for every 168 hours, the specimens were taken out from the oven, followed by grinding and polishing to reveal the cross section of the solder joint as shown in Fig. 3.2 b). The specimens were then etched with ethanol and hydrochloric acid solution (20 vol.% concentrated hydrochloric acid + 80 vol.% ethanol) to remove the solder matrix by chemical reaction and thus reveal the interfacial Cu_6Sn_5 and Cu_3Sn layers. Olympus BX60M microscope was utilised for the observation of interfacial IMCs. The thickness of the interfacial IMC layers was then

measured by calculating the average distance between the traces that fit the boundaries of different layers (i.e. interfacial Cu_6Sn_5 , Cu_3Sn layers) with the software Image Pro (an image analysis software), as illustrated in Fig. 3.3.

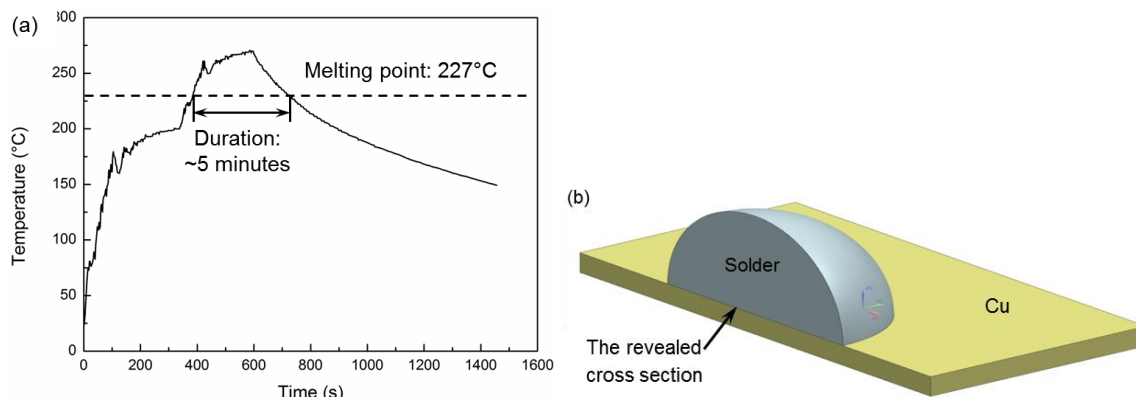


Fig. 3.2 Preparation of specimens: (a) reflow profile; (b) the schematic of specimens for the investigation of planar growth of IMCs.

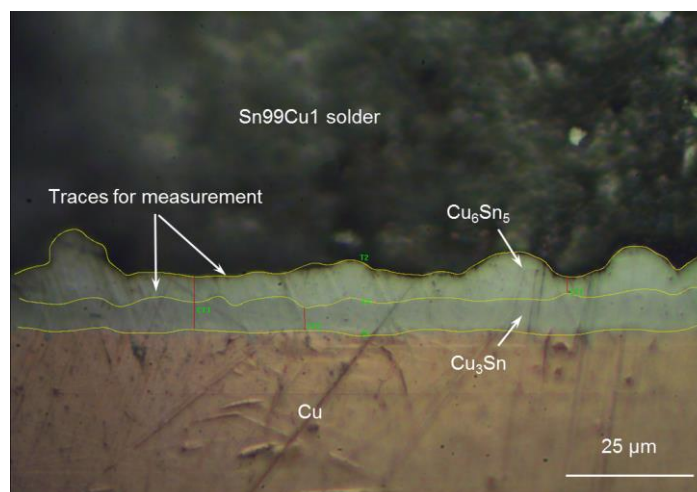


Fig. 3.3 The measurement of the thickness of planar Cu_6Sn_5 and Cu_3Sn layers.

3.2.2 Planar growth of interfacial IMC layers

Fig. 3.4 shows the comparison of the planar IMC layer in Sn99Cu1 solder/Cu solder joint before aging and after aging at 175°C for 1006.5 hours. It can be observed that the interfacial IMC layers grew significantly during aging, from about 5 μm before aging to approximately 15 μm after aging for 1006.5 hours.

Furthermore, from Fig. 3.4 a), only interfacial Cu_6Sn_5 layer can be identified at the solder/Cu interface without any notable Cu_3Sn layer. However, the interfacial Cu_3Sn layer was reported to be present after extended reflowing [147-149]. The absence of the Cu_3Sn layer at the Sn99Cu1 solder/Cu interface in this work could be attributed to the insufficient reflowing time for the formation of the interfacial Cu_3Sn layer before cooling [150-152]. It could also be due to the low magnification of the used microscope and SEM that were incapable to reveal the thin interfacial Cu_3Sn layer. After aging, the Cu_6Sn_5 layer thickened notably and a layer of Cu_3Sn was produced between the Cu_6Sn_5 layer and Cu substrate, as shown in Fig. 3.4 b).

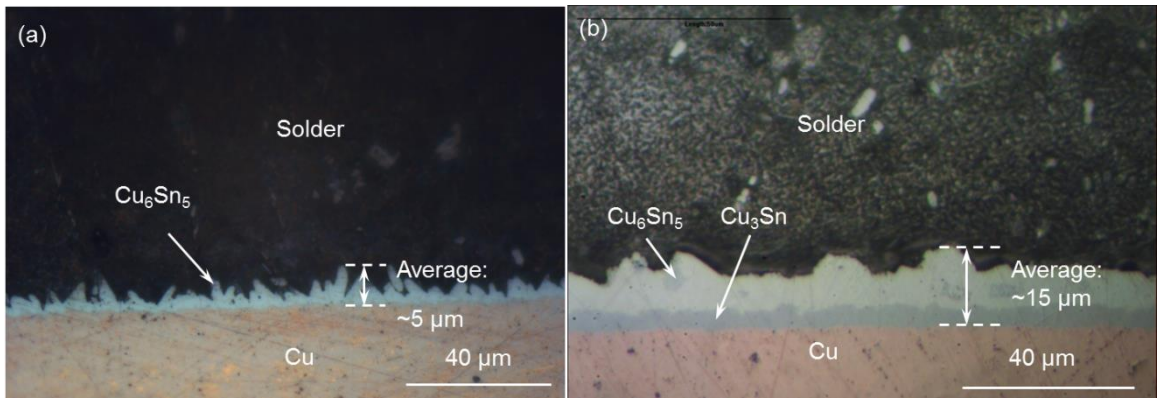


Fig. 3.4 The thickness of interfacial IMC layers at the Sn99Cu1 solder/Cu interface (a) before aging and (b) after aging at 175°C for 1006.5 hours.

The thicknesses of the interfacial Cu_6Sn_5 , Cu_3Sn and entire IMC layers were measured with the method explained in section 3.2.1 and plotted as a function of aging durations in Fig. 3.5. The value of each data point in the figure is the average thickness derived from six specimens, and the error bars indicate the standard deviation of the measurement. The linear fitting was based on the understanding that the planar growth of interfacial IMC layers is primarily dominated by the opposing diffusion of Sn and Cu atoms during aging, and it follows parabolic law with aging durations [153]. The curve fitting results in Fig. 3.5 shows that the thickness of the interfacial IMC layers increased linearly with the square root of aging durations, which can be expressed as;

$$h_{IMC} = 0.27t^{1/2} + 4.6, h_{Cu_6Sn_5} = 0.16t^{1/2} + 4.1 \text{ and } h_{Cu_3Sn} = 0.17t^{1/2} \quad (3.1)$$

where t is aging durations in hour, h is thickness of each layer in μm . In comparison to the reported diffusion coefficients in reference [153], the obtained value in this work is within a reasonable range. The constants in the equation, 4.6 and 4.1, indicate the initial thickness of IMC layer before aging. They are supposed to be the same, since only Cu_6Sn_5 layer can be observed before aging (Fig. 3.4 a)). The minor variation between them could be attributed to the error induced by the measurements and curve fitting.

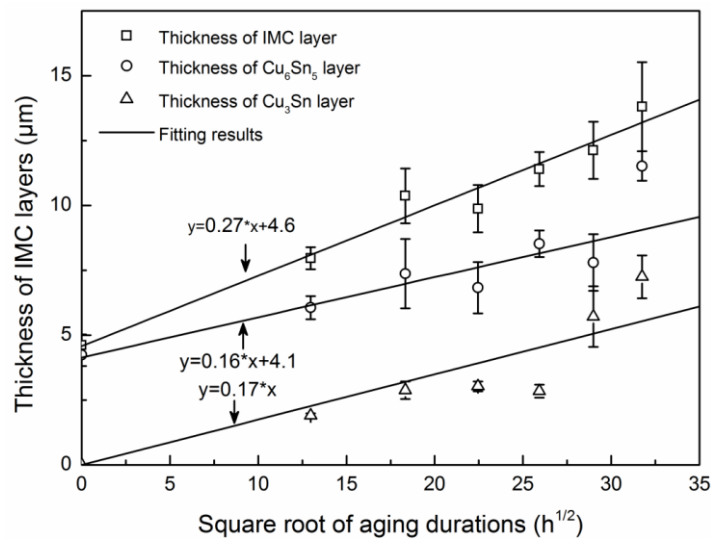
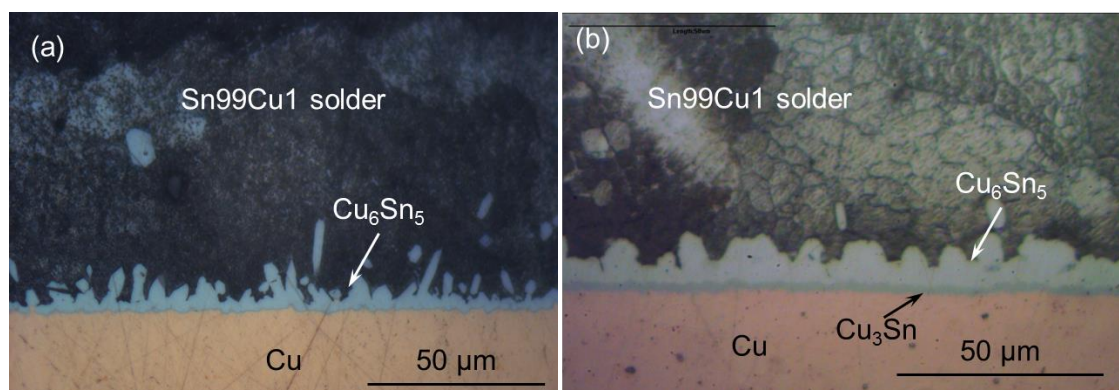


Fig. 3.5 The correlation between the growth of interfacial IMC layers and aging durations at 175°C.

From Fig. 3.5, it can also be found that the growth rates of interfacial Cu_3Sn and Cu_6Sn_5 layers were generally close to each other during aging. This can be attributed to two possible factors, the higher activation energy of the growth of Cu_3Sn and the possible consumption of Cu_6Sn_5 by the growth of Cu_3Sn during aging. From reference [154], the activation energy of the growth of Cu_3Sn (1.27 eV) is higher in comparison to that of the growth of Cu_6Sn_5 (0.47 eV). This indicates the solid-state reaction that produces Cu_3Sn is less likely to happen. However, the growth of interfacial Cu_3Sn layer at the Cu_6Sn_5/Cu_3Sn interface can possibly lead to the decomposition of Cu_6Sn_5 layer during aging [155]. The growth of interfacial Cu_3Sn layer requires the supply of both Sn and Cu atoms by solid-state diffusion. The Cu substrate adjacent to the Cu_3Sn layer can serve as the source of Cu atoms, which can be regarded as unlimited. But the supply of Sn atoms from the solder side is restricted by the growth of Cu_6Sn_5 layer, resulting in the lack of Sn atoms near the Cu_6Sn_5/Cu_3Sn interface. Therefore, the Cu_6Sn_5 layer is likely to decompose to release the Sn atoms for the growth of Cu_3Sn [155]. Consequently, the growth of Cu_3Sn layer can restrain the increase in the thickness of interfacial Cu_6Sn_5 layer during aging. Therefore, the growth rates of Cu_6Sn_5 and Cu_3Sn layers are close to each other during aging.

3.2.3 Morphological evolution of planar interfacial IMC layers

Fig. 3.6 shows representative images of the interfacial IMC layers in Sn99Cu1/Cu solder joints after aging at 175 °C for 0 hour, 168 hours, 672 hours, 840 hours and 1006.5 hours. Before aging, only the dendritic Cu_6Sn_5 layer can be observed at the solder/Cu interface in Fig. 3.6 a). After aging at 175 °C for 168 hours, the interfacial Cu_6Sn_5 layer grew and transformed to scalloped shape, and a layer of Cu_3Sn can be identified at the Cu_6Sn_5/Cu interface as shown in Fig. 3.6 b). As the aging prolonged, the interfacial Cu_6Sn_5 layer transformed to layer-type gradually, and the thickness of interfacial Cu_3Sn layer increased significantly with aging durations, as illustrated in Fig. 3.6 c), d) and e).



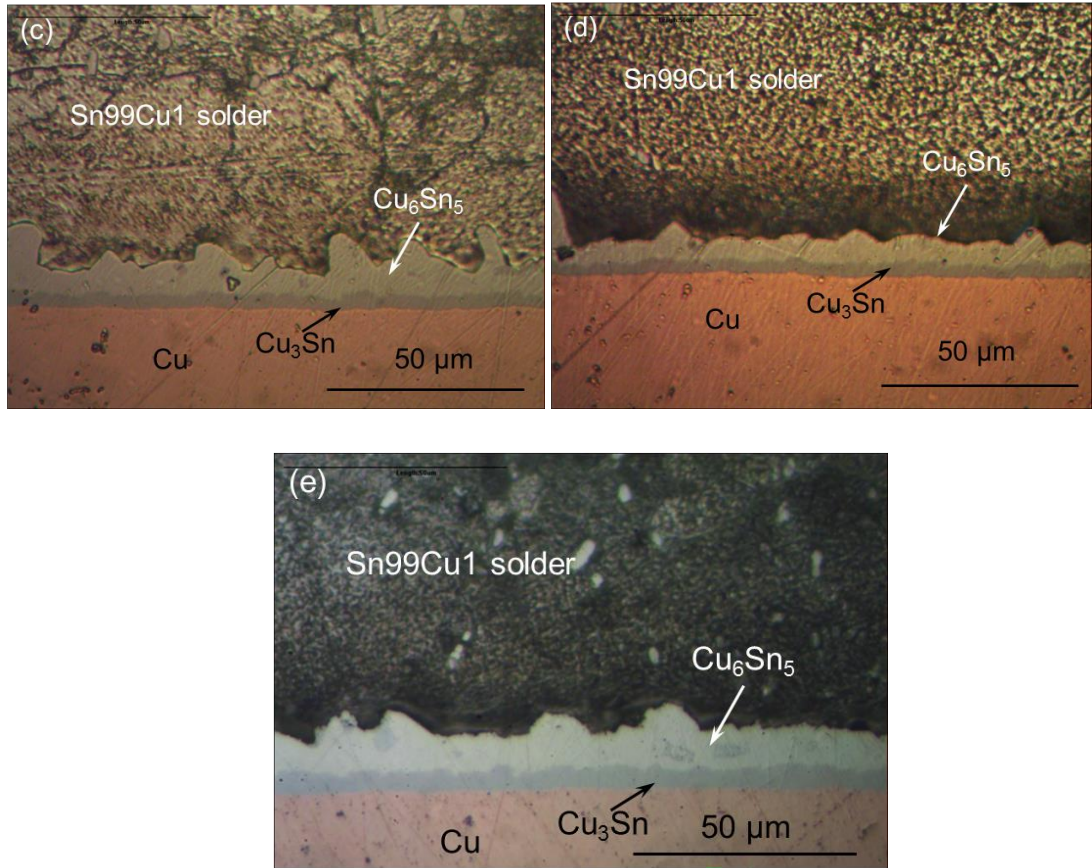


Fig. 3.6 Morphological evolution of the interfacial IMC layers after aging at 175°C for (a) 0 hours; (b) 168 hours; (c) 672 hours; (d) 840 hours and (e) 1006.5 hours.

The dendritic Cu_6Sn_5 layer in Fig. 3.6 a) was formed during reflowing due to its higher thermodynamic stability in reflowing [25]. In a molten solder/layer-type IMC system as illustrated in Fig. 3.7, the correlation of interfacial energy between the adjacent two parts follows $\sigma_{SS} \geq \frac{2}{3}\sigma_{GB} \geq \sigma_{LS}$, where σ_{GB} , σ_{SS} and σ_{LS} represent grain boundary energy in Cu_6Sn_5 , interfacial energy between solid solder and Cu_6Sn_5 , and interfacial energy between molten solder and Cu_6Sn_5 , respectively [25]. The inequality equation indicates that the interfacial energy of large angle grain boundaries in interfacial Cu_6Sn_5 layer is higher than the smaller angle grain boundaries when it is in contact with molten solder [25]. Therefore, the dendritic Cu_6Sn_5 layer is more thermodynamically stable than the layer-type Cu_6Sn_5 in reflowing, which results in the growth of dendritic Cu_6Sn_5 layer.

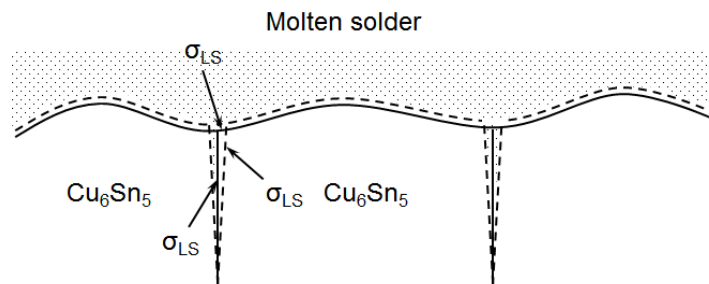


Fig. 3.7 Different parts in molten solder/ Cu_6Sn_5 system in reflowing.

In the followed aging, the dendritic interfacial Cu_6Sn_5 layer transformed to layer-type as the aging duration prolonged (Fig. 3.6 b) - e)). Two mechanisms could contribute to the morphological transformation of interfacial Cu_6Sn_5 layer during aging: the variation in distance and the curvature effect.

The growth of interfacial IMC layers in Sn99Cu1/Cu solder joints during aging is due to solid-state reactions between Sn and Cu atoms in interdiffusion. Therefore, for the scalloped IMCs in Fig. 3.8 a), the diffusion distances through the peaks (D_1) and valleys (D_2) follow the relation $D_1 > D_2$, which results in variations in the growth rate at different locations. Consequently, the lower growth rate at the peaks and higher growth rate at the valleys could lead to gradual flattening of interfacial Cu_6Sn_5 layer. After the IMC layer at the interface becomes layer-type, the diffusion distances are close to each other ($D_3 \approx D_4$). Hence, the growth rate of the interfacial Cu_6Sn_5 layer is more homogeneous at various locations.

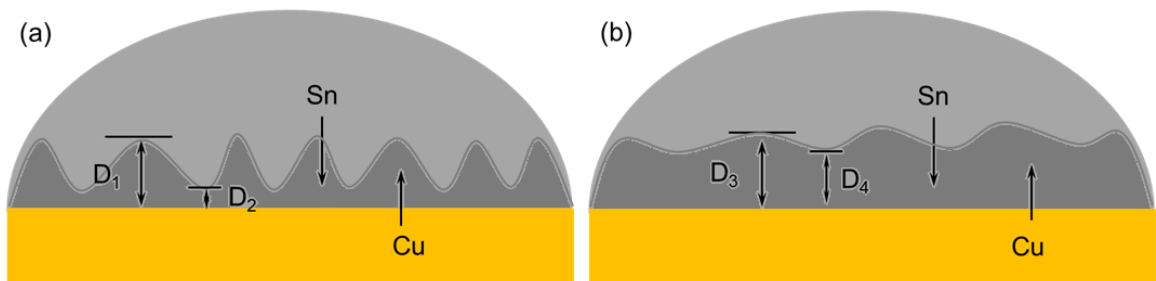


Fig. 3.8 Comparison of diffusion distances at the peaks and valleys in the (a) dendritic and (b) layer-type interfacial IMC layers in aging.

Furthermore, curvature effect could also contribute to the morphological evolution of interfacial Cu_6Sn_5 layer. The curvatures of Cu_6Sn_5 dendrites vary with positions, so the Cu concentrates at the peaks of the Cu_6Sn_5 dendrites [156]. Due to the concentration gradient, Cu atoms would diffuse from the peaks to the valleys [55, 157], which leads to curved region more even in the interfacial Cu_6Sn_5 layer at the Sn99Cu1/Cu interface (Fig. 3.9 b)).

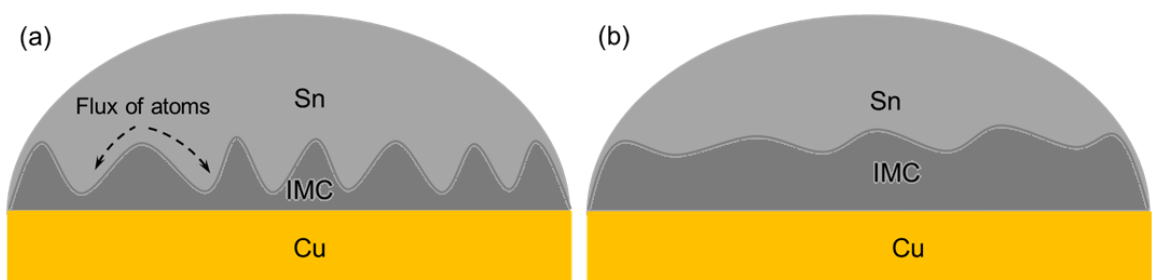


Fig. 3.9 Curvature effect in morphological evolution: (a) the Cu atoms move from positions with higher curvature to those less curved; (b) the curvature of IMCs becomes more homogeneous as the aging prolongs.

3.3 Perpendicular growth of IMCs

3.3.1 Experimental details

3.3.1.1 Experimental procedures

In order to investigate the perpendicular growth of IMCs, a pocket with the dimensions of 15 mm × 15 mm × 2.5 mm was machined within a Cu (purity: 99.9%) sheet. Proper amount of Sn99Cu1 solder was placed in the pocket and reflowed with the profile illustrated in Fig. 3.2 a). After reflowing, the four specimens were ground and polished to ensure that the top surface across the solder/Cu interface was in one plane. The specimen after polishing is schematically shown in Fig. 3.10. The specimens were then stored in an oven at 175°C to facilitate the growth of IMCs. After aging for every 168 hours until 1006.5 hours, the specimens were taken out of the oven, followed by the surface profiling across the Cu/solder interface with Zygo NewView 5000. The areas of the scanned regions were no smaller than 1.5 mm × 1.0 mm to ensure the reliability of obtained surface profiles. The obtained surface morphology was then converted into series of profiles for the calculation of the average height of perpendicular IMCs in the specimen. After the measurement, SEM was used to observe the perpendicular growth of IMCs. Focused ion beam (FIB) was also utilized to mill the specimen across the Sn99Cu1/Cu interface to reveal the perpendicular IMCs after aging.

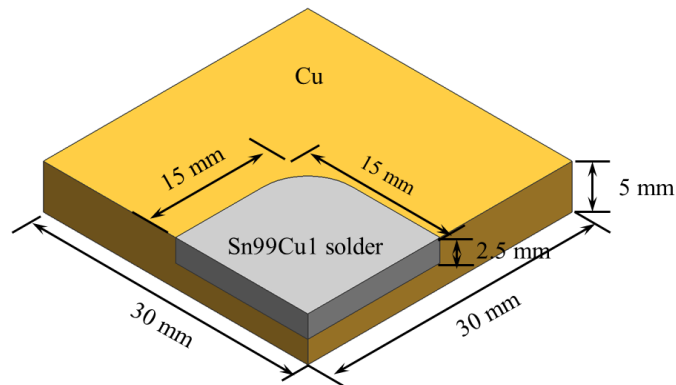


Fig. 3.10 Schematic of specimen used for measuring the perpendicular IMCs.

3.3.1.2 Mechanism of the surface profiler

Fig. 3.11 a) shows the Zygo NewView 5000 used in this work. It is a non-destructive optical surface profiler based on the interference of light (Fig. 3.11 b)). In the instrument, the light from the source is split and directed onto a test surface and a reference surface respectively, which is then reflected and recombined to form light and dark bands known as interference fringes. In the interference fringes, each transition from light to dark represents one-half a wavelength of difference in distance between the reference path and the test path. If the wavelength is known, it is possible to calculate the height differences across a surface [158, 159]. With well-calibrated optical profilers, the accuracy could reach about ± 1 nm [160].

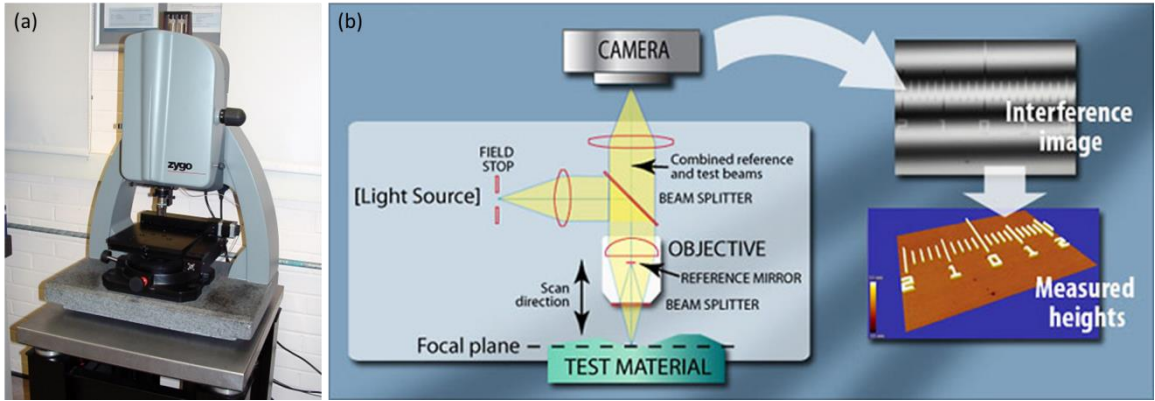


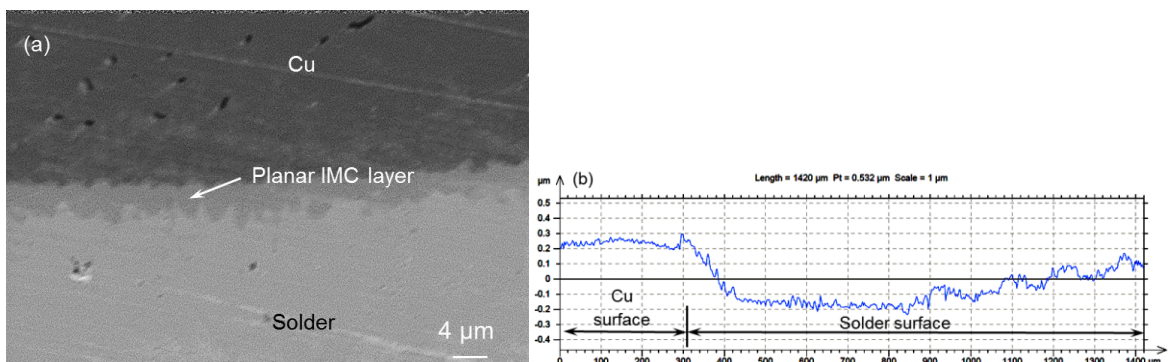
Fig. 3.11 The illustration of (a) Zygo Newview used in this work and (b) the mechanism of the measurement.

3.3.2 Results & discussions

3.3.2.1 Experimental results

Fig. 3.12 a), c) and e) illustrate the evolution of the perpendicular IMCs on the top surface of Sn99Cu1/Cu solder joints after progressively prolonged aging. The corresponding examples of surface profiles from the specimen are shown in Fig. 3.12 b), d) and f), which were levelled with the profile of Cu surface to remove the angle between the specimen and the instrument in measurement. Before aging, the surface of Sn99Cu1 solder joints were smooth across the solder/Cu interface after polishing as illustrate in Fig. 3.12 a). No protrusion of perpendicular IMCs can be observed. The scalloped grey layer at the solder/Cu interface is the planar interfacial Cu_6Sn_5 layer. Therefore, there is no notable peak at the solder/Cu interface in the corresponding surface profile in Fig. 3.12 b). The height difference between the solder and Cu surface is probably due to the higher polishing rates on the softer solder part in comparison to the polishing on Cu in the sample preparation.

After aging at 175°C for 168 hours, a line of IMCs was observed at the Sn99Cu1 solder/Cu interface on the free surface as shown in Fig. 3.12 c). The spike of the protrusion of IMCs can also be identified in the corresponding surface profile in Fig. 3.12 d). The average height of the perpendicular IMCs can be estimated as 0.5 μm with the profile of the Cu surface as the reference. As the aging extended to 1006.5 hours, the perpendicular IMCs grew significantly in both height and width as shown in Fig. 3.12 e), which is also reflected in the surface profile in Fig. 3.12 f).



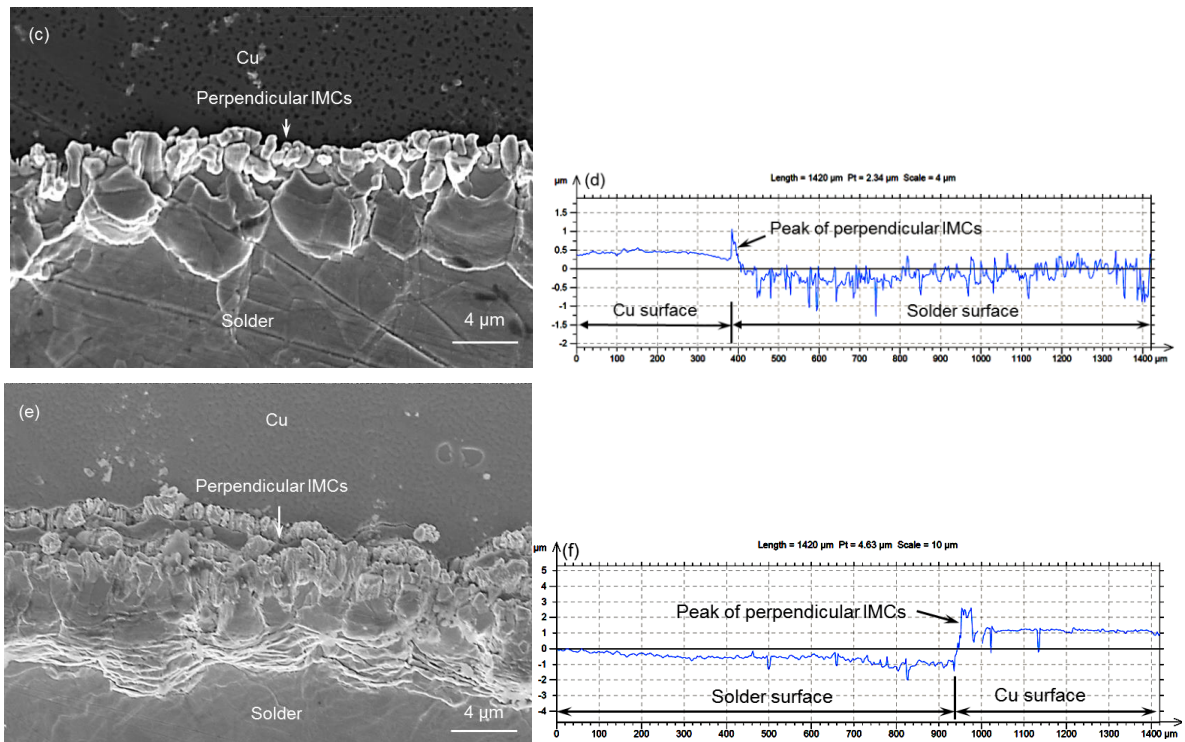
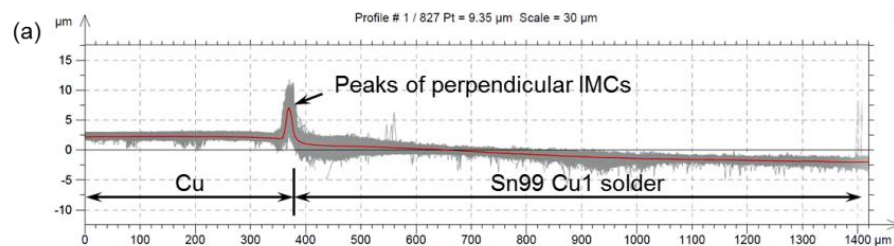


Fig. 3.12 The growth of perpendicular IMCs: (a), (c), (e) are the SEM images of the perpendicular IMCs after aging at 175 °C for 0h, 168 hours and 1006.5 hours and (b), (d) and (f) are the examples of surface profiles of the corresponding specimens.

Fig. 3.13 a) shows an example of a series of surface profiles across the Sn99Cu1/Cu interface of a specimen after aging. The peaks in the profiles represent the perpendicular IMCs on the surface of the sample. The average height of the perpendicular IMCs can then be estimated by calculating the average height of the peaks with the Cu surface as the reference. Because only solid-state diffusion and reactions can contribute to the perpendicular growth of IMCs, it is reasonable to assume that the perpendicular growth of IMCs is primarily governed by the interdiffusion between Sn and Cu. Therefore, the average heights of perpendicular IMCs from four specimens were plotted as a function of aging durations in Fig. 3.13 b), which can be expressed as:

$$y = 0.11\sqrt{t} \quad (3.2)$$

where t is the aging duration in hour, and y is the height of perpendicular IMCs in μm. The excellent compliance between the experimental data and the curve fitting result confirms that the perpendicular growth of IMCs is dominated by solid-state diffusion [153].



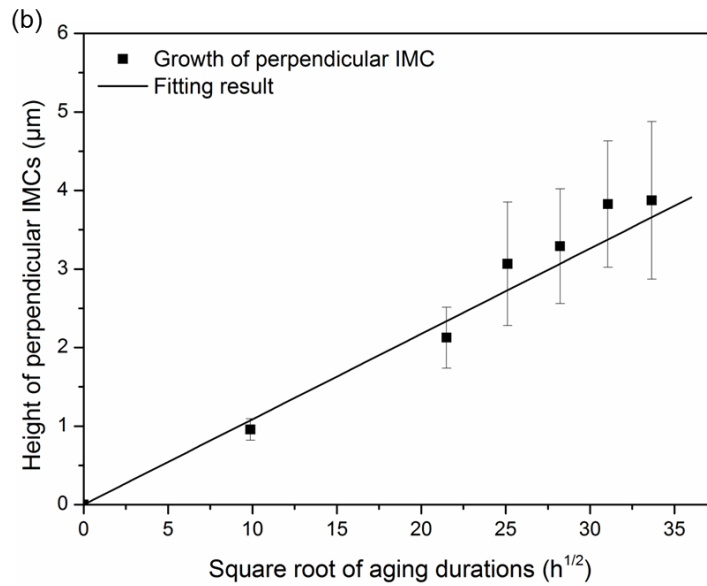


Fig. 3.13 Estimation of the heights of perpendicular IMCs: (a) an example of series of profiles derived from the scanned area. The red line is the average profile and the grey area is the all the surface profiles of the area; (b) the average height of perpendicular IMC versus square root of aging durations.

FIB was also utilised to reveal the protrusion of IMCs at the solder/Cu interface, as presented in Fig. 3.14. It is evident that the morphology of perpendicular IMCs is dendritic, which is different from the layer-type planar IMC layer in section 3.2. Both Cu_6Sn_5 and Cu_3Sn can be found in the perpendicular IMCs with the latter as the 'root'. Therefore, it is reasonable to assume that the perpendicular Cu_3Sn formed before the Cu_6Sn_5 in aging. Furthermore, it can also be found that the Cu/ Cu_3Sn interface and Cu_3Sn/Cu_6Sn_5 interface shifted towards the Cu side at the region close to the sample surface. However, the Cu_6Sn_5 /solder interface at this region remains unchanged.

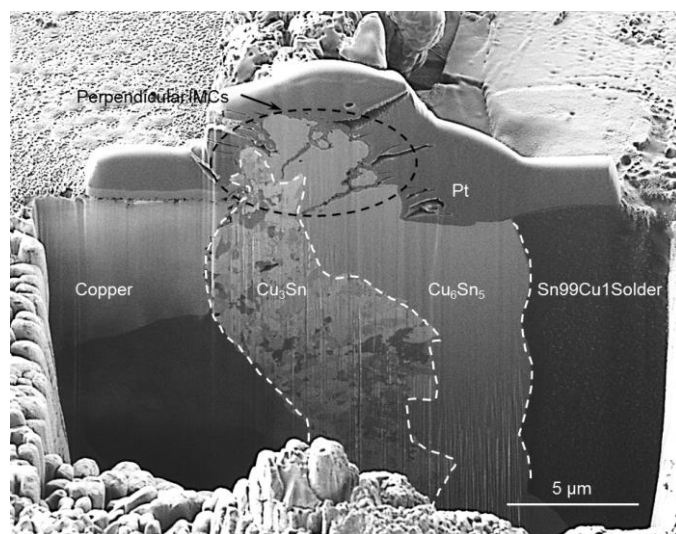


Fig. 3.14 The perpendicular IMCs at the Sn99Cu1 solder/Cu interface after aging at 175°C for 1006.5 hours. The Pt on the top of the cross section was deposited before the milling with ion beam to protect the sample beneath it during milling.

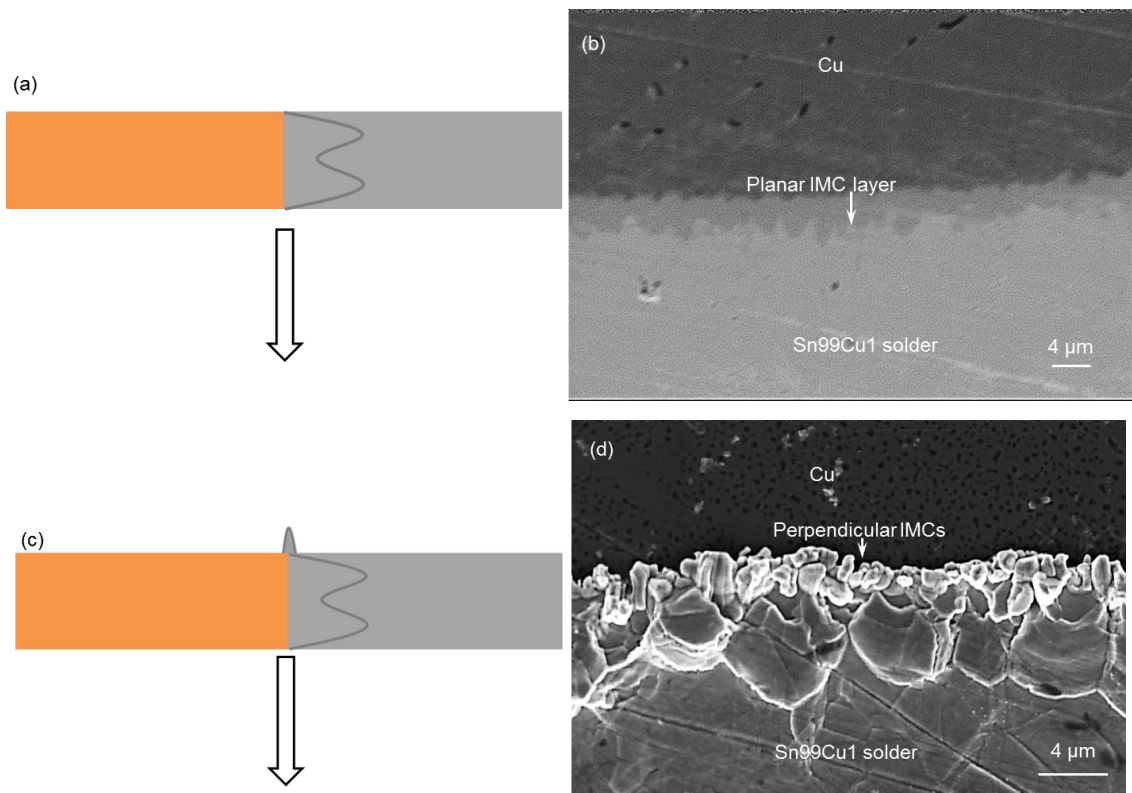
The growth of perpendicular IMCs in solder joints was seldom studied in literatures. However, in electromigration tests, some hillocks in solder joint was reported to be squeezed out at the anode side due to the compressive stress induced by current stressing [56, 161-163]. During aging, the growth of IMCs is accompanied by the volume shrinkage due to the increase of densities in solid-state reactions, which can lead to the build-up of compressive stress at the solder/substrate interface [104]. Therefore, it is reasonable to assume that the compressive stress within the IMC layer in aging can also contribute to the growth of perpendicular IMCs in aging.

3.3.2.2 Morphological evolution of perpendicular IMCs

Based on the observation with SEM, the growth of perpendicular IMCs can be divided into four stages: formation of the 1st line of IMCs, formation of the 2nd line of IMCs, contact of the two line of IMCs and the merging of the two lines of IMCs, which are illustrated in Fig. 3.15 a)- j).

Before aging, no protruded IMCs could be observed in the specimens after polishing in Fig. 3.15 b). After aging at 175°C for one week, a line of IMC spikes formed at the Cu/Cu_3Sn interface. As the aging prolonged, a second line of perpendicular IMC grew out of the specimens, as shown in Fig. 3.15 e) and f). A gap between these two lines of IMCs can be identified. As the perpendicular IMCs grew both vertically and transversely with aging, the gap between the two lines of IMCs was narrowed (Fig. 3.15 g) and h)). After aging at 175°C for six weeks, the two lines of perpendicular IMCs merged together (Fig. 3.15 i) and j)). In some specimens, a third line of perpendicular IMCs was identified adjacent to the merged IMCs.

During the perpendicular growth of IMCs from Fig. 3.15 c) to Fig. 3.15 j), the composition at the top should have transformed from Cu_3Sn to Cu_6Sn_5 due to the sequential growth. But the time of the transition is uncertain.



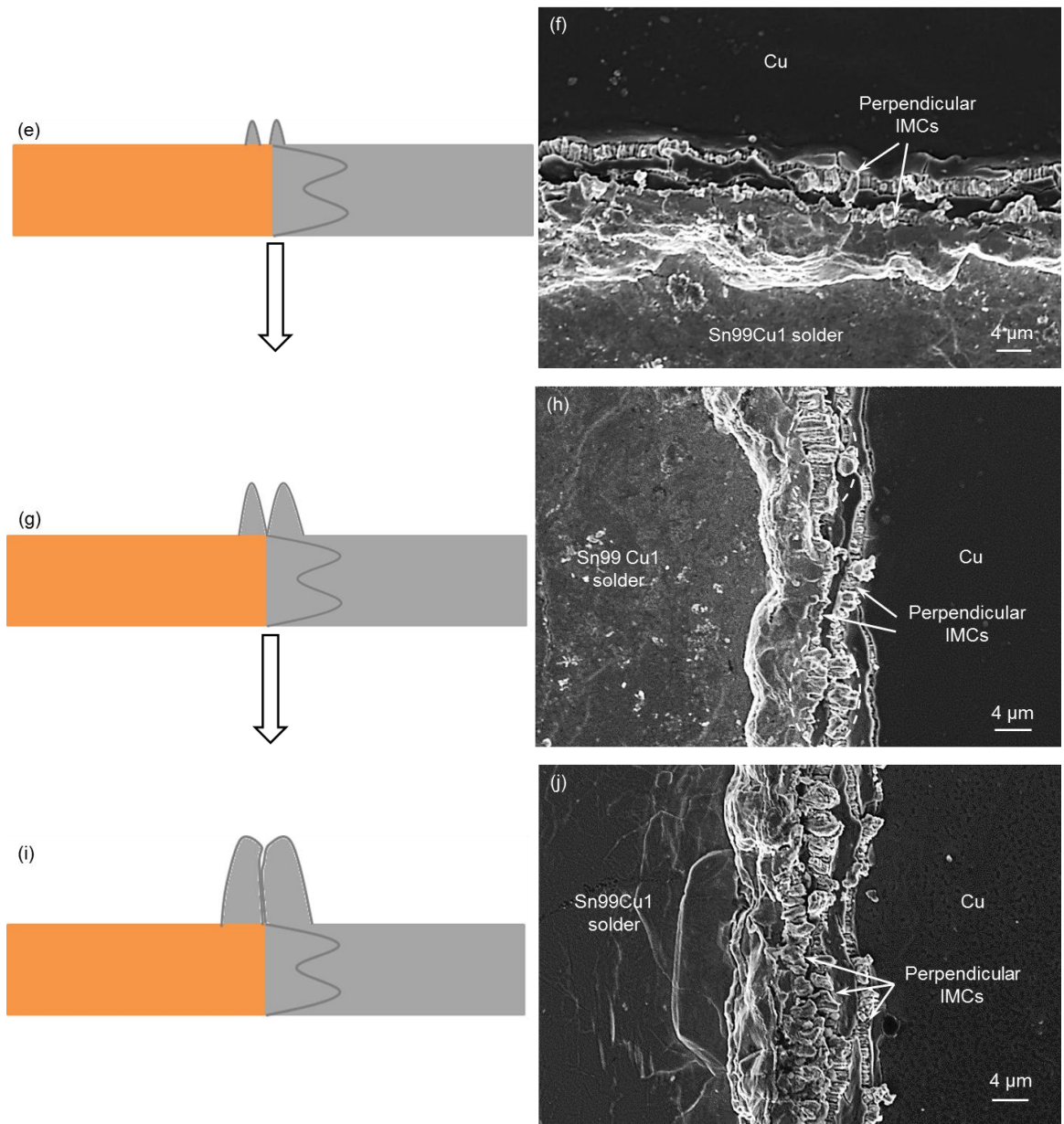


Fig. 3.15 Growth of perpendicular IMCs: (a), (c), (e), (g) and (i) illustrate the different stages of the growth of perpendicular IMCs; (b), (d), (f) and (j) show the observed evolution of perpendicular IMCs with SEM after aging at 175°C for 0 week, 1 week, 4 weeks, 5 weeks and 6 weeks.

3.3.2.3 Movement of $\text{Cu}/\text{Cu}_3\text{Sn}$ and $\text{Cu}_3\text{Sn}/\text{Cu}_6\text{Sn}_5$ interfaces

The cross section of Sn99Cu1/Cu solder joint in Fig. 3.16 illustrates that the $\text{Cu}_6\text{Sn}_5/\text{Cu}_3\text{Sn}$ and $\text{Cu}/\text{Cu}_3\text{Sn}$ interfaces moved towards the Cu side in the region close to the free surface of the Sn99Cu1/Cu solder joint while the $\text{Cu}_6\text{Sn}_5/\text{solder}$ interface remains stable. The shift of these two interfaces leads to the significant expansion of Cu_6Sn_5 layer. Given the composition of Sn and Cu in these two types of Cu-Sn IMCs, it can be deduced that the concentration of Sn grows remarkably near the free surface of the solder joints.

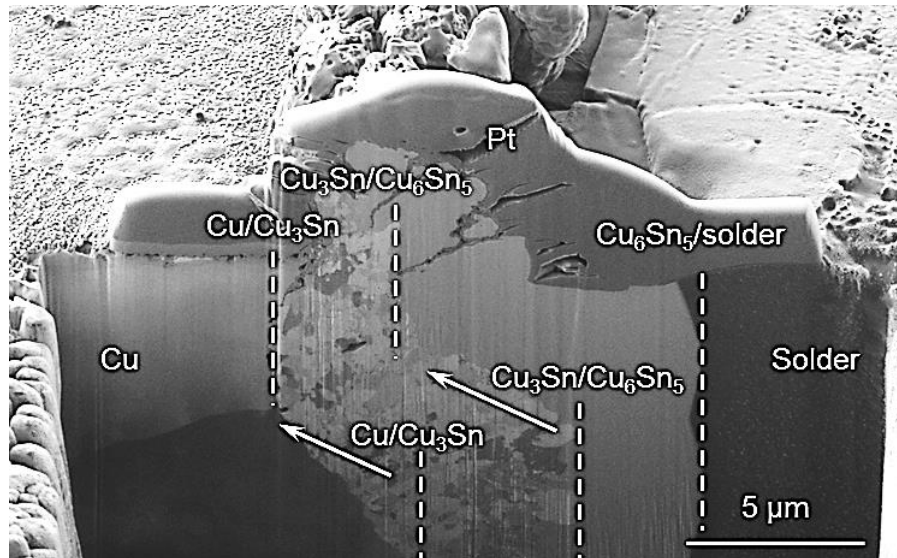


Fig. 3.16 Shift of the Cu_3Sn/Cu_6Sn_5 and Cu/Cu_3Sn interfaces in the region close to the surface of Sn99Cu1/Cu solder joint. The Pt on the top was deposited to protect the sample beneath it during milling.

In the region close to the surface, both the bulk diffusion through the Cu_6Sn_5 layer and the surface diffusion on the Cu_6Sn_5 layer can serve the supply of Sn atoms to the perpendicular growth of IMCs during aging. However, for the region farther from the surface, Sn atoms can only move by bulk diffusion in the Cu_6Sn_5 layer. Therefore, the observed increase in Sn concentration near the sample surface indicates that the surface diffusion of Sn atoms is much faster than its bulk diffusion in the Cu_6Sn_5 layer.

Furthermore, the increase in the concentration of Sn near the surface of solder joints also indicates the reduction of the fraction of Cu atoms in the same region. Since the major diffusion mechanism for both Cu and Sn atoms is surface diffusion in this area, it can be concluded that the surface diffusion of Sn is faster than that of Cu.

3.4 Comparisons and general discussions

3.4.1 Rate-controlling process in the growth of IMCs

In Sn99Cu1/Cu solder joints, both the planar and perpendicular growth of IMCs during aging involved the diffusion of Sn and Cu atoms along opposing directions and the subsequent solid-state reactions. For the discussion, D and R are used to denote the diffusion rate and the reaction rate of Sn and Cu atoms in aging, respectively. If $D \gg R$, the growth of IMC layer is governed by the reaction between Sn and Cu atoms, and the thickness of the IMC layer should grow linearly with aging durations [164]. In contrast, if $R \gg D$, the diffusion of Cu and Sn is the process that limits the growth of IMCs [164] and the thickness of interfacial IMC layers would increase parabolically with aging durations. Equation (3.1) in section 3.2.2 and Equation (3.2) in section 3.3.2 demonstrate that both the planar and perpendicular growth of IMCs in Sn99Cu1/Cu solder joints follow parabolic law with aging durations, which indicates that they are generally diffusion-controlled processes.

However, the growth of interfacial IMC layers may not be dominated by the same mechanism during aging. It was reported that the growth of the Cu_6Sn_5 phase could change from a reaction-controlled process when it was thin to a diffusion-controlled process when the thickness of Cu_6Sn_5 layer was thick enough to make the diffusion rate lower than the reaction rate [51]. Furthermore, the growth of interfacial Cu_3Sn layer could be dominated by both diffusion and reaction as its growth at the Cu/Cu_3Sn and Cu_3Sn/Cu_6Sn_5 interfaces could be dictated by different mechanisms [165-167].

3.4.2 Formation sequence of Cu_6Sn_5 and Cu_3Sn

At the solder/Cu interface, the planar IMC layers are normally formed during reflowing. Though it is controversial about the existence of Cu_3Sn layer in Sn based solder/Cu solder joints after reflowing, it is generally accepted that the growth of Cu_6Sn_5 and Cu_3Sn is not simultaneous, and the formation of Cu_6Sn_5 is prior to that of Cu_3Sn [168-171]. However, in perpendicular IMCs, the Cu_3Sn is the produced first, followed by the formation of Cu_6Sn_5 . The different formation sequences of Cu_6Sn_5 and Cu_3Sn in planar and perpendicular IMCs can be attributed to the diffusion of Sn and Cu atoms in aging.

The production of planar IMC layer in a solder joint (i.e. Sn99Cu1/Cu solder joint in this work) relies on the reaction between liquid solder and Cu during reflowing. When the liquid solder is in contact with solid Cu, Cu_6Sn_5 is generated quickly due to the comparable concentration of Sn and Cu atoms in a localised region until it covers the entire solder/Cu interface [172]. Since the formation of Cu_3Sn layer requires a Cu-enriched region [173], Cu_3Sn layer can only be produced until the diffusion distance of Sn atoms is long enough to significantly reduce the concentration of Sn atoms at the Cu_6Sn_5/Cu interface. This can only be achieved when the thickness of interfacial Cu_6Sn_5 layer exceeds a certain threshold. Therefore, the formation of Cu_3Sn is after the emergence of Cu_6Sn_5 in the planar IMC layer.

However, the perpendicular growth of IMCs started at the Cu_3Sn/Cu interface in Sn99Cu1/Cu solder joint, as illustrated in Fig. 3.14. It is evident that the Cu_3Sn/Cu interface is a Cu-enriched region, which can serve as the source of Cu atoms to the perpendicular growth of IMCs. As presented in section 3.3.2.3, the surface diffusion of Cu is slower than that of Sn in this work. Hence, the Sn atoms need to diffuse through the entire planar Cu_6Sn_5 and Cu_3Sn layers to react with the Cu atoms. In the beginning of the perpendicular growth of IMCs, the diffusion distance for Cu atoms was negligible. The proportion of Cu was therefore much higher than that of Sn atoms, which resulted in the growth of Cu_3Sn phase. However, the diffusion distance for Cu atoms increased with the growth of the perpendicular Cu_3Sn . It can lead to the decreasing supply of Cu atoms at the front of the perpendicular IMCs. When the diffusion distance reached a certain threshold, the fractions of Cu and Sn atoms were in a comparable level, which resulted in the formation of Cu_6Sn_5 . Hence, the formation of Cu_6Sn_5 is after the growth of Cu_3Sn in the perpendicular growth of IMCs.

3.4.3 Growth rates of perpendicular and planar IMCs

Equation (3.2) in section 3.3.2 reveals the parabolic correlation between the perpendicular growth of IMCs and aging durations. Compared with Equation (3.1) for the planar growth of IMCs in section 3.2.2, the perpendicular growth is much slower, though the surface diffusion that contribute to the perpendicular growth is faster than that the bulk diffusion in the planar growth. This can be ascribed to the longer diffusion distance for the diffusion of Sn and Cu atoms in the perpendicular IMCs.

For the perpendicular growth of IMCs, the diffusion distance include the diffusion through both planar and perpendicular IMCs, $D_{perpendicular} = H_{planar\ IMCs} + H_{perpendicular\ IMCs}$, where $D_{perpendicular}$ is the sum diffusion distance of both Sn and Cu for the perpendicular growth of IMCs, $H_{planar\ IMCs}$ is the thickness of planar IMC layer and $H_{perpendicular\ IMCs}$ is the height of perpendicular IMCs. However, for the growth of planar IMC layer, the diffusion distance equals the thickness of planar IMC layer, $D_{planar} = H_{planar\ IMCs}$, where D_{planar} is the sum diffusion distance of both Sn and Cu for the growth of planar IMC layer. Obviously, the height of perpendicular IMCs, $H_{perpendicular\ IMCs}$, in $D_{perpendicular}$ should be positive. Therefore, it is reasonable to conclude that the diffusion distance for the perpendicular growth of IMCs ($D_{perpendicular}$) is always longer than that for the planar growth of IMCs, $D_{perpendicular} > D_{planar}$.

3.5 Summary

In this chapter, both the planar and perpendicular growths of Cu_6Sn_5 and Cu_3Sn phases at the Sn99Cu1 solder/Cu interface were investigated. From the presented results and discussions, it can be concluded that:

1. In the planar IMC layer after reflowing, interfacial Cu_6Sn_5 layer was observed but Cu_3Sn layer was not visible before aging. After aging for at 175°C for about 1006.5 hours, the thickness of both Cu_6Sn_5 and Cu_3Sn layers increased significantly.
2. During the aging at 175°C, The correlation between planar growth of interfacial IMC layer and aging durations can be expressed as $h_{IMC} = 0.27t^{1/2} + 4.6$, $h_{Cu_6Sn_5} = 0.16t^{1/2} + 4.1$ and $h_{Cu_3Sn} = 0.17t^{1/2}$, where t is aging duration in hour, and h is thickness of each IMC layer in μm . The minor variation between the constants in the equation, 4.6 and 4.1, is due to the error induced by the measurements and curve fitting.
3. The morphology of planar Cu_6Sn_5 layer transformed from dendritic shape to layer-type after aging at 175°C for 1006.5 hours.
4. The perpendicular growth of IMC also follows parabolic law with aging duration, which can be expressed as $y = 0.11\sqrt{t}$, where t is aging duration in hour and y is the height of the perpendicular IMCs in μm . The growth rate of perpendicular IMCs is much lower than that of planar IMC layer due to longer diffusion distance.
5. The shift of Cu/Cu_3Sn and Cu_3Sn/Cu_6Sn_5 interfaces in the region close to the sample surface indicates that the surface diffusion of Sn atoms is much faster than its bulk diffusion and the surface diffusion of Cu atoms.

6. Both the planar and perpendicular growths of IMCs in Sn99Cu1/Cu solder joints are diffusion-controlled processes.
7. In planar IMC layers, the Cu_6Sn_5 phase forms prior to Cu_3Sn . In contrast, the Cu_6Sn_5 can only start growing after the height of Cu_3Sn in perpendicular IMCs reaches a certain threshold.

Chapter 4 Tensile fracture behaviour of Cu-Sn intermetallic compounds

4.1 Introduction

The integrity of solder interconnects is essential to the reliability of electronic devices in service. The formation of a reliable solder interconnect fundamentally relies on the metallurgical reaction between the solder and pad metallization of the substrate during reflowing. However, the produced IMC layer can grow excessively thick in long-term service. This could pose a significant impact on the reliability of solder joints [174-177] due to the incompatible deformation induced by the dissimilar mechanical properties of IMC (i.e. Cu_6Sn_5 and Cu_3Sn phases) in comparison to those of solder alloy (i.e. Sn) and substrate (i.e. Cu) [8-10]. Hence, characterizing the mechanical properties of interfacial IMC layers is essential to elaborate the reliability of solder interconnects in electronic devices.

Significant efforts have been made on characterizing the mechanical properties of IMC layers at the solder/pad interface in solder joints. Various methods including casting and annealing were often utilized to prepare IMC samples in relatively big volume to enable mechanical tests at a macro-scale [70] due to the challenge in direct test on the micro scale of interfacial IMC layers in solder joint [70, 178]. Numerical analysis was also employed to estimate the elastic moduli of Cu_6Sn_5 , Cu_3Sn and Ag_3Sn [65, 66, 179]. However, nanoindentation was mostly employed to obtain the Young's modulus and hardness of interfacial IMC layers through indentation on the thick IMCs layers formed at the interface of solder joints [20, 71, 180-183].

The fracture behaviour of interfacial IMC layers, which governs the failure behaviour of solder joints and poses significant effect on the reliability of solder joints, remains seldom investigated. Therefore, it requires further attention and examination. There have been certain investigations on the compression and shear fracture behaviour of Cu_6Sn_5 layer formed at the solder/Cu interface [9, 73, 74]. Given the significant contribution of interfacial Cu_6Sn_5 and Cu_3Sn layers to the failure of Sn-based solder joints [3, 31, 184, 185], more work on the fracture behaviour of interfacial Cu_6Sn_5 and Cu_3Sn layers is demanded to study the influence of interfacial IMC layers on the reliability of the entire solder joint.

In this chapter, the tensile fracture behaviour of both Cu_6Sn_5 and Cu_3Sn in Sn99Cu1/Cu solder joints was investigated by micro cantilever bending tests on micro Cu_6Sn_5 and Cu_3Sn pillars prepared with focused ion beam (FIB) after aging. The fracture surfaces of tested Cu_6Sn_5 and Cu_3Sn pillars were then analysed with SEM and EDX. EBSD was also employed to reveal the orientations of IMCs (i.e. Cu_6Sn_5 and Cu_3Sn phases) grains at the solder/Cu interface. The recorded test data was then used to validate the Cu_6Sn_5 and Cu_3Sn finite element models built with Abaqus for the estimation of tensile fracture strength of interfacial IMCs.

4.2 Experimental and modelling details

4.2.1 Methodology

In a normal solder joint, such as Sn99Cu1/Cu solder joint, the thickness of interfacial IMC layers is normally in micro scale. The first challenge in the study on the fracture behaviour of

interfacial IMC layers is to expose the interfacial IMCs properly to prepare IMC specimens at the interface.

From literatures, there are generally three different ways to expose the interfacial IMC layers in solder joints: polishing [68], extended etching [74] and milling with FIB [73]. Polishing is often used to reveal the entire interfacial IMC layers in solder joints from the cross section, which is for nanoindentation test on the IMCs. However, the IMC layer cannot be used for fracture tests without involving the adjacent materials.

The interfacial IMCs in solder joints can also be exposed by extended etching to remove the entire solder part [74]. However, after etching, several IMC dendrites could be involved in the mechanical test because of the lack of space between two adjacent IMC dendrites and the big size of the tool for applying load on the IMC in mechanical tests. Furthermore, ordinary etchants are designed to expose the Cu_6Sn_5 by reacting with the Sn-based solder, which are incapable to reveal the interfacial Cu_6Sn_5 and Cu_3Sn phases separately. Hence, the interfacial Cu_3Sn layer beneath the Cu_6Sn_5 layer cannot be properly revealed by etching.

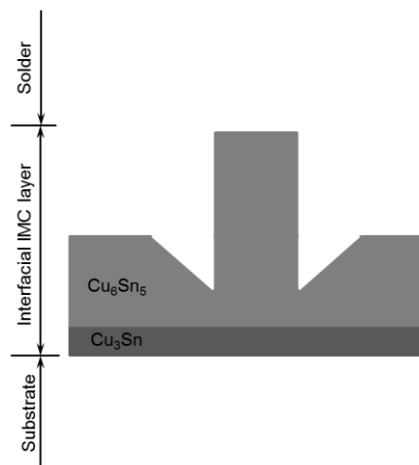


Fig. 4.1 The cylindrical Cu_6Sn_5 pillar fabricated with FIB in perpendicular to the solder/Cu interface in reference [9, 73].

It was reported that milling with FIB is capable to machine the specimens in nano-regime [186, 187], which is good enough to reveal the interfacial Cu_6Sn_5 and Cu_3Sn layers individually in Sn99Cu1/Cu solder joint. With FIB, the IMC specimens at the interface can be milled into various geometries. Some researchers have reported their works on cylindrical Cu_6Sn_5 pillars fabricated by FIB [9, 73], as illustrated in Fig. 4.1. This design can enable the application of a nano indenter with the size much bigger than the pillar to apply the compression load from the top of the pillar. This can lower the requirement of the alignment precision between the indenter and the pillar in the tests. However, because the direction of milling with FIB is perpendicular to the plane of the solder/Cu interface, the Cu_6Sn_5 layer needs to be removed totally prior to exposing the beneath Cu_3Sn layer. This poses significant challenge to the control of milling depth.

Therefore, in this work, the IMC pillars were designed to be parallel to the solder/Cu interface as illustrated in Fig. 4.2 a) and b), so that both the micro Cu_6Sn_5 and Cu_3Sn pillars can be exposed individually within the corresponding interfacial IMC layer in Sn99Cu1/Cu solder joint. In order to

minimize the amount of material that needed to be removed by FIB, the pillars were located at a corner of the bulk solder joint as illustrated in Fig. 4.2.

Due to the micro-scale IMC pillars within interfacial IMC layers in solder joint, the positioning accuracy of the indenter in the mechanical tests should be high enough to target the IMC specimen. It was demonstrated that nanoindentation is capable to target micro-scale features precisely [9, 73, 188, 189]. Therefore, nanoindentation system was employed to implement mechanical tests on micro IMC pillars in this work. Furthermore, an indenter with a flat end was used to apply the load to avoid the penetration of the indenter into specimens and the localised stress at the indenter/specimen contact region during tests.

In order to evaluate the tensile fracture behaviour of micro Cu_6Sn_5 and Cu_3Sn pillars by nanoindentation, cantilever bending test is a promising way to fracture the prepared micro Cu_6Sn_5 and Cu_3Sn pillars as the maximum tensile stress is located on the top surface at the bottom of the pillar during the cantilever bending test [190, 191]. After the tests, flexural formula can be applied to estimate the tensile fracture strength of the tested IMC pillars. For comparison, finite element modelling can also be employed to estimate the stress distribution in the micro Cu_6Sn_5 and Cu_3Sn pillars during the cantilever bending test.

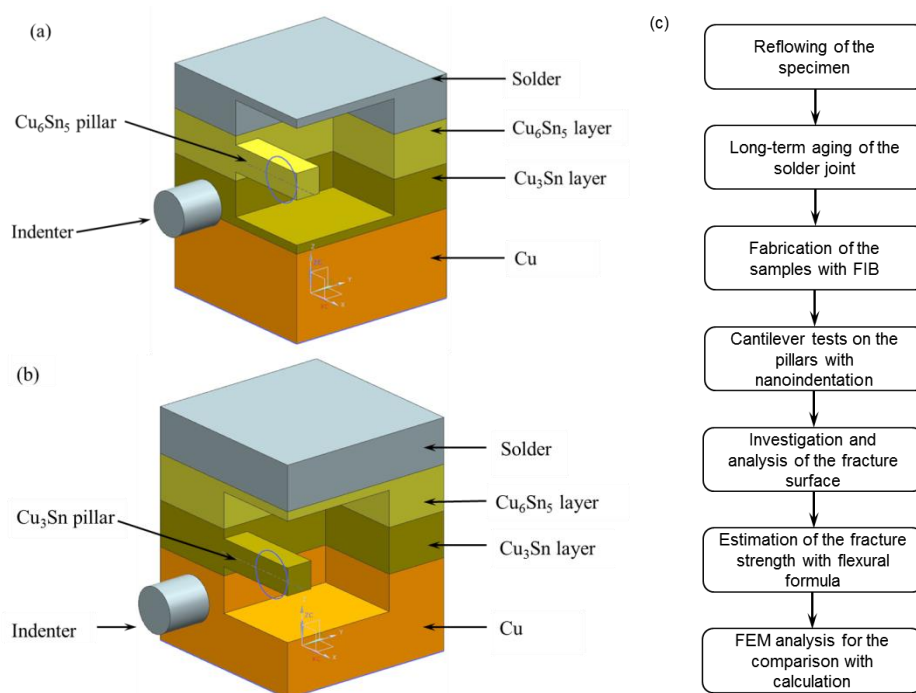


Fig. 4.2 The micro (a) Cu_6Sn_5 and (b) Cu_3Sn pillars in parallel to the solder/Cu interface at the corner of the solder joint; (c) A brief procedures of the work.

Therefore, the procedures of the work are illustrated in Fig. 4.2 c). The isothermal aging at elevated temperature was to facilitate the growth of interfacial IMC layers, so that both the Cu_6Sn_5 and Cu_3Sn layers at the solder/Cu interface were thick enough for the milling with FIB and followed mechanical tests. After the test, the fracture surface of Cu_6Sn_5 and Cu_3Sn pillars were examined with SEM and EDX to analyse the fracture mechanism. Finite element modelling was also applied to evaluate the maximum stress within the fabricated micro IMC pillars during the tests.

4.2.2 Experimental procedures

4.2.2.1 Experiment details

Sn99Cu1 solder was reflowed on polished Cu sheets (purity: 99.9%) in an oven. The temperature of specimens was monitored by attaching a thermal couple to the Cu substrate. A representative reflow profile was recorded and illustrated in Fig. 4.3. It is shown that the highest temperature during reflowing was 270°C.

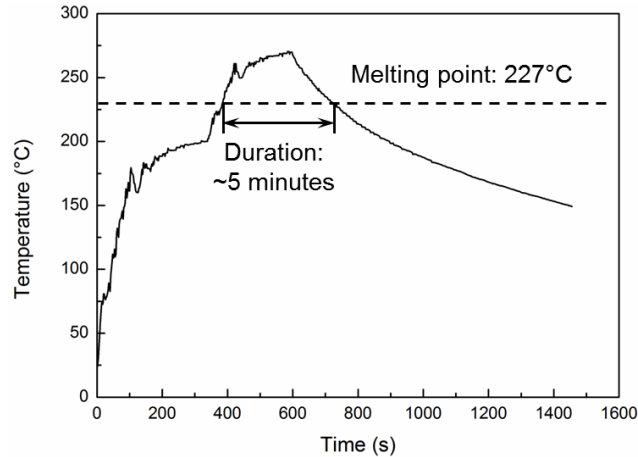


Fig. 4.3 The reflow profile obtained with the thermal couple attached to the sample during reflowing.

The reflowed six specimens were then stored in an oven at 175°C to facilitate the growth of interfacial IMC layers. After aging for 1132.5 hours, the six specimens were ground and polished to reveal the interfacial IMC layers at the Sn99Cu1/Cu interface. Micro IMC (i.e. Cu_6Sn_5 and Cu_3Sn) pillars were then fabricated within the corresponding IMC (i.e. Cu_6Sn_5 , Cu_3Sn) layer with dual-beam FIB. The material around the fabricated pillars was also cleared to avoid any potential contact between the rear of the indenter and the bulk material in the specimen during the mechanical tests.

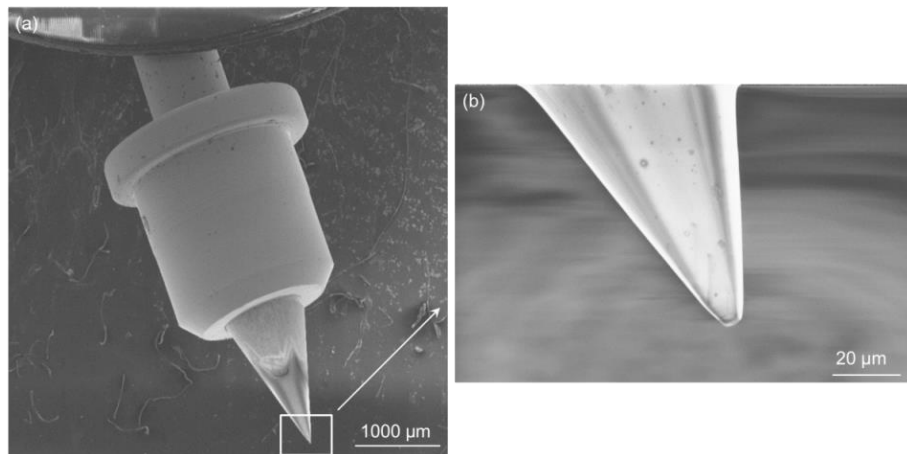


Fig. 4.4 The Nano flat indenter used in the work: (a) the shape of the indenter; (b) an enlarged image of the tip of the indenter.

The micro cantilever bending tests on the fabricated Cu_6Sn_5 and Cu_3Sn pillars were then conducted with Nanotest Platform 3. In the tests, a flat indenter with the diameter of 5 μm (Fig. 4.4) was used, so that the localized stress at the indenter/pillar contact region could be minimized.

Before the tests, the positioning accuracy of the indentation system (the distance from the actual indent to the target) was calibrated repeatedly until the new indent was made exactly at the designated location without visible shift under the microscope in the instrument (Fig. 4.5). This ensured that the positioning error was within 1 μm . In the tests, the flat indenter was located at the free end of the pillar to apply the load, about 7.5 μm away from the centre of the indenter to the bottom of the pillar. The settings of the cantilever bending tests are listed in Table 4.1. The loading rate 0.1 mN/s was used. The cantilever bending tests were terminated once the displacement of the indenter exceeded the pre-set value in Table 4.1. After the tests, the fracture surface of the pillars was examined with SEM. The composition was analysed with EDX.

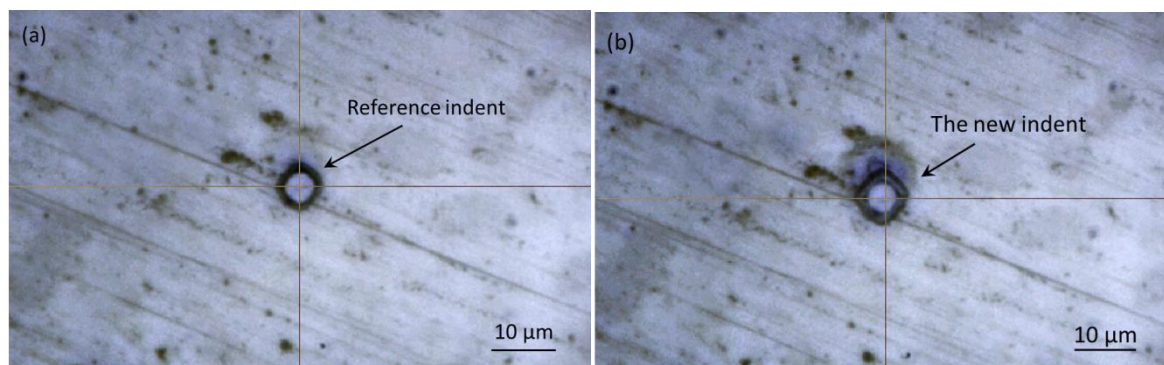


Fig. 4.5 Calibration of the positioning accuracy of the nanoindentation instrument: (a) a reference indent; (b) the new indent overlapped perfectly on the reference indent.

Table 4.1 Parameters and settings for cantilever bending tests on micro Cu_6Sn_5 and Cu_3Sn pillar

Parameters	Cu_6Sn_5	Cu_3Sn
Termination conditions	First condition	First condition
Maximum Load	100 mN	50 mN
Maximum Depth	4 μm	1 μm
Initial load	0.05 mN	0.05 mN
Loading rate	0.10 mN/s	0.02 mN/s
Unloading rate	0.10 mN/s	0.02 mN/s
Dwelling time at maximum load	0 s	0 s

4.2.2.2 Fabrication of micro IMC pillars

Fig. 4.6 schematically illustrates the milling with FIB. The electron beam functions as the beam in normal SEM for observing specimens. The ion beam in FIB is for milling the specimen by applying proper current and voltage [192]. Before the milling with FIB, the specimen must be placed on a pre-tilted specimen stub for adjusting the angle between the place of interest in the specimen and the ion beam. This angle should be checked again with the imaging of ion beam at low current.

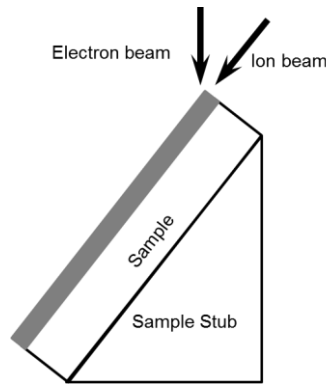


Fig. 4.6 Schematic of the milling with FIB.

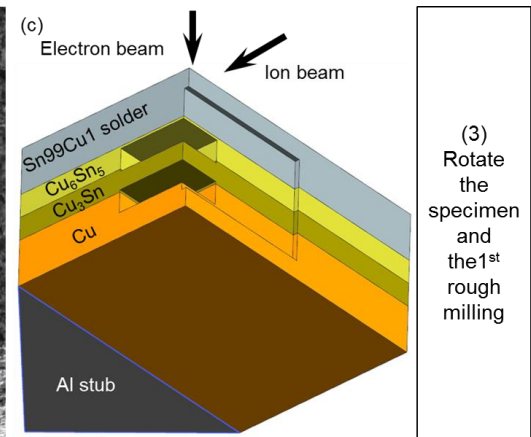
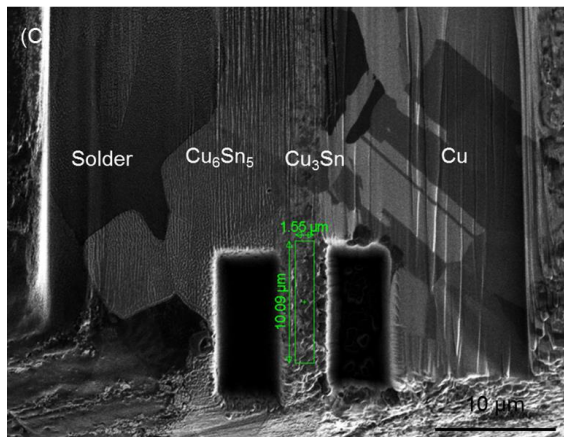
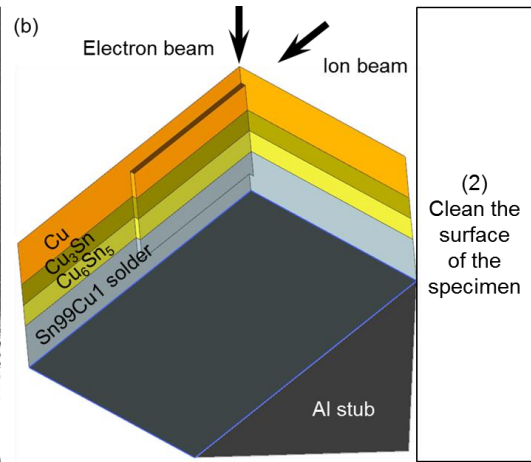
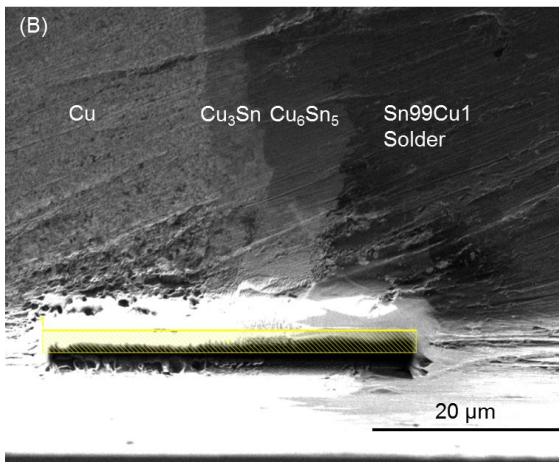
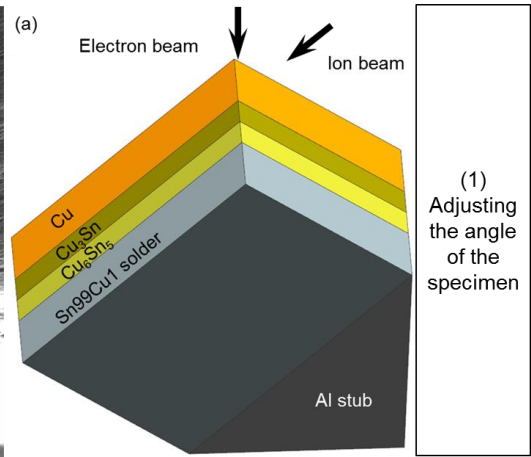
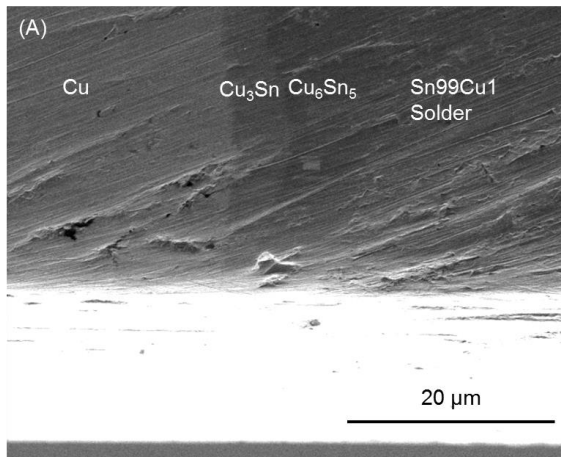
The procedures for the fabrication of an IMC pillar in Sn99Cu1/Cu solder joint are illustrated in Fig. 4.7. The specimen shown in Fig. 4.7 A) – G) were attached on an Al stub which was already tilted about 52° , so that the optimal angle between the specimen and the ion beam could be achieved by slight adjustment before the milling. Given the milling rate of FIB, the IMC pillars were located at the corner of the specimen to minimize the amount of material that needed to be removed by FIB.

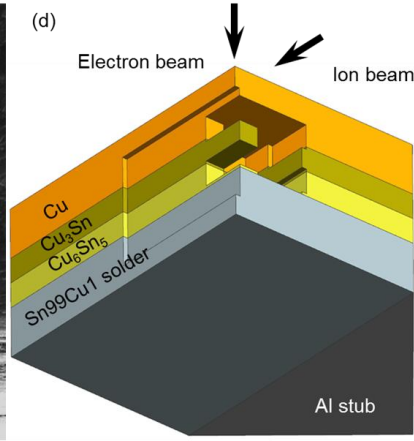
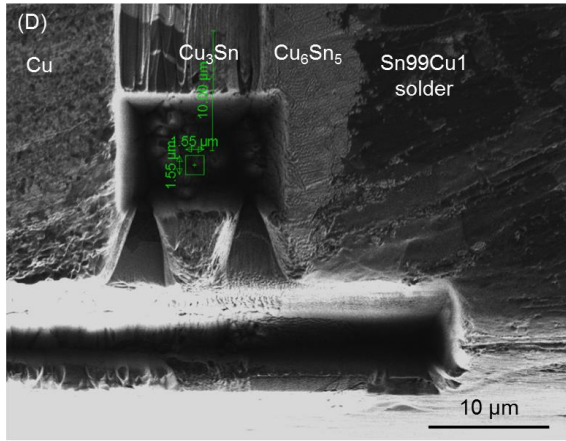
During the preparation of micro IMC pillars, the milling with FIB could be generally divided into two types: rough milling and cleaning. The major difference between these two was that the rough milling was the machining with higher current while the cleaning was under low current. Higher current in ion beam could elevate the milling rate significantly, but could also cause more serious damage to the place of interest and the adjacent material in the specimen. This would leave a rough surface after milling. The undesirable re-deposition, the phenomenon that the material removed by the ion beam at the place of interest deposited again on the milled surface and the adjacent regions, was also more evident when milling with higher current. In contrast, the milling with lower current was relatively slower, but the revealed fresh surface was cleaner with less damage. And the re-deposition was negligible at low current.

Therefore, rough milling was mainly used to create a large flat area on the wavy sample and roughly shape the target interfacial IMC layers into an IMC pillar with a margin of about $1\sim 2\ \mu\text{m}$. The current applied during rough milling in this work was in the range of $2\ \text{nA}\sim 7\ \text{nA}$, at which the milling rate was high enough and the damage to the specimen was also acceptable.

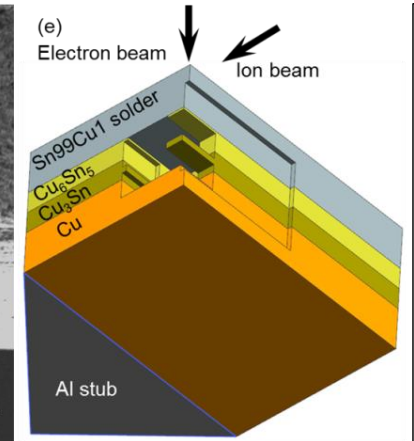
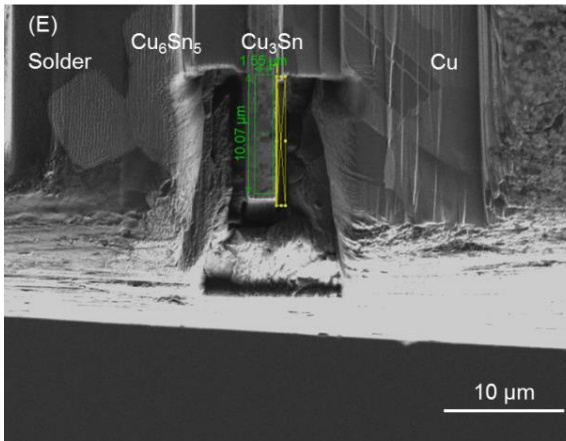
After the IMC pillar was generally formed at the designated location of specimen with rough milling, the cleaning was used to: (1) adjust the location of the IMC pillars to ensure their right locations within the designated interfacial IMC layers; (2) improve the bevel and curved edges due to the rough milling; (3) adjust the dimensions and angle of the IMC pillars; (4) remove the re-deposited materials on the surface of pillar during milling. The current of the ion beam during cleaning was about $0.5\ \text{nA}\sim 1\ \text{nA}$, with which the quality of the cleaned surface was smooth and satisfactory.

As the specimen was a cuboid pillar, the milling needed to be implemented from both the front and the top of the pillar. Therefore, the specimen had to be rotated between these two directions. The angle between the specimen and ion beam after rotation should be checked again.

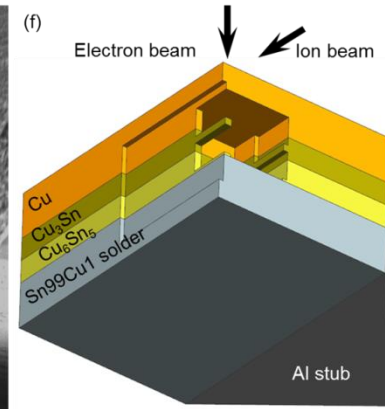
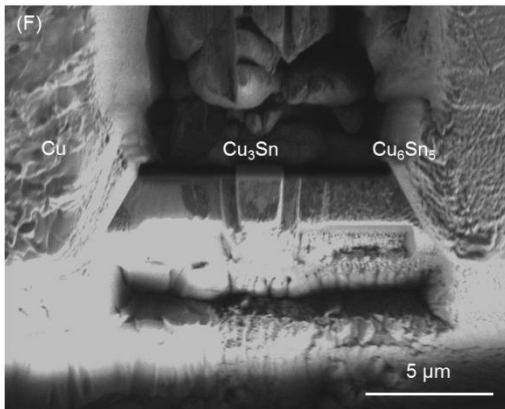




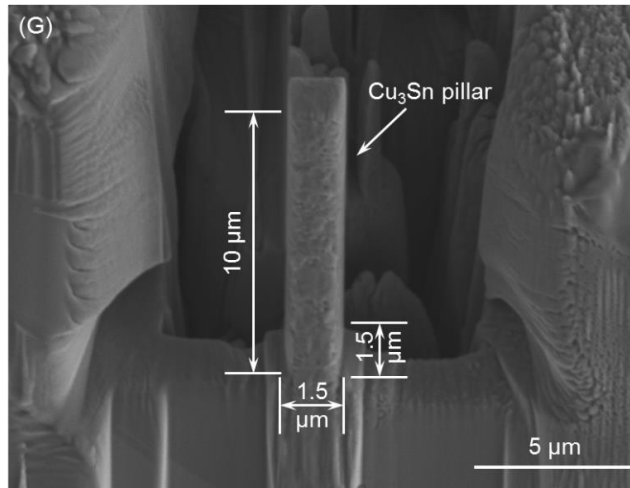
(4) Rotate the specimen and the 2nd rough milling



(5) Rotate the specimen and the 1st cleaning



(6) Rotate the specimen and 2nd cleaning



(7) Finish

Fig. 4.7 (A)~(G) the SEM images of an IMC pillar at the Sn99Cu1 solder/Cu interface during the preparation with FIB, (a)~(f) schematics to illustrate the direction and position of the specimen during milling; (1)~(7) the explanations of the corresponding procedures.

4.2.3 Numerical modelling

Modelling was also employed to analyse the stress distribution in the IMC pillar in the micro cantilever bending test. Hence, the tensile fracture strength of the tested IMCs (i.e. Cu_6Sn_5 , Cu_3Sn) can be estimated from the modelling results.

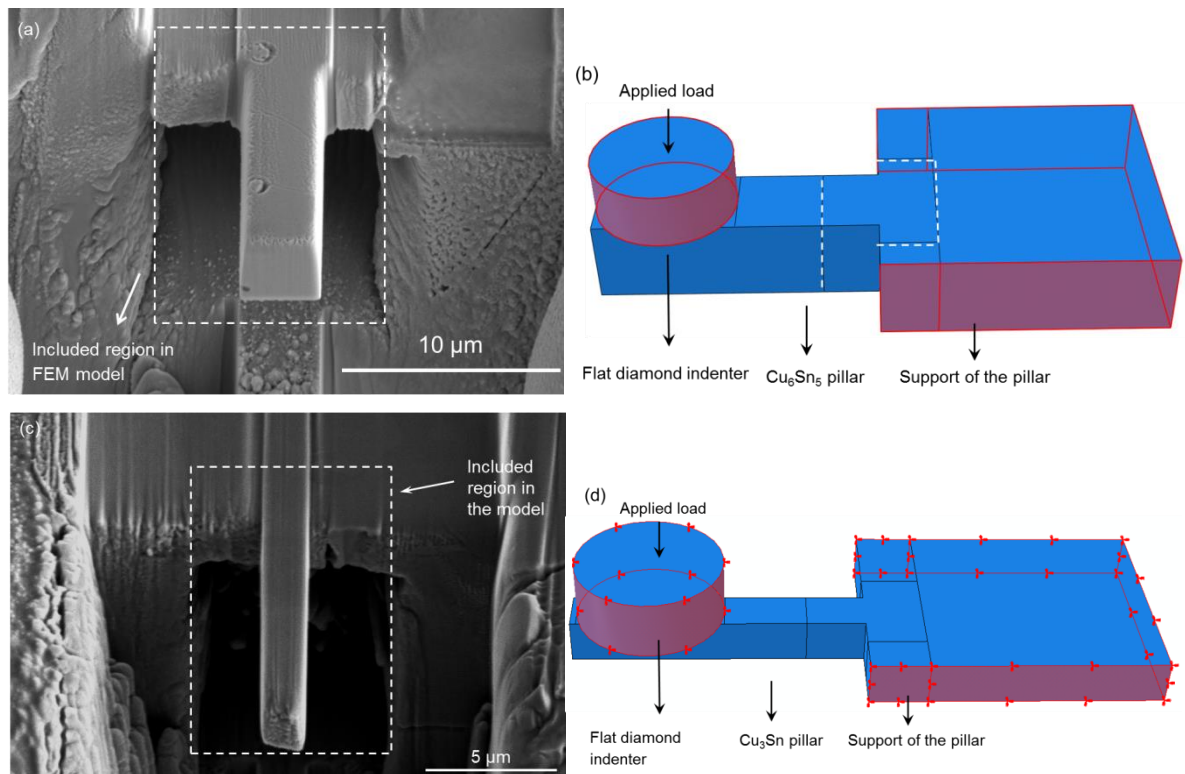


Fig. 4.8 Finite element models of micro Cu_6Sn_5 and Cu_3Sn pillars built in Abaqus: (a) and (c) The regions included in the finite element models; (b) and (d) the geometry of the built models with Abaqus. The red surfaces of the support of the IMC pillar were fixed along all the three directions. The red surfaces of the indenter were constrained along x and y direction.

The finite element models for the tested Cu_6Sn_5 and Cu_3Sn pillars were built with Abaqus as shown in Fig. 4.8 a) and c). Both the micro IMC pillar and the materials around it were included in the finite element models in Fig. 4.8 b) and d), so that the stress and deformation of the tested IMC pillar could be simulated more accurately.

In the model, the force measured in micro cantilever bending was converted into pressure load and applied on the top surface of the indenter to simulate the cantilever bending test. Five more assumptions were made in the built models: (1) The taper angle of the micro Cu_6Sn_5 pillar was negligible in this work [73, 193]; (2) The flat end of the indenter was parallel to the surface of the micro Cu_6Sn_5 pillar at the beginning of the test; (3) Both the diamond indenter and the micro Cu_6Sn_5 pillars were elastic during the cantilever bending tests; (4) Both Cu_6Sn_5 and Cu_3Sn were assumed

to be isotropic in the modelling; (5) The deformation in the area excluded from the finite element models was negligible.

The models were established through meshing into two different sizes with quadratic elements (C3D20). The application of quadratic elements (C3D20) could provide an extra node at every edge compared to linear element (C3D8), as illustrated in Fig. 4.9, which offers more degrees of freedom in deformation to simulate the bending more precisely [194].

The model was then meshed into two different sizes, fine mesh (0.15 μm) in the regions around the bottom of the micro IMC pillar (the region within the dash square in Fig. 4.10 and coarse mesh (0.4 μm) for the rest of the model, so that the total number of the elements could be minimised and the reliability of the modelling results can be guaranteed.

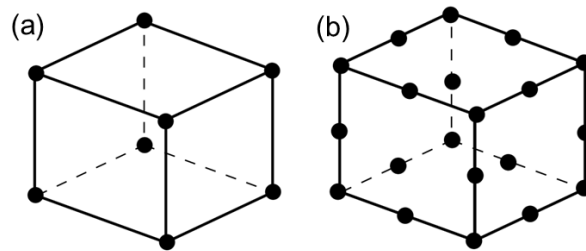


Fig. 4.9 Comparison between (a) linear (C3D8) and (b) quadratic (C3D20) element. The black dots denote the nodes in the element.

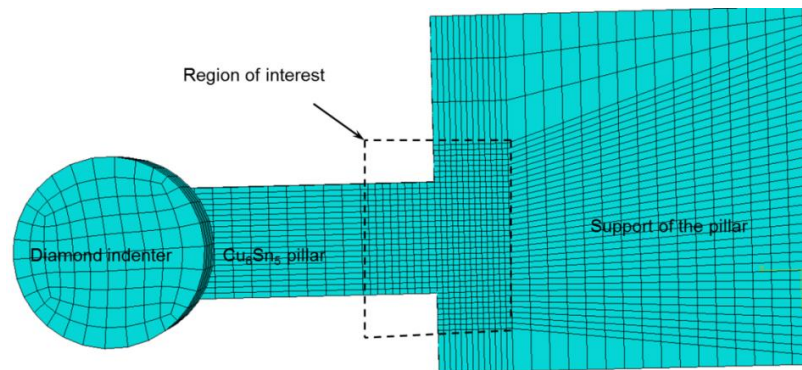


Fig. 4.10 An example of the model after meshing.

Other major parameters and setting in the modelling are listed in Table 4.2. The assignment of materials in the finite element model was based on the SEM results. For example, the interfacial Cu_3Sn layer was about 3 μm thick in the Sn99Cu1/solder joint. The adjacent materials to the Cu_3Sn pillar were Cu and Cu_6Sn_5 phase. Hence, Cu and Cu_6Sn_5 were assigned to the regions on the left and right of the Cu_3Sn micro pillar accordingly.

Table 4.2 Parameters and settings in the finite element modelling

	Young's Modulus	Poisson's Ratio	Mesh size-fine	Mesh size-coarse
Cu_6Sn_5 pillar	115.5 GPa [73]	0.31 [73]	0.15 μm	0.5 μm
Cu_3Sn pillar	134.2 GPa [195]	0.299 [16]	0.12 μm	0.4 μm
Diamond indenter	1141 GPa [196]	0.07 [196]	0.5 μm	0.5 μm
Cu	129.8 GPa [16]	0.339 [16]	0.4 μm	0.4 μm

4.3 Fracture behaviour of Cu_6Sn_5

4.3.1 Experimental results of micro cantilever bending tests

Fig. 4.11 a) shows an example of micro Cu_6Sn_5 pillar fabricated by FIB in this work. The size of the pillar was $3 \times 3 \times 10$ (L \times W \times H in μm). A taper angle (approximately 2°) could be observed from the fabricated pillar, which was due to the imperfect angle between the specimen and ion beam of FIB during milling. But the effect of the taper angle on the followed mechanical tests was negligible [73, 193].

The composition of the micro pillar was analysed by EDX and the result is shown in Fig. 4.11 b), which confirmed that the pillar is Cu_6Sn_5 phase as expected.

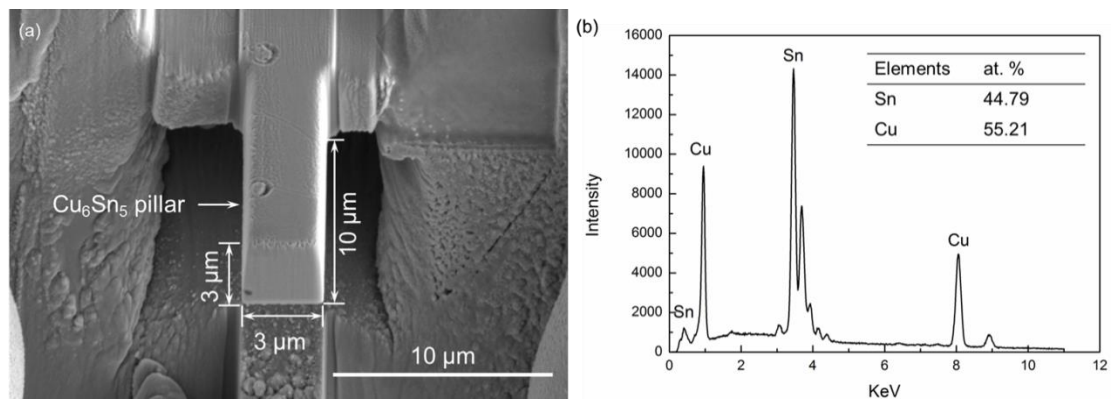


Fig. 4.11 An example of micro Cu_6Sn_5 pillar fabricated by FIB in this work: (a) an example of the Cu_6Sn_5 pillar; (b) the EDX spectrum of the IMC pillar.

The fabricated micro Cu_6Sn_5 pillars were then tested by cantilever bending tests with Micromaterials NanoTest platform 3. Before the tests, the Cu_6Sn_5 pillars were located at the Sn99Cu1 solder/Cu interface at the corner of the specimens, as illustrated in Fig. 4.12 a). The crosshair in Fig. 4.12 a) indicates the designated location of the load on the micro Cu_6Sn_5 pillar. After the cantilever tests, the Cu_6Sn_5 pillar fractured from the bottom, as illustrated in Fig. 4.12 b).

During the cantilever bending tests, the load applied on the micro Cu_6Sn_5 pillars and the displacement of the indenter were recorded and plotted in Fig. 4.12 c). The load-displacement curve from the micro cantilever bending tests can be generally divided into three stages: i) mechanical response of Cu_6Sn_5 pillar; ii) the free movement of nano indenter; iii) the unloading of the indenter. When the flat indenter was in contact with the micro Cu_6Sn_5 pillar in the tests, the applied load on the Cu_6Sn_5 pillar increased linearly with the growing deflection until its fracture. After the fracture of the Cu_6Sn_5 pillar, the load from the flat indenter cannot be sustained by the fractured IMC pillar anymore. Hence, the indenter moved forward freely without any increase in load, which is represented by the plateau in the curve. In the movement, the rear of the indenter was in contact with the bulk specimen again due to the overall conical shape of the indenter. Hence, the indenter was sustained by the 2nd contact between the rear surface of the indenter and the specimen. Consequently, the movement of the indenter was stopped. Due to this 2nd contact, some damage could be introduced to the fracture surface of the micro Cu_6Sn_5 pillar if the indenter reached the

fracture surface prior to its contact with the surrounding material. Finally, the system started responding to the sudden and dramatic increase in the displacement of the indenter. And it was then unloaded and withdrawn to the initial position to finish the cantilever bending test, which is represented by the last stage of the curve.

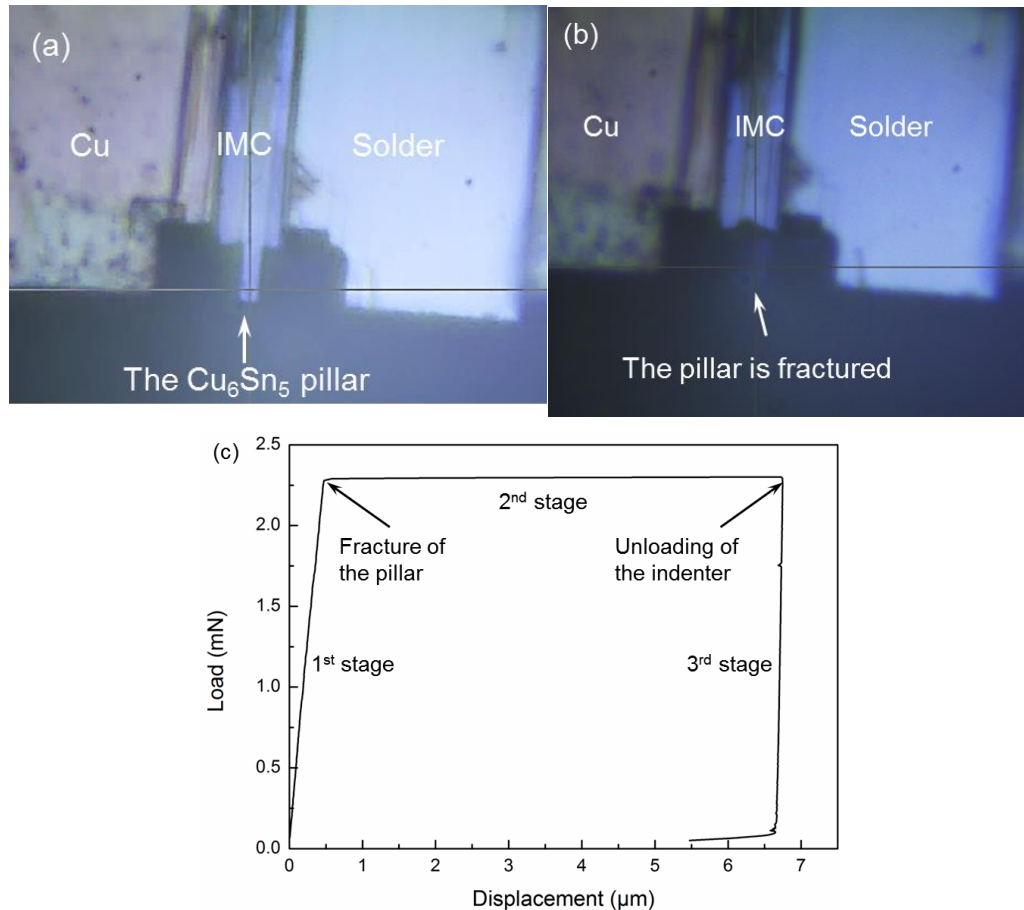


Fig. 4.12 Cantilever bending test on a micro Cu_6Sn_5 pillar: optical images of the specimen (a) before the test and (b) after the test; (c) the obtained load-displacement curve from the test.

Consequently, only the 1st stage of the load-displacement curves can represent the mechanical response of the micro Cu_6Sn_5 pillar under the applied load during the cantilever bending test. Therefore, the 1st stage of the load-deflection curves from the three tested micro Cu_6Sn_5 pillars are summarized in Fig. 4.13. The fracture forces of the pillars could then be estimated to range from 2.06 mN to 2.25 mN and the corresponding deflection was within 0.45~0.5 μm . Furthermore, it can also be observed that the force applied on the micro Cu_6Sn_5 pillars generally increased linearly with the deflection of the pillars before the fracture, which indicates that the micro Cu_6Sn_5 pillars remained elastic before its fracture during the test.

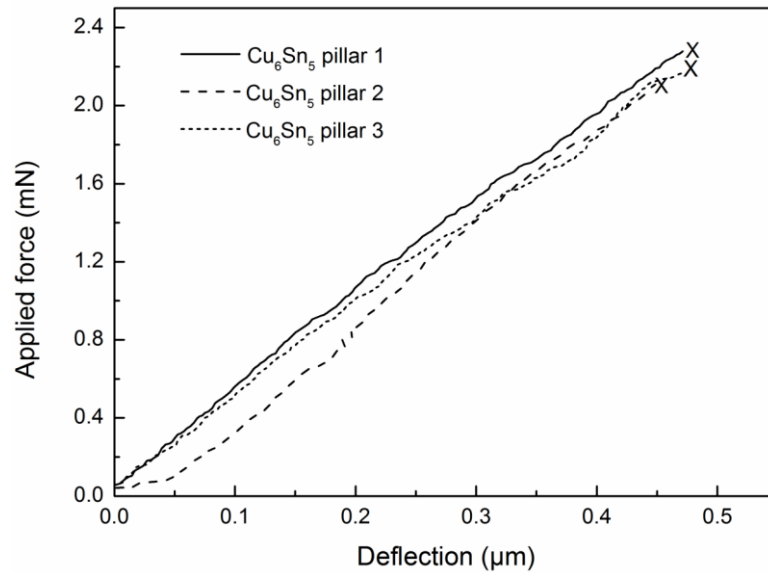


Fig. 4.13 Load-deflection curves from cantilever bending tests on three micro Cu_6Sn_5 pillars. The crosses at the end of the curves denote the fracture points of IMC pillars.

After the cantilever bending test, the fracture surface of the tested micro Cu_6Sn_5 pillars was examined by SEM. An example of the Cu_6Sn_5 pillars after the cantilever bending test was shown in Fig. 4.14 a). From the image, no plastic deformation can be observed in the micro Cu_6Sn_5 pillar, which confirms that the pillar was elastic before the fracture during the cantilever bending test. The mark on the surface of the micro Cu_6Sn_5 pillar was due to the contact between nanoindenter and the pillar in the test, which indicates that the contact point was about 5 μm away from the end of the indenter to the bottom of the pillar as expected.

Fig. 4.14 b) and c) illustrate two examples of the fracture surface of Cu_6Sn_5 pillars. The damage at the edge of the fracture surface in Fig. 4.14 b) could be attributed to the 2nd contact between the rear of the indenter and the specimen after the fracture of the IMC pillars in the cantilever bending tests. It is evident that Fig. 4.14 b) and c) demonstrate two typical fracture surfaces of the tested Cu_6Sn_5 pillars, which indicates two types of fracture modes. The smooth finish of bending fracture in Fig. 4.14 b) indicates a cleavage fracture mode as reported elsewhere [197]. However, Fig. 4.14 c) presents a typical intergranular fracture surface, which appears to be a different fracture mode. The difference in the observed two types of fracture modes can be attributed to the number of Cu_6Sn_5 grains that involved at the bottom of the micro Cu_6Sn_5 pillars, which will be discussed in details in section 4.3.3.1. The composition of the fracture surface of the Cu_6Sn_5 pillar was then analysed with EDX, which shows the tested pillar was Cu_6Sn_5 phase as designed (Fig. 4.14 d)).

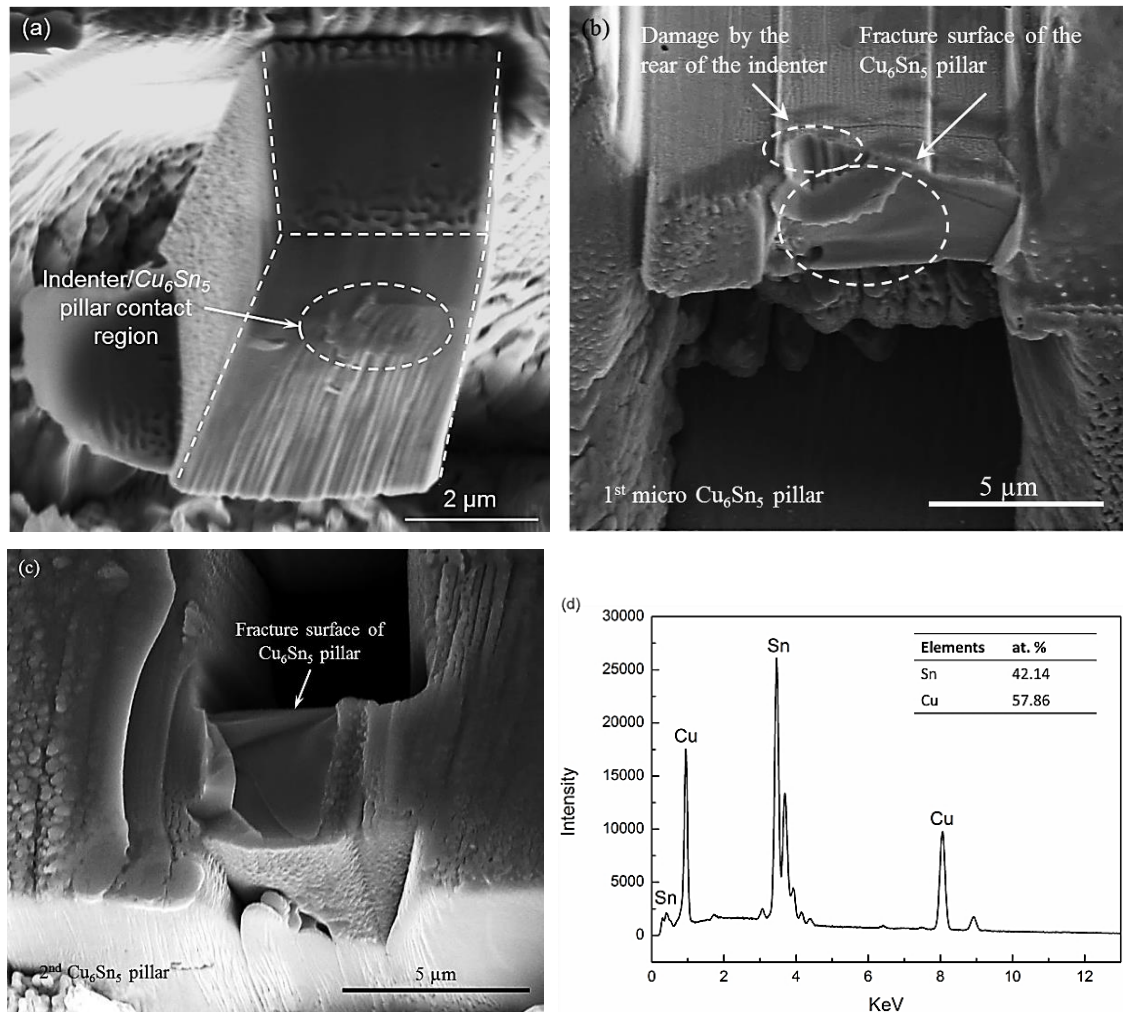


Fig. 4.14 Observation and composition analysis of the fracture surface of micro Cu_6Sn_5 pillar after cantilever bending test: (a) the Cu_6Sn_5 pillar after cantilever bending test; (b) and (c) two types of fracture surface observed from the tested micro Cu_6Sn_5 pillars; (d) the EDX spectrum of the fracture surface.

Fig. 4.14 b) and c) also demonstrate that the micro Cu_6Sn_5 pillars failed from the bottom of the pillar where the maximum tensile stress was induced during the cantilever bending tests. Therefore, it can be assumed that the Cu_6Sn_5 pillars were fractured by the maximum tensile stress on the top surface at the bottom of the micro pillar, which can be estimated by flexural formula [198],

$$\sigma_m = FL/(I/y) \quad (4.1)$$

where F is the applied bending force; L is the distance between the bottom of the beam and the point where the force is applied; I is the moment of inertia of the beam cross section, and y is the vertical distance between the upper surface and the neutral plane.

For cuboid micro Cu_6Sn_5 pillars with a rectangular cross section illustrated in Fig. 4.15, the moment of inertia of the cross section can be calculated by $I = bh^3/12$. Therefore, the tensile fracture strength of Cu_6Sn_5 pillar can be estimated to be 2.4 ± 0.1 GPa.

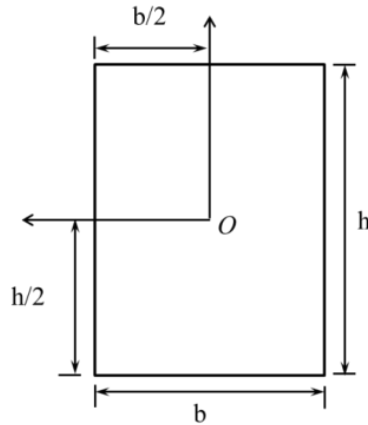


Fig. 4.15 Rectangular cross section of a cuboid pillar.

However, it has been understood that the flexural formula relies on the hypothesis that only the deformation of the pillar is accounted in calculation while the deformation in the adjacent material is excluded, which is violated in micro-scale tests [199]. Hence, modelling is recommended, which may be more reliable for evaluating the maximum tensile stress during micro cantilever bending tests [199-201].

4.3.2 Modelling results

From the setting of modelling in section 4.2.3, the loads in the micro cantilever bending tests and in the modelling were the same. Therefore, it is possible to validate the built finite element models by comparing the deflections of the pillars from experiments and the deflection from modelling. The accordance between the modelling and experimental load-deflection curves can then determine whether the stress distribution in the finite element model fits the corresponding experimental result. Fig. 4.16 illustrates an example of the comparison between load-deflection curves from experimental test and the modelling, which demonstrates excellent accordance between the two curves. The modelling was based on two fundamental assumptions that the micro Cu_6Sn_5 pillar was isotropic and the indenter was perpendicular to the pillar before the mechanical test. Hence, the good agreement between the experimental and modelling curves indicates an approximately ideal angle between the indenter and the pillar in the mechanical tests. But, the assumption of an isotropic pillar in modelling was probably violated in experiments due to the limited number of Cu_6Sn_5 grains in the micro pillar, which cannot be reasonably solved because of the lack of anisotropic data of Cu_6Sn_5 phase.

Therefore, the tensile fracture strength of Cu_6Sn_5 , which is the maximum tensile stress in the micro Cu_6Sn_5 pillar in cantilever bending test, can be estimated by extracting the tensile stress on the top surface at the bottom of the pillar in the finite element model.

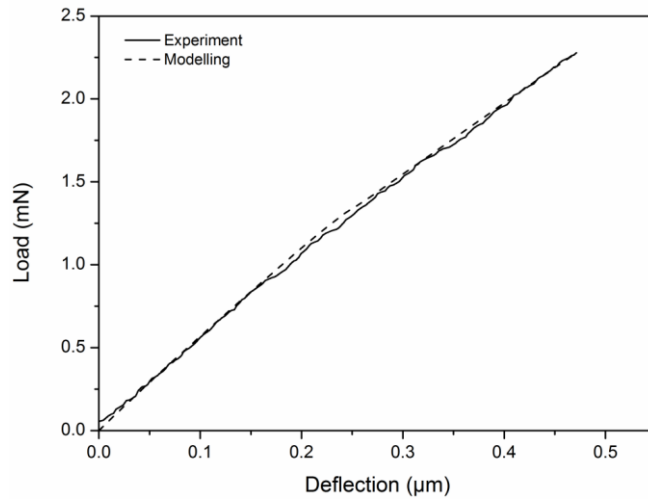


Fig. 4.16 An example of the comparison of load-deflection curves from experiment and modelling.

Due to the sharp corners at the Cu_6Sn_5 pillar/support interface as shown in Fig. 4.17, the tensile stress at these two regions were found to increase continuously with refined mesh, which is named as stress singularity regions in modelling [202]. The convergence of the stress within the stress singularity region requires additional fillets with the minimum diameter of approximately $2\ \mu\text{m}$, which is not reasonable to the actual micro Cu_6Sn_5 pillar. However, the effect of stress singularity is limited within a small range (Fig. 4.17), leaving the stress in the middle of the IMC pillar independent of the mesh size (the red line in Fig. 4.17). Hence, the tensile strength of Cu_6Sn_5 was derived from the middle of the pillar, which can provide a more reliable estimation. The results are listed in Table 4.3. The average tensile fracture strength of Cu_6Sn_5 was evaluated to be $1.3 \pm 0.1\ \text{GPa}$, and the corresponding fracture strain is about 0.011.

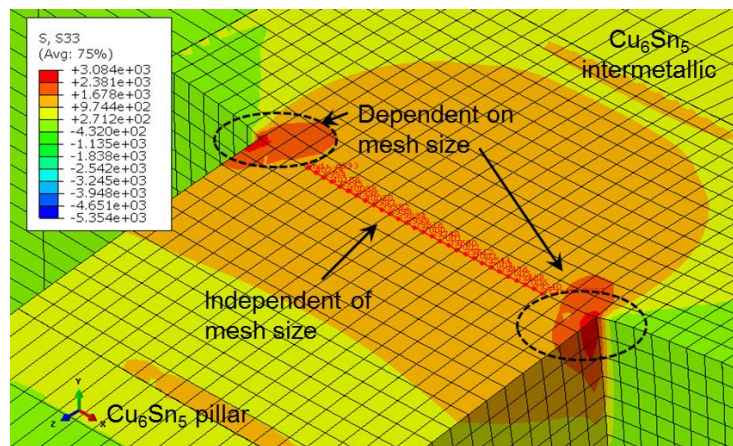


Fig. 4.17 The selected region where the stress is independent of mesh size for the evaluation of tensile fracture strength of Cu_6Sn_5 .

Table 4.3 The tensile fracture strength of Cu_6Sn_5 based on modelling.

	Tensile fracture strength (GPa)
Pillar 1	1.4 GPa
Pillar 2	1.2 GPa
Pillar 3	1.3 GPa
Average	1.3 ± 0.1 GPa

It is found that the tensile fracture strength of Cu_6Sn_5 from modelling (1.3 ± 0.1 GPa) is significantly lower than the fracture strength calculated with flexural formula (2.4 ± 0.1 GPa). The difference can be attributed to the assumption in the flexural formula that the tested pillar is attached to an ideally rigid support, which will be discussed in detail in section 4.5.1.

4.3.3 Discussion

4.3.3.1 Tensile fracture modes of Cu_6Sn_5

Two fracture mechanisms were identified from the fractured surfaces of Cu_6Sn_5 pillar in Fig. 4.14, which could be attributed to the number of grains involved at the bottom of the pillar. Fig. 4.18 is an EBSD image across the Sn99Cu1/Cu interface after aging at 175 °C for 1132.5 hours. It is shown that the size of Cu_6Sn_5 grains that initially formed in reflowing increased to about 10 μm after aging for 1132.5 hours, while the size of the grains that emerged in aging process was approximately 2 μm .

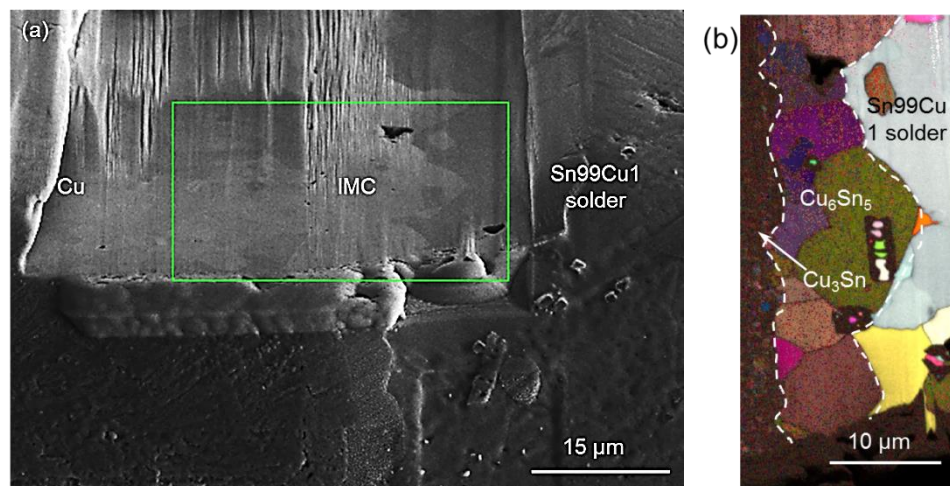


Fig. 4.18 The Cu_6Sn_5 grains at the solder/Cu interface in Sn99Cu1/Cu solder joint after aging at 175 °C for 1132.5 hours: (a) the region on the specimen for the scanning with EBSD; (b) grain orientations of Cu_6Sn_5 grains at the interface.

Therefore, the bottom of a micro Cu_6Sn_5 pillar could be within a single big Cu_6Sn_5 grain or across several Cu_6Sn_5 small grains, as illustrated in Fig. 4.19. For the former case, the micro Cu_6Sn_5 pillar will fracture along a crystalline plane close to the bottom of the micro pillar in the cantilever bending test, which is cleavage fracture. If several Cu_6Sn_5 grains are involved at the bottom of a Cu_6Sn_5 pillar, the crack will preferentially propagate along the grain boundaries that are adjacent to the bottom of the pillar where the weakest adhesion is located in comparison to the strength within grains, leading to the intergranular fracture. Therefore, both cleavage and intergranular fracture were observed from the fracture surface of the tested micro Cu_6Sn_5 pillars.

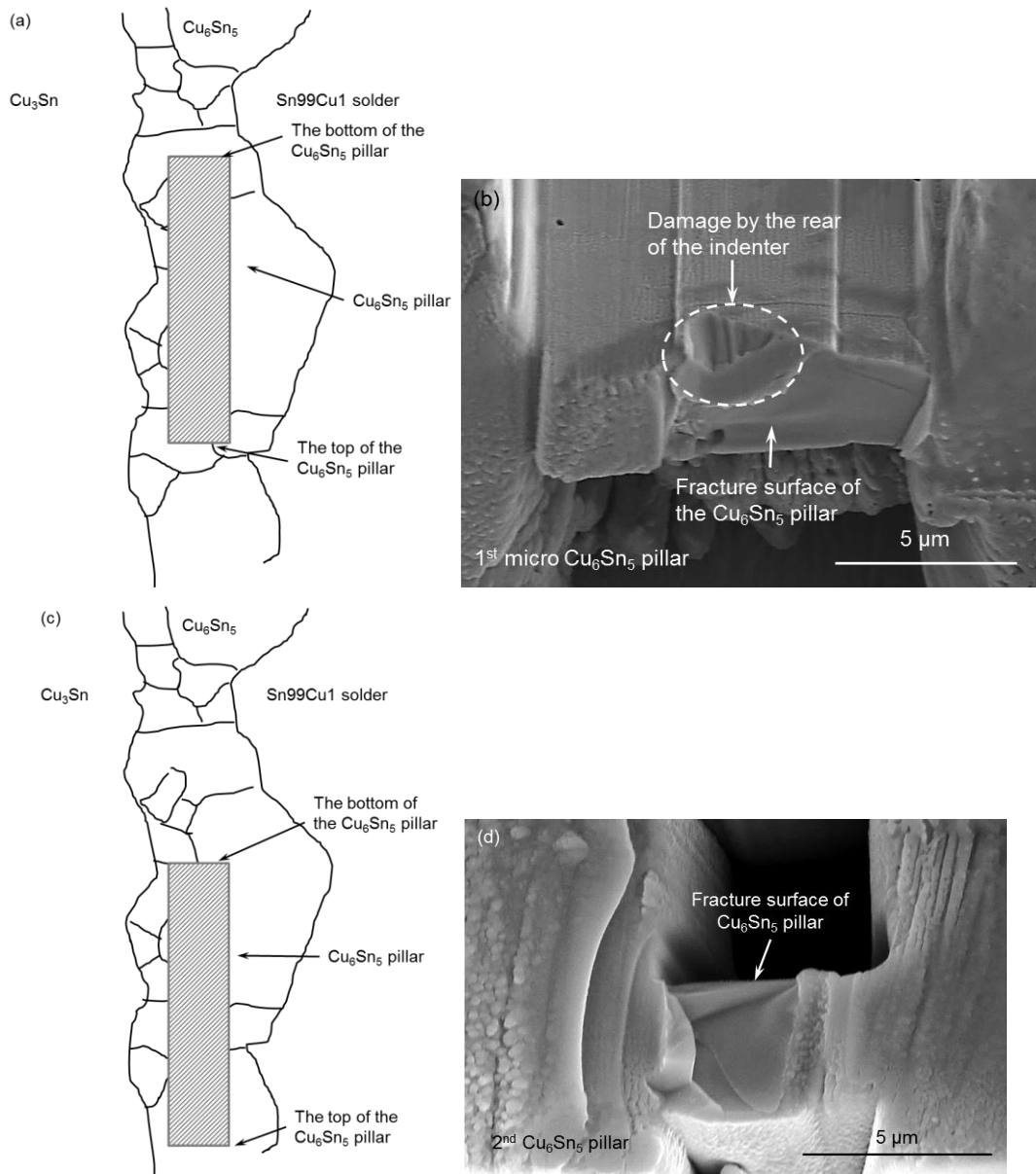


Fig. 4.19 Two different fracture modes of micro Cu_6Sn_5 pillars after cantilever bending test; (a) and (c) illustrate the two possible locations of the bottom of micro Cu_6Sn_5 pillar in the Cu_6Sn_5 layer; (b) and (d) are the SEM images of the two corresponding fracture surfaces after cantilever bending tests.

4.3.3.2 Tensile fracture strength of Cu_6Sn_5

From the analysis based on experimental and modelling results, the tensile fracture strength of Cu_6Sn_5 can be estimated to be about 1.3 GPa which is comparable to the reported compression strength of Cu_6Sn_5 in solder joint (approximately 1.36 GPa) [73]. However, it is generally believed that the tensile strength of a material is supposed to be significantly lower than its compression strength, which does not fit the comparison here. This can be primarily ascribed to the underestimation of compression strength of Cu_6Sn_5 in the literature.

The compression strength of Cu_6Sn_5 was characterised by the nanoindentation test on cylindrical micro Cu_6Sn_5 pillars with flat indenter in reference [73]. Ideally, a precise measurement of the compression strength of Cu_6Sn_5 could be achieved if the surface of the indenter is parallel to the top surface of the fabricated micro Cu_6Sn_5 pillars during the compression test (Fig. 4.20 a)). However, there was always an angle between the end of the indenter and the pillar in actual experiments, as illustrated in Fig. 4.20 b). This would inevitably lead to stress concentration at the indenter/ Cu_6Sn_5 pillar contact region. When the load applied on the micro Cu_6Sn_5 pillars increased, the localised stress can easily lead to the fracture of Cu_6Sn_5 pillar due to the limited contact region. The compression strength of Cu_6Sn_5 was then estimated by dividing the force at the first fracture of Cu_6Sn_5 pillar by the nominal area [73]. This could lead to serious underestimation of the fracture strength, because the actual contact area between the indenter and micro Cu_6Sn_5 pillar was far less than the nominal area due to the angle.

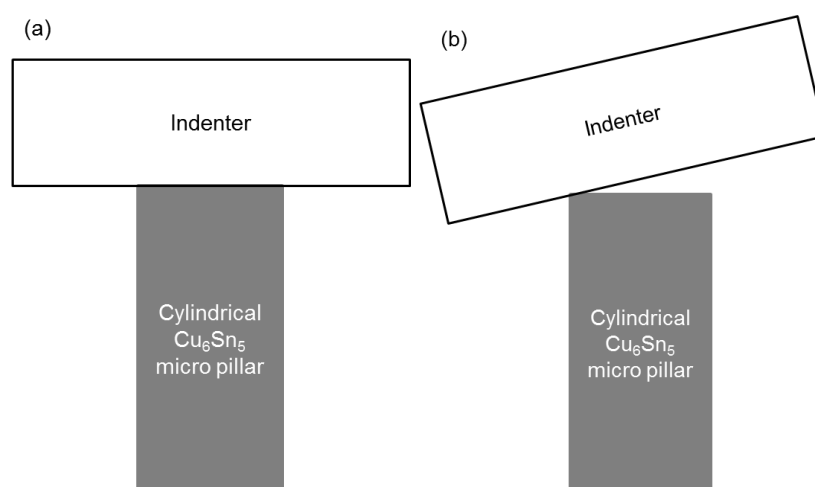


Fig. 4.20 The compression test on micro Cu_6Sn_5 pillar in reference [73]: (a) the indenter was parallel to the top surface of the Cu_6Sn_5 pillar in ideal case; (b) the indenter was not parallel to the top surface of micro Cu_6Sn_5 pillar in real case.

In contrast, characterising the tensile strength of Cu_6Sn_5 by cantilever bending test eliminate the potential initiation of crack induced by stress concentration at the indenter/IMC pillar contact region. From the modelling, the stress inevitably concentrated at the indenter/ Cu_6Sn_5 pillar contact point during the mechanical test. However, the micro Cu_6Sn_5 pillars were fractured from the bottom due to the maximum tensile stress on the top surface at the pillar/support interface, which was

approximately 5 μm away from the stress concentration area. Hence, it is acceptable to assume a negligible influence of the stress concentration on the fracture behaviour of micro Cu_6Sn_5 pillars in the micro cantilever bending tests.

4.4 Fracture behaviour of Cu_3Sn

4.4.1 Experimental results

Fig. 4.21 illustrates an example of the micro Cu_3Sn pillars fabricated with FIB according to the procedures in section 4.2.2.2. The dimensions of the pillar were measured to be $1.5 \times 1.5 \times 10 \mu\text{m}$ (L \times W \times H in μm). The composition of the pillar was analysed by EDX, which confirms that the micro pillar was Cu_3Sn as expected.

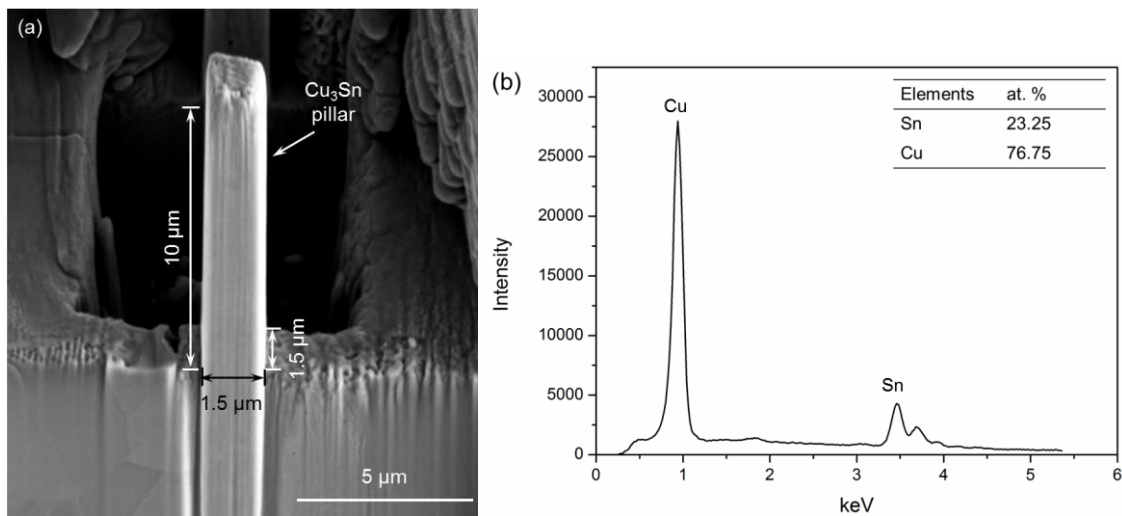


Fig. 4.21 An example of the micro Cu_3Sn pillars fabricated with FIB: (a) the dimensions of the Cu_3Sn pillar; (b) the EDX spectrum of the fabricated pillar.

The cantilever bending tests on the micro Cu_3Sn pillars were assisted with an optical microscope for observation. Before the cantilever bending test, the micro Cu_3Sn pillar was located at the solder/Cu interface at the corner of the specimen, as illustrated in Fig. 4.22 a). After the test, the micro Cu_3Sn pillar was fractured from the bottom of the pillar as designed (Fig. 4.22 b)). An example of the load-displacement curves from the cantilever bending test is depicted in Fig. 4.22 c). The curve generally consists of three stages: i) mechanical response of Cu_3Sn pillar; ii) free movement of nano indenter; iii) the unloading of the indenter. The three stages were divided by the fracture of Cu_3Sn pillar and the unloading of the indenter, as shown in Fig. 4.22 c), which is similar to the process for micro Cu_6Sn_5 pillar described in section 4.3.1.

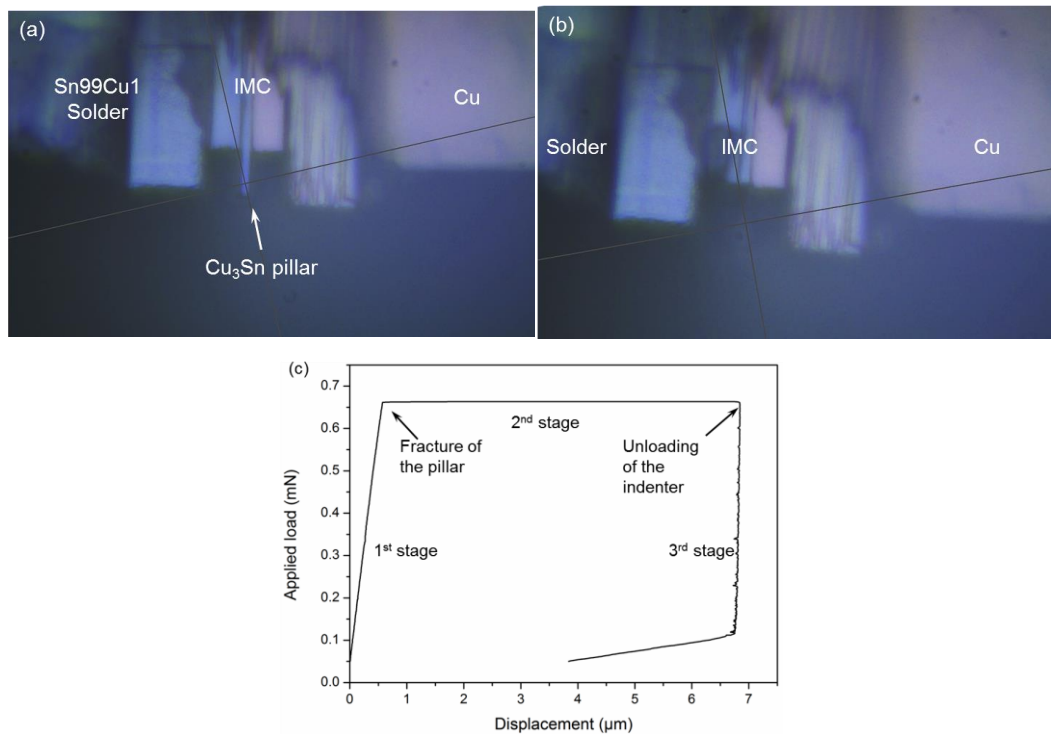


Fig. 4.22 Cantilever bending test on Cu_3Sn pillar: images of the micro Cu_3Sn pillar (a) before test, (b) after test and (c) a representative load-displacement curve from the test.

The 1st stage of the load-displacement curve represents the mechanical response of the micro Cu_3Sn pillar to the applied load during the cantilever bending test. Therefore, the 1st stages of the load-displacement curves from the three tested micro Cu_3Sn pillars were summarised and plotted together in Fig. 4.23. The fracture force of the micro Cu_3Sn pillars was estimated as 0.64 mN~0.78 mN, and the corresponding deflections were from 0.54 μm to 0.77 μm . Furthermore, from Fig. 4.23, the load applied on the Cu_3Sn micro pillars increased linearly with the deflection before the fracture of the pillar during the micro cantilever bending tests, which indicates the micro Cu_3Sn pillars were elastic under the applied load in the tests.

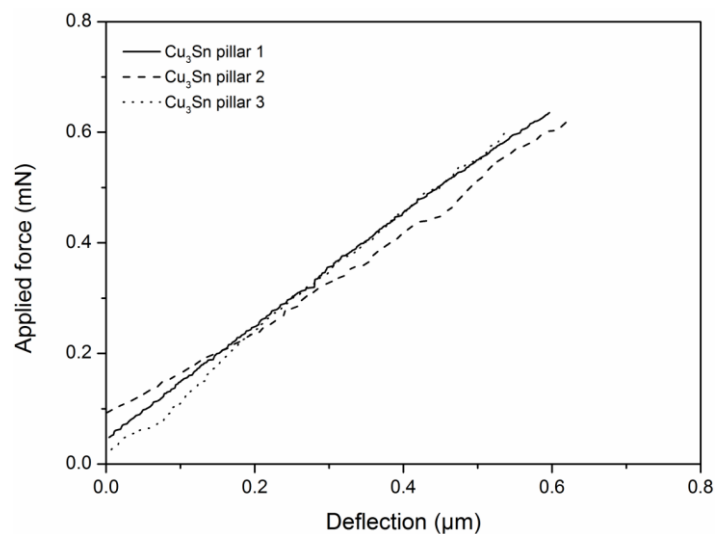


Fig. 4.23 Load-deflection curves of the micro Cu_3Sn pillars from cantilever bending tests.

After the cantilever bending tests, the tested micro Cu_3Sn pillars were examined with SEM, as illustrated in Fig. 4.24 a). It shows no observable plastic deformation in the tested pillar, which reinforces the assumption that micro Cu_3Sn pillars remained elastic before its fracture based on the load-deflection curves in Fig. 4.23.

Furthermore, it could be observed that the micro Cu_3Sn pillar was fractured from the bottom of the pillar, which indicates that the fracture was resulted by the maximum tensile stress at the bottom of the pillar. According to the flexural formula in equation (4.1), the maximum tensile stress at the bottom of micro Cu_3Sn pillars was calculated to be within 5.6–6.0 GPa. Due to the potential overestimation of the calculation with the formula, modelling was utilised for the further evaluation of the tensile fracture strength of the micro Cu_3Sn pillars.

The fracture surface of the tested Cu_3Sn pillar is illustrated in Fig. 4.24 b). Many sub-micrometer facets can be identified in the figure, which indicates that the crack propagated along the Cu_3Sn grain boundaries at the bottom of the micro pillar in the test. The tensile fracture mode of Cu_3Sn can then be categorized as intergranular fracture [203]. The composition of the fracture surface was also analysed with EDX and the result is illustrated in Fig. 4.24 c), which proves that the fractured pillar consisted of Cu_3Sn phase only.

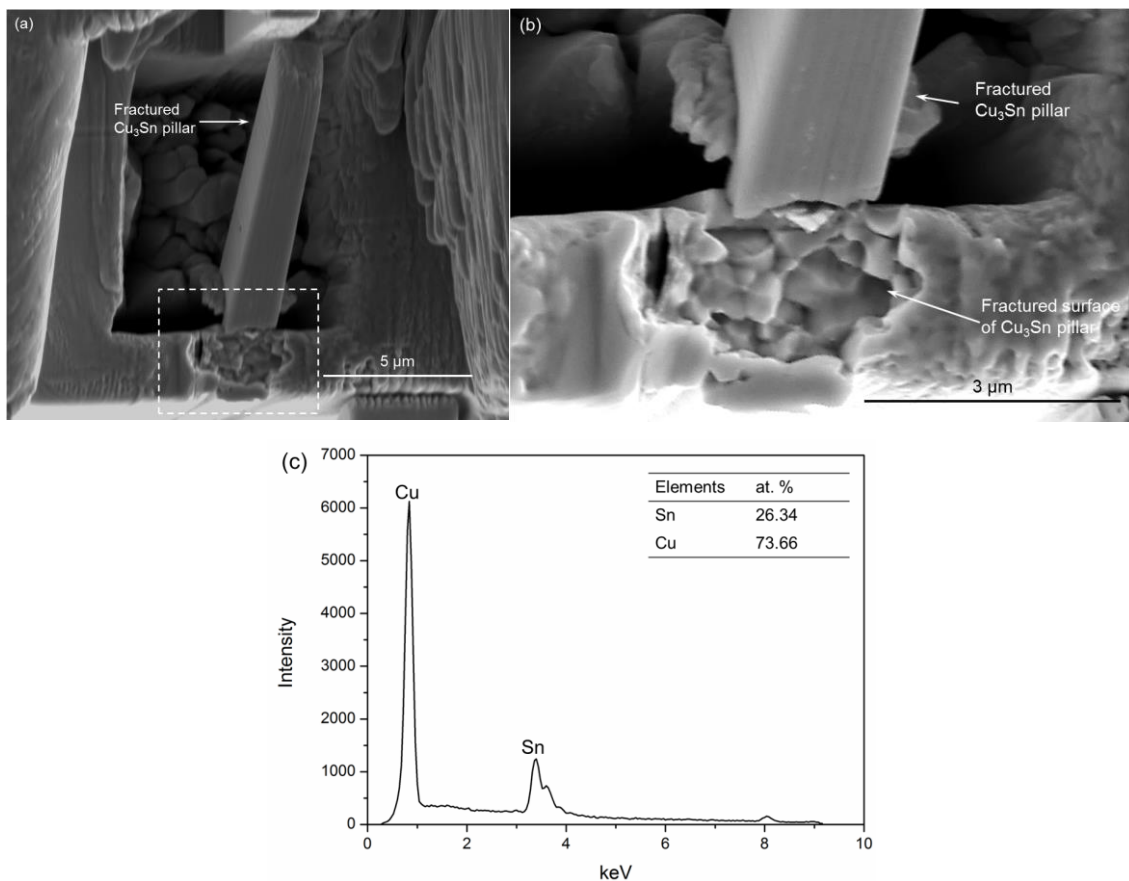


Fig. 4.24 The micro Cu_3Sn pillar after cantilever bending tests: (a) the fractured micro Cu_3Sn pillar; (b) The enlarged view of the fracture surface of micro Cu_3Sn pillar; (c) the EDX spectrum of the fracture surface of the test pillar.

4.4.2 Modelling results

Due to the possible overestimation in the calculation with the flexural formula, finite element modelling was employed for a more reliable evaluation of the maximum tensile stress on the top surface at the bottom of the micro Cu_3Sn pillar. The settings and boundary conditions involved in the finite element model are listed in section 4.2.3.

The forces applied on the micro Cu_3Sn pillars in the tests were converted to pressure load on the indenter in the modelling to simulate the loading process of the cantilever bending tests. Therefore, load-displacement curves can be extracted from modelling results for the comparison with the recorded experimental curves in Fig. 4.23 to examine the validity of the modelling. Fig. 4.25 shows an example of the comparison between the modelling and experimental load-deflection curves, which demonstrates excellent accordance between them. The variation between these two could be attributed to the assumption in modelling that the indenter was perpendicular to the top surface of the micro IMC pillar before the test, which might be violated in the experimental tests. It is also worth of notice that there is an initial load before the test in the experimental curve due to the unbalanced load sensor in the nanoindentation instrument, which was inevitable but within a reasonable range.

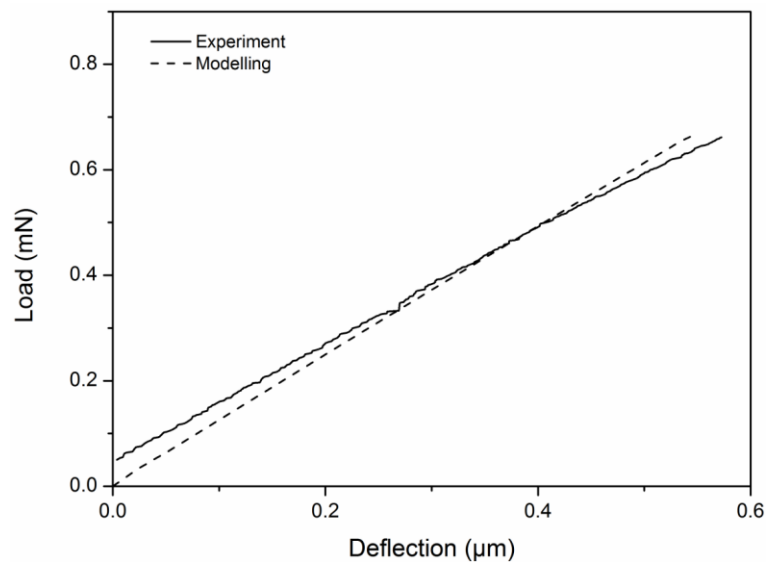


Fig. 4.25 Comparison between the load-deflection curves from the experiment and modelling.

Therefore, the tensile fracture strength of Cu_3Sn can be evaluated by extracting the maximum tensile stress at the bottom of the pillar in the model as illustrated in Fig. 4.26. Due to the sharp corners between the Cu_3Sn pillar and the support, the stress close to these two regions (illustrated in Fig. 4.26) increased significantly with refined mesh. But the size of fillets that required eliminating the stress singularity region cannot fit the actual features of the micro Cu_3Sn pillar. Therefore, the tensile fracture strength was evaluated based on the average stress at the centre of the bottom of the micro Cu_3Sn pillar (the red line in Fig. 4.26) where the stress was independent of the mesh size. Hence, the tensile strength of Cu_3Sn were derived and listed in Table 4.4 with the average value of 2.3 ± 0.1 GPa. The corresponding average fracture strain was about 0.017 [195].

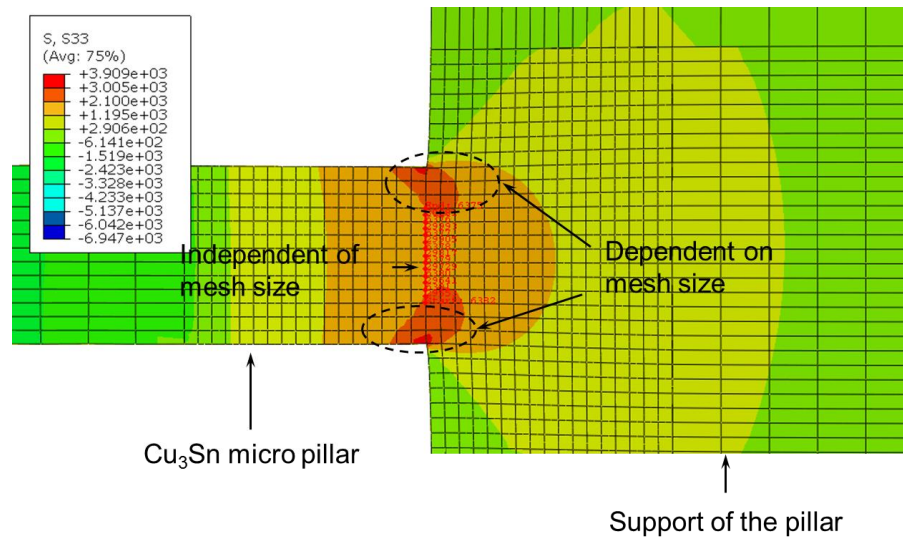


Fig. 4.26 The stress at the selected region was independent of mesh size.

Table 4.4 Tensile fracture strength of Cu_3Sn from modelling.

	Tensile fracture strength
Pillar 1	2.4 GPa
Pillar 2	2.2 GPa
Pillar 3	2.5 GPa
Average	2.3 ± 0.1 GPa

4.4.3 Discussions

The tensile fracture mode of Cu_3Sn was observed to be intergranular in this work, which can be attributed to the microstructure of the interfacial Cu_3Sn layer in the Sn99Cu1/Cu solder joint after aging. Due to the limit of the spatial resolution of EBSD, the Cu_3Sn grains at the Sn99Cu1 solder/Cu interface cannot be revealed clearly in Fig. 4.18 b). Therefore, the ion beam in FIB was utilised for imaging to show the contrast of the grain orientations in the interfacial Cu_3Sn layer [204, 205]. Fig. 4.27 presents an example of the ion-beam image of micro Cu_3Sn pillar, which shows many sub-micrometer grains within the interfacial Cu_3Sn layer. Similar microstructure was also reported by P. J. Shang *et al.* with TEM [22].

Therefore, it is reasonable to assume that the bottom of micro Cu_3Sn consisted of many sub-micrometer Cu_3Sn grains after the fabrication with FIB. When the pillar was subjected to the load applied by the indenter during cantilever bending test, the tensile stress concentrated at the bottom of the pillar. Hence, the crack preferentially initiated and propagated along the Cu_3Sn grain boundaries close to the bottom of Cu_3Sn pillar where the adhesion was weak. Consequently, the intergranular fracture of Cu_3Sn pillar was observed in Fig. 4.24 b).

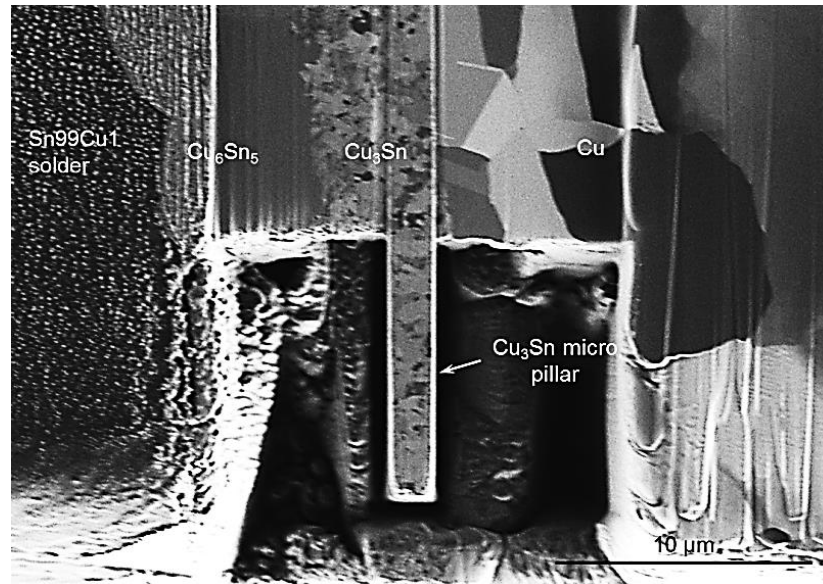


Fig. 4.27 The contrast of grain orientations in the interfacial Cu_3Sn layer by the ion beam in FIB.

4.5 General discussions

4.5.1 Modelling and flexural formula

The tensile fracture strength of Cu_6Sn_5 and Cu_3Sn evaluated by the calculation with flexural formula and finite element modelling are listed in Table 4.5. The fracture strength calculated by flexural formula is found to be 1.9 times and 2.5 times higher than the modelling results for Cu_6Sn_5 and Cu_3Sn , respectively. The lower difference in the comparison of fracture strengths from the two different methods in Cu_6Sn_5 pillar could be caused by the bigger size of micro Cu_6Sn_5 pillars, since the accuracy of the calculation with flexural formula depends on the geometry of the pillar [206]. Furthermore, the reliability of the fracture strengths derived from modelling and calculation should be discussed. In section 4.3.2 and 4.4.2, the load-deflection curves of micro Cu_6Sn_5 and Cu_3Sn pillars from modelling demonstrate excellent accordance with the curves measured in experiments. Therefore, it is reasonable to assume the fracture strength of Cu_6Sn_5 and Cu_3Sn derived from the modelling is more reliable.

Table 4.5 Comparison of tensile strengths of Cu_6Sn_5 and Cu_3Sn estimated by modelling and flexural formula

	Flexural formula	Modelling
Cu_6Sn_5	2.4 ± 0.1 GPa	1.3 ± 0.1 GPa
Cu_3Sn	5.7 ± 0.2 GPa	2.3 ± 0.1 GPa

For the calculation with flexural formula, the hypothesis that the support of the tested IMC pillars is rigid without any deformation [199] could be violated in the micro cantilever bending test in this work. The materials beneath the micro Cu_6Sn_5 and Cu_3Sn pillars was the same as the pillars,

which also underwent a similar level of deformation during the cantilever bending test under applied load. Hence, both the micro IMC pillar and the material beneath it contributed to the measured deformation of the entire specimen. However, according to the hypothesis in flexural formula, the support of the micro cantilever was rigid. Hence, the deformation which was in both the pillar and its support was considered as the deformation of the IMC pillars only, as schematically illustrated in Fig. 4.28. Therefore, the deformation in the micro IMC pillar was inevitably overestimated in the calculation with flexural formula. Consequently, it is reasonable to conclude that the tensile strength of Cu_6Sn_5 and Cu_3Sn estimated by modelling is more reliable in this work.

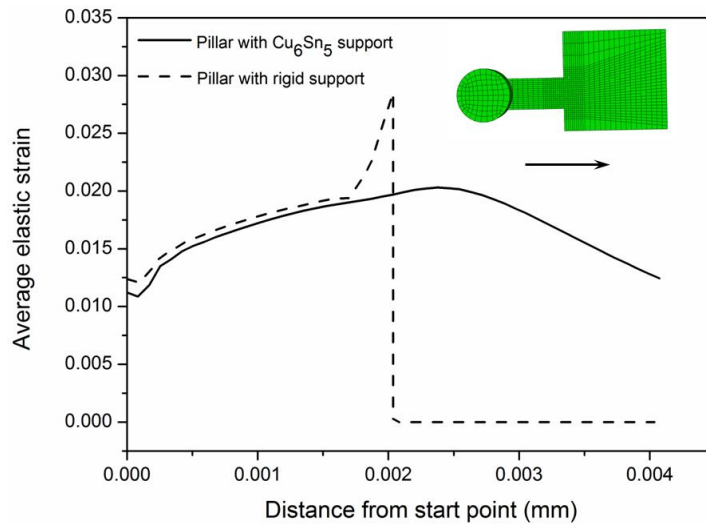


Fig. 4.28 Schematic of the comparison between the strain distribution across the bottom of micro Cu_6Sn_5 pillar in finite element model with Cu_6Sn_5 support and the model with ideally rigid support.

4.5.2 Effects of aging on the fracture strength of solder joints

The work in this chapter demonstrates that the fracture strength of both Cu_6Sn_5 and Cu_3Sn are much higher than the reported fracture strength of solder joints (normally within 30~80 MPa). Furthermore, when the interfacial IMC layers in solder joints grew excessively thick, the fracture strength of the solder joints could further drop [100, 207], and the crack preferentially initiated and propagated through the interfacial IMC layers rather than within the bulk solder [3, 208, 209]. This can be attributed to the microstructural evolution in the interfacial Cu_6Sn_5 and Cu_3Sn layers in the solder joint during the aging. For the discussion, tensile fracture of Sn-Cu solder joints was used as an example for the explanation.

When the solder joint is under tension, the tension stress concentrates at the solder/substrate interface because of the necking of the solder matrix [210] and the incompatible deformation of solder and IMCs at the solder/substrate interface due to the dissimilar mechanical properties (such as Young's modulus) [3, 211]. For solder joints with thin interfacial IMC layers, limited number of Cu_6Sn_5 grains and Cu_3Sn grains formed along the thickness direction of the IMC layers [22, 212]. In such case, the interfacial IMC layer is compact without much defect. Therefore, the concentrated stress in the interfacial IMC layers is insufficient to lead to the fracture of IMC layer as the

concentrated stress cannot reach the fracture strength of the IMCs. Therefore, the crack can only initiate and propagate within the solder matrix which is much weaker. Consequently, the observed fracture of solder joints is predominantly ductile fracture within solder matrix when the interfacial IMC layer is thin [213].

In a solder joint after extended aging, many defects could be induced in the interfacial IMC layers during its growth, such as Kirkendall voids in the interfacial Cu_3Sn layer [47, 208, 214] and Ag_3Sn particles on the surface of Cu_6Sn_5 grains in Sn-Ag-based solder joints [32, 215]. Furthermore, the growth of IMCs could also lead to the build-up of internal stress within the interfacial IMC layers which will be demonstrated in chapter 6. This can also promote the level of the stress concentration within the interfacial IMC layers. Hence, when the solder joint is subjected to tensile load, the localised stress can easily exceed the fracture strength of IMCs (i.e. Cu_6Sn_5 and Cu_3Sn) at the defects. Hence, the crack within the interfacial IMC layers can be initiated. Due to the lower fracture toughness (the ability to resist an existed crack, not the fracture strength) of IMCs (i.e. Cu_6Sn_5 and Cu_3Sn) [138, 216], the initiated crack within the interfacial IMC layers would further propagate through the IMC layers because of the lower resistance to crack propagation. Hence, the IMC layer at the solder/substrate interface could be fractured by a load much lower than the fracture strength of IMCs after long-term aging.

Consequently, it is reasonable to conclude that the decrease in the fracture strength of solder joints after aging is due to the accumulation of defects within the interfacial IMC layers.

4.6 Summary

The tensile fracture behaviours of Cu_6Sn_5 and Cu_3Sn were investigated by cantilever bending tests on micro Cu_6Sn_5 and Cu_3Sn pillars fabricated with FIB after aging at 175°C for 1132.5 hours. The fracture surfaces of the tested micro IMC pillars were examined with SEM and EDX. Both the calculation with flexural formula and modelling were applied to evaluate the fracture strength of Cu_6Sn_5 and Cu_3Sn . From the presented experimental works, modelling results and the discussions, it can be concluded that:

1. The micro Cu_6Sn_5 pillar remained elastic before the fracture when subjected to the applied load during micro cantilever bending tests.
2. The tensile fracture strength of Cu_6Sn_5 is approximately 1.3 GPa, and the fracture strain is 0.011.
3. Both transgranular and intergranular fracture were identified from the fractured surface of micro Cu_6Sn_5 pillars. The differences in fracture modes could be attributed to the number of Cu_6Sn_5 grains involved at the bottom of micro Cu_6Sn_5 pillars.
4. The micro Cu_3Sn pillar was elastic until the fracture during cantilever bending test.
5. The tensile fracture strength of Cu_3Sn was estimated to be 2.3 GPa, and the corresponding fracture strain is 0.017.
6. Only intergranular fracture can be identified in the fractured surface of micro Cu_3Sn pillars.
7. The intergranular fracture of Cu_3Sn was resulted by the crack propagation along the grain boundaries of the sub-micrometer Cu_3Sn grains at the bottom of the pillar.

8. The calculation with flexural formula for cantilever bending test could lead to overestimation in the fracture strength of IMCs, which can be attributed to the hypothesis that the support of the micro pillar is rigid during cantilever bending test.
9. The reported decrease in the fracture strength of solder joints with the growth of interfacial IMC layers in literatures can be primarily ascribed to the accumulation of defects within the interfacial IMC layers in aging.

Chapter 5 Collapse of Sn99Cu1/Cu solder joints due to isothermal aging

5.1 Introduction

The growth of interfacial Cu_6Sn_5 and Cu_3Sn layers in the Sn99Cu1/Cu solder joint relies on the solid-state reactions between the solder and Cu substrate. During the reactions, the densities increase from the reagents (i.e. Cu and Sn) to the products (i.e. Cu_6Sn_5 and Cu_3Sn), which can lead to the volume shrinkage at the solder/Cu interface during aging.

Due to its potential correlation with the deterioration of the mechanical reliability of solder joints after aging, the volume shrinkage is often estimated based on theoretical calculations because of the difficulty in quantitative derivation through experimental measurements [83, 93, 94]. However, subject to the geometry and formation of solder joints on a substrate, the volume shrinkage can also be reflected by the reduction of joint height after aging [89]. Therefore, evaluating the collapse of solder joint can become an applicable approach to verify the volume shrinkage resulted from the growth of the interfacial IMC layers, thus providing further understanding on the growth of IMCs and its potential impact on the reliability of solder joints.

In this chapter, Sn99Cu1/Cu solder joints, which were purposely designed to enable precise measurements of the dimensional change, were investigated to reveal the reduction of joint height due to after aging. Such formed solder interconnect specimens were then stored in a vacuum oven for aging at elevated temperature to facilitate the growth of interfacial IMC layers. After aging for different durations, the joint heights were measured using a white light interferometer to the accuracy of about ± 1 nm [160]. Dual-beam FIB was then utilised to observe the interfacial IMC layers and the collapse of joint joints due to the aging. Following the experimental works, a comparison between experimental results and numerical analysis was made, and the accuracy of the measurement was further discussed.

Modelling was also employed to evaluate the potential build-up of internal stress in the solder joints induced by the volume shrinkage. The microstructural evolution induced by the resultant residual stress was examined by identifying the Cu grains close to the solder/Cu interface, which were revealed by the colour of Cu oxide films during aging. Another bare Cu specimen was machined and aged under the same conditions for the comparison with the Sn99Cu1/Cu solder joint specimens, so that possible reasons of the observed microstructural change in the solder joints could be proposed.

5.2 Collapse of solder joints

5.2.1 Experiment procedures

To measure the small collapse of joint height, the specimens for measuring the dimensional change of solder joints were designed as schematically shown in Fig. 5.1 a). The solder interconnects between Cu and solder alloy were initially prepared to have straight and coplanar transition across Cu/ solder interface prior to aging (Fig. 5.1 b)). After aging, as expected, the solder side shrinks due to the growth of IMC layers along the bottom Cu/solder interface. In such case, the

Cu side remained unchanged, which could be used as a reference for measuring the collapse of the solder joints, as illustrated in Fig. 5.1 c).

As the height difference between solder and Cu could be minimal, the quantitative characterisation of the collapse of solder joint depends on the resolution and reliability of the measurement. As presented in chapter 3, white light interferometer is a promising instrument for the measurement of collapse of joint height in this work due to its high accuracy. The region for the measurement should be large enough to minimize the constraint of the vertical solder/Cu interface perpendicular to the top surface of the specimen in aging.

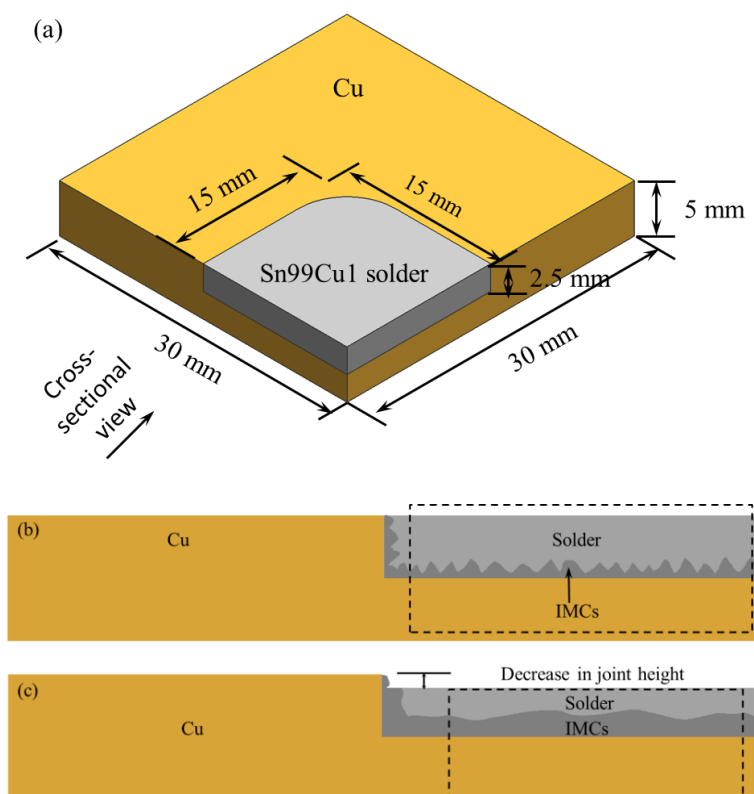


Fig. 5.1 A schematic view of the test specimens (the interfacial IMC layer is exaggerated): (a) the geometry and dimensions; (b) cross-sectional view before aging test: the Cu and solder are at the same height; (c) cross-sectional view after aging: the solder collapses due to the further growth of IMC layers at the interface.

In the preparation of the test samples, the 5 mm thick Cu sheet (purity: 99.9%) was firstly milled to form the pockets as shown in Fig. 5.1 a), then a suitable amount of bulk Sn99Cu1 solder alloy was placed onto the pocket followed by reflowing with a peak temperature of 270°C. In reflowing, a thermal couple was attached to the specimen to monitor the change in temperature. After reflow, the interconnect samples were ground and polished with 1 μm diamond paste to ensure Cu and solder were in exactly the same plane, so that the Cu surface could serve as the reference of the measurement of solder collapse (Fig. 5.1 b)). In the subsequent handling, any contact with the polished surface was prohibited to preserve the integrity of the sample surface and the reliability of the height difference between Cu and solder surfaces after aging.

The polished specimens were then stored in a vacuum oven at 175°C to facilitate the growth of the interfacial IMC layers. The pressure inside the oven was kept at approximately 3 KPa to restrain the oxidation of the samples at elevated temperature. However, during aging, the oxidation of the specimen cannot be eliminated due to the residual air within the oven, which was concerned in the experiment as the thickness of Cu and Sn oxide films could exceed the measurable reduction of joint height. Therefore, the degree of the oxidation of specimens should be properly monitored during the aging of the Sn99Cu1/Cu solder joints.

For the oxidation of solder part, the Sn oxide film was reported to be self-protective and it can prevent the bulk solder from further oxidation once it is formed [217]. Hence, the effect of Sn oxide on the measurement was negligible in this work. However, the Cu oxide film could grow continuously in the Cu part of the Sn99Cu1/Cu solder joints in aging. Hence, the oxidation of the Cu part in the specimens was monitored during aging. Because the polished sample surface should be preserved for the measurement of reduction of joint height after aging, the evaluation of the thickness of Cu oxide film should be non-destructive. It was suggested that the colour of Cu oxide film was related with its thickness during aging at elevated temperature [218]. The correlation between the colour of Cu oxide film and its thickness was further reported by H. A. Miley [219], which is listed in Table 5.1. Therefore, the thickness of the Cu oxide films can be roughly estimated by its colour during the aging.

Table 5.1 The colour of Cu oxide films and its corresponding thickness [219].

Colour	Thickness (nm)
Dark brown	37
Red-brown	41
Purple	46
Violet	48.5
Blue	52
Silvery green	80
Yellow	94
Orange	117
Red	124

After aging for a different length of time up to 1132.5 hours, the top surfaces of specimens were scanned across the solder/Cu boundary using Zygo Newview 5000 to measure the average height difference between the two parts. The accuracy of the height measurement was about ± 1 nm [160] and the lateral resolution of the imaging was approximately 1.2 μ m. To ensure a high accuracy and consistency of the measurement, the scanned areas were selected which were larger than 1.5 mm \times 1.0 mm at the similar region of each specimen using same settings and parameters. After Zygo measurements, the cross-section view across the solder/Cu boundary was prepared by FIB as schematically illustrated in Fig. 5.1 b) and c), then observed by SEM to investigate the IMCs formation and their effects on the dimension of the solder interconnects.

5.2.2 Collapse of solder joints induced by growth of IMCs

Fig. 5.2 a) illustrates an example of the surface morphology data across the Sn99Cu1 /Cu boundary from the measurement with Zygo. During the measurement, the sample could be slightly tilted along a random direction with an unknown angle as shown in Fig. 5.2 a). This could result in a significant error in the calculation of the average step height between the solder part and Cu part due to the slope. Hence, the obtained surface morphology in Fig. 5.2 a) must be levelled to eliminate the angle of the sample surface in measurements. In the levelling, the Cu part was utilised as the reference to the entire solder joint as the surface of bulk Cu was more stable during aging due to much less reactions involved in aging. Fig. 5.2 b) shows the surface morphology of the scanned area in the solder joint after levelling. It is clear that the solder part and Cu part were at different heights after aging.

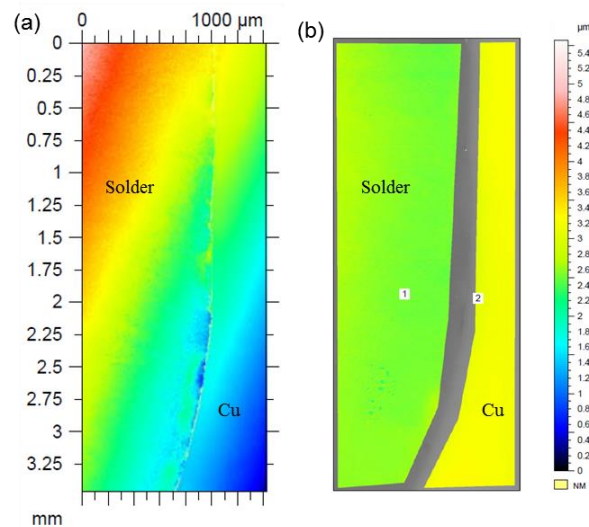


Fig. 5.2 An example of the surface morphology obtained by Zygo Newview 5000: (a) the original data from the measurement with Zygo; (b) the surface morphology after the levelling with the Cu surface.

In order to estimate the height difference between the solder part and Cu part in the solder joint after aging, the surface morphology of the sample surface from the measurement with Zygo was converted into series of height profiles. Fig. 5.3 a) shows an example of the converted surface profiles, which consists of 640 individual profiles of the scanned region. The average surface profile of the scanned region can then be derived for the specimen after aging, as illustrated in Fig. 5.3 b). It shows that the solder part was lower than the Cu part in the Sn99Cu1/Cu solder joint after aging. The peaks at the solder/Cu interface in Fig. 5.3 a) and b) were the protruded perpendicular IMCs which has been discussed in chapter 3.

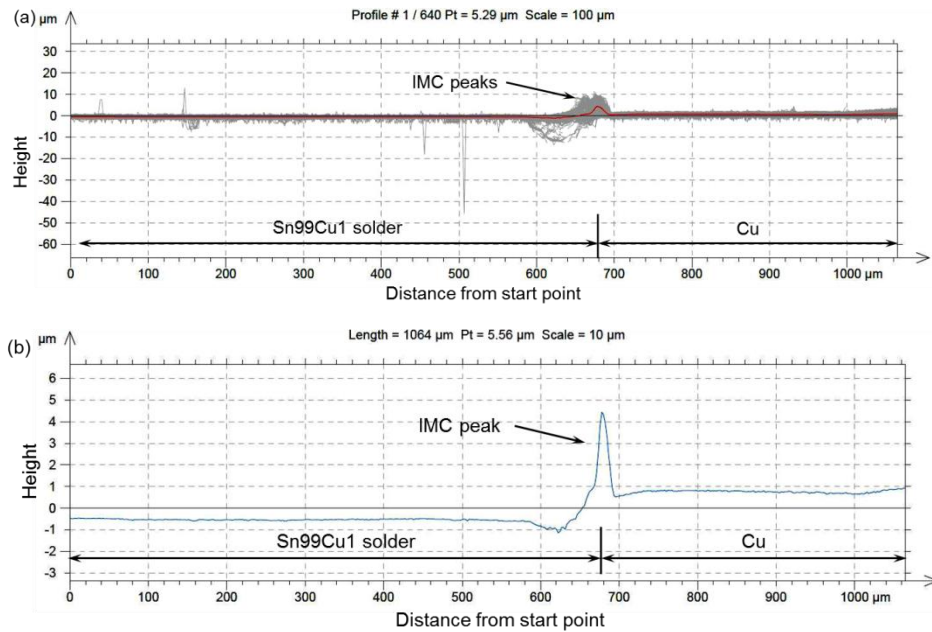


Fig. 5.3 An example of series of surface profiles derived from the measurement with Zygo; (a) The height-distance curves of the scanned region across the Sn99Cu1 solder/Cu interface; (b) the derived average surface profile of the region.

Fig. 5.4 a) shows a family of the average profiles of the same region in the same specimen after aging at 175 $^{\circ}\text{C}$ for 0, 97.5, 630.5 and 1132.5 hours. It is evident that the aging caused an inevitable collapse of the solder side of the joints, and the degree of the reduction of the solder heights was a function of the aging duration. The longer the aging time the greater the height reduction was. Based on these profiles, it is possible to estimate the change in joint height by finding the difference in the average height between Cu and solder. This should also take an initial approximately 0.25 μm height difference into account (Fig. 5.4 a)) which was primarily attributed to the sample preparation. The initial height difference was constant throughout the experiment as no contact with the polished surface was made after polishing. And it had little to do with the solid-state reactions due to aging, so this initial difference must be subtracted from the total value of height changes.

The final calculated results are thereby plotted in Fig. 5.4 b), showing the trend of the height reduction as a function of aging time. Accordingly, a parabolic correlation of the change in joint height with aging durations can be found. After aging for 1132.5 hours, the solder collapse reached approximately 1.2 μm .

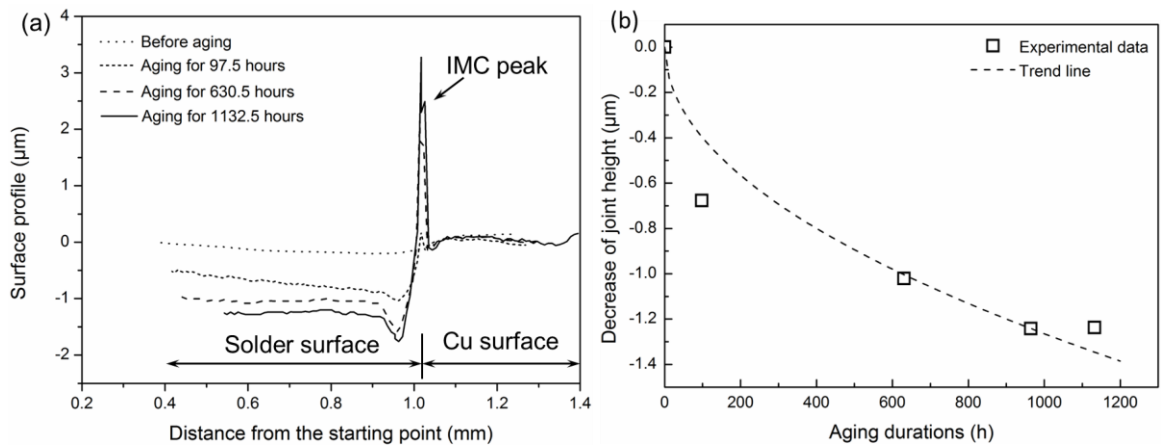


Fig. 5.4 Zygo surface profiling across the Cu/solder boundaries to evaluate the height reduction due to the collapse of solder joints after aging: (a) A series of average surface profiles from one specimen aged at 175°C for 0, 97.5, 630.5 and 1132.5 hours; (b) The plot of decrease in solder height of one specimen vs aging time showing parabolic relationship.

The reduction of joint height was also observed by examining the cross sections of the samples prepared with FIB. As schematically illustrated in Fig. 5.1 b) and c) for un-aged and aged specimens, the solder collapse can be seen from the SEM cross-sectional views of samples before and after aging in Fig. 5.5. For the sample without aging (Fig. 5.5 a)), no noticeable height difference between the solder and Cu could be detected. However, after aging at 175°C for 1132 hours (Fig. 5.5 b)), the solder collapse became notable due to the decrease of the height of the solder joint. The reduction of joint height is approximately 1.29 μm from Fig. 5.5 b).

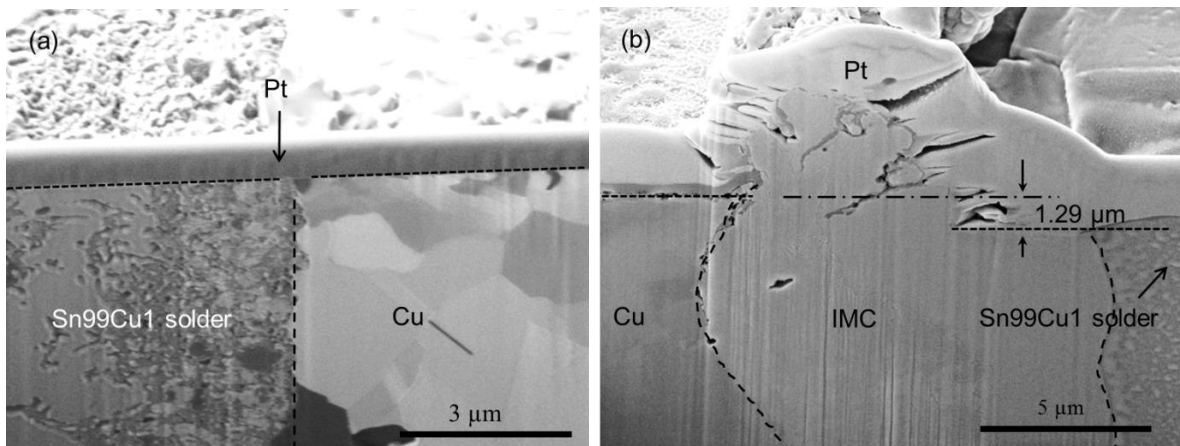


Fig. 5.5 Cross-sectional views of Cu/Sn99Cu1 samples prepared by FIB: (a) before, and (b) after aging at 175 °C for 1132.5 hours. The Pt on the top was deposited to protect the sample beneath it during milling.

With the same data analysis procedures, the collapse of all the investigated four solder joints was estimated and plotted in Fig. 5.6. Each mean value of the height in this figure was derived from four specimens to ensure the reproducibility of the measurements. From Fig. 5.6, the decrease in joint height follows a linear relation with the square root of aging durations. Based on the curve

fitting, this linear correlation can be expressed by

$$\Delta h_{\text{experiment}} = -0.031 \times \sqrt{t} \quad (5.1)$$

where t is aging duration in hour; Δh is the reduction of height in μm . The negative value of Δh indicates the decrease in joint height while a positive value means the height increases with time.

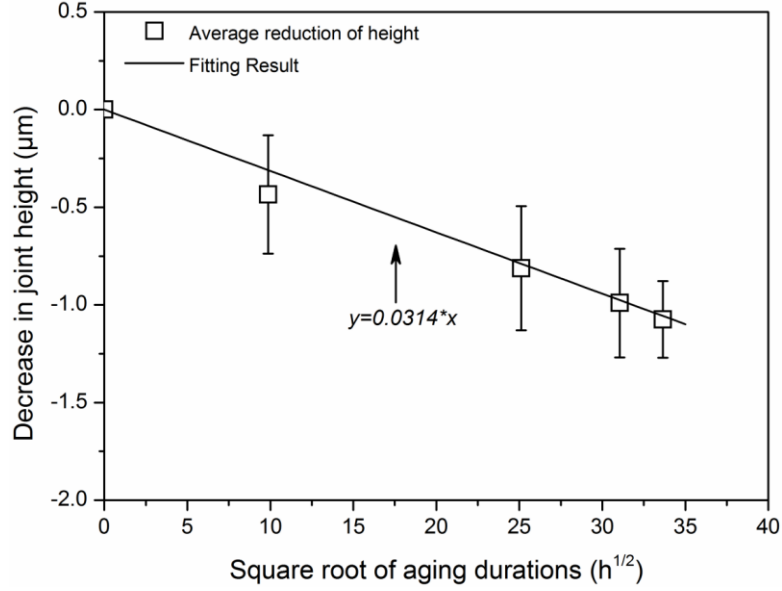


Fig. 5.6 The average height reduction of four specimens vs aging durations at 175°C.

The measured reduction of joint height in Fig. 5.6 could be ascribed to the reactions in the Sn99Cu1/Cu solder joint during aging, including the oxidation of Cu and Sn and the solid-state reactions between Sn and Cu. However, the oxidation of Cu and Sn was limited due to the low oxygen pressure in the vacuum oven, so its effect on experimental results was negligible, which will be discussed in details in section 5.2.4. Furthermore, the parabolic relation between the height reduction of solder joint and aging duration indicates that the collapse of solder joint is very likely to be related with solid-state diffusion and reactions between Sn and Cu in aging. Hence, it is reasonable to assume that the measured collapse of the solder interconnects was primarily caused by the growth of IMCs at the interface.

The growth of individual IMC layers (i.e. Cu_6Sn_5 , Cu_3Sn), and the entire IMC layer ($\text{Cu}_6\text{Sn}_5 + \text{Cu}_3\text{Sn}$) after aging at 175°C were characterised in chapter 3. Based on the experimental data, the growth of each IMC layer with aging time can be expressed as $h_{\text{IMC Total}} = 0.27 \times \sqrt{t} + 4.6$, $h_{\text{Cu}_6\text{Sn}_5} = 0.16 \times \sqrt{t} + 4.1$ and $h_{\text{Cu}_3\text{Sn}} = 0.17 \times \sqrt{t}$ respectively. The constants 4.6 and 4.1 in the formulas are the thickness of the interfacial IMC layers before aging. The variation between these two is possibly caused by the deviation in curve fitting. In order to evaluate the degree of dimensional change in the connection with the growth of IMC layers, the ratio between the reduction of joint height ($\Delta h_{\text{experiment}}$) and the growth of IMC layer ($h_{\text{IMC Total}}$) is used to define the coefficient of dimensional change ($\alpha = \Delta h / h_{\text{IMC Total}}$). As Δh could be positive or negative which depends on the increase or decrease of joint height after aging, α should also range from -1 to 1. For the investigated specimens in this work, this coefficient can be derived experimentally as:

$$\alpha_{\text{experiment}} = \Delta h_{\text{experiment}} / h_{\text{IMC Total}} = -0.114 \quad (5.2)$$

The negative value of α in this work means the collapse of the joint height due to the growth of IMC layers at the interface of Sn99Cu1/Cu interconnects.

5.2.3 Comparison with numerical analysis

As can be seen, the collapse of solder joint due to aging was resulted from the growth of IMCs. Though equation (5.1) presents a mathematical correlation between the measured reduction of joint height and the aging durations with the given experimental conditions, the fundamental reasoning of the parabolic relation in the equation remains unclear. This section will address the mechanism by numerical analysis.

If the volume shrinkage coefficient is defined as $\beta = \Delta V/V$, where V is the growth of volume of interfacial IMC layers during aging and ΔV is the volume shrinkage induced by it. The following relationship can be derived [220]

$$\beta = 3\alpha \quad (5.3)$$

It is worth of mentioning that equation (5.3) is obtained based on the assumption that the products, Cu_6Sn_5 and Cu_3Sn are isotropic during the volume shrinkage and free of pores or defects. The dimensional change coefficient α can thus be derived from the theoretical volume change. And it yields $\Delta h_{theory} = h_{IMC Total} \times \alpha_{theory} = \frac{1}{3}\beta \times h_{IMC Total}$, which can subsequently be compared with the experimental results.

The ideal volume change can be calculated by the change of densities due to the conversion from reagents (e.g. Sn, Cu) to products (e.g. Cu_6Sn_5 , Cu_3Sn) [104]. For the Sn99Cu1/Cu solder joints in this work, the three solid-state reactions that contribute to the volume shrinkage during aging are: $6Cu+5Sn \rightarrow Cu_6Sn_5$, $Cu+3Sn \rightarrow Cu_3Sn$, $9Cu+Cu_6Sn_5 \rightarrow 5Cu_3Sn$ [221]. Due to the thick Cu_6Sn_5 layer, the supply of Sn atoms at the Cu_6Sn_5/Cu_3Sn interface is minimal, so the possible effect of the reaction $Sn+Cu_3Sn \rightarrow Cu_6Sn_5$ is neglected in the discussion. Base on the values of densities listed in Table 5.2 [16, 75-77], the theoretical volume shrinkage induced by the growth of interfacial Cu_6Sn_5 and Cu_3Sn layers can be estimated with the method introduced in reference [104]. For the growth of interfacial Cu_6Sn_5 layer, the volume shrinkage induced by the reaction, $6Cu+5Sn \rightarrow Cu_6Sn_5$, can be estimated by:

$$\Delta V_{Cu_6Sn_5} = V_{Cu_6Sn_5} - (V_{Cu} + V_{Sn}) = -0.0542V_{Cu_6Sn_5} \quad (5.4)$$

The growth of interfacial Cu_3Sn layer involves two reactions, $Cu+3Sn \rightarrow Cu_3Sn$ and $9Cu+Cu_6Sn_5 \rightarrow 5Cu_3Sn$. In the beginning of the aging, the first reaction dominated the growth of interfacial Cu_3Sn layer when the supply of Sn atoms was sufficient. As the aging prolonged, the thickness of interfacial Cu_6Sn_5 layer grew continuously with time, which reduced the supply of Sn atom in the interfacial Cu_3Sn layer due to the increasing diffusion distance. Hence, the decomposition of Cu_6Sn_5 gradually contributed more to the growth of interfacial Cu_3Sn layer as the aging prolonged [104]. Since the volume shrinkage induced by these two types of reactions is different, a percentage x is introduced to denote the contribution fraction of the reaction, $9Cu+Cu_6Sn_5 \rightarrow 5Cu_3Sn$, to the growth of Cu_3Sn layer. Therefore, the volume shrinkage induced by the growth of interfacial Cu_3Sn layer can be evaluated by:

$$\begin{aligned}\Delta V_{Cu_3Sn} &= (1 - x) \times (V_{Cu_3Sn} - (V_{Cu} + V_{Sn})) + x \times (V_{Cu_3Sn} - (V_{Cu} + V_{Cu_6Sn_5})) \\ &= (-0.3784 + 0.0468x)V_{Cu_3Sn}\end{aligned}\quad (5.5)$$

Consequently, the overall volume shrinkage induced by the growth of interfacial Cu_6Sn_5 and Cu_3Sn layers can be estimated by:

$$\Delta V_{total} = -0.0542V_{Cu_6Sn_5} - V_{Cu_3Sn}(0.3784 - 0.0468x) \quad (5.6)$$

where ΔV_{total} is the total theoretical volume change; $V_{Cu_6Sn_5}$ and V_{Cu_3Sn} are the produced volume of Cu_6Sn_5 and Cu_3Sn during solid-state reactions; x is the contribution fraction of $9Cu + Cu_6Sn_5 \rightarrow 5Cu_3Sn$ to the total volume of Cu_3Sn in aging process.

Table 5.2 Densities and relative atomic masses of reagents (Sn, Cu) and products (Cu_6Sn_5 , Cu_3Sn) in the reactions in the aging of Sn99Cu1/Cu solder joints [16, 75-77].

Materials	Sn	Cu_6Sn_5	Cu_3Sn	Cu
Density (g.cm ⁻³)	7.29	8.28	11.33	8.93
Relative atomic mass	118.7	974.5	309.2	63.5

From equation (5.6), the volume change coefficients of Cu_6Sn_5 and Cu_3Sn can be obtained, and the values are $\beta_{Cu_6Sn_5} = -0.0542$ and $\beta_{Cu_3Sn} = -(0.3784 - 0.0468x)$, respectively. Hence, the theoretical dimensional change coefficients can be derived from equation (5.3) for Cu_6Sn_5 and Cu_3Sn as $\alpha_{Cu_6Sn_5} = -0.018$ and $\alpha_{Cu_3Sn} = -(0.126 - 0.016x)$, respectively. As mentioned earlier, the volume shrinkage due to the growth of interfacial IMC layers was confined between the Sn99Cu1 solder and Cu substrate during aging. Therefore, it is reasonable to assume that the contraction of IMC layers was restricted, which ultimately caused a resultant transverse tension stress, thereby the further reduction of the solder joint height may be induced because of the Poisson's effect. In such case, the theoretical dimensional change coefficients can thus be deduced as:

$$\begin{aligned}\alpha_{Cu_6Sn_5} &= -0.018 \times (1 + 2\nu_1) = -0.03 \quad \text{and} \\ \alpha_{Cu_3Sn} &= -(0.126 - 0.016x) \times (1 + 2\nu_2) = -0.2 + 0.026x\end{aligned}\quad (5.7)$$

where ν_1 and ν_2 are Poisson's ratios of Cu_6Sn_5 and Cu_3Sn , respectively, and their values can be found in reference [16]. Equation (5.7) is derived based on the assumption that Cu_6Sn_5 and Cu_3Sn are isotropic during volumetric shrinking. In addition, the significant difference in the dimensional change coefficients between Cu_6Sn_5 and Cu_3Sn in Equation (5.7) could contribute considerably to the reported phenomenon that the voids predominantly formed in the Cu_3Sn layer rather than Cu_6Sn_5 layer after aging [44, 222-225].

Therefore, the theoretical estimation of the reduction of joint height induced by the growth of interfacial Cu_6Sn_5 and Cu_3Sn layers can then be expressed as

$$\Delta h_{theory} = \alpha_{Cu_6Sn_5} \times h_{Cu_6Sn_5} + \alpha_{Cu_3Sn} \times h_{Cu_3Sn} = -0.03h_{Cu_6Sn_5} - (0.2 - 0.026x)h_{Cu_3Sn} \quad (5.8)$$

During the aging, the growth of interfacial Cu_6Sn_5 and Cu_3Sn layers in aging process follows the linear relation with \sqrt{t} and they can be expressed as $h_{Cu_6Sn_5} = 0.155 \times \sqrt{t}$ and $h_{Cu_3Sn} = 0.174 \times \sqrt{t}$, respectively, where t is the aging durations in hour, h is the thickness of IMC layer in μm . By the substitution of $h_{Cu_6Sn_5}$ and h_{Cu_3Sn} in equation (5.8) with the measured growth of IMC layer, the theoretical dimensional change that should be induced by the measured growth of interfacial IMC

layers can be estimated as

$$\Delta h_{theory} = -(0.04 - 0.004x) \sqrt{t} \quad (5.9)$$

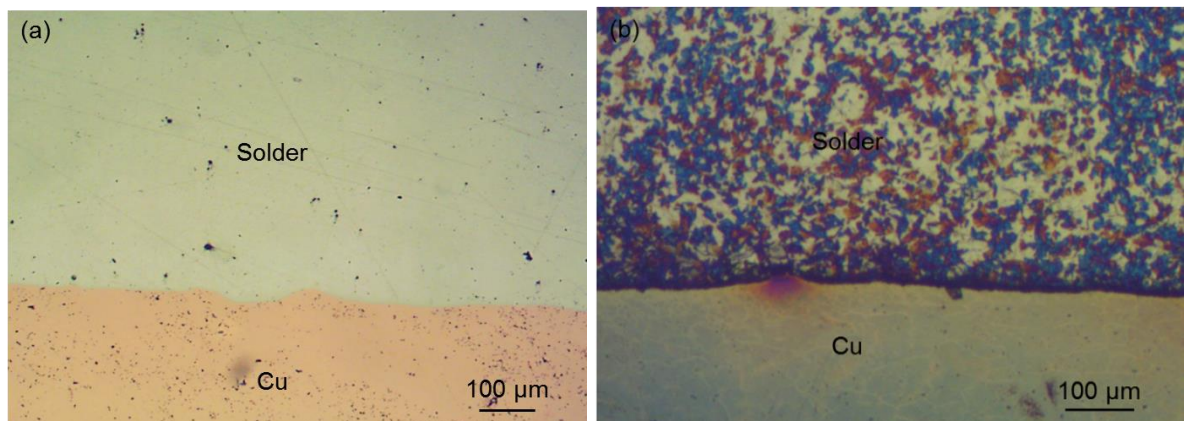
Equation (5.9) shows a parabolic relation between the expected reduction of joint height and aging durations, which is the theory base to the observed parabolic correlation in Fig. 5.6. Hence, in comparison to the experimental dimensional coefficient in equation (5.2), the theoretical dimensional change coefficient can be derived:

$$\alpha_{theory} = \Delta h/h_{IMC} = -(0.04 - 0.004x) \sqrt{t} / (0.272 \times \sqrt{t}) = -0.147 + 0.0147x \quad (5.10)$$

It can thus be concluded that the theoretical estimation of dimensional change coefficient in equation (5.10) has a very close approximation to the dimensional change coefficient obtained through experimental measurements within the acceptable measuring accuracy. The relatively smaller experimental value may be attributed to the volume shrinkage that can be partially compensated by the formation of voids within IMC layer during aging process [89], which was not considered as a factor in the theoretical calculations. The voids generated due to volume shrinkage as well as Kirkendall voids due to interdiffusion [226, 227] are inevitable, which can further block the diffusion path between the solder and Cu to hinder the growth of IMC layer and cause relative less collapse of solder joint.

5.2.4 Effect of oxidation

As discussed in section 5.2.1, the oxidation of Cu could pose some effects on the reliability of the measurement of the collapse of solder joints after aging and the thickness of the Cu oxide film can be estimated based on its colour. Fig. 5.7 shows the colour of the specimen after aging at 175°C for 0, 168 and 1132.5 hours. It is illustrated that the colour of the bulk Cu evolved from the initial yellow to violet blue (Fig. 5.7 b)) and finally red after aging for 1132.5 hours (Fig. 5.7 c)). The thickness of Cu oxide film after aging for 1132.5 hours can be estimated to be about 100~200 nm according to Table 5.1.



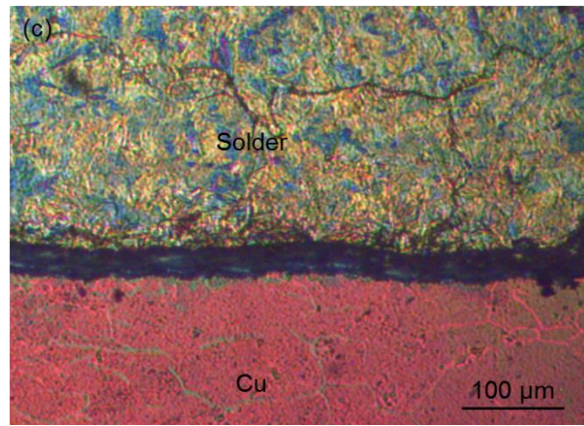


Fig. 5.7 The colour of the Cu part in the Sn99Cu1/Cu solder joints after aging at 175°C for (a) 0 hour, (b) 168 hours and (c) 1132.5 hours.

The observation of specimens with optical microscope confirmed that the oxidation of specimens cannot be entirely eliminated. Therefore, the measurements of solder collapse should take this into account. However, the rough estimation of the thickness of Cu oxide through its colour cannot be used for the evaluation of the effect of oxidation on the accuracy of the measurement due to following reasons: (i) the potential chromatic aberration in the images of the specimens from microscope; (ii) the deviation of subjective interpretation of the colour of the Cu oxide film; (iii) the potential wide range of the oxide thickness for the corresponding single type of colour.

Hence, both the thickness of Cu oxide and Sn oxide films were further investigated by sectioning the Sn99Cu1 solder joint across the solder/Cu interface after aging for 1132.5 hours by FIB. The obtained cross sectional view in Fig. 5.8 shows an enlarged image of the oxide films on Cu and solder. Both Cu_2O and SnO films formed after aging in the vacuum oven and the thickness can be estimated within a range of 0.05-0.40 μm . Based on the densities of materials involved in the conversion from the reagents (Cu and Sn) to the products (Cu_2O and SnO) in Table 5.3 and the calculation in section 5.2.3, the dimensional change coefficient due to the expansion in volume resulted from the oxidations can be estimated to be $\alpha_{SnO} = 0.053$ and $\alpha_{Cu_2O} = 0.134$.

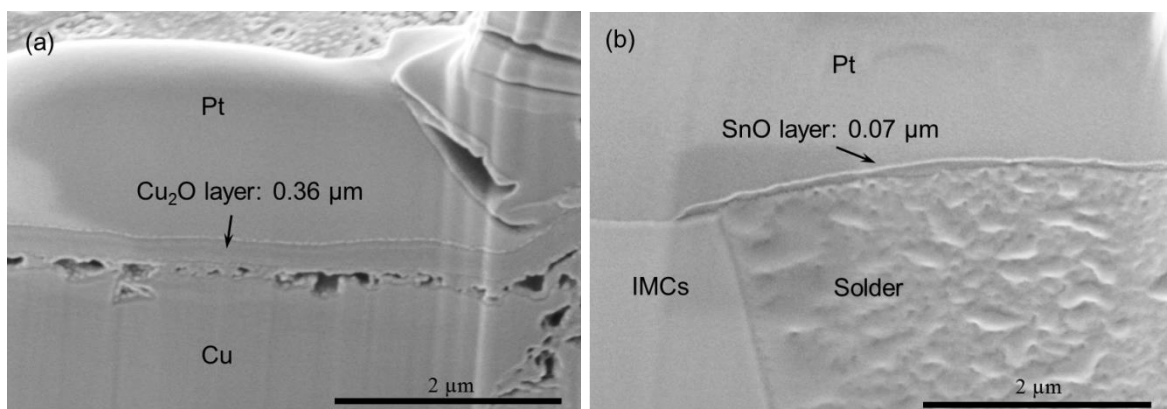


Fig. 5.8 Evaluation of the oxide layer on Cu and Sn after aging at 175°C for 1132.5 hours: (a) copper oxide layer ($\sim 0.36 \mu m$); (b) tin oxide layer ($\sim 0.07 \mu m$). The Pt on the top was deposited to protect the sample beneath it during milling.

Therefore, the increase in the height due to the volume expansion induced by the oxidation of Cu and Sn can be estimated by

$$\Delta h_{Cu_2O} = h_{Cu_2O} \times \alpha_{Cu_2O} = 0.134 \times 0.36 = 0.05 \mu m$$

$$\Delta h_{SnO} = h_{SnO} \times \alpha_{SnO} = 0.053 \times 0.07 = 0.004 \mu m$$

Hence, the variation of approximately 0.05 μm in the measurements of the change of joint height can be estimated as the result of Sn or Cu oxidations, which is minimal comparing with the overall height change induced by the growth of interfacial IMC layers.

Table 5.3 Densities and relative atomic masses of the reagents (Sn and Cu) and the products (Cu_2O and SnO) in the oxidation of Sn99Cu1/Cu solder joints.

Materials	SnO	Cu_2O	Sn	Cu
Density (g.cm-3)	6.95	6	7.29	8.93
Relative atomic mass	134.7	143	118.7	63.5

Furthermore, it was also concerned with the accuracy of Zygo measurement in terms of the errors that may be involved due to the colouring effect of the measured surfaces. It was reported that the error induced by diverse optical properties of specimen in white light interferometer was likely to be 0.05 μm or less [228]. These measurement errors can only cause small variations of the total measured values.

5.3 The effect of collapse of solder joints

After the measurement of the collapse of Sn99Cu1/Cu solder joint induced by the growth of interfacial IMC layers, its effect on the entire solder joint was also preliminarily investigated. It was reported that the solid-state reactions between Sn and Cu can lead to internal strain within thin Sn and Cu films due to the volume shrinkage after aging [229]. The work by J.Y. Song *et al.* also confirmed that the solid-state reactions between Sn and Cu can lead to stress evolution in the produced IMC layers (i.e. Cu_6Sn_5 and Cu_3Sn) in Cu-Sn thin films [104].

Therefore, the potential build-up of residual stress due to the collapse of solder joint was investigated by finite element modelling in this work, and its effect on the microstructure of Cu part in the Sn99Cu1/Cu solder joint was studied experimentally.

5.3.1 Modelling and experimental approaches

In order to evaluate the internal stress in a solder joint induced by the collapse of solder due to the growth of interfacial IMC layers in aging, finite element models (FEM) were built with Abaqus. The models were incorporated with the obtained dimensional change coefficients of Cu_6Sn_5 and Cu_3Sn layer in section 5.2 to induce the volume shrinkage in the modelling. The geometry of the models were based on a flip chip bump in reference [56] with 10 μm thick interfacial Cu_6Sn_5 layer and 7 μm thick Cu_3Sn layer (Fig. 5.9) based on the experimental results in chapter 3. Major mechanical properties and settings in the model are listed in Table 5.4. The interfacial Cu_3Sn and

Cu_6Sn_5 layers were simulated as brittle material based on references [3, 100, 230] and the experimental results in chapter 4. So it was assumed that no plastic deformation was involved in the interfacial IMC layers during the collapse of solder joint in aging. In order to include the plastic deformation of the solder matrix in the modelling, Table 5.4 was primarily based on reference [16], in which the mechanical properties of Cu_6Sn_5 and Cu_3Sn were slightly different from the values in Table 4.2 in section 4.2.3. But, most of the listed mechanical properties in these two tables are close to each other.

Because there is no particular module designed for the volume change induced by phase transformation in Abaqus, it was suggested that the change in volume could be simulated with the thermal expansion module [231, 232]. Therefore, the thermal expansion coefficients of Cu_6Sn_5 and Cu_3Sn were set as the corresponding dimensional change coefficients in this modelling. And an 1°C increase in the temperature was introduced in the model to enable the volume shrinkage of the interfacial IMC layers during aging.

Table 5.4 Major parameters and settings of the involved materials in a solder joint in modelling [16].

Materials	Solder	Cu_6Sn_5	Cu_3Sn	Cu
Young's Modulus (GPa)	52.73	114.7[9]	108.3	133.3
Poisson's Ratio	0.36	0.309	0.299	0.330
Plastic Stress-Strain Curve	[233]	-	-	[234]
Dimensional change coefficient	-	-0.018	-0.126	-

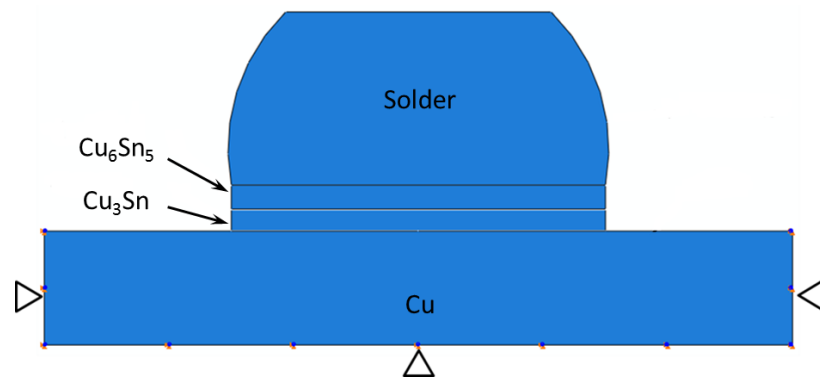


Fig. 5.9 The geometry and the boundary conditions of the finite element model. The three edges with triangles were fixed in both X and Y directions.

The potential effect of the residual stress induced by the solid-state reactions on the solder joint was experimentally investigated by examining the microstructural changes in the solder joint. During the characterisation of the reduction of joint height, the polished surfaces of the Sn99Cu1/Cu solder joints were preserved from any contact or damage. Hence, the microstructural change of the solder joint should also be examined by non-contact and non-destructive methods. One of the viable ways is to identify the grain boundaries of the Cu substrate by the different colours at the grains and grain boundaries due to the variation in the thickness of oxide films.

When the Sn99Cu1/Cu solder joints were stored in the vacuum oven at 175°C, the pressure within the oven was kept at about 3 KPa. The residual oxygen in the oven could react with both the solder and Cu in the specimen during aging. For the solder part, the SnO film was self-protective which can prevent further oxidation, so the Sn oxide film was normally thin and uniform [217]. However, for the oxidation of Cu substrate, the Cu atoms at the grain boundaries reacted with the oxygen more easily in aging due to lower activation energy in comparison with the reaction within the Cu grains [235]. The difference in oxidation rates further resulted in the variation in the thickness of Cu oxide film at the grains and grain boundaries after aging, which can further lead to the observable difference in colour at these two locations [219]. Therefore, it is feasible to identify the Cu grains by its colour after aging. The change in Cu grains could further indicate the microstructural evolution in the Cu side close to the solder/Cu interface due to the build-up of residual stress within the interfacial IMC layers.

Therefore, after the measurement of collapse of solder joints in section 5.2, the Sn99Cu1/Cu solder joints were further examined with optical microscope to investigate the microstructural evolution. Another bare Cu specimen was machined into the geometry as schematically shown in Fig. 5.10 for the comparison with the Cu part in Sn99Cu1/Cu solder joints. The Cu specimen was polished and then stored in the vacuum oven at 175°C for one week to undergo the same procedures as the Sn99Cu1/Cu solder joints did. After aging, optical microscope was utilised to observe the microstructural changes in the Cu specimen for comparison with the observation on the Sn99Cu1/Cu solder joints after aging for the same period.

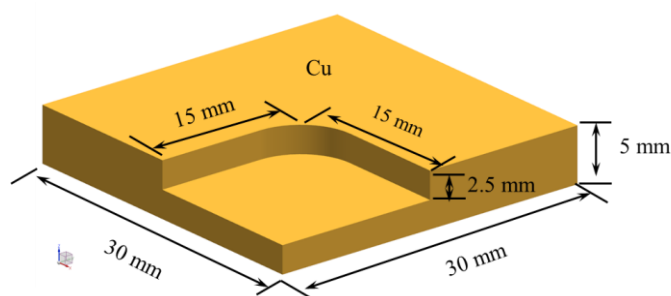


Fig. 5.10 The schematic and dimensions of the Cu specimen for the comparison with Sn99Cu1/Cu solder joints.

5.3.2 Internal stress induced by the collapse of solder joint

The residual stress which could be potentially resulted from the collapse of solder joints was investigated by modelling. Fig. 5.11 a) illustrates the distribution of von Mises stress in the solder joint induced by the volume shrinkage due to the growth of interfacial Cu_6Sn_5 and Cu_3Sn layers during aging. It shows that the resultant stress concentrates within the interfacial Cu_6Sn_5 and Cu_3Sn layers while the stress in solder and Cu is significantly lower. Fig. 5.11 b) illustrates the stress distribution from the top of solder to the bottom of Cu substrate in the solder joint. It can be found that the stress increased sharply from lower than 500 MPa in solder and Cu parts to higher than 6 GPa in both Cu_6Sn_5 and Cu_3Sn layers.

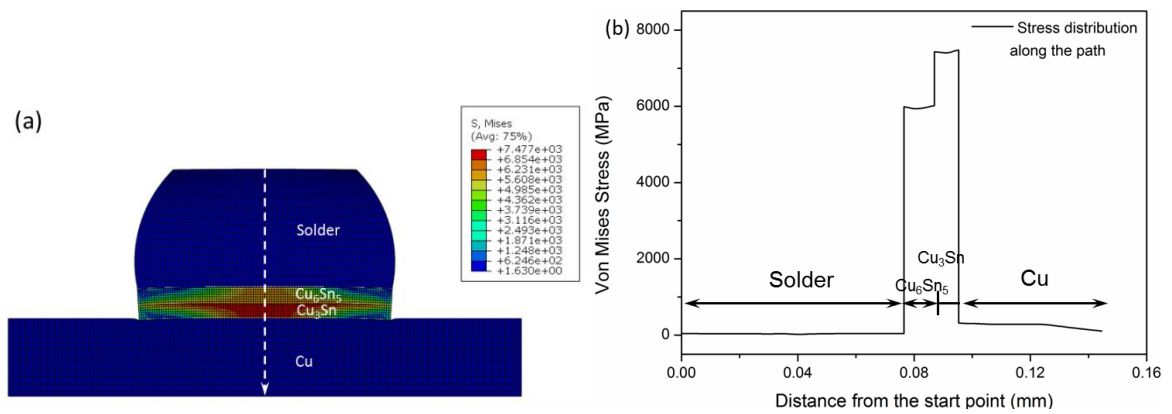


Fig. 5.11 Redistribution of stress within solder joint due to the collapse of solder joint: (a) The overall distribution of internal stress due to the growth of interfacial IMC layers; (b) The distribution of von Mises stress along the dash path in (a).

In order to illustrate the stress distribution within solder and Cu parts more clearly, the stress within these two regions are shown individually in Fig. 5.12 a) and c). Fig. 5.12 a) illustrates that the solder part is generally under relatively higher stress with some exceptions at the corner and centre of the solder. The stress distribution along the centre line of the solder is illustrated in Fig. 5.12 b). It can be estimated that the stress in the solder is about 40 MPa with a slight decrease to approximately 20 MPa at the centre of the solder. The distribution of resultant stress in Cu is shown in Fig. 5.12 c) and d). It is shown that the stress generally concentrates along the Cu_3Sn/Cu interface. From the Cu/IMC interface to the bottom of Cu, the stress decreases continuously, from over 300 MPa to about 100 MPa as shown in Fig. 5.12 d).

However, based on the results in references [104] and [229], the stresses within different parts in a solder joint were approximately within 60~120 MPa in solder, 40~120 MPa in Cu and 0.8~1.54 GPa in the interfacial Cu_3Sn layer. It can be found that the stresses estimated by modelling in this work are much higher. The overestimation of the stress resulted from the growth of interfacial IMC layers can be attributed to the limited capability of the thermal expansion module in Abaqus. The module is only capable to simulate the mechanical deformation of models. However, microstructural evolution that can release the stress, such as the formation of voids and recrystallization of grains [89, 236], was excluded from the modelling. Furthermore, the voids generated by volume shrinkage and Kirkendall voids due to interdiffusion [226, 227] in the interfacial IMC layers are inevitable and can also significantly release the generated internal stress within the interfacial IMC layers. But, the formation of voids in aging cannot be accounted in this finite element model. Therefore, the internal stress induce by the volume shrinkage at the solder/Cu interface due to the growth of interfacial IMC layers was overestimated in the modelling.

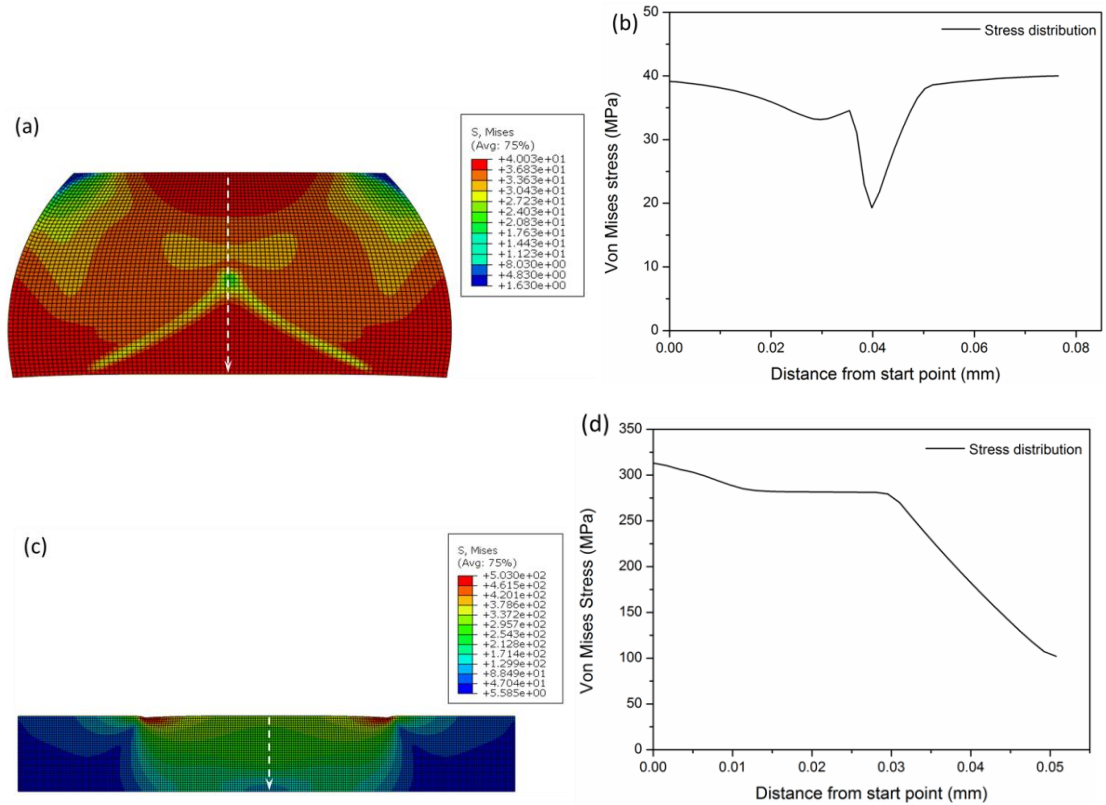


Fig. 5.12 Stress distribution in (a) solder and (c) Cu substrate; (b) and (d) illustrates the stress distribution along path in solder and Cu, respectively. The dash lines in (a) and (c) represent the path for the stress distribution in (b) and (d).

5.3.3 Grain redistribution in Cu substrate

Fig. 5.13 shows an example of the Cu part in Sn99Cu1/Cu solder joint specimen and the bulk Cu specimen after aging at 175°C for one week. The relatively lighter lines in Cu matrix close to the solder/Cu interface (Fig. 5.13 a)) and darker lines in Cu specimen (Fig. 5.13 b)) are the grain boundaries revealed by the oxidation during aging. It is shown in Fig. 5.13 a) that the grains within the region between the two dash lines close to the solder/Cu interface are much smaller than those farther from the interface. However, there is no notable variation in grain size in the Cu specimen in Fig. 5.13 b). Moreover, the size of grains in the Cu specimen in Fig. 5.13 b) is similar to the Cu grains farther from the interface in Sn99Cu1/Cu solder joint in Fig. 5.13 a).

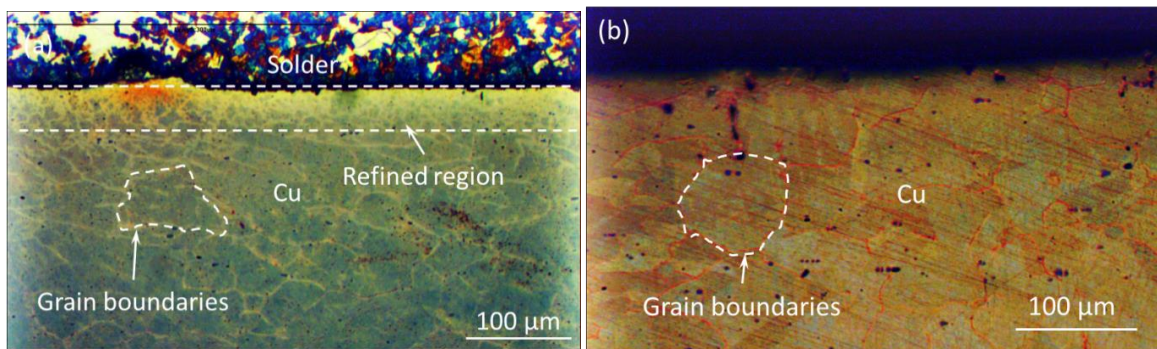


Fig. 5.13 Grain boundaries in Cu revealed by oxidation: (a) the grains in the Cu part of Sn99Cu1/Cu solder joints and (b) the grains in the machined Cu specimen after aging at 175 °C for one week.

The refinement of grains is normally because of serious plastic deformation or build-up of residual stress. Therefore, there are two possible factors that may contribute to the refinement of grains in Fig. 5.13 a), the stress due to the collapse of solder joint and the stress induced by the machining the pocket in Cu part during sample preparation. However, the uniform size of grains in the bare Cu specimen in Fig. 5.13 b) implies that the machining didn't result in any notable change in grain size in Cu. Furthermore, if the refined grains at the solder/Cu interface were because of the mechanical machining, the Cu grains should be distorted along the machining direction due to the plastic flow of material [237, 238]. However, no specific direction can be identified from the grain refinement region in Fig. 5.13 a), which indicates that the refinement of Cu grains close to the solder/Cu interface was possibly not resulted from the residual stress induced by machining during sample preparation.

Consequently, the refinement of grains in the Cu part in the solder joint can be attributed to the internal stress resulted from the collapse of solder joint due to the growth of interfacial IMC layers in aging. Because of the constraint from the adjacent Cu and solder, the volume shrinkage could introduce significant stress at the solder/Cu interface, which further led to the microstructural evolution in the Cu part close to the interface.

Fig. 5.14 shows the comparison of Cu grains in the Cu part close to the Sn99Cu1 solder/Cu interface after aging for 168 hours and 672 hours. It can be observed that the colour of the Cu grains changed from violet blue to blue and the colour of grain boundaries evolved from yellow to red after the extended aging. For the solder joint after aging for 168 hours, the Cu grains were measured to be approximately 16 μm wide at about 30 μm away to the interface and about 6 μm at 10 μm to the interface. For the solder joint after aging for 672 hours, the sizes of grains at these two locations were estimated to be 18 μm and 10 μm , respectively.

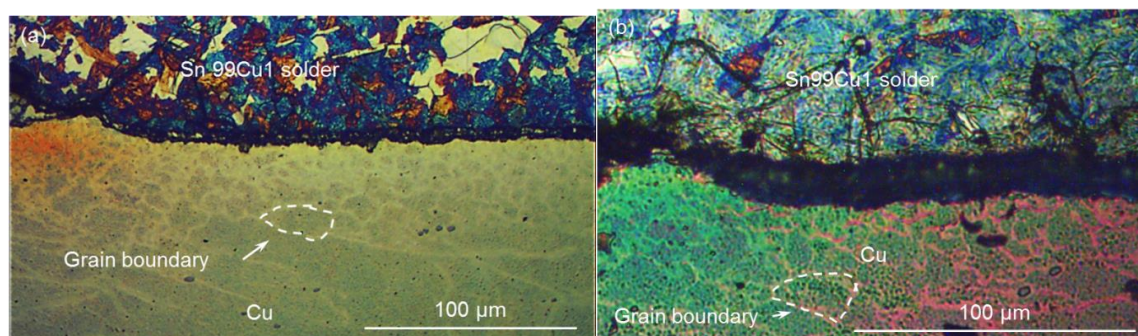


Fig. 5.14 The comparison of the size of Cu grains close to the solder/Cu interface after aging at 175°C for (a) 168 hours and (b) 672 hours.

It is notable that the Cu grains were larger after aging for 672 hours than those in the specimens after aging for 168 hours at the corresponding distance to the solder/Cu interface. The increase of the grain size with aging could be attributed to two possible factors, the coarsening of the Cu grains in aging and the possible movement of the solder/Cu interface. During the aging, the grains can grow continuously with the prolonged durations [239], which could lead to the observed increase of grain dimensions in Fig. 5.14. Furthermore, the growth of interfacial IMC layers, particularly the growth of Cu_3Sn layer, relies on the consumption of Cu atoms from the Cu substrate,

which may result in the movement of solder/Cu interface towards the Cu side. Therefore, the Cu grains were observed to be expanding from the comparison between the grains in Sn99Cu1/Cu solder joints after aging for 168 hours and the grains after aging for 672 hours in Fig. 5.14.

5.4 Summary

In summary, the collapse of Sn99Cu1 /Cu solder joint due to the growth of interfacial IMC layers during aging was measured with a white light interferometer. The cross section of the solder joint was prepared and observed with FIB. It was verified that the growth of IMC layers was essentially the cause that can lead to volume shrinkage and detectable collapse of the height of solder joints. Modelling and observation with optical microscope were then employed to preliminarily investigate the effect of collapse of solder on the entire solder joints. The main findings gained from this study can be summarised as:

1. The collapse of solder joint height induced by the growth of IMC layers in solid-state reactions reached 1.2 μm after aging at 175°C for 1132 hours. Its correlation as function of aging duration can be expressed as $\Delta h = -0.031 \times \sqrt{t}$ under the given experimental conditions. The dimensional change coefficient based on experimental measurements is $\alpha_{\text{experiment}} = -0.114$.
2. Observations of the cross sections of Sn99Cu1/Cu solder joint confirmed that the solder joint collapsed because of the growth of IMCs through the solid-state reactions during aging.
3. Based on the hypothesis that Cu_6Sn_5 and Cu_3Sn are isotropic and dense, the theoretical estimation of the reduction of joint height induced by the growth of interfacial IMC layers under experimental conditions can be made and expressed as $\Delta h_{\text{total}} = -(0.04-0.004x)\sqrt{t}$. And the theoretical dimensional change coefficient was estimated as $\alpha_{\text{ideal}} = -0.147+0.0147x$, which demonstrated an excellent accordance with the experimental measurements.
4. The modelling results show that the stress induced by the constrained collapse of solder joint mainly concentrates within interfacial IMC layers, which is significantly higher than the stress in solder and Cu.
5. The internal stress induced by the collapse of solder joint due to the growth of interfacial IMC layers in aging can lead to the refinement of grains in Cu near the solder/Cu interface. And the size of Cu grains close to the Sn99Cu1 solder/Cu interface expanded after the extended aging at 175°C.

Chapter 6 Residual stress induced by the growth of interfacial IMC layers

6.1 Introduction

The growth of interfacial IMC layers (i.e. Cu_6Sn_5 and Cu_3Sn) is the transformation from the reagents (i.e. Sn and Cu) to the products (i.e. Cu_6Sn_5 and Cu_3Sn) during solid-state reactions. In chapter 5, it is demonstrated that the transformation is accompanied by volume shrinkage due to the increase in densities. In solder joints, the volume shrinkage is subjected to the constraint from both the Cu substrate and the solder matrix, which can lead to the evolution of residual stress within solder joints without any exterior loads.

The build-up of residual stress could pose significant threat to the mechanical reliability of solder joints and facilitate the growth of Sn whiskers [3, 54, 95, 100, 240]. It was reported that the residual stress within solder joint could evolve with current stressing and thermal cycling [99, 241, 242]. However, the residual stress induced by the growth of interfacial IMC layers in solder joint has seldom been systematically investigated. Given the miniaturized solder joints, S. Suresh *et al.* reported that nanoindentation with a sharp indenter could be utilised to evaluate the internal stress [114]. This method was employed for measuring the residual stress within various materials [111, 112, 115, 116, 243, 244].

Therefore, in this chapter, the evolution of residual stress was investigated by nanoindentation tests on interfacial Cu_6Sn_5 and Cu_3Sn layers, the solder and Cu close to the Sn99Cu1/Cu interface after aging for increasing durations. The residual stress within different parts of the solder joint was then estimated based on the obtained load-displacement curves. The factors that may contribute to the evolution of residual stress in solder joints after aging were also discussed.

6.2 Theoretical attributes and methodology

The hardness of a specimen (H) characterised by nanoindentation test is defined as the average stress within the contact area [245]

$$H=F/A \quad (6.1)$$

where H is the measured hardness; F is the maximum force applied in the nanoindentation test; A is the projected contact area of the indent. The effect of residual stress within the specimen on the nanoindentation tests is illustrated in Fig. 6.1. For a specimen under compression stress, the applied maximum load (F_1) should be higher than the load from a stress-free reference specimen (F_0) at the same indentation depth, because the compression stress within the sample can act as an additive force to resist the penetration of the indenter into the specimen. Contrarily, the maximum load (F_2) from specimens under tension stress to reach the same depth is lower than the force in reference specimen (F_0), due to the lower resistance to the deformation during the indentation. Consequently, for depth-controlled nanoindentation tests on specimens in different stress states, the applied maximum load should follow the relationship $F_1 > F_0 > F_2$, as illustrated in Fig. 6.1 d) [111, 114, 116, 246].

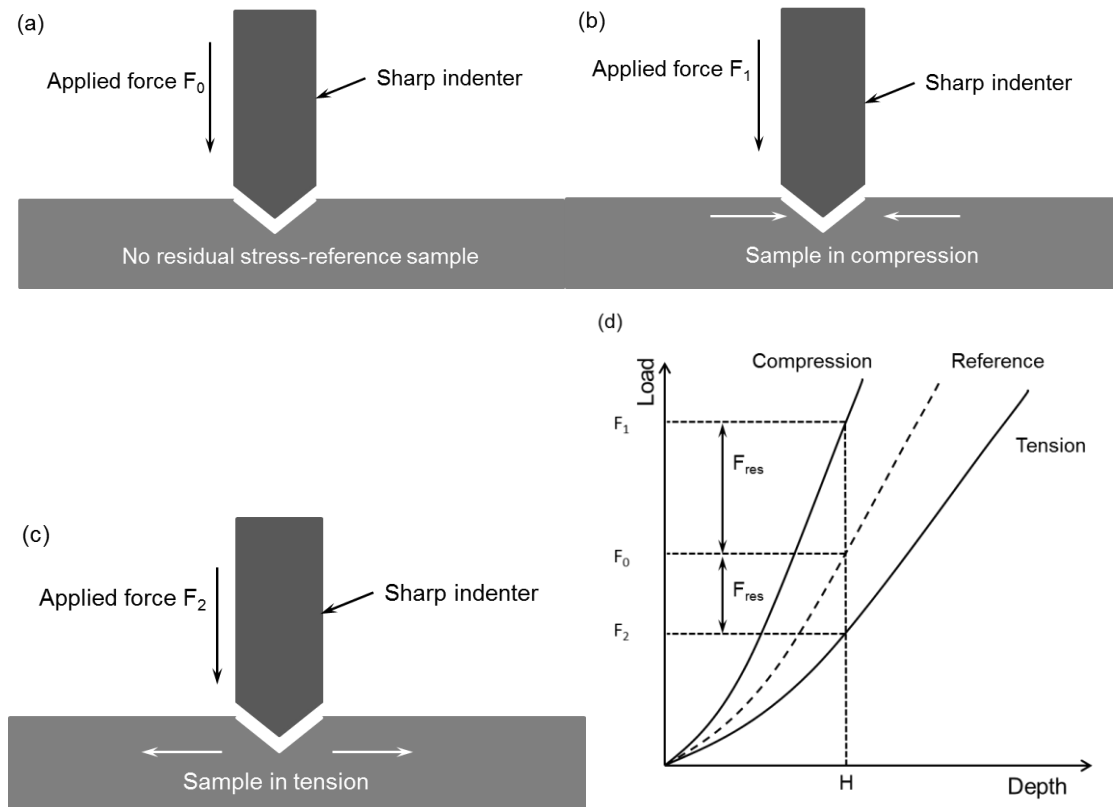


Fig. 6.1 Schematics of the effect of residual stress on nanoindentation tests: (a) the indentation on specimens without any residual stress; (b) and (c) the effect of compression and tension stress on the nanoindentation tests; (d) the comparison of load-depth curves from nanoindentation tests on specimens in different stress states.

Therefore, the variation between the maximum loads from depth-controlled nanoindentation tests on the stressed specimens and stress-free specimens (i.e. F_1 , F_2 and F_0) can be utilised to evaluate the residual stress. The residual stress in a specimen can be estimated by [116]

$$\sigma_{res} = F_{res}/A_c = (F_{max} - F_0)/A_c \quad (6.2)$$

where F_{max} is the maximum load measured in stressed specimens by nanoindentation tests; F_0 is the referential maximum load from the indents at the same depth in stress-free specimen; A_c is the projected contact area between the indenter and the specimen in indentation.

Consequently, obtained positive σ_{res} indicates that the specimen is under compression as an extra load is needed to reach the same depth. Contrarily, a negative σ_{res} means that the specimen is under tension, because the load in the stressed specimen is lower than the force in reference specimen in the depth-controlled nanoindentation.

Both F_{max} and F_0 in equation (6.2) can be directly recorded in the nanoindentation tests on the stressed specimens and stress-free specimens. For the projected contact area of the indents (A_c), it is a standard practice to assume that the area of contact A_c at a specified depth is the cross-sectional area of the diamond indenter at that depth. The value of the cross-sectional area can be fitted as a function of the prescribed depth [247]. For Vickers indenter with the angle of 22° , the nominal contact area between an ideal indenter and the specimen can be estimated by the

following function [244]

$$A_{nominal} = \left(\frac{2h_{max}}{\tan 22^\circ}\right)^2 = 24.5h_{max}^2 \quad (6.3)$$

where h_{max} is the maximum depth in the nanoindentation test.

However, the geometry of an actual indenter could vary with individuals, which makes the depth-area formula equation (6.3) violated in some applications [248]. Hence, the contact area A_c between the indenter and the specimen during indentation test should be adjusted by [116]

$$A_c = C_0h_c^2 + C_1h_c + C_2h_c^{1/2} + C_3h_c^{1/4} + C_4h_c^{1/8} + \dots + C_7h_c^{1/64} + C_8h_c^{1/128} \quad (6.4)$$

where $C_0=24.5$, describing a perfect pyramidal Vickers or Berkovich indenter; the other constants C_1 to C_8 represent the deviations of a real indenter from the indenter with perfect geometry [249]. The values of these constants can be determined by polynomial-fitting procedures; h_c is the contact depth.

The nanoindentation tests were carried out with Nanotest Platform 3 in this work. The correlation between the projected contact area of the used nano Vickers indenter and the plastic depth is illustrated in Fig. 6.2. The constants in equation (6.4), C_1 - C_8 , can then be derived by fitting the curve. And the values of the constants are listed in Table 6.1.

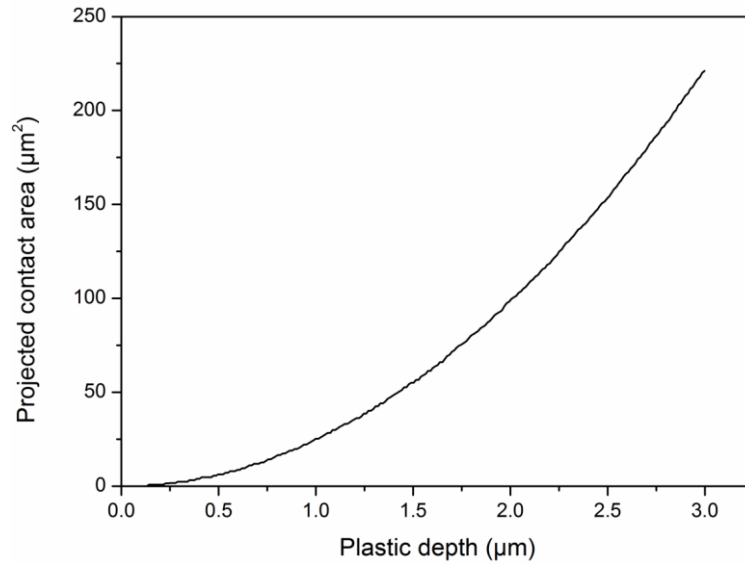


Fig. 6.2 Projected contact area vs plastic depth of the Nanotest platform 3 in this work.

Table 6.1 Values of constants, C_1 - C_8 , in Equation (4) derived by fitting the contact area-plastic depth curve in Fig. 6.2.

C_1	C_2	C_3	C_4	C_5	C_6	C_7	C_8
0.9523	-14.35	186.6	-1210	3612	-3868	-483.6	1776

In order to derive the projected contact area A_c , the contact depth h_c in equation (6.4) should be obtained first. Oliver and Pharr proposed a theory based on the analysis of load-displacement curves from nanoindentation tests [247, 250, 251]

$$h_c = h_{max} - \epsilon \frac{F_{max}}{S} \quad (6.5)$$

where h_{max} is the maximum depth recorded by the instrument during nanoindentation tests; ϵ is a

constant that depends on the geometry of the indenter. The values of ϵ for different types of indenters are listed in Table 6.2 [252]; S is the initial unloading contact stiffness of the material, which can be derived by calculating the slope of the initial portion of the unloading curve, as illustrated in Fig. 6.3.

Table 6.2 Correction factor ϵ for different indenter geometries [252].

Indenter geometry	ϵ
Flat punch	1
Conical	0.73
Paraboloid revolution (including spherical)	0.75
Berkovich, Vickers	0.75

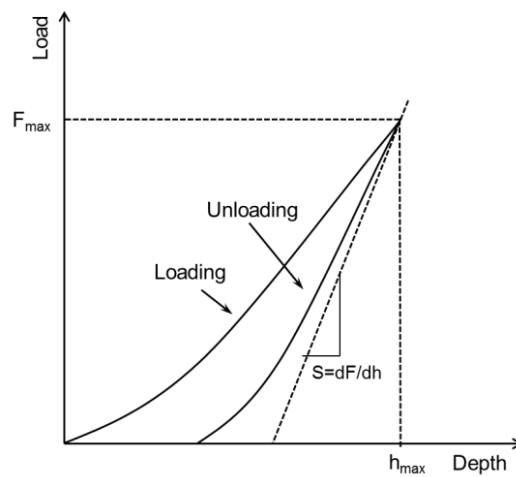


Fig. 6.3 Estimation of the initial unloading stiffness S by deriving the slope of the beginning of the unloading curve after nanoindentation tests.

Consequently, all the parameters in equation (6.2) for the estimation of residual stress can be obtained by nanoindentation tests. The general procedures are summarized in Fig. 6.4.

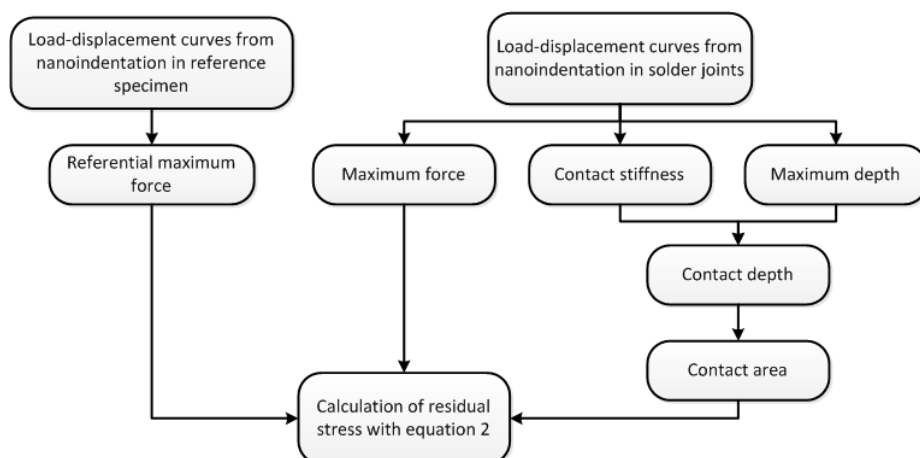


Fig. 6.4 Procedures for the estimation of residual stress within solder joints by nanoindentation tests.

6.3 Experimental details

From the modelling results in section 5.3 in chapter 5, the volume shrinkage due to the growth of interfacial IMC layers could result in significant build-up of residual stress within solder joints. It also shows that the resultant stress concentrates within the interfacial Cu_6Sn_5 and Cu_3Sn layers and the solder and Cu close to the solder/ Cu_6Sn_5 interface and Cu/Cu_3Sn interface. Therefore, the characterisation of residual stress by nanoindentation tests in this work was carried out within the interfacial Cu_6Sn_5 layer, interfacial Cu_3Sn layer, solder matrix next to the solder/ Cu_6Sn_5 interface and the Cu next to the Cu/Cu_3Sn interface. The indentation tests were implemented at both the centre and the edge of the solder joint for comparison. The locations of the planned indentations are illustrated in Fig. 6.5.

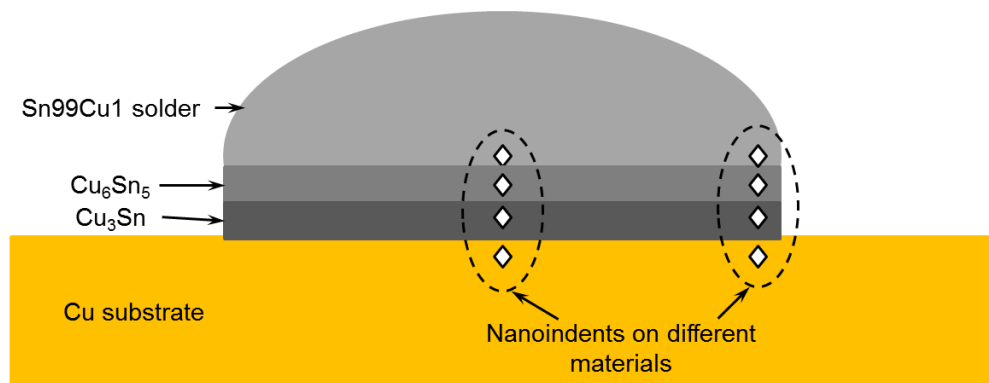


Fig. 6.5 Planned locations of the nanoindentations in the entire solder joint.

Sn99Cu1 solder was reflowed on Cu (purity: 99.9%) to form the joints. The specimens were then stored in an oven at 175 °C for 0 - 500 hours. After aging for every 100 hours, a set of the specimens were ground and polished to expose the cross section of the specimens. The polishing speed was controlled within 100~200 rpm to minimize the possibly resultant stress at the sample surface. In the sample preparation, the specimens were not mounted, so that any potential effects from the contraction of resin on the stress state of the solder joint could be avoided. Another set of bare Cu samples and bulk Sn99Cu1 solder specimens were reflowed, ground and polished with the same settings in each step for the preparation of stress-free specimens to derive the referential maximum force.

The polished solder joint specimens were then tested by nanoindentation with Nanotest platform 3. Nano Vickers indenter was used to implement the indentation tests at the designated locations illustrated in Fig. 6.5. Due to the micro thickness of the interfacial Cu_6Sn_5 and Cu_3Sn layers in Sn99Cu1 solder joints, the depth of the indents within the interfacial IMC layers was set to be 0.3 μm , so that the nano indents could be accommodated within one specific IMC layer without involving the adjacent materials.

The indents in the solder and Cu were located approximately 10 μm from the solder/ Cu_6Sn_5 and Cu_3Sn/Cu interfaces respectively, so that the shortest distance from the nano indents to the interfaces was approximately 5 μm . As such, the pile-up or sink-in of the material could be accommodated during the nanoindentation tests. For each position illustrated in Fig. 6.5, five to seven indents with a horizontal interval of 20 μm were made to derive the average residual stress at

the designated position and minimize the mutual effect between the adjacent indents. The parameters and settings of the nanoindentation tests on different parts in the solder joint are listed in Table 6.3.

Table 6.3 Parameters and settings of the nanoindentation tests.

	Maximum Load	Maximum Depth	Termination	Initial load	Loading rate	Unloading rate	Dwelling time at maxi load
Cu	50 mN	1 μm	Depth control	0.05 mN	1 mN/s	1 mN/s	0 s
Solder	50 mN	1 μm	Depth control	0.05 mN	0.2 mN/s	0.2 mN/s	0 s
Cu_6Sn_5	50 mN	0.3 μm	Depth control	0.05 mN	0.2 mN/s	0.2 mN/s	0 s
Cu_3Sn	50 mN	0.3 μm	Depth control	0.05 mN	0.4 mN/s	0.4 mN/s	0 s

In order to derive the contact depth h_c by equation (6.5) to estimate the residual stress, the values of the maximum force (F_{max}), maximum depth (h_{max}), and the contact stiffness (S) were estimated by analysing the load-displacement curves from nanoindentation tests. The parameters used in the analysis are listed in Table 6.4.

Table 6.4 Parameters and settings used for the analysis of the load-displacement curves from nanoindentation tests.

Fitting method	Fitting region	Frame compliance	Geometric factor (Vickers indenter)
Power law	100%~20%	0.653572 nm/mN	1.012

The contact area-depth curve of the Nanotest platform 3 in Fig. 6.2 covers the range of indent depth from 0 to 3 μm . The depth of the indents in the solder and Cu was 1 μm , about 1/3 of the entire range of the A_c - h_c curve. It is reasonable to assume that the calculated contact area of the indents within the solder and Cu is reliable. However, the depth of the nano indents within interfacial Cu_6Sn_5 and Cu_3Sn layers was 0.3 μm , about 1/10 of the entire range. Therefore, the accuracy of the calculated contact area A_c for the nano indents within the interfacial IMC layers needs to be verified.

Therefore, after the nanoindentation tests, the nano indents in the solder, Cu and interfacial Cu_6Sn_5 and Cu_3Sn layers were profiled with Alicona Infinite Focus with the vertical resolution of 10 nm. The projected contact area of the nano indents can then be measured for the verification of numerically calculated results by equation (6.4). Furthermore, the profile of nano indents can also be used to evaluate the effect of the surface roughness of the sample on the nanoindentation tests.

6.4 Experimental results

6.4.1 Projected contact area of nano indents

Fig. 6.6 illustrates representative surface profiles across the centre of the nano indents in solder, Cu, interfacial Cu_6Sn_5 and Cu_3Sn layers. The locations of the profiles in the indents were guaranteed by the assistance of real-time location indicator while extracting the profiles. Based on the presented curves, the fluctuation of the sample surface after polishing can therefore be estimated to be within 50 nm. In comparison to the depth of the nano indents (300 nm to 1000 nm), the effect of surface roughness on the nano indents was minimal.

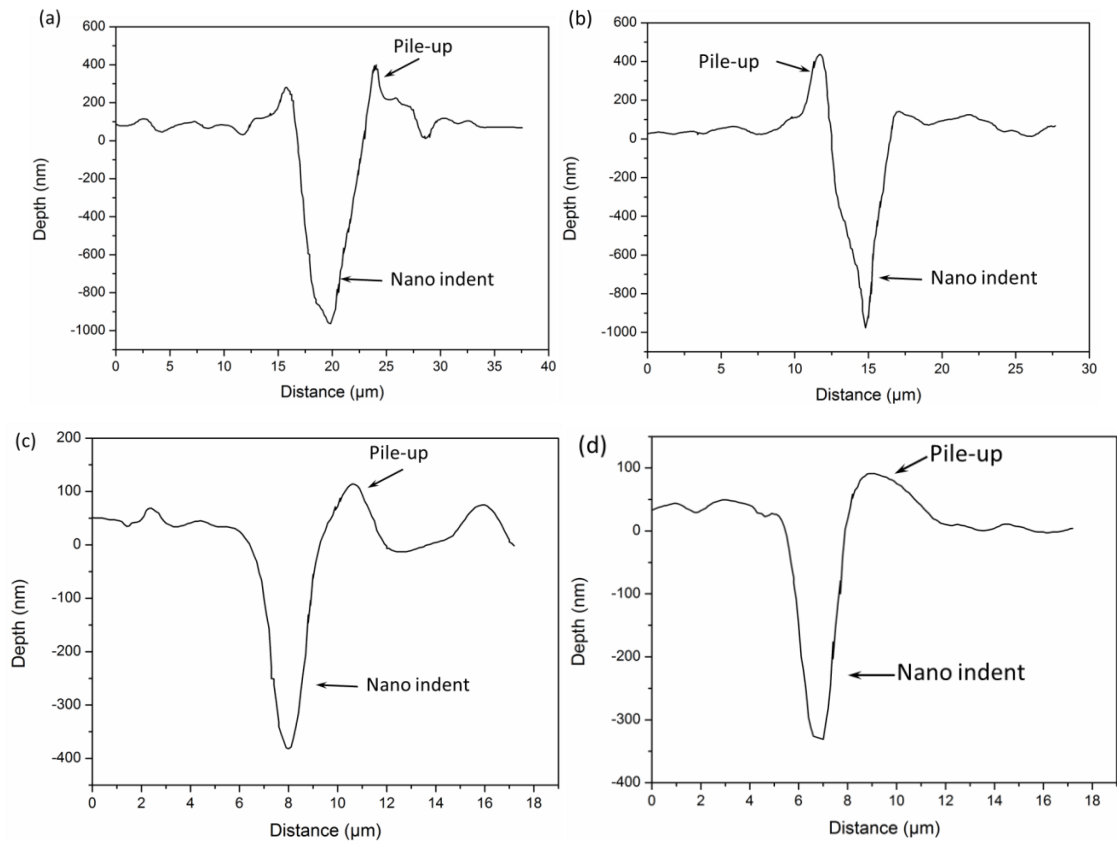


Fig. 6.6 Representative surface profiles of nano indents made within (a) solder, (b) Cu, (c) interfacial Cu_6Sn_5 layer and (d) interfacial Cu_3Sn layer.

During the nanoindentation tests, the maximum force of nano indents in reference samples and solder joints can be directly recorded by the instrument in the indentation tests. Hence, the estimation of residual stress within solder joints primarily relies on the evaluation of projected contact area of nano indents according to the procedures in Fig. 6.4.

As presented in section 6.2, the projected contact area can be estimated by analysing the load-displacement curves from the indentation tests. In order to validate the calculation, the projected areas of the indents made in Sn99Cu1 solder joints were measured with the optical images from Alicona after the nanoindentation tests. Fig. 6.7 illustrates an example of the comparison between the measured areas and the calculated areas of the indents with the depth of 0.3 μm in the interfacial Cu_3Sn layer. It can be observed that the average contact area from the measurement is

about $1.4 \mu\text{m}^2$, which is slightly higher than the corresponding calculated average contact area $1.1 \mu\text{m}^2$. Given the potential angle between the specimen and the optical microscope, it is reasonable to conclude that the contact area of the indents calculated with equation (6.4) is reliable for the evaluation of residual stress by nanoindentation tests.

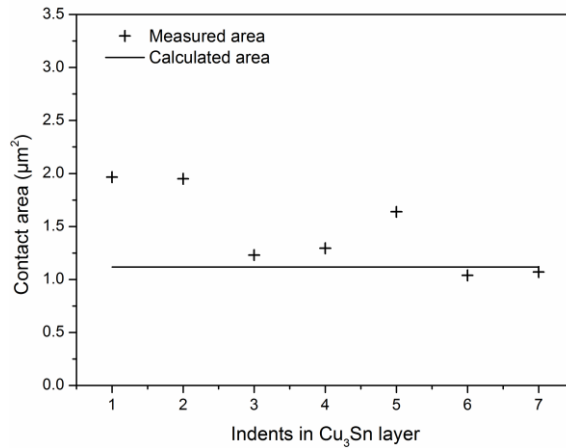
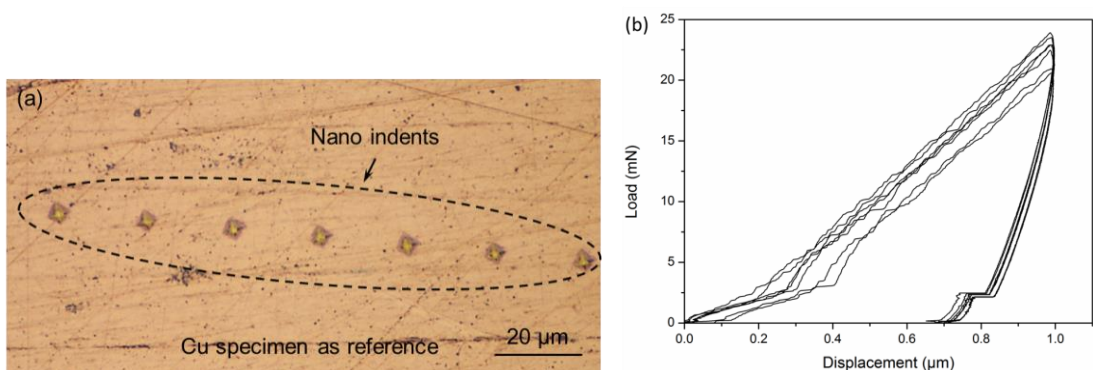


Fig. 6.7 An example of the comparison between the measured contact area and the calculated contact area based on equation (6.4) for the nano indents in the interfacial Cu_3Sn layer.

6.4.2 Residual stress in Cu and Sn99Cu1 solder

The calculation of residual stress in solder joints by equation (6.2) requires the referential maximum force from nano indents in stress-free solder and Cu specimens to reveal the effect of residual stress in solder joints on nanoindentation test results. Fig. 6.8 a) and c) give examples of the nano indents made in reference Cu and solder specimens after the tests. Seven indents were made to derive the average maximum force of each specimen. The corresponding load-displacement curves from the indentation tests are illustrated in Fig. 6.8 b) and d). The referential maximum force for the indents in solder part and Cu substrate can then be evaluated to be 22 ± 1 mN for the indents in Cu and 5.7 ± 0.7 mN for the indents in Sn99Cu1 solder.



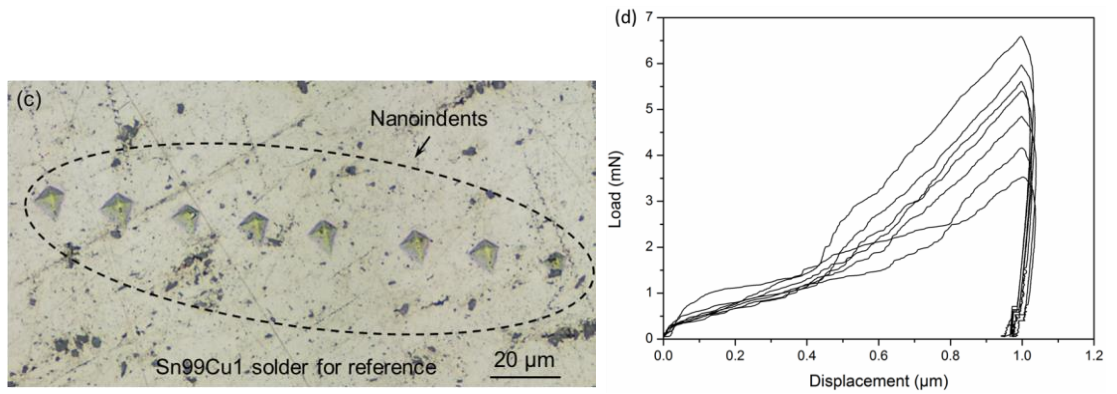


Fig. 6.8 The nano indents in reference solder and Cu specimen: (a) and (c) are the indents in reference Cu and solder specimens, respectively; (b) and (d) illustrate the corresponding load-displacement curves from the nano indents.

6.4.2.1 Residual stress within Cu

The evaluation of the residual stress within Cu was implemented at both the centre and the edge of the Cu substrate close to the Cu/Cu_3Sn interface after aging for progressively prolonged aging. Fig. 6.9 illustrates the nano indents made within the Cu substrate and their locations in the entire Sn99Cu1/Cu solder joint. It shows that the nano indents were about $10\ \mu\text{m}$ away from the Cu_3Sn/Cu interface at both the centre and edge of the solder joint as designed.

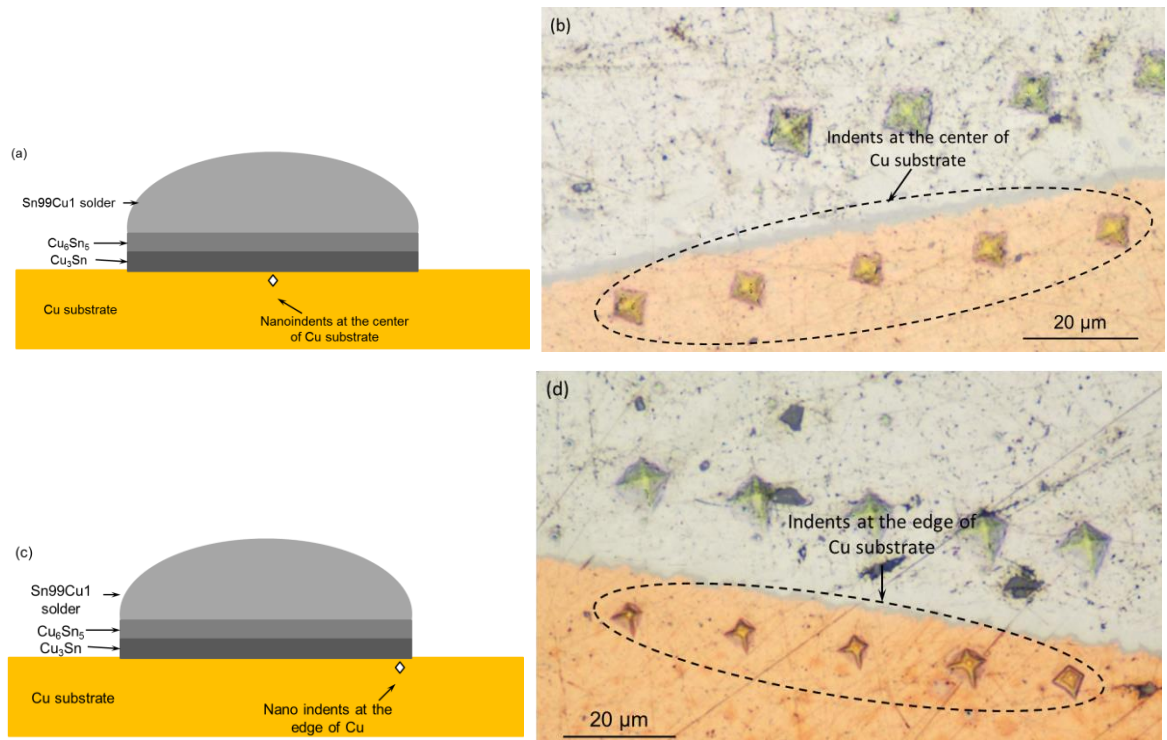


Fig. 6.9 Nano indents in the Cu substrate: (a) and (c) illustrate the overall location of the nano indents at the centre and at the edge of the solder joints respectively; (b) and (d) show the examples of nano indents at the corresponding locations.

The maximum forces of the nano indents in Cu substrate after aging for 0 to 500 hours are

summarized in Fig. 6.10. Each data point in the figure represents the average maximum force of five to seven nano indents in the Cu substrate. From the figure, the maximum forces of the nano indents in the Cu substrate at the centre of the solder joint were much higher than the referential forces from the reference Cu samples (Fig. 6.10 a)). According to the analysis in section 6.2, this indicates that the Cu substrate at the centre of Sn99Cu solder joints was under compression during aging.

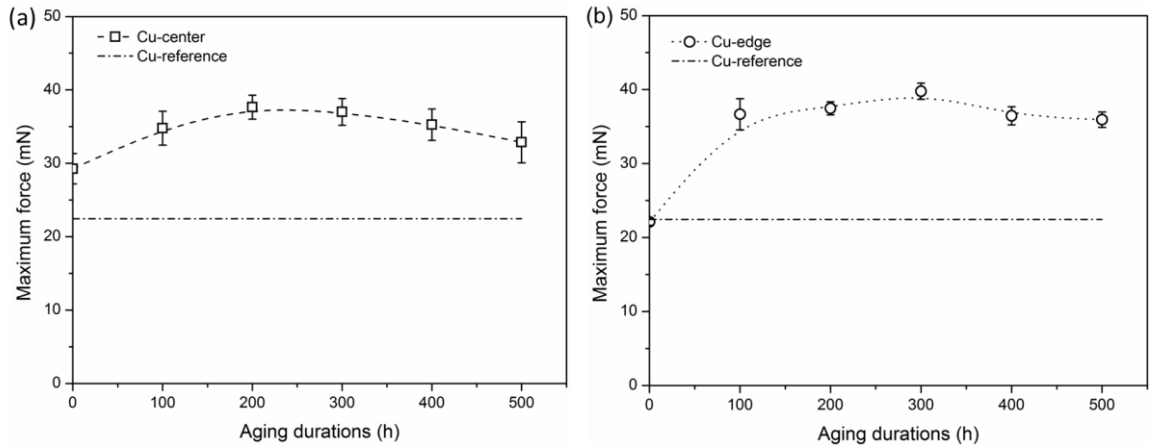


Fig. 6.10 Evolution of maximum forces of the nano indents (a) at the centre and (b) at the edge of Cu substrate after prolonged aging.

Fig. 6.10 b) illustrates that the maximum forces of the nano indents with the same depth at the edge of Cu substrate are also generally higher than the referential force from Cu reference specimen. Before aging, the maximum force of the nano indents at the edge of Cu was close to the reference force (F_0), which indicates that the Cu substrate at the edge of the solder joint was free of stress. After aging, the maximum indentation force increased to about 37 mN and remained stable as the aging prolonged. The higher maximum force in comparison to the reference value means that the Cu substrate at the edge of Sn99Cu1/Cu solder joint was under compression during the aging.

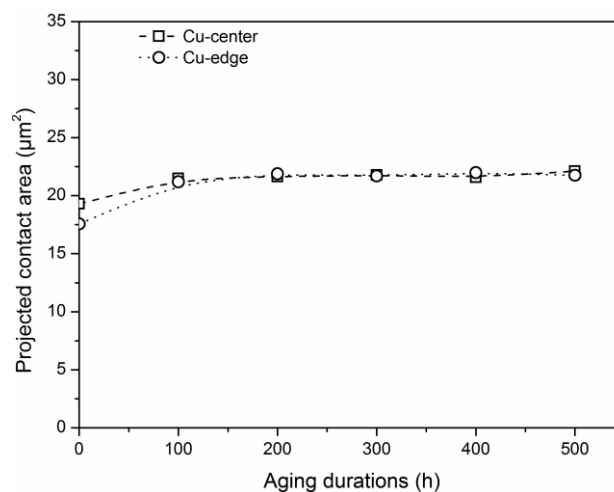


Fig. 6.11 Projected contact areas of the nano indents at the center and at the edge of Cu substrate with prolonged aging.

The projected contact areas of the nano indents were then estimated based on the load-displacement curves from the indentation tests and the calculation with equation (6.4). The derived average contact areas of the nano indents at the centre and at the edge of Cu substrate were plotted with increasing aging durations in Fig. 6.11. During aging, the average contact areas between the indenter and the Cu substrate were within the range $21 \pm 1 \mu\text{m}^2$ for the indents at the centre of Cu substrate and $21 \pm 2 \mu\text{m}^2$ for the indents at the edge of Cu.

Consequently, the residual stress within Cu substrate was estimated by equation (6.2) with the obtained maximum force within the Cu substrate, referential maximum force and the projected contact area. The derived residual stress within Cu was then plotted against aging durations in Fig. 6.12.

The positive residual stress at the centre of Cu substrate in Fig. 6.12 a) indicates that the Cu substrate was under compression at the centre in aging. The compression stress was about 200 MPa in the beginning, but increased to approximately 700 MPa after aging at 175°C for 200 hours, followed by a gradual decrease as the aging prolonged. In order to compare the general stress states within different parts and locations at the solder/Cu interface, the average compression stress at the centre of Cu substrate during the aging was estimated to be approximately 560 MPa.

The initial compression stress at the centre of Cu substrate before aging probably originated from the incompatible shrinkage in the solder and the Cu substrate during the cooling process in reflowing, because the thermal expansion coefficient of solder is higher than that of Cu (CTE: 22.2×10^{-6} for solder and 16.4×10^{-6} for Cu [16]). In aging, the interfacial Cu_3Sn layer started growing, which led to the volume shrinkage. For the adjacent Cu substrate, the tend of shrinkage in Cu_3Sn layer can lead to the compression stress within the Cu substrate, so the compression stress within Cu increased with aging durations. As the aging prolongs, the gradual decrease of compression stress could be attributed to the stress relaxation in Cu substrate, since at the aging temperature, 175°C, is high enough to enable the microstructural evolution in long-term aging [253].

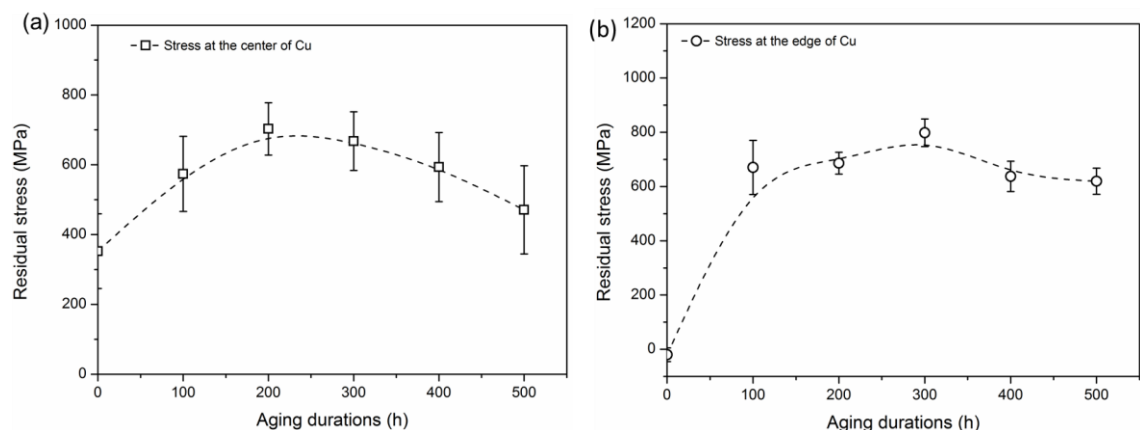


Fig. 6.12 Residual stress (a) at the centre and (b) at the edge of Cu substrate after progressively increasing aging durations.

The evolution of residual stress within the Cu substrate at the edge of the solder joints is illustrated in Fig. 6.12 b). Before aging, the Cu substrate was generally free of residual stress at the edge of the solder joint, which was probably due to the lack of constraint from the adjacent

materials. As the aging started, the compression stress at the edge of Cu substrate increased significantly to about 700 MPa and stabilized at this level as the aging continued. The increase in stress after aging was possibly caused by the contraction of the interfacial Cu_3Sn layer during aging. The followed slight decrease in compression stress after further extended aging can be attributed to the potential stress relaxation in Cu due to the high enough aging temperature. For comparison, the average compression stress within the Cu substrate at the edge of solder joint was about 565 MPa, which is close to the compression stress at the centre of solder joint.

6.4.2.2 Residual stress in Sn99Cu1 solder

Fig. 6.13 illustrates the characterisation of residual stress within the Sn99Cu1 solder matrix close to the solder/ Cu_6Sn_5 interface in Sn99Cu1 solder joints by nanoindentation tests. The locations of the nano indents are illustrated in Fig. 6.13 a) and c), and examples of the nano indents at the corresponding locations are illustrated in Fig. 6.13 b) and d).

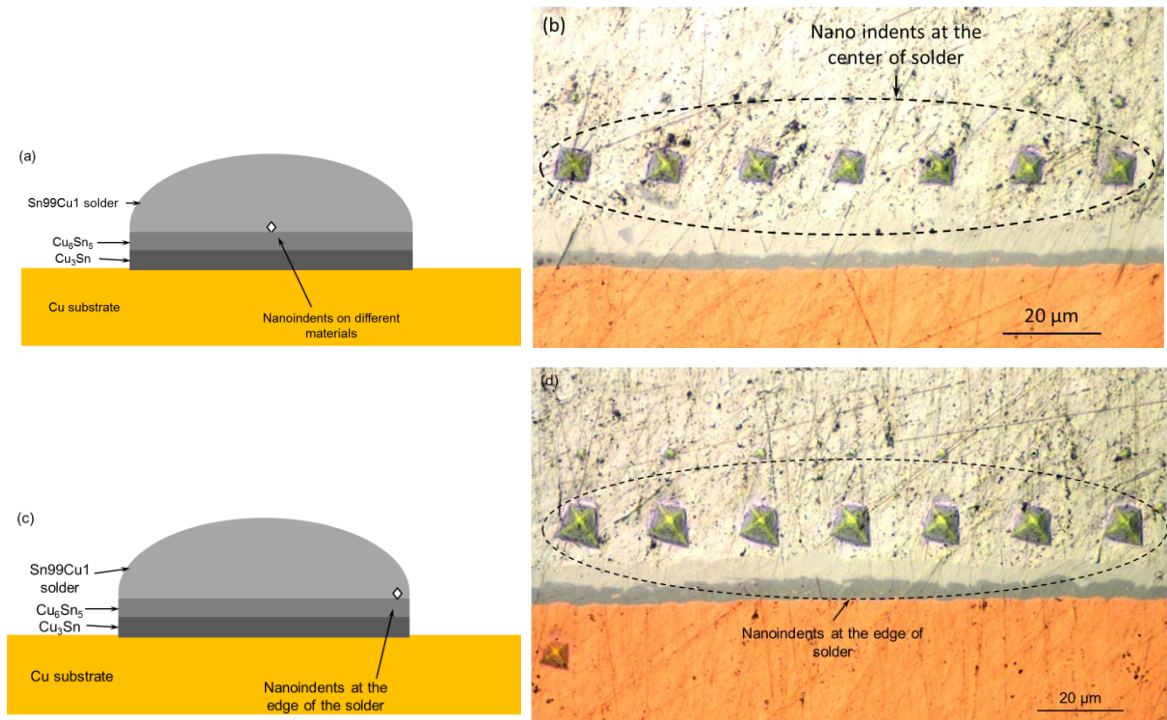


Fig. 6.13 Nano indents in the Sn99Cu1 solder matrix close to the solder/ Cu_6Sn_5 interface: (a) and (c) illustrates the overall location of the indents in the Sn99Cu1 solder joints; (b) and (d) show the indents made at the corresponding locations in the solder.

The maximum forces of the nano indents at the two designated locations in the solder matrix were derived from the load-displacement curves and summarized in Fig. 6.14. Each data point represents the average maximum forces from 5~7 nano indents. It can be found that the maximum forces at both the centre and the edge of Sn99Cu1 solder close to the solder/ Cu_6Sn_5 interface were higher than the forces from reference samples. This indicates that the solder part in the solder joint was under compression during aging.

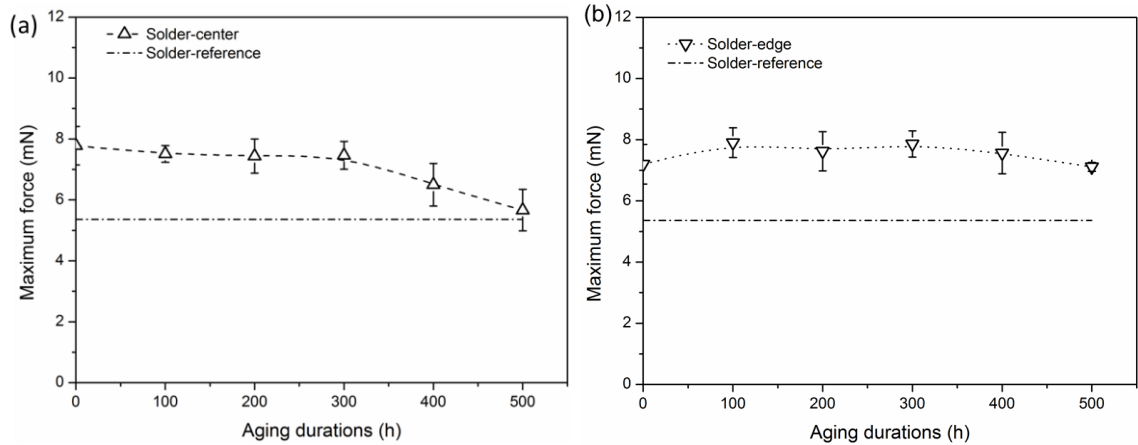


Fig. 6.14 Maximum forces of the nano indents (a) at the centre and (b) at the edge of the Sn99Cu1 solder joints close to the solder/ Cu_6Sn_5 interface after aging.

The projected contact areas of the nano indents in the solder matrix were then evaluated by equation (6.4) based on the load-displacement curves from the indentation tests. The results for the indents at the centre and at the edge of solder joints were summarized in Fig. 6.15. The average contact areas between the indenter and the Sn99Cu1 solder were about $24 \pm 1 \mu\text{m}^2$ for the indents at the centre and $24 \pm 2 \mu\text{m}^2$ for the indents at the edge.

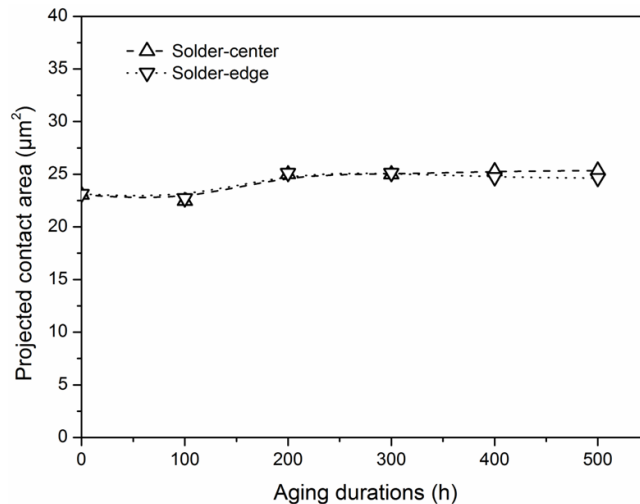


Fig. 6.15 Calculated projected contact areas of nano indents in solder matrix close to the solder/ Cu_6Sn_5 interface at the centre and at the edge of Sn99Cu1 solder joints.

The residual stress within solder matrix can then be evaluated based on the obtained maximum force and the contact area of the nano indents in solder matrix. The evolution of residual stress at the centre and at the edge of the solder is plotted against aging durations in Fig. 6.16. At the centre of solder joint, the solder matrix was under progressively decreasing compression stress after aging, from the initial 100 MPa before aging to about 10 MPa after aging at 175°C for 500 hours. The average compression stress within the solder matrix at the centre of solder joints was about 70 MPa in the aging. The observed reduction of compression stress at the centre of solder can be

ascribed to the creep and stress relaxation during aging, because the homologous temperature (measured temperature/ melting point of the material) of the aging temperature was 0.8, which was high enough to enable the creep of solder matrix in aging [254, 255].

In contrast, the compression stress in the solder matrix at the edge of solder joint was within the range 70 MPa to 120 MPa during aging. And the average compression stress was about 90 MPa.

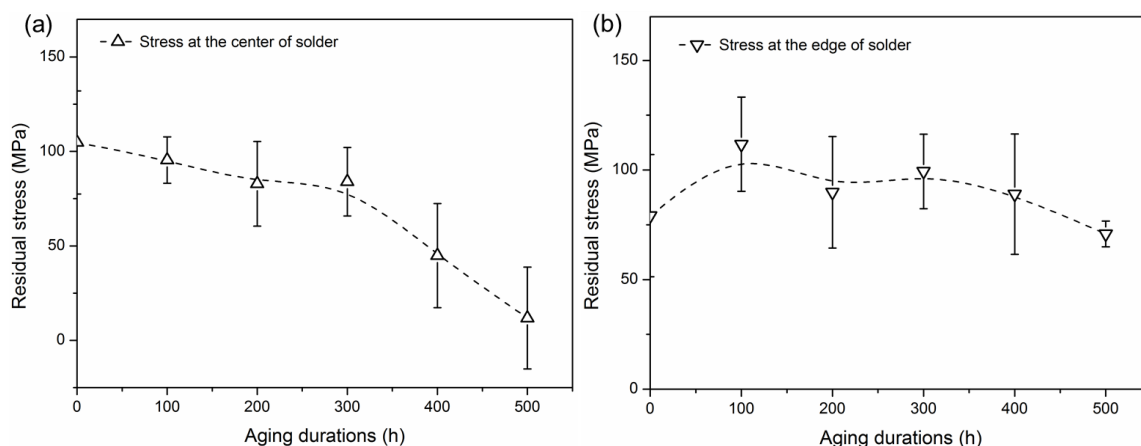


Fig. 6.16 The residual stress within solder matrix (a) at the centre and (b) at the edge of the Sn99Cu1/Cu solder joints.

6.4.3 Stress evolution in Cu_6Sn_5 and Cu_3Sn layers

The growth of interfacial IMC layers (i.e. Cu_6Sn_5 and Cu_3Sn) is accompanied by volume shrinkage that is confined by the attached solder and Cu. The residual stress could therefore rise during aging. Consequently, the interfacial IMC layers are possibly the stress concentration sites during aging.

According to the procedures for evaluating residual stress by nanoindentation in Fig. 6.4, nanoindentation test results from stress-free specimens are required to demonstrate the influence of residual stress on the nanoindentation tests in stressed samples. However, the growth of interfacial Cu_6Sn_5 and Cu_3Sn layers in solder joints is intrinsically accompanied by constrained volume shrinkage in the growth during aging. This brings significant challenges to the preparation of stress-free Cu_6Sn_5 and Cu_3Sn specimens.

Therefore, in this work, the interfacial Cu_6Sn_5 layer before aging and the Cu_3Sn layer after aging for 100 hours at the centre of the solder joint were selected to be the reference to the followed tests on the corresponding IMC layer. As such, the stress evolution within Cu_6Sn_5 and Cu_3Sn layers after longer aging durations could be evaluated. Hence, the estimated residual stress can only represent the stress evolution within interfacial Cu_6Sn_5 and Cu_3Sn layers while the absolute values depend on both the evolution of the stress and the initial stress state of the each IMC layer.

6.4.3.1 Residual stress within interfacial Cu_6Sn_5 layer

Fig. 6.17 gives examples of the nano indents at the centre and at the edge of interfacial Cu_6Sn_5 layer in Sn99Cu1/Cu solder joints. The overall locations of the indents are illustrated in Fig. 6.17 a) and c). Examples of actual indents at the corresponding locations are shown in Fig. 6.17 b) and d). As expected, the nano indents were located within the interfacial Cu_6Sn_5 layers without involving the

adjacent solder and interfacial Cu_3Sn layer.

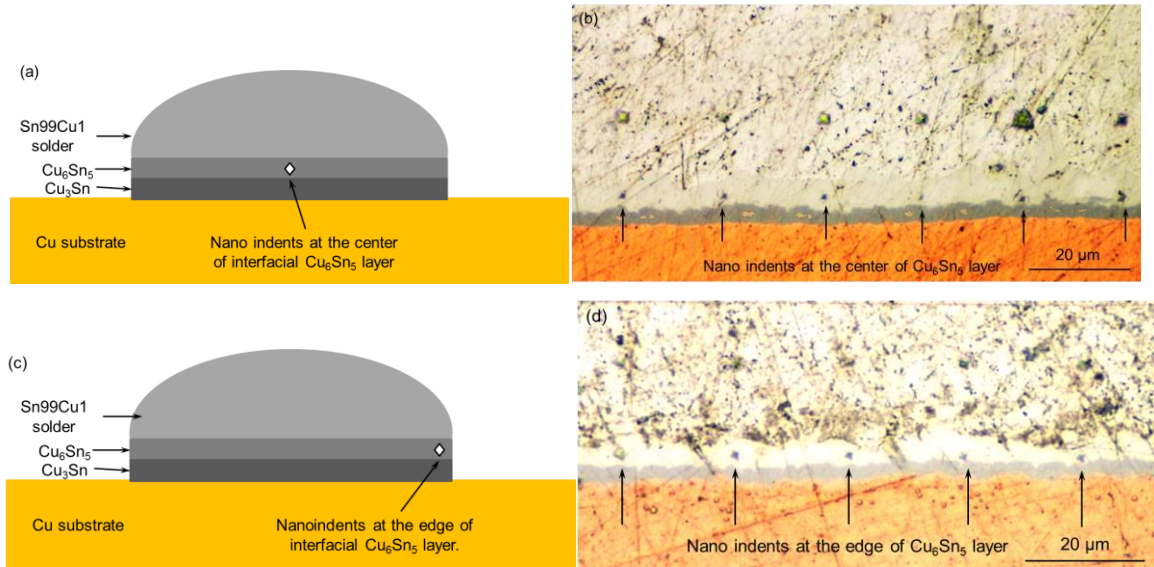


Fig. 6.17 Nanoindents within the interfacial Cu_6Sn_5 layer: (a) and (c) the overall locations of the indents in the entire solder joints; (b) and (d) examples of the indents at the corresponding locations, which are indicated by the arrows.

From the nanoindentation tests at the designated locations within the interfacial Cu_6Sn_5 layer, the maximum loads of the indents were summarized in Fig. 6.18 a) and b). Generally, the maximum forces at both the centre and the corner of the interfacial Cu_6Sn_5 layer were above the referential maximum force, indicating the increase in compression stress in the interfacial Cu_6Sn_5 layer during aging.

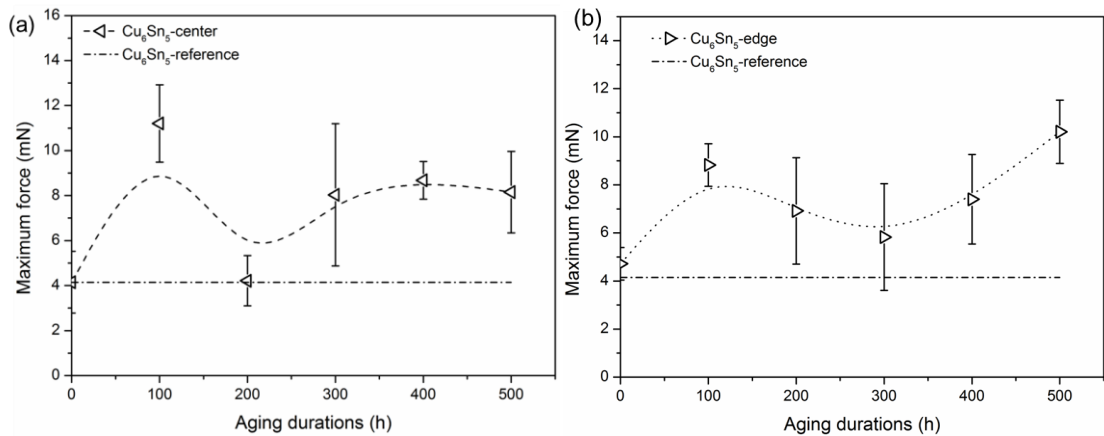


Fig. 6.18 Maximum forces of the nanoindents (a) at the centre and (b) at the edge in the interfacial Cu_6Sn_5 layer in Sn99Cu1 solder joints.

The projected contact areas of the nano indents within interfacial Cu_6Sn_5 layer were estimated and plotted against aging durations in Fig. 6.19. The average areas of the indents at the centre of the interfacial Cu_6Sn_5 layer were $1.2 \pm 0.3 \mu m^2$ and $1.1 \pm 0.2 \mu m^2$ for the indents at the edge.

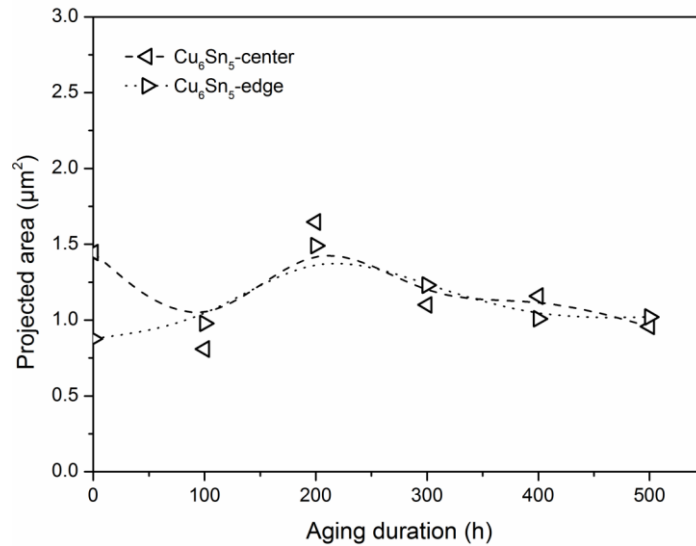


Fig. 6.19 Projected contact areas of the nano indents made at the center and at the edge of the interfacial Cu_6Sn_5 layer after aging for 0h - 500h.

With the obtained maximum force and projected contact area of the nano indents, the residual stress within interfacial Cu_6Sn_5 layer after aging was evaluated based on equation (6.2). Fig. 6.20 depicts the evolution of residual stress within the interfacial Cu_6Sn_5 layer with increasing aging durations. Each point in the figure was the average stress of 5~7 nano indents. Generally, the residual stress evolved with a similar trend at the centre and at the edge of the interfacial Cu_6Sn_5 layer in aging. The compression stress rose significantly at both the centre and edge of interfacial Cu_6Sn_5 layer after aging for 100 hours, followed by a sharp decrease when the aging prolonged to 200 hours. A steady growth of the compression stress was observed again when the aging proceeded longer. The growth in compression stress with aging durations could be ascribed to the thickening of interfacial IMC layers due to the reactive interdiffusion between the solder and Cu substrate. Throughout the aging, the average compression stress was about 4 GPa at the centre and 3 GPa at the edge of the interfacial Cu_6Sn_5 layer.

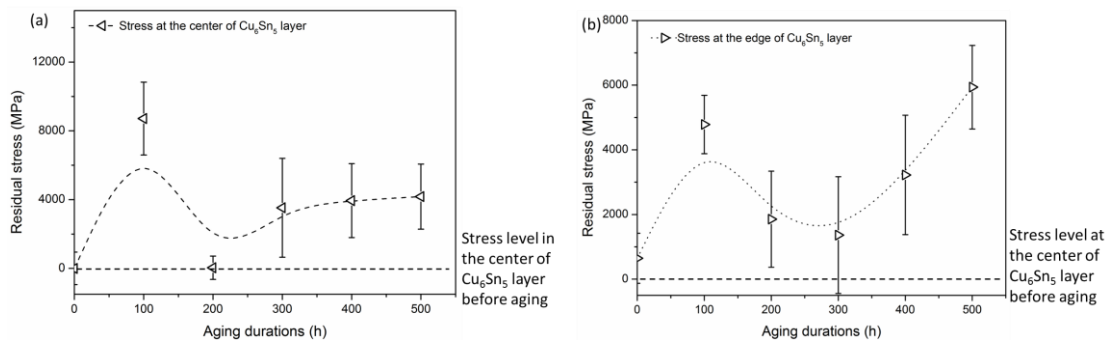


Fig. 6.20 Evolution of compression stress (a) at the centre and (b) at the edge of the interfacial Cu_6Sn_5 layer in the progressively prolonged aging.

During aging, the evolution of the stress generally consists of two stages, which can be divided by the 200 hours for the indents at the centre of interfacial Cu_6Sn_5 layer and 300 hours at the edge. In the first stage, the residual stress within the Cu_6Sn_5 layer varied with prolonged aging within first

200 or 300 hours. The reason is still unclear yet. Factors that potentially contributed to it include the volume shrinkage induced by the growth of IMCs, the mismatch of CTEs of the involved materials (CTEs: $22.2 \times 10^{-6} \text{ }^\circ\text{C}^{-1}$ for solder [256], $16.3 \times 10^{-6} \text{ }^\circ\text{C}^{-1}$ for Cu_6Sn_5 [16] and $19.0 \times 10^{-6} \text{ }^\circ\text{C}^{-1}$ for Cu_3Sn [16]) and microstructural evolution of the adjacent solder during aging. However, the fluctuation within the first stage of the aging is arguable, since the peak could also be interpreted as errors in the experiments.

In the second stage, the increase in compression stress in the interfacial Cu_6Sn_5 layer after aging for longer than 300 hours was probably resulted from the continuous volume shrinkage due to the growth of the adjacent interfacial Cu_3Sn layer. During the growth of Cu_3Sn layer in aging, the volume shrinkage coefficient is significantly higher than the coefficient of Cu_6Sn_5 layer. Hence, the shrinkage of interfacial Cu_3Sn layer in aging was severer and constrained by the $\text{Cu}_6\text{Sn}_5/\text{Cu}_3\text{Sn}$ interfaces. Consequently, the compression stress within interfacial Cu_6Sn_5 layer grew continuously at both the centre and the edge of the specimens as the aging proceeded.

6.4.3.2 Residual stress in interfacial Cu_3Sn layer

The indents made in interfacial Cu_3Sn layer for the evaluation of residual stress are shown in Fig. 6.21. The overall locations of the indents in the entire solder joint are illustrated in Fig. 6.21 a) and c). The examples of the actual nano indents at the corresponding locations are given in Fig. 6.21 b) and d). It clearly demonstrates that the nano indents were located within the interfacial Cu_3Sn layer precisely as expected. It should also be noted that the last indentation in Fig. 6.21 d) involved the adjacent Cu substrate, so the data from this point was excluded from following analysis.

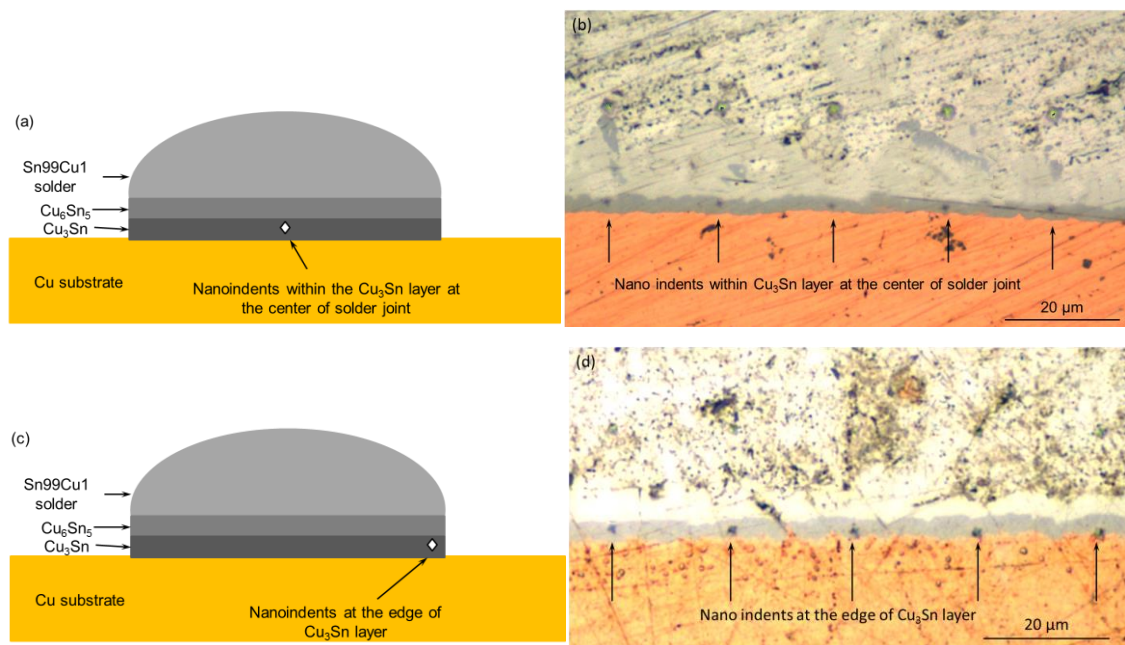


Fig. 6.21 Nano indents in the interfacial Cu_3Sn layer for evaluating the residual stress: (a) and (c) the location of the indents at the centre and at the edge of interfacial Cu_3Sn layer; (b) and (d) examples of the nano indents made at the corresponding locations.

The average maximum forces from the indents within interfacial Cu_3Sn layer after aging were plotted against aging durations in Fig. 6.22. From the force-aging duration curves, the maximum forces of the indents at both the centre and the edge of the interfacial Cu_3Sn layer were lower than the referential maximum load from the selected reference Cu_3Sn layer. This indicates the increase in the tension stress within interfacial Cu_3Sn layer during aging at 175 °C.

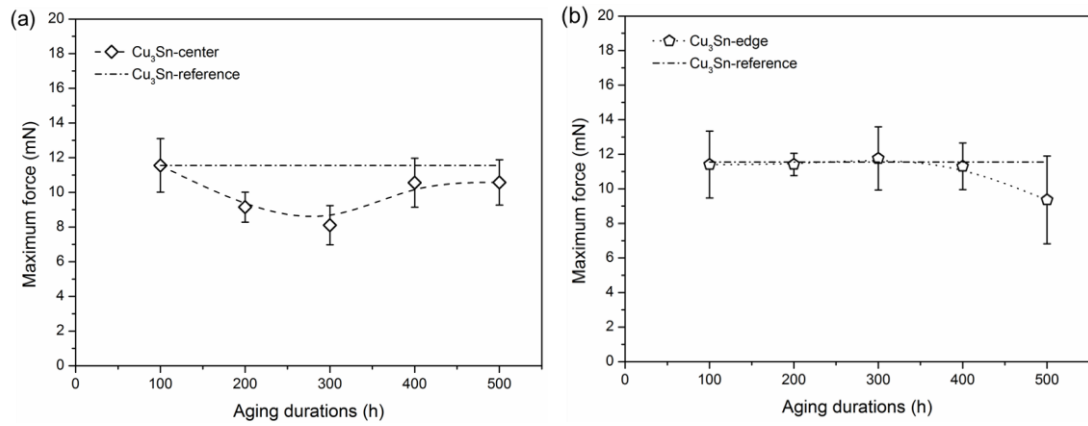


Fig. 6.22 Summary of the maximum force of the nano indents (a) at the centre and (b) at the edge of the interfacial Cu_3Sn layer in Sn99Cu1/Cu solder joints after aging.

Fig. 6.23 elucidates the contact area of the nano indents within interfacial Cu_3Sn layer estimated based on the load-displacement curves from the nanoindentation tests. The average projected areas were within the range $1.1 \pm 0.1 \mu m^2$ and $1.0 \pm 0.1 \mu m^2$ for the indents at the centre and the edge of interfacial Cu_3Sn layer, respectively.

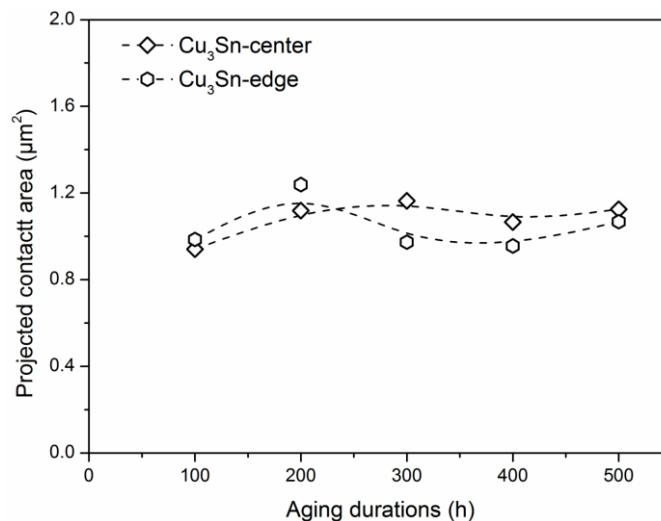


Fig. 6.23 Projected contact area of the nano indents in interfacial Cu_3Sn layer after aging at 175°C for 0 ~ 500 h.

Therefore, the residual stress within the interfacial Cu_3Sn layer was evaluated by following the procedures illustrated in Fig. 6.4. The obtained results are then summarized in Fig. 6.24. It can be observed that the stress within the interfacial Cu_3Sn layer after aging was generally lower than the stress in the reference Cu_3Sn specimen. This was due to the increase in tension stress in the

Cu_3Sn layer.

The stress evolution at the centre of Cu_3Sn layer could be divided into two stages separated by the 300 h in Fig. 6.24 a). When the aging duration increased from 100 hours to 300 hours, the tension stress rose significantly, reaching the peak of about 3 GPa. This could be probably resulted from the growth of interfacial Cu_3Sn layer. As presented in chapter 5, the growth of interfacial Cu_3Sn layer at the solder/Cu interface was accompanied by the notable 20% shrinkage in volume. But it was constrained by the attached interfacial Cu_6Sn_5 layer. Hence, the tension stress within the interfacial Cu_3Sn layer rose remarkably with increasing aging durations, reaching the peak after aging for 300 hours.

In contrast, before the aging duration exceeded 300 hours, the stress at the edge of the interfacial Cu_3Sn layer remained the same level as the referential stress from selected reference Cu_3Sn layer. When the aging lasted for 400 h and 500 h, a slight increase in the tension stress at the edge of interfacial Cu_3Sn layer were observed. Generally, the average tension stress was about 0.5 GPa at the edge of interfacial Cu_3Sn layer during aging.

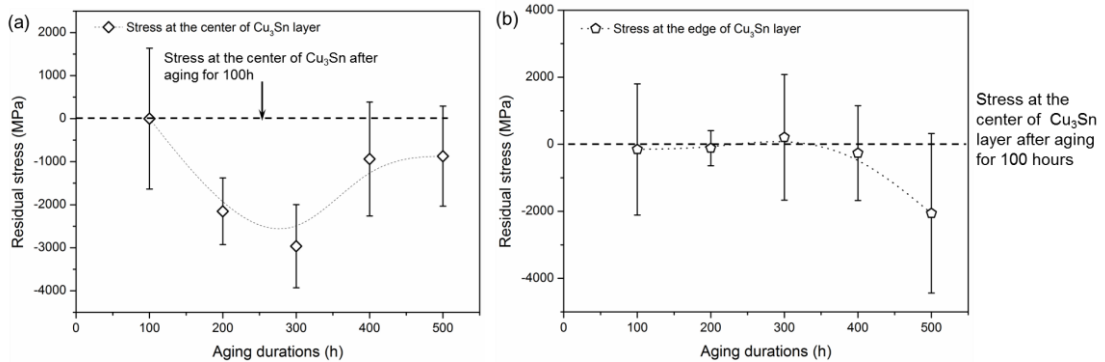


Fig. 6.24 The evolution of residual stress (a) at the centre and (b) at the edge of the interfacial Cu_3Sn layer in Sn99Cu1/Cu solder joints after aging. The negative values of the stress represent the tension stress within the Cu_3Sn layer.

6.5 Discussions

6.5.1 Correlation of evolution of residual stress

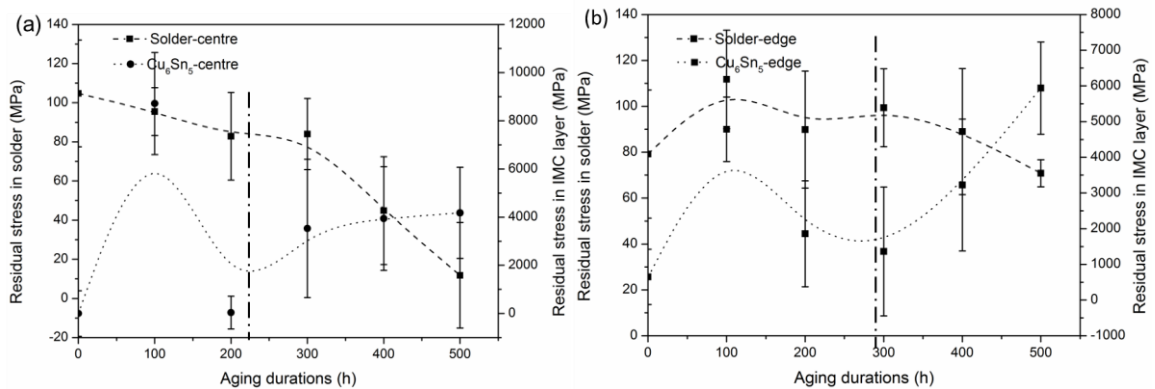
At the Sn99Cu1 solder/Cu interface, the solder, interfacial Cu_6Sn_5 layer, Cu_3Sn layer and Cu substrate are bonded as multilayer structure. So, it is reasonable to assume that the stress evolution within two adjacent parts was mutually affected during aging. In order to reveal this mutual effect, the evolution of residual stress in different parts at the solder/Cu interface was summarised for comparison in Fig. 6.25. For discussion, $S_{solder-center}$, $S_{solder-corner}$, $S_{Cu_6Sn_5-center}$, $S_{Cu_6Sn_5-corner}$, $S_{Cu_3Sn-center}$, $S_{Cu_3Sn-corner}$, $S_{Cu-center}$ and $S_{Cu-corner}$ are used to denote the residual stress within the corresponding parts in the Sn99Cu1/Cu solder joints and t represents the aging durations. Among these, the stress within interfacial Cu_6Sn_5 layer could be affected by the constraint from both the solder matrix and the Cu_6Sn_5/Cu_3Sn interface. Similarly, the stress evolution within Cu_3Sn layer was also under the influence from the Cu_6Sn_5/Cu_3Sn interface and Cu substrate. Therefore, it is essential to clarify the dominant influence in the evolution of residual stress within each layer.

Generally, the $S-t$ curves from different parts within Sn99Cu1 solder joints can be divided into two stages, as illustrated by the vertical dash lines in Fig. 6.25. The first stage usually started from the beginning of the aging to around 200 hours, and the second stage covers the range between 300 h and 500 h. From the illustrated comparison of curves, normally, there is no notable correlation between the two curves in one pair in the first stage. However, when the aging reached the second stage, the correlations between the stress evolutions within the two adjacent parts are evident in Fig. 6.25. Consequently, the second stages of the $S-t$ curves are focused for the discussion of the relationship of the stress evolution within two adjacent parts

Among the investigated parts of solder joints, only the interfacial Cu_3Sn layer was under tension during aging as both $S_{Cu_3Sn\text{-centre}}$ and $S_{Cu_3Sn\text{-corner}}$ are negative. The tension stress within the interfacial Cu_3Sn layer was probably resulted from the constraint from both the adjacent Cu and the interfacial Cu_6Sn_5 layer. Hence, the stress evolution within the Cu_3Sn layer is opposite to the trend of stress within the adjacent Cu at the centre of the solder joint, as illustrated in Fig. 6.25 e). This also indicates that the Cu substrate posed the dominant confinement to the contraction of interfacial Cu_3Sn layer at the centre of the solder joint during aging. For the stress state at the edge of the solder joint, there was no observable correlation between the stress evolution within the interfacial Cu_3Sn layer and the evolution in the adjacent Cu.

Because the stress state of interfacial Cu_3Sn layer was dominated by the Cu substrate at the centre, no noticeable correlation was identified between the stress within the adjacent interfacial Cu_6Sn_5 and Cu_3Sn layers in Fig. 6.25 c). But, at the edge of the solder joint, the increase in tension stress within the interfacial Cu_3Sn layer is accompanied by a sharp growth in the compression stress within the interfacial Cu_6Sn_5 layer. It could therefore be concluded that the stress state at the edge of the Cu_3Sn layer was governed by the constraint from the interfacial Cu_6Sn_5 layer, not the constraint from Cu.

For the bulk solder within the Sn99Cu1 solder close the solder/ Cu_6Sn_5 interface in Fig. 6.25 a) and b), the stress generally decreased with prolonged aging durations, though the stress within the interfacial Cu_6Sn_5 layer evolved gradually with aging at both the centre and the edge of the solder joint. This is possibly due to the low deformation resistance of bulk solder, which can compensate the generated residual stress at the solder/ Cu_6Sn_5 interface induced by the growth of IMCs in aging. Therefore, no notable correlation can be found between the stress evolution in solder and Cu_6Sn_5 layer.



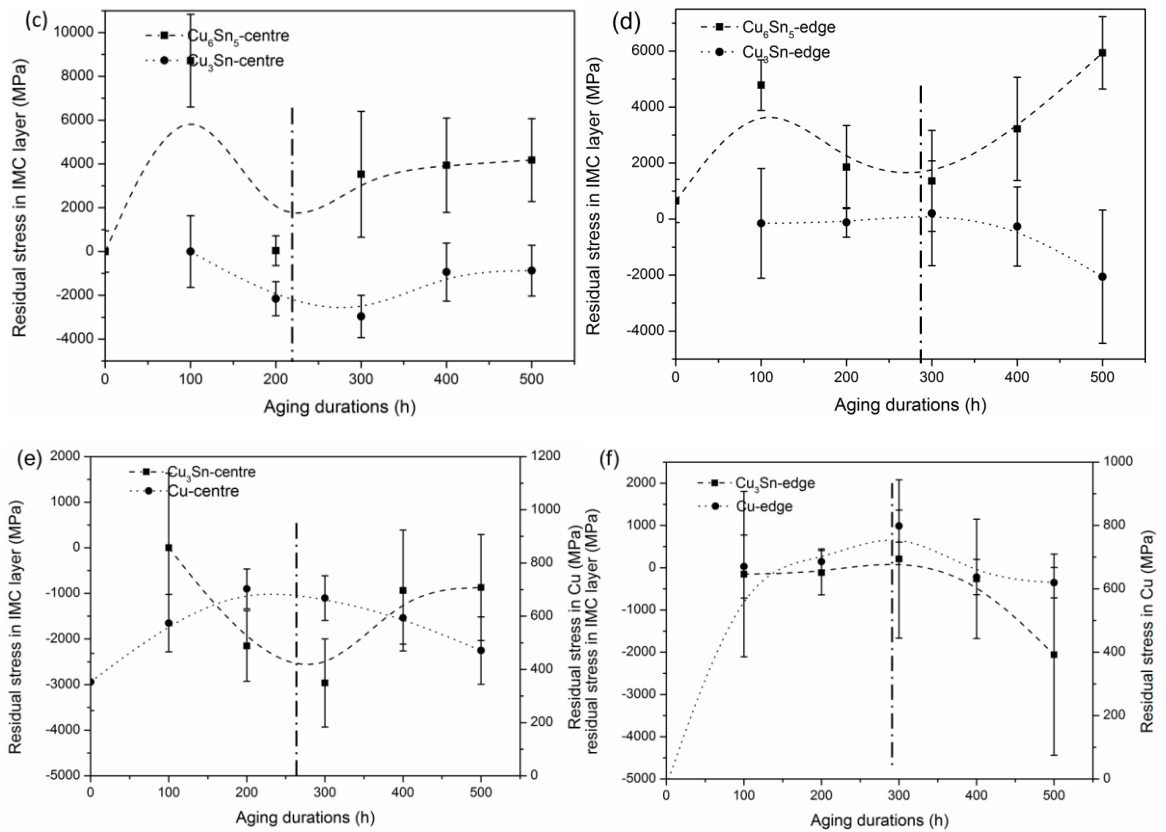


Fig. 6.25 The comparison of the evolution of residual stress within two adjacent parts in Sn99Cu1/Cu solder joints in aging: (a), (c) and (e) illustrate the evolution of stress close to the Sn99Cu1 solder/ Cu_6Sn_5 , Cu_6Sn_5 / Cu_3Sn and Cu_3Sn /Cu interfaces at the centre of the solder joint; and (b), (d) and (f) are the stress within the same parts at the edge.

6.5.2 Factors contributing to the evolution of residual stress

During the aging of specimens, several factors can contribute to the stress evolution at the solder/Cu interface, including mismatch of CTEs between different parts, volume shrinkage induced by growth of IMCs, creep and stress relaxation within solder and Cu. These pose diverse influence on the build-up of residual stress.

Both the thermal expansion and volume shrinkage can lead to the increase of residual stress within solder joints, while creep/stress relaxation and the growth of Sn whiskers can release the stress. In the experiments, the Sn99Cu1 solder joints underwent several thermal cycles, including heating during aging and cooling before taking the specimens out. These thermal experiences could lead to noticeable build-up of residual stress within solder joints due to the incompatible thermal expansion coefficients of different parts in the Sn99Cu1/Cu solder joints, as listed in Table 6.5. The thermal expansion coefficients of Cu, Cu_6Sn_5 and Cu_3Sn are close to each other, but significantly lower than that of the bulk solder. Therefore, during the thermal processes, the mismatch of CTEs can lead to significant increase in compression stress within the bulk solder in the solder joint.

Table 6.5 Coefficients of thermal expansion of solder, Cu_6Sn_5 , Cu_3Sn and Cu in Sn99Cu1/Cu solder joints [16].

	Solder	Cu_6Sn_5	Cu_3Sn	Cu
CTE ($^{\circ}C^{-1}$)	22.2e-6 [256]	16.3e-6	19.0e-6	16.42e-6

Fig. 6.25 c) and d) illustrate that the interfacial Cu_3Sn layer was under tension at both the centre and the edge of the solder joint in aging. From the listed CTEs, it is reasonable to assume that the interfacial Cu_3Sn layer should be under compression due to the higher expansion. But it is contradicted to the experimental observation.

As discussed in chapter 5, the growth of interfacial IMC layers is accompanied by the volume shrinkage. Because of the higher dimensional change coefficient of Cu_3Sn layer, the contraction of the interfacial Cu_3Sn layer was more evident than that of the Cu_6Sn_5 layer. Hence, the Cu_3Sn layer was under tension due to the constrained shrinkage. Consequently, it can be concluded that the stress evolution within the interfacial Cu_3Sn layer was dominated by the volume shrinkage, not thermal expansion.

During the aging, the homologous temperature for solder reached about $0.7T_m$, which is high enough to enable the creep/stress relaxation within solder in aging [257, 258] to release the build-up of residual stress. It is believed that the continuous drop of the residual stress in solder matrix during aging in Fig. 6.25 a) and b) was a result of it.

Furthermore, after the aging of Sn99Cu1/Cu solder joints, Sn whiskers were also observed within the solder matrix close to the solder/ Cu_6Sn_5 interface, as illustrated in Fig. 6.26. It was reported that the growth of Sn whiskers or hillocks was resulted from the compressive stress within solder joint and it can effectively release the stress within solder joints in aging [46, 87, 229, 259]. The observed growth of Sn whiskers confirms that the solder matrix was under compression during aging. And the growth can lower the stress level within the solder matrix.

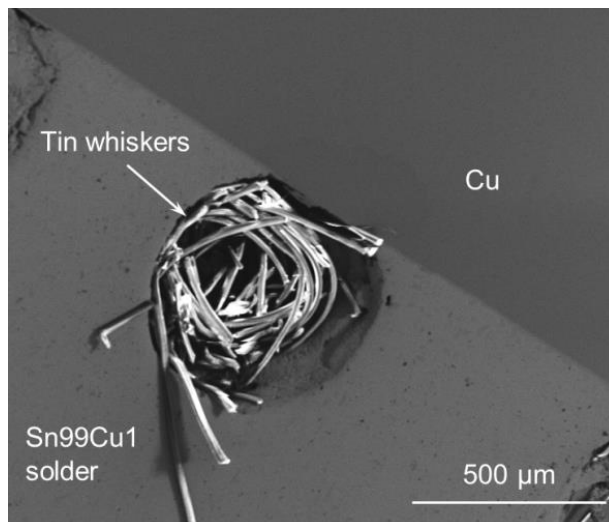


Fig. 6.26 Growth of Sn whiskers within a void in Sn99Cu1 solder next to the Sn99Cu1 solder/Cu interface.

6.5.3 Deviations in experimental results

In the presented residual stress within different parts of solder joints, noticeable deviation can be identified in the residual stress in interfacial Cu_6Sn_5 and Cu_3Sn layers in Fig. 6.20 and Fig. 6.24. The residual stress was estimated by the calculation with equation (6.2). Two of the required parameters, the maximum force of the indents in solder joints (F_{max}) and the referential maximum force (F_0), can be precisely measured by the nanoindentation system. From the force-time curves in Fig. 6.18 and Fig. 6.22, the standard deviations of them are within a reasonable range. Furthermore, the evaluation of projected contact area depends on the accuracy of equation (6.4). And, Fig. 6.7 in section 6.4.1 demonstrates that the estimation of contact area with equation (6.4) is reliable.

However, in the calculation of residual stress with equation (6.2), the units of the maximum force F_{max} are mN and the unit of the contact area A_c is μm^2 . Hence, the calculation of residual stress with the unit of MPa takes the form, $1 mN/(1 \mu m^2) = 10^9 Pa = 10^3 MPa$. Therefore, any deviation in the values of contact area or maximum force would be magnified 1000 times in the value of calculated residual stress with the unit of MPa . Consequently, in section 6.4.3, the standard deviations of the residual stress in interfacial Cu_6Sn_5 and Cu_3Sn layers are notably high.

6.6 Summary

The residual stress within solder, interfacial Cu_6Sn_5 layer, interfacial Cu_3Sn layer and Cu in Sn99Cu1/Cu solder joints was evaluated by nanoindentation tests after aging for 0~500 hours. From the presented results and discussions, it can be concluded that:

1. During the aging, Cu substrate was under compression with the average stress 560 MPa at both the centre and edge of the solder joint. The average compression stress within solder was 70 MPa at the centre and 90 MPa at the edge.
2. The interfacial Cu_6Sn_5 was also under compression with the average compression stress 4GPa at the centre and 3GPa at the edge during the aging. In contrast, the interfacial Cu_3Sn layer was under tension with the stress 1.7GPa at the centre and 0.5GPa at the edge.
3. There is no observable correlation between the $S-t$ curves from solder and the adjacent interfacial Cu_6Sn_5 layer due to the low resistance to deformation in the solder matrix.
4. The Cu substrate posed the dominant constraint to the contraction of interfacial Cu_3Sn layer during its growth at the centre of Sn99Cu1 solder joint. However, for the growth of interfacial Cu_3Sn layer at the edge, the interfacial Cu_6Sn_5 layer contributed more to confine the shrinkage of interfacial Cu_3Sn .
5. Both the thermal expansion and volume shrinkage can lead to the increase of residual stress within the interfacial IMC layers, while creep/stress relaxation and the growth of Sn whiskers can release the stress within the bulk solder.
6. The observed growth of Sn whiskers confirms that the solder matrix was under compression during aging. But, the compression stress could also be partly relieved by the formation of Sn whiskers.

Chapter 7 Modelling on the fracture behaviour of solder joints

7.1 Introduction

From the presented experimental results in previous chapters, the growth of interfacial IMC layers can pose various influences on the mechanical reliability of solder joints, such as the coalescence of voids due to volume shrinkage and residual stress. Due to these effects, the most notable effect of the interfacial IMC layers on the entire solder joints are the decrease in fracture strength [260] and the transition of fracture modes [175, 261, 262] with increasing aging durations. However, it is still unclear that how these various effects can alter the fracture behaviour of solder joints.

Since the growth of interfacial Cu_6Sn_5 and Cu_3Sn layers is intrinsically accompanied by both the volume shrinkage and build-up of residual stress, it is challenging to reveal the effect of individual factors experimentally. Furthermore, due to the small size and brittleness of interfacial IMC layers, it is difficult to capture the crack initiation and propagation within the interfacial IMC layers under external loads in experiments. Moreover, the common sample preparation methods, such as mounting, grinding and polishing, can probably induce new cracks within the solder joints due to the mechanical loads exerted on the sample during these sample preparation procedures. Alternatively, focused ion beam or broad ion beam can be employed to minimise the induced damage in sample preparation, but specific instruments are required. In contrast, finite element modelling could be a more accessible and efficient approach to investigate the effect of individual factors induced by the growth of interfacial IMC layers on the crack initiation and propagation within solder joints under external loads.

7.2 Numerical simulation and geometries of the models

7.2.1 Methodology

From the experimental results and discussions in previous chapters, the factors that may affect the fracture behaviour of solder joints under exerted loads include the microstructure of solder joints, the failure of interfacial IMC layers and the residual stress at the solder/substrate interface in the solder joint. In order to reveal the effect of individual factors on the fracture behaviour of solder joints, the methodology utilised in the modelling is illustrated in Fig. 7.1. The original two finite element models were built with two types of interfacial IMC layers with different thicknesses and morphologies. The modelling results from them can serve as the reference to the followed modelling incorporated with additional factors. Therefore, the influence of individual factors on the fracture behaviour of solder joint can be revealed step by step.

In the solder joint, various microstructural factors can possibly influence the fracture behaviour of solder joints, such as grain boundaries, voids and heterogeneous particles. To simplify the involved issues in the modelling, only the grain boundaries were incorporated in the models for

investigating the microstructural effect on the fracture behaviour of solder joint. Hence, arbitrary grain boundaries should be introduced in the model.

The influence of the residual stress on the fracture behaviour of solder joints was investigated by coupled stress-fracture modelling. The distribution of residual stress within the solder joint was evaluated by the modelling on the combined effect of thermal expansion, volume shrinkage within the interfacial IMC layers and the potential creep/stress relaxation of the solder joint in the heating and cooling process.

Finally, models with both residual stress and microstructure were built to simulate the combined effects of these two factors on the failure of solder joint. Consequently, the effects of individual factors and the combined effect of them can be revealed by modelling.

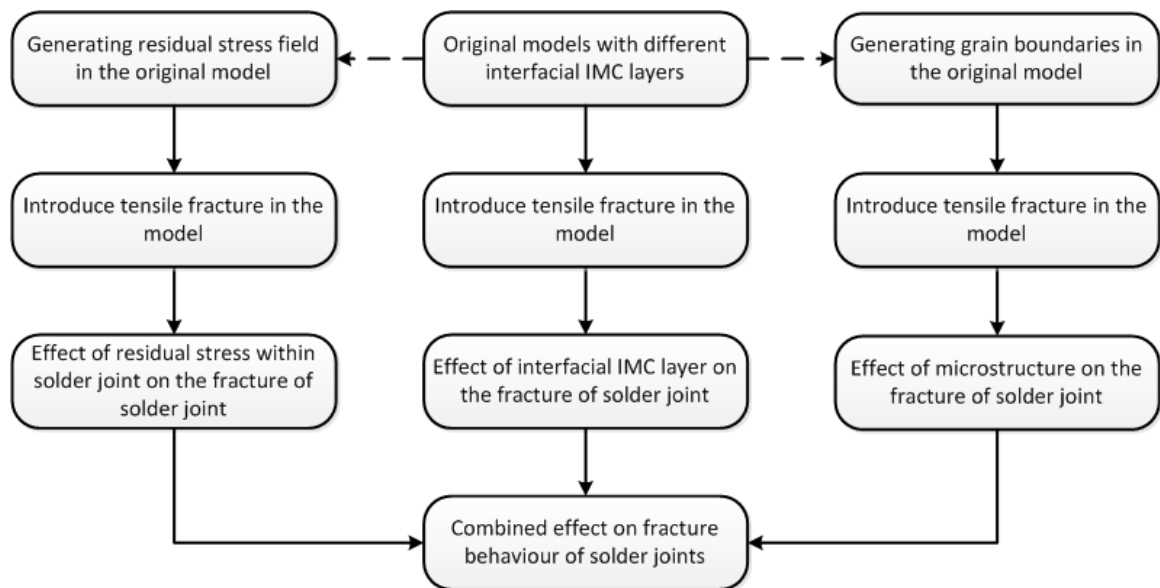


Fig. 7.1 Methodology of the modelling on the effect of residual stress, microstructure and interfacial IMC layers on the fracture behaviour of solder joints.

7.2.2 The original finite element models

Fig. 7.2 a) and b) show the interfacial IMC layers in Sn99Cu1 /Cu solder joints before aging and after aging at 175°C for 1006.5 hours, respectively. It can be observed that the thickness and morphology of the interfacial IMC layers evolved notably at the solder/Cu interface after aging. In order to elaborate the effect of the thickness of interfacial IMC layers on the modelling results, two finite element models were built with two types of interfacial IMC layers before and after extended aging. The thickness of the interfacial IMC layers and the radius of the scallops were measured based on Fig. 7.2, and the results are listed in Table 7.1 for creating the geometry of the original model. The built two original models are illustrated in Fig. 7.3.

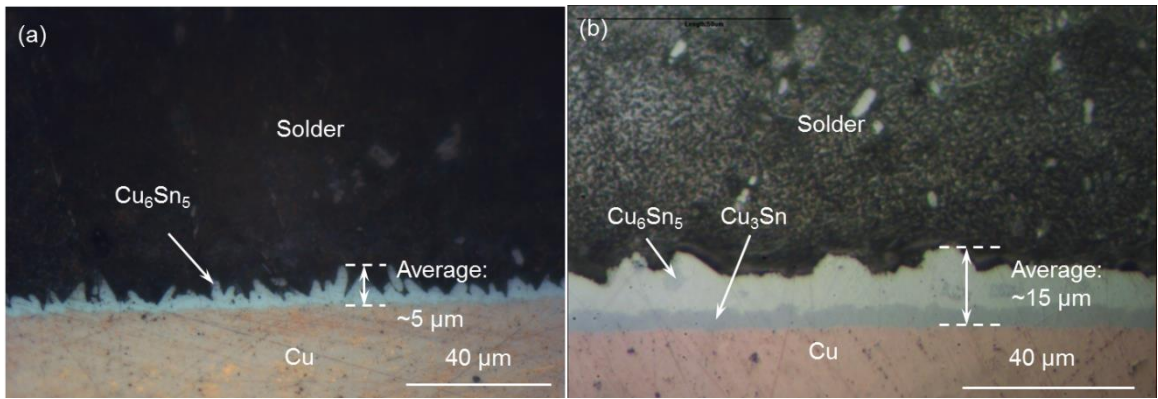


Fig. 7.2 Interfacial IMC layers (a) before aging and (b) after aging at 175 °C for 1006.5 hours in Sn99Cu1/Cu solder joints.

Table 7.1 Dimensions of the interfacial IMC layers in the original finite element models.

	0 h		1006.5 h	
	Cu_6Sn_5 (μm)	Cu_3Sn (μm)	Cu_6Sn_5 (μm)	Cu_3Sn (μm)
Thickness	4.2	-	11.5	7.2
Bottom-to-scallop distance	3	-	7.5	-
Average radius of scallops	2	-	7	-

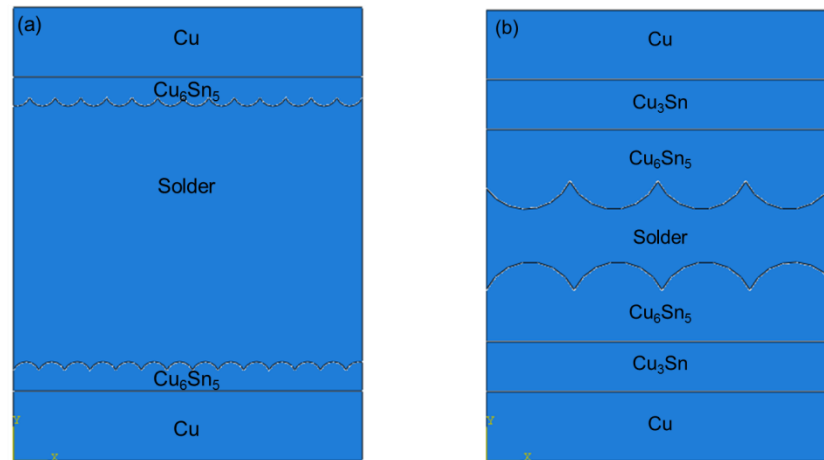


Fig. 7.3 Geometries of the original finite element models for the solder joints (a) before aging and (b) after aging for 1006.5 hours.

The boundary conditions introduced in the model are illustrated in Fig. 7.4 a) and b). The bottom Cu part in the model was fixed along both X and Y directions and a 10 μm displacement along Y direction was applied on the top Cu part to simulate the process of tensile tests.

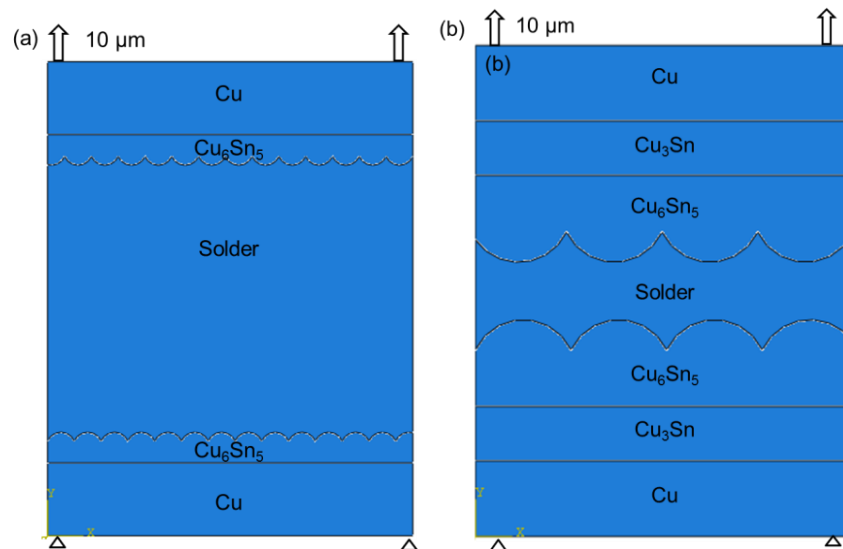


Fig. 7.4 Boundary conditions for the simulation on the tensile fracture of solder joints (a) before aging and (b) after aging.

7.2.3 Finite element models with residual stress field

In chapter 6, it was found that the factors that may contribute to the development of residual stress within solder joints include the mismatch of CTEs, creep/stress relaxation during aging and the volume shrinkage induced by the growth of interfacial IMC layers. The thermal experience, such as the cooling in reflowing and heating in aging, could induce residual stress within solder joints due to the incompatible thermal expansion of different parts. The volume shrinkage induced by the growth of interfacial IMC layers during aging was hindered by the attached solder and Cu, which can lead to diverse evolution of the residual stress within different parts at the solder/Cu interface. In contrast, creep/stress relaxation in both solder and Cu may partly release the build-up of residual stress in the solder joints, which can occur even at room temperature [263, 264].

Hence, the procedures for simulating the distribution of residual stress within solder joints after aging are illustrated in Fig. 7.5. The thermal experience of solder joints before tensile tests can be generally divided into three periods: (1) the cooling in reflowing; (2) the long-term aging at elevated temperature; (3) the cooling after aging. In the reflowing of solder joints, the contraction of solder part during cooling can lead to the build-up of residual stress only after the solidification of the solder. Therefore, the cooling process in the modelling started from the liquidus temperature of solder, 221°C, to room temperature [16]. During the long-term aging at elevated temperature, the interfacial IMC layers can grow significantly, which would further lead to the contraction of interfacial IMC layers in solder joints. Since there is no specific module for simulating the volume shrinkage induced by the growth of interfacial IMC layers during aging, the swelling feature in Abaqus was employed and the swelling strain rate was calculated based on the measured dimensional change coefficient in chapter 5.

During the aging at elevated temperature, creep/stress relaxation can likely happen in both the solder and Cu substrate, which reduces the level of residual stress. This is particularly true in solder joints as it was confirmed that the stress within bulk solder dropped gradually with prolonged aging

in chapter 6. In the modelling, the creep behaviours of solder and Cu were modelled by time-hardening model in Abaqus, $\dot{\epsilon}^{cr} = A\tilde{\sigma}^n t^m$, where $\dot{\epsilon}^{cr}$ is the uniaxial equivalent creep strain rate; $\tilde{\sigma}$ is the uniaxial equivalent deviatoric stress; t is the total time. In the modelling, the creep behaviour of Cu and solder were extracted from the curves in references [265] and reference [266], respectively. Hence, the constants A , m and n can be derived by fitting a specific creep strain-time curve with the formula. Consequently, the major parameters and settings involved in the modelling on the development of residual stress are listed in Table 7.2.

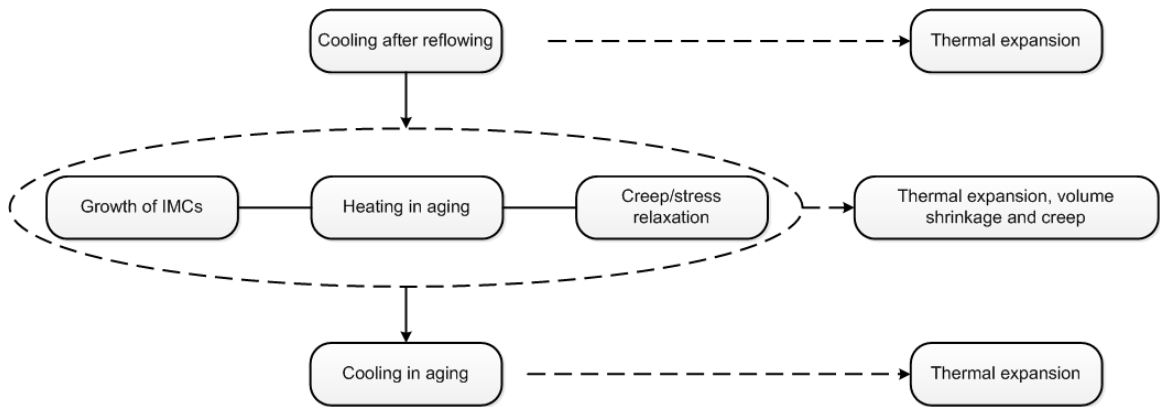


Fig. 7.5 Procedures for simulating the residual stress within solder joints in finite element modelling.

Table 7.2 Parameters for the modelling on the distribution of residual stress within solder joints after aging.

	Creep			CTE	Swelling strain rate
	A	m	n		
Cu	1.93E-11 [265]	1.097 [265]	-0.79 [265]	16.42e-6[16]	-
solder	9.48E-14 [266]	1.4 [266]	-0.726 [266]	22.2e-6[16]	-
Cu_6Sn_5	-	-	-	16.3e-6[16]	-0.03/1000 h
Cu_3Sn	-	-	-	19.0e-6[16]	-0.2/1000 h

In the modelling, the boundary conditions of the model were illustrated in Fig. 7.6. The Cu parts in the models of solder joints before aging and after aging were fixed, as illustrated in Fig. 7.6 a) and b). The solder part and the Cu in the model were able to expand in heating, deform plastically and creep in aging in the simulation. For the IMC layer at the interface, the interfacial Cu_6Sn_5 and Cu_3Sn layers were set to be elastic without any plastic deformation during aging based on the experimental results in chapter 4. Furthermore, both the thermal expansion and volume shrinkage were also included in for the deformation of the interfacial IMC layers in solder joints.

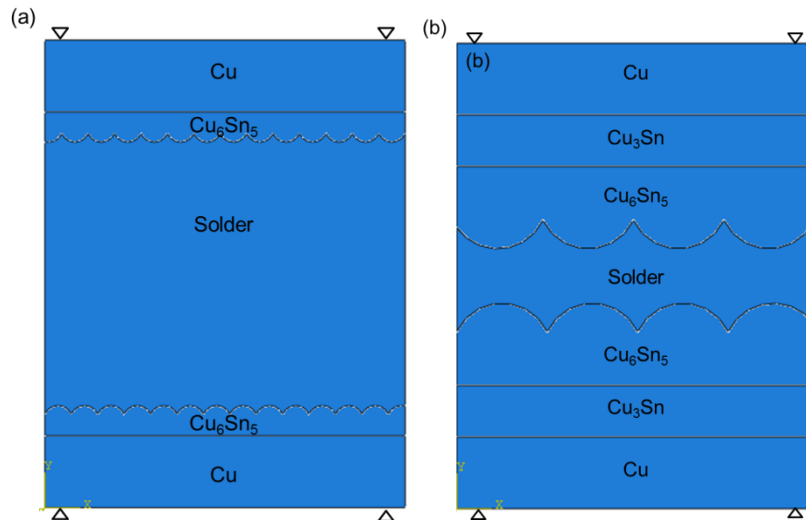


Fig. 7.6 Boundary conditions and settings in the models of solder joints (a) before aging and (b) after aging for 1006.5 hours in the modelling on residual stress.

The obtained distribution of residual stress within Sn99Cu1/Cu solder joints before aging and after aging for 1132.5 hours is illustrated in Fig. 7.7. It can be found that the stress within the Cu substrate and interfacial IMC (Cu_6Sn_5 and Cu_3Sn) layers was higher than the residual stress within solder matrix in both two models. The stress particularly concentrated at the corners of the interfaces, such as the Cu_6Sn_5 /Cu interface in Fig. 7.7 a) and the Cu_3Sn /Cu interface in Fig. 7.7 c). The relatively lower stress within solder is possibly due to the lower resistance to the deformation and lower yield strength. During aging, the long-term deformation behaviours, creep/stress relaxation within solder matrix, can further relieve the stress within the solder matrix. In contrast, the interfacial IMC layers and the adjacent Cu are much more rigid. Hence, the residual stress within the interfacial IMC layers and Cu substrate was much higher than the stress in bulk solders.

The detailed distributions of von Mises stress within the solder matrix in solder joints with thin and thick IMC layers are illustrated in Fig. 7.7 b) and d), respectively. Before aging, the solder joint mainly consisted of bulk solder, so the induced stress can be partly accommodated by localised deformation of the solder. Therefore, the stress was lower close to the centre of the bulk solders and it preferentially concentrated at the solder/ Cu_6Sn_5 interface, where the most serious incompatible deformation was located. For the model of solder joints after aging for 1132.5 hours, the interfacial Cu_6Sn_5 and Cu_3Sn layers composed the majority of the solder joint, leaving only about 20% of solder matrix. Due to the limited amount of solder, the build-up of residual stress cannot be effectively compensated by the deformation of the solder. Hence, the stress within the bulk solder in Fig. 7.7 d) is homogeneously high, which is evidently caused by the increasing proportion of interfacial Cu_6Sn_5 and Cu_3Sn layers.

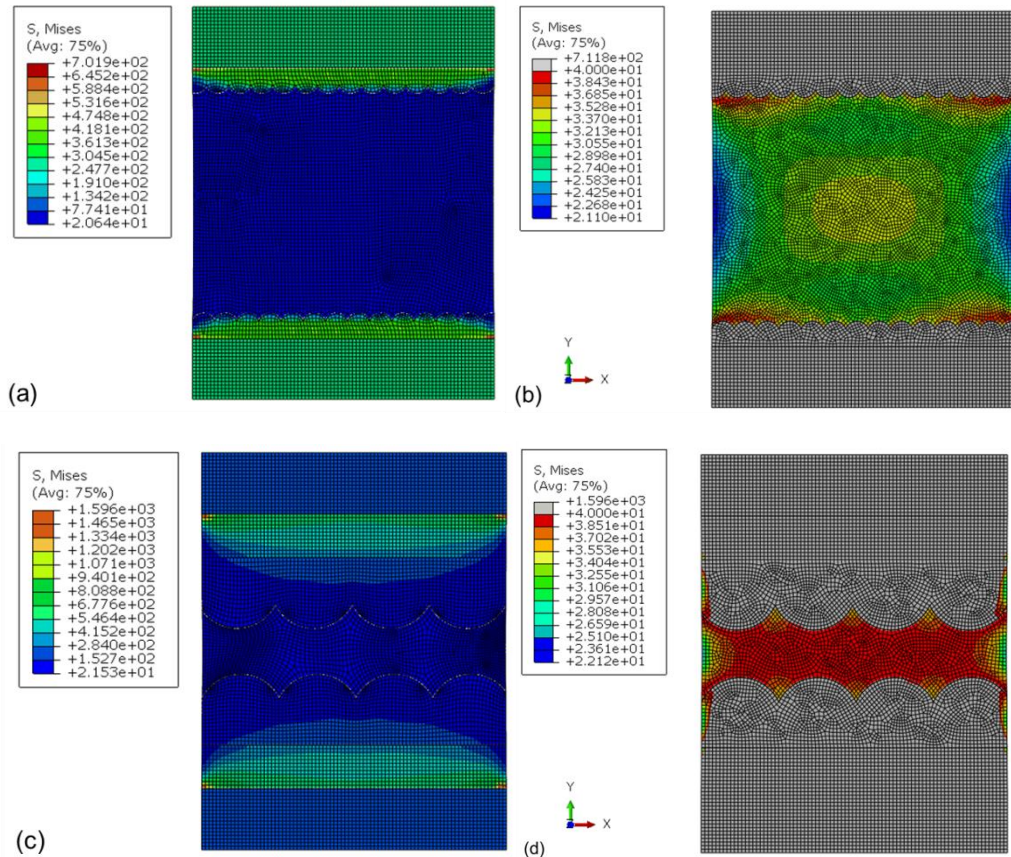


Fig. 7.7 Stress distribution within solder joints: the overall distribution of residual stress in the (a) solder joint with thin interfacial IMC layer and (c) solder joint with thick interfacial IMC layer; (b) and (d) are the detailed stress distribution within the solder matrix in corresponding models.

The distribution of residual stress obtained by modelling can then be mapped in corresponding models to introduce the initial stress for the followed modelling on the fracture behaviour of solder joints. Since the crack normally propagates within the solder joint excluding the Cu substrate [267-269], the failure of the bulk solder and the Cu_6Sn_5 and Cu_3Sn layers was enabled in the modelling for further investigation on the effect of residual stress on the fracture behaviour of solder joints. The constraints and boundary conditions in the fracture modelling are the same as those illustrated in Fig. 7.4.

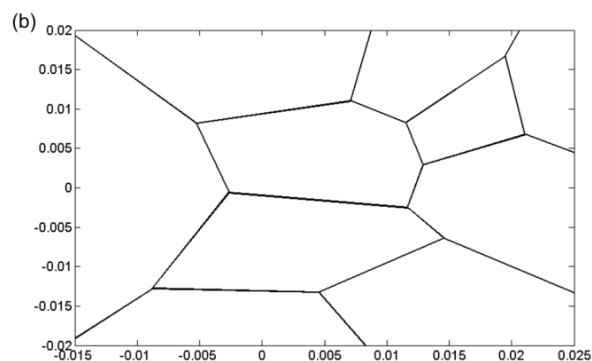
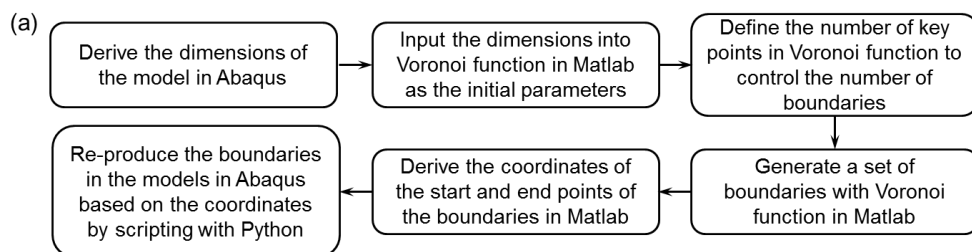
7.2.4 Finite element models with grain boundaries

The microstructure within solder joints includes various factors, such as grain boundaries, IMC particles and voids. The effect of microstructure on the fracture of solder joints becomes dominant when the interfacial IMC layers grow excessively thick. It was reported that the solder joint normally fractures intergranularly within interfacial Cu_6Sn_5 and Cu_3Sn layers after long-term storage at elevated temperature, not within the solder matrix [3, 24, 270]. Therefore, it is reasonable to assume that the adhesion strength of the grain boundaries within interfacial IMC layers degrades significantly with prolonged aging, even lower than the fracture strength of the bulk solder joint after long-term aging. The Kirkendall voids near the Cu_3Sn/Cu interface [224, 271, 272] can also be regarded as the deterioration of the adhesion of the boundaries. Hence, for simplicity, only the grain

boundaries were introduced in the models for the simulation on the microstructural effect on the fracture behaviour of solder joint.

The distribution of grain boundaries in materials generally follows these rules: (1) the true angles between grain boundaries at three-grain junctions are close to 120 degrees [273]; (2) the distribution of grain boundaries is arbitrary. Hence, the grain boundaries generated in the finite element models should also comply with these rules.

However, there is still no such available feature in Abaqus to enable the generation of grain boundaries in the finite element models. Therefore, Matlab was employed for creating arbitrary grain boundaries in this work. In Matlab, the incorporated Voronoi diagram function can segregate the given space into a set of random regions around a set of key points. The size of the segregated space can be controlled by the number of key points set in input parameters. Fig. 7.8 a) shows the procedures for generating grain boundaries in finite element model. From the built models of solder joints in Abaqus, the dimensions of the model were derived for the followed computation with Matlab, which is the first step in Fig. 7.8 a). With the dimensions of the finite element model, the limits in the computation with Matlab were also determined, so that the grain boundaries can be generated with the Voronoi diagram function as illustrate in Fig. 7.8 b). The randomness of the produced features was ensured by the Voronoi function. As such, the coordinates of the start points and end points of the generated boundaries in Matlab can be used to re-draw the grain boundaries in the models of solder joints in Abaqus by scripting with Python. Fig. 7.8 c) and d) shows the model of solder matrix without and with grain boundaries in Abaqus. It is found that the generated grain boundaries within solder matrix in Fig. 7.8 d) generally comply with the observed rules in real grain boundaries [274]. The width of the grain boundaries were set as $0.2 \mu\text{m}$ to ensure both the narrow width of the grain boundaries and the reasonable size of the meshes within it.



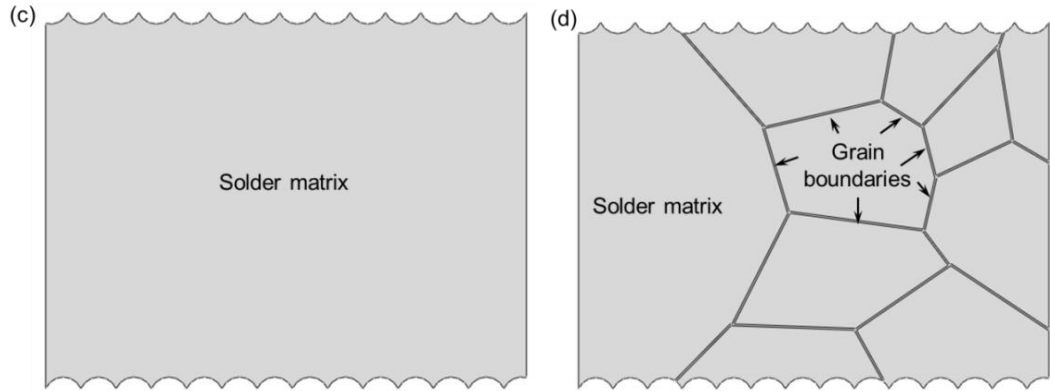


Fig. 7.8 Generated grain boundaries in finite element models: (a) general procedures for producing the grain boundaries; (b) the Voronoi diagram generated in Matlab; (c) the original finite element model of solder matrix before introducing grain boundaries; (d) the finite element model with grain boundaries.

The procedures illustrated in Fig. 7.8 a) were then repeated in the models of the solder joint with thin and thick interfacial IMC layers. Fig. 7.9 a) and b) show the obtained geometries of the finite element models for the study on the effect of microstructure on crack propagation under tension. Before aging, the solder matrix consisted of several big grains [275] while there was only one or two grains along the thickness direction in the interfacial Cu_6Sn_5 layer [276]. After aging for 1006.5 hours, the bulk solder was consumed during the growth of interfacial Cu_6Sn_5 and Cu_3Sn layers, leaving a small proportion of solder matrix in the solder joint. Hence, the number of grains in the solder matrix along the thickness direction decreased to one or two after prolonged aging. In contrast, the number of grains in interfacial Cu_6Sn_5 layer increased slightly with the expansion of the size of existing grains [277]. The number of Cu_3Sn grains at the solder/pad interface raised significantly due to the dramatic thickening during prolonged aging [278].

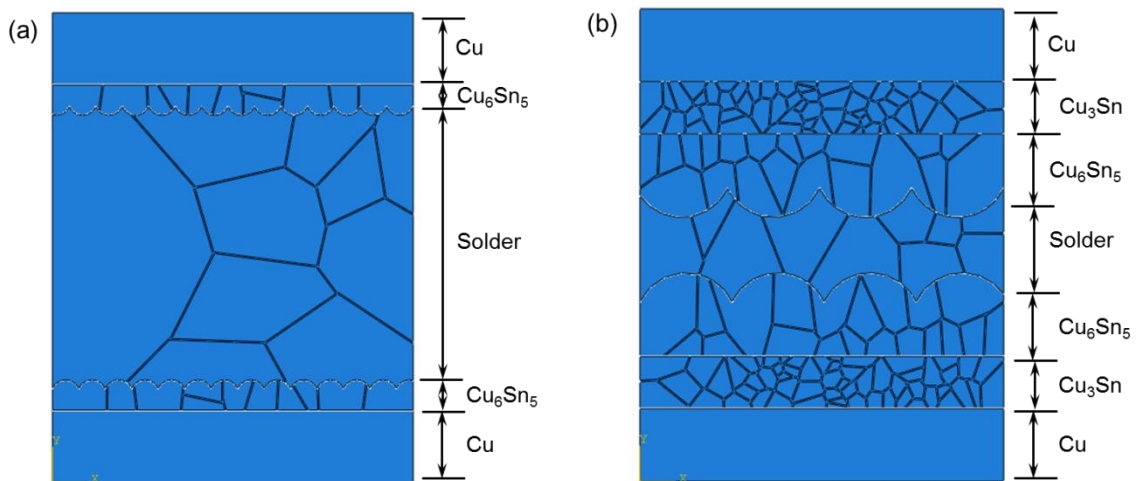


Fig. 7.9 The finite element models incorporated with grain boundaries: (a) the model of solder joint before aging and (b) after aging for 1006.5 hours.

In order to simulate the effect of the grain boundaries on the fracture behaviour of solder joint, the bottom Cu parts in the models in Fig. 7.9 were fixed along X and Y directions, and the top Cu parts were moved upwards 10 μm , which is similar to the boundary conditions illustrated in Fig. 7.4.

7.2.5 Finite element models with both residual stress and microstructure

The distribution of residual stress obtained in Fig. 7.7 in section 7.2.3 was then incorporated in the models of solder joint with microstructures in Fig. 7.9 in section 7.2.4 to be the initial load in the modelling. In such case, the combined effects of the residual stress and microstructure on the tensile fracture behaviour of solder joints can be investigated. The models with combined residual stress and grain boundaries are illustrated in Fig. 7.10. However, when the fracture criterions were introduced into the model, it was found that the residual stress at the $\text{Cu}_3\text{Sn}/\text{Cu}$ interfaces exceeded the fracture strength of the Cu_3Sn grain boundaries, which cannot be processed in the Abaqus explicit module. This also implies that the crack within solder joint could probably be initiated during the aging before mechanical tests.

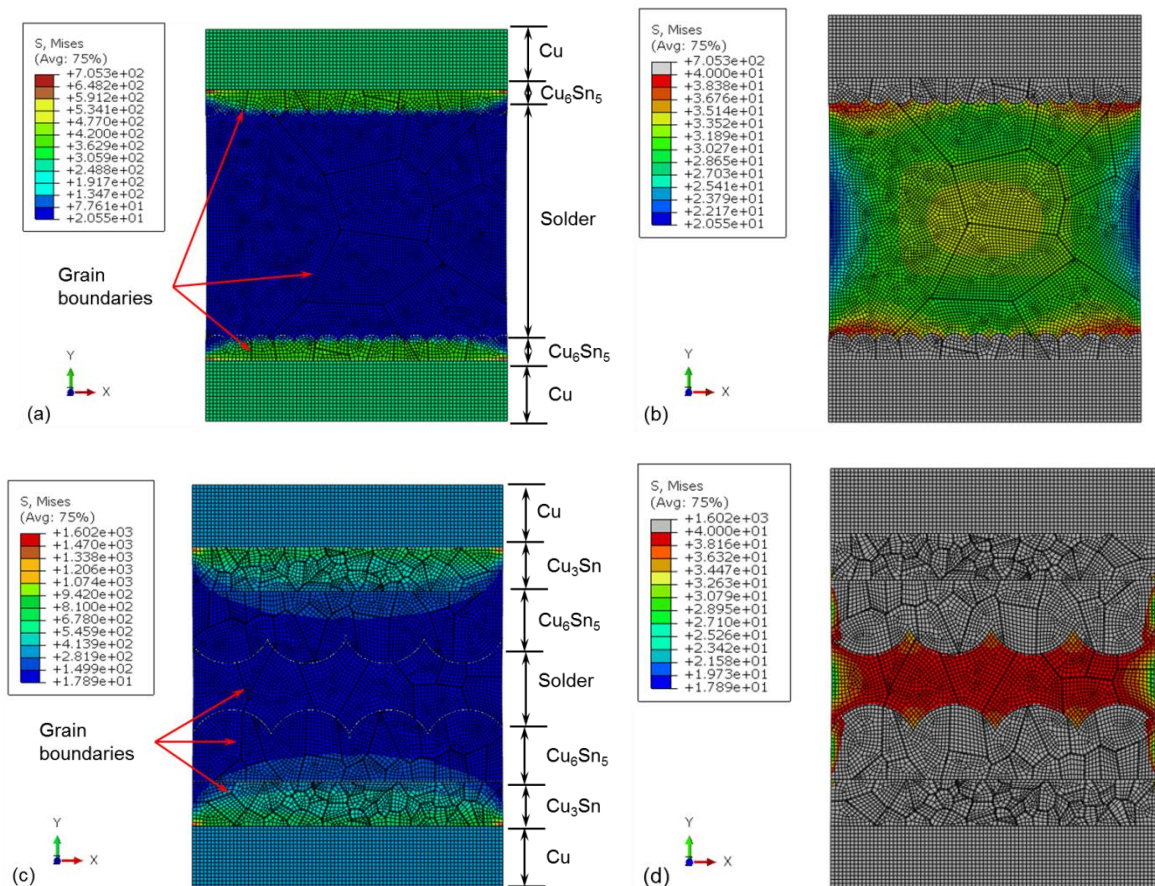


Fig. 7.10 The model of solder joint (a) before aging and (c) after aging with combined residual stress and grain boundaries; (b) and (d) illustrates the detailed stress distribution within the bulk solder.

Consequently, the settings for the modelling on the build-up of residual stress within solder joints in section 7.2.3 were incorporated within the fracture simulation of models with grain

boundaries. Hence, the residual stress within the solder joint can be generated during the modelling with grain boundaries, followed by the fracture modelling. The procedures of the modelling are illustrated in Fig. 7.11.

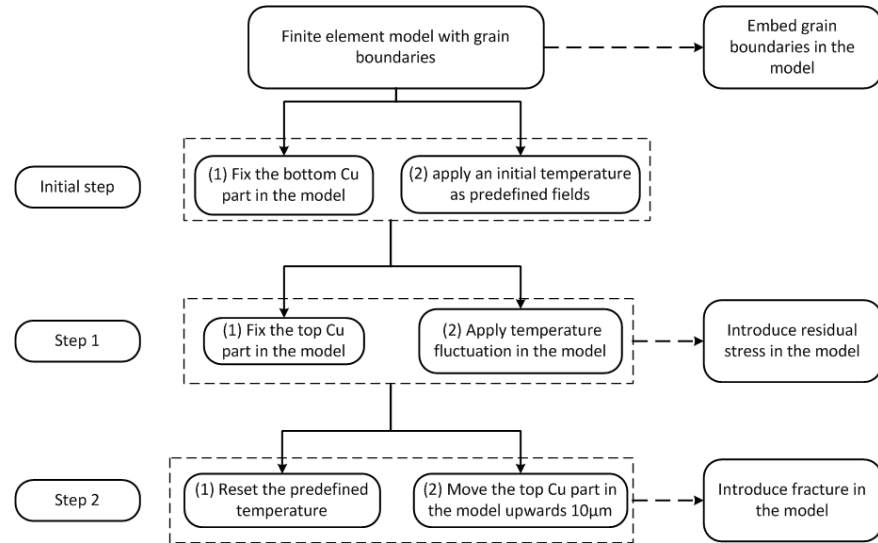


Fig. 7.11 The steps in the modelling for investigating the combined effects of residual stress and grain boundaries on the fracture behaviour of solder joints.

In the calculation of the distribution of residual stress in section 7.2.3, the involved factors, such as thermal expansion, volume shrinkage induced by the growth of interfacial IMC layers and the creep/stress relaxation in the solder and Cu, were all accounted for the build-up of residual stress in the solder joints. However, the simulation on the failure of interfacial IMC layers requires the explicit module in Abaqus, which ruled out the volume shrinkage and creep/stress relaxation. Hence, only thermal expansion of different parts in the solder joint was accounted for the build-up of residual stress in solder joint in this set of simulation.

7.3 Major parameters and settings in the simulations

7.3.1 Fracture parameters of bulk solder

In mechanical tests, the deformation within bulk solder can be generally divided into three stages: elastic deformation, plastic deformation and the failure. The elastic deformation of bulk solder under tension can be described by the Young's modulus and Poisson's ratio,

The plastic deformation of bulk solder is defined based on true stress-strain curve in Abaqus [279]. However, normally, only nominal stress-strain curves can be exported from the tensile test results of bulk solder, which needs to be converted to true stress-strain curve for the modelling. The conversion from nominal stress-strain curve to true stress-strain curve is given as [279, 280]

$$\begin{aligned}\varepsilon &= \ln(1 + \varepsilon_{nom}) \\ \sigma &= \sigma_{nom}(1 + \varepsilon_{nom})\end{aligned}\quad (7.1)$$

where ε and σ are the true strain and stress, and ε_{nom} and σ_{nom} are the nominal strain and stress, which are also engineering strain and stress.

Fig. 7.12 a) illustrates an example of a nominal tensile stress-strain curve of a lead-free solder

[233]. The true stress-strain curve of the solder was derived by equation (7.1), and the result is illustrated in Fig. 7.12 b). From the true stress-strain curve at the strain rate of 0.01, the fracture stress and fracture strain of the solder are 40 MPa and 0.08, respectively.

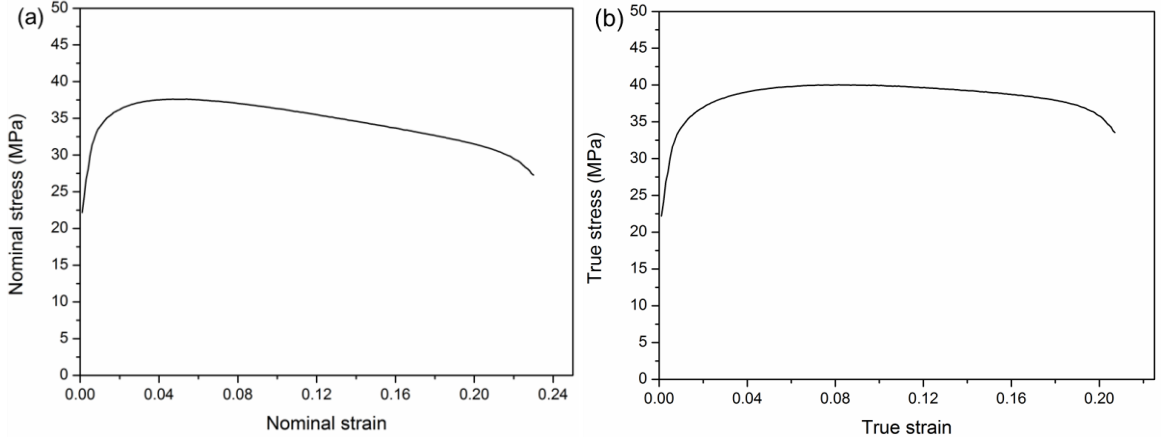


Fig. 7.12 (a) nominal stress-strain curve [233] and (b) the derived true stress-strain curve of lead-free solder at the strain rate of 0.01.

Once the plastic deformation exceeds the deformation limits, the fracture of solder occurs. The fracture mechanism of the solder joint is often found to be ductile fracture in solder joints [35, 281], which is induced by the nucleation, growth and coalescence of voids. In Abaqus, the ductile damage module was employed for the simulation. the initiation of ductile damage was evaluated by equivalent plastic strain, $\bar{\varepsilon}_D^{pl}$, which is a function of stress triaxiality and strain rate, $\bar{\varepsilon}_D^{pl}(\eta, \dot{\varepsilon}^{pl})$ [279]

$$\omega_D = \int \frac{d\bar{\varepsilon}^{pl}}{\bar{\varepsilon}_D^{pl}(\eta, \dot{\varepsilon}^{pl})} \quad (7.2)$$

where η is the stress triaxiality and $\dot{\varepsilon}^{pl}$ is the strain rate. For uniaxial tension, $\dot{\varepsilon}^{pl}$ is the same as the tension strain rate, $\dot{\varepsilon}_t^{pl} = \dot{\varepsilon}_{11}^{pl}$. The onset of the damage is set as $\omega_D = 1$. The stress triaxiality η is defined as $\eta = p/q$ [279], where p is the pressure stress, q is the Mises equivalent stress. For uniaxial tension test, $\eta=1/3$.

After the initiation of crack, the propagation of the crack is defined by damage evolution in Abaqus. The damage evolution is defined by evolution equation[279]

$$\dot{\bar{u}}^{pl} = L\dot{\varepsilon}^{pl} \quad (7.3)$$

where \bar{u}^{pl} is the effective plastic displacement after the initiation of crack; L is the characteristic length of the mesh, and $\dot{\varepsilon}^{pl}$ is the strain after damage.

The definition of the characteristic length, L , depends on the element geometry and formulation. It is a typical length of a line across an element for a first-order element and it is half of the same typical length for a second-order element [279]. The element size of the model in this work was approximately 0.6 μm , and the increase of strain after damage was $\dot{\varepsilon}^{pl}=0.12$. Therefore, the effective plastic displacement of the mesh in this work can be calculated: $\bar{u}^{pl}=0.072 \mu\text{m}$.

After the crack initiation, the development of the damage can be defined as relative plastic displacement in linear or exponential form [279]. For simplicity, the degradation behaviour of the solder joint after crack initiation was defined as linear in this work. Therefore, the parameters for the

crack initiation and propagation in the solder are listed in Table 7.3.

In order to investigate the effect of grain boundaries on the mechanical integrity of solder joints, the parameters for the fracture behaviour of grain boundaries should also be defined. However, when the solder joint failed from the bulk solder, the crack seldom propagates along the grain boundaries [282], which indicates the strength of the grain boundaries is comparable to the strength within the grains. Therefore, in this work, the fracture strain and damage evolution criterion of grain boundaries were assumed to be 80% of the solder grains due to the lack of data about the fracture of grain boundaries in solder.

Table 7.3 Parameters for the fracture of bulk solder in solder joints.

	Damage initiation			Damage evolution (linear)
	Fracture strain	Stress triaxiality	Strain rate	
Solder	0.08	0.333333	0.01	7.2e-5 mm
Solder grain boundaries	0.064	0.333333	0.01	5.76e-5 mm

7.3.2 Fracture parameters of Cu_6Sn_5 and Cu_3Sn

The fracture of interfacial Cu_6Sn_5 and Cu_3Sn layers is frequently reported to be brittle failure. The cantilever bending tests on the micro Cu_6Sn_5 pillars and Cu_3Sn pillars in chapter 4 also confirmed the brittle fracture of the micro pillars. Therefore, in the modelling, the mechanical response of the interfacial Cu_6Sn_5 and Cu_3Sn layers consisted of two parts: the elastic deformation in the beginning of the loading and the brittle failure once the load exceeded the limit.

The elastic deformation of the interfacial Cu_6Sn_5 and Cu_3Sn layers can be simulated based on the Young's modulus and Poisson's ratio of the corresponding IMCs in modelling. The followed brittle fracture of the IMCs was simulated by the brittle cracking feature in Abaqus. The brittle cracking model in Abaqus is designed for modelling the fracture behaviour of concrete, but it can also be employed for the modelling on other materials, such as ceramics and brittle rocks. This feature is applicable in the modelling on the failure of Cu_6Sn_5 and Cu_3Sn as the fracture of the IMC layers is also dominated by tensile cracking [279].

The brittle cracking model in Abaqus includes two steps: the detection of the crack and the post-failure stress-strain relation. The criterion used for crack detection in Abaqus is the Rankine criterion, which states that a crack forms when the maximum principal tensile stress exceeds the tensile strength of the brittle material [279]. Based on the experimental results in chapter 4, the fracture strengths of Cu_6Sn_5 and Cu_3Sn are 1.3 GPa and 2.34 GPa, respectively.

After the cracks emerge within the model, the post-failure behaviour was defined by post-failure stress-strain curves, so that the development of the crack can be simulated. From the load-displacement curves of the micro Cu_6Sn_5 and Cu_3Sn pillars in chapter 4, the increase in the strain can be assumed to 0.001 with linear degradation, as illustrated in Fig. 7.13. So, the instability of the model can also be minimized.

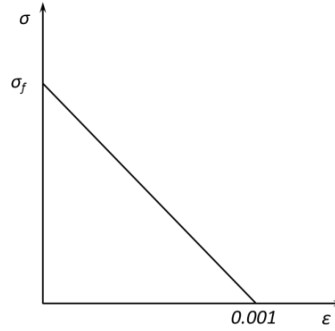


Fig. 7.13 The post-failure behaviour of interfacial Cu_6Sn_5 and Cu_3Sn .

An important feature of the brittle cracking model is that, whereas crack initiation is based on Mode I fracture only, post-crack behaviour includes Mode II as well as Mode I. The Mode II shear behaviour is based on the common observation that the shear behaviour depends on the amount of crack opening. More specifically, the cracked shear modulus is reduced as the crack opens. However, when the brittle cracking was modelled with implicit module in Abaqus, the built model cannot converge even after running continuously for one week. Therefore, Abaqus/Explicit was utilised in this study. And it offers a shear retention model in which the post-crack shear stiffness is defined as a function of the opening strain across the crack; the shear retention model must be defined in the cracking model, and zero shear retention should not be used [279]. The shear retention is defined as:

$$\rho(e_{nn}^{ck}) = \left(1 - \frac{e_{nn}^{ck}}{e_{max}^{ck}}\right)^p \quad (7.4)$$

where p defines the form of the shear retention model; e_{nn}^{ck} is the crack opening strain. Fig. 7.14 presents some typical examples of the ρ - e_{nn}^{ck} correlation [279].

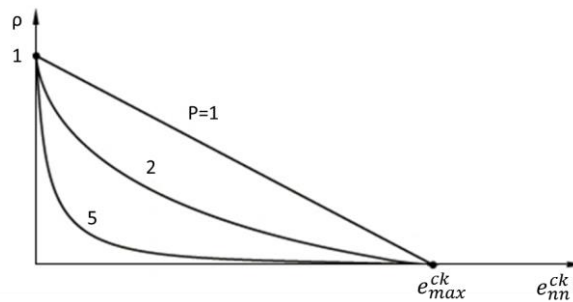


Fig. 7.14 Power law form of the shear retention model [279].

For simplicity, a linear shear retention model is defined in this work. The parameters of the brittle cracking of interfacial Cu_6Sn_5 and Cu_3Sn layers in the modelling are listed in Table 7.4. Due to the lack of data about crack opening strain of Cu_6Sn_5 and Cu_3Sn , the opening strain was set to be 0.001 for both these two IMCs. As far as the author is aware, the fracture strengths of the Cu_6Sn_5 and Cu_3Sn grain boundaries were seldom reported. But, for solder joint with thick interfacial IMC layer after prolonged aging, the solder joint failed preferentially from the grain boundaries within interfacial IMC layers [281, 283], which indicates that the bulk solder is stronger than the grain

boundaries in the thick interfacial IMC layer after aging. Therefore, it is reasonable to assume that the adhesion strength between the Cu_6Sn_5 and Cu_3Sn grains is lower than the fracture strength of the solder matrix. Therefore, in this work, the fracture criterions of Cu_6Sn_5 and Cu_3Sn grain boundaries were assumed to be 0.03 of the corresponding IMC, which is lower than the fracture strength of the bulk solder.

Table 7.4 Brittle cracking of Cu_6Sn_5 and Cu_3Sn .

	Brittle cracking		Brittle shear (power law)	
	Direct stress after cracking	Direct cracking strain	e	p
Cu_6Sn_5	1300	0	1e-3	1
	0	0.001		
Grain boundaries in Cu_6Sn_5	39	0	3e-5	1
	0	3e-5		
Cu_3Sn	2340	0	1e-3	1
	0	1e-3		
Grain boundaries in Cu_3Sn	70.2	0	3e-5	1
	0	3e-5		

7.3.3 Other settings and parameters

Table 7.5 listed other major parameters involved in the modelling. The plastic deformation behaviours of solder and Cu substrate were modelled by true stress-strain curves that were converted from the reported nominal stress-strain curves in literatures. The listed densities of all the involved materials in the model were for the explicit modelling on the fracture behaviour of interfacial IMC layers.

Table 7.5 Settings and parameters for the major mechanical properties of the involved materials in modelling.

	Young's modulus	Poisson's Ratio	Density	Plasticity
Solder	46.9 GPa [195]	0.36[16]	7.4 g/cm ³ [16]	[233]
Grain boundaries in solder	46.9 GPa	0.36	7.4 g/cm ³	[233]
Cu_6Sn_5	112.3 GPa [195]	0.309[16]	8.28 g/cm ³ [16]	-
Grain boundaries in Cu_6Sn_5 layer	112.3 GPa	0.309	8.28 g/cm ³	-
Cu_3Sn	134.2 GPa [195]	0.299[16]	8.90 g/cm ³ [16]	-
Grain boundaries in Cu_3Sn layer	134.2 GPa	0.299	8.90 g/cm ³	-
Cu	116.5 GPa [195]	0.339[16]	8.94 g/cm ³ [16]	[284]

7.4 Modelling results

7.4.1 Crack initiation and propagation in original models

As illustrated in Fig. 7.3, the original models of solder joint were built with two types of interfacial IMC layers with different thicknesses and morphologies. No residual stress or grain boundaries were introduced in these models. So that, the influence of the thickness of interfacial IMC layers on the fracture behaviour of solder joints can be revealed. Furthermore, the crack initiation and propagation within the original model can serve as the reference to the followed modelling with stress and grain boundaries.

Therefore, the crack propagation paths within the original models are illustrated in Fig. 7.15. In solder joints before aging, the crack initiated from the two corners of the solder/ Cu_6Sn_5 interfaces and propagated across the entire solder matrix, which agrees quite well with the reported crack propagation path in reference [261]. This is possibly due to the notable variation between the mechanical properties of the bulk solder and the properties of Cu_6Sn_5 layer. Severe stress concentration can occur at the corner of the heterogeneous interfaces, particularly the corners, which can easily exceed the fracture strength of bulk solder in tension. Therefore, the model with thin interfacial Cu_6Sn_5 layer failed across the bulk solder.

In the finite element models of solder joints with thick IMC layers in Fig. 7.15 b), the solder joint generally fractured through the solder matrix with significant amount of Cu_6Sn_5 scallops exposed at the two ends of the fracture path. The limited amount of solder matrix between the two thick interfacial Cu_6Sn_5 layers led to the lack of adjustment to the induced stress within solder matrix during loading and thus more serious stress concentration along the solder/ Cu_6Sn_5 interface. Hence, the solder joint fractured along a mixture of solder/ Cu_6Sn_5 interface and solder matrix. However, for the solder joints with such thick IMC layer in experiments, the solder joint primarily fractured from the IMC layers [261], which the modelling result does not comply with.

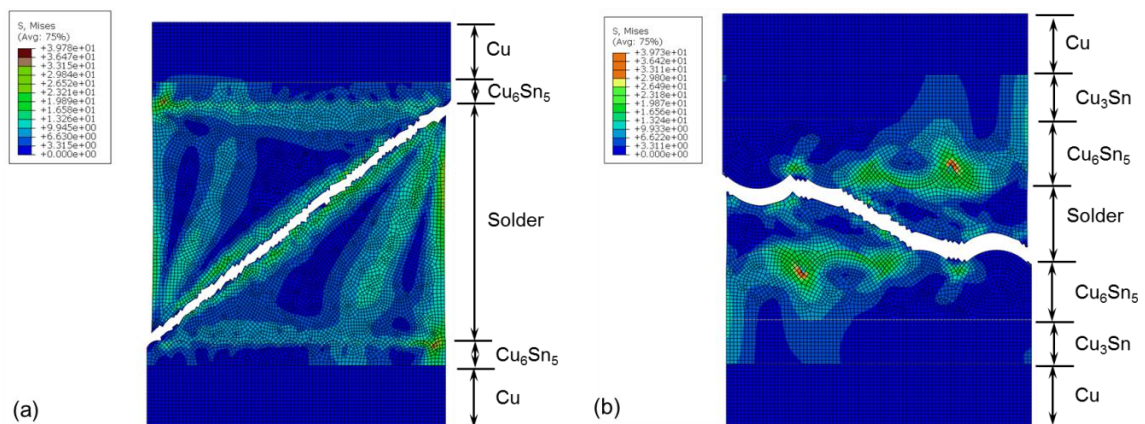


Fig. 7.15 Crack propagation within the original models of Cu/solder/Cu solder joints (a) with thin interfacial IMC layer and (b) with thick interfacial IMC layers.

7.4.2 Effect of residual stress on the fracture behaviour

In order to investigate the effect of residual stress on the fracture behaviour of solder joints, the obtained stress distribution in section 7.2.3 was introduced in the modelling on the fracture behaviour of solder joint as an initial stress load. Therefore, the crack propagation path in the

modelling results can reveal the effects of residual stress on the fracture of solder joints.

Fig. 7.16 depicts the modelling results on the crack propagation in pre-stressed Sn99Cu1 solder joints with thin interfacial IMC layer. Fig. 7.16 a) illustrates the stress concentration sites near the solder/ Cu_6Sn_5 interface in the solder matrix after introducing the residual stress. Because the stress at these two regions was close to the fracture stress of bulk solder, the crack initiated at both these two sites simultaneously. The emergence of the cracks can then alter the distribution of residual stress within the solder joints, as illustrated in Fig. 7.16 b). The stress within the band connecting the two crack initiation sites rose significantly. As the tension proceeded, the two cracks merged, leading to the fracture of the solder joint (Fig. 7.16 c)). After the failure within the bulk solder, the stress within the solder matrix dropped dramatically.

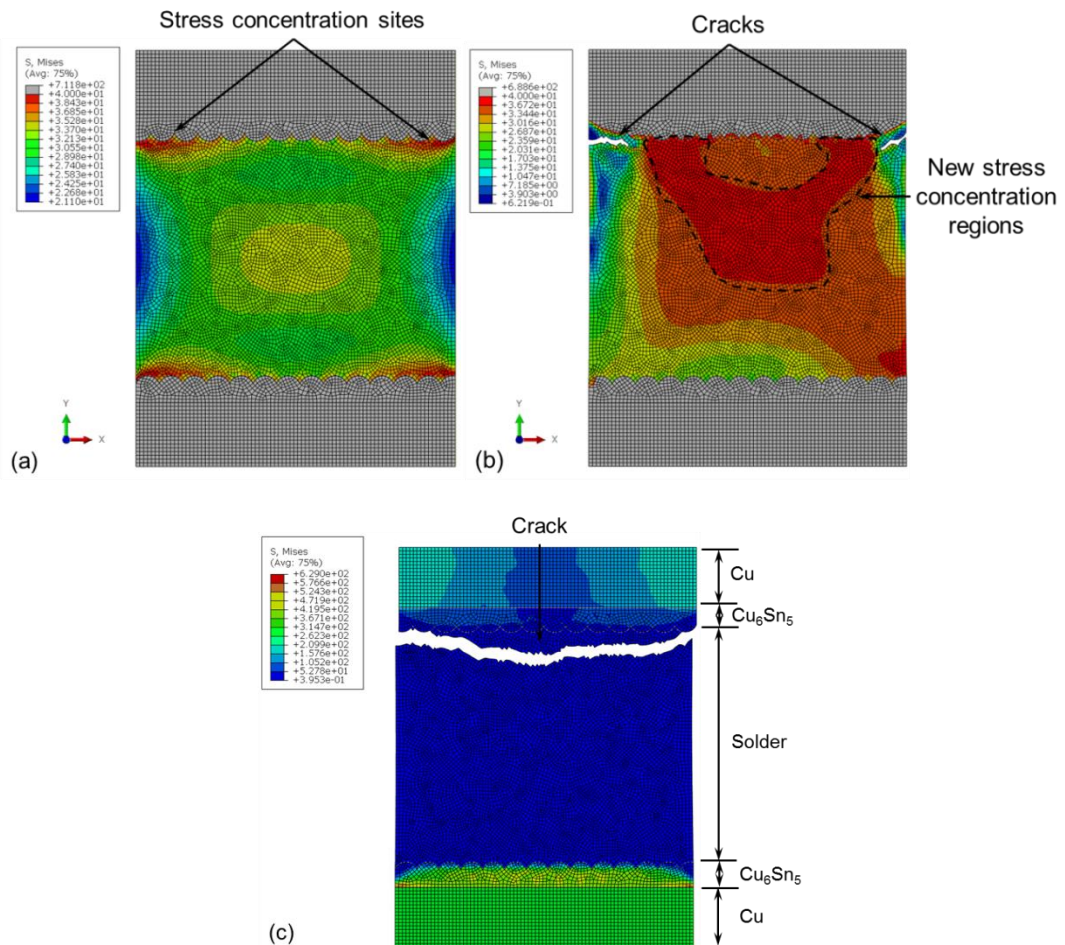


Fig. 7.16 Effect of residual stress on the crack initiation and propagation in solder joints with thin interfacial IMC layer: (a) the distribution of residual stress in solder matrix before tension; (b) the initiation of cracks within the solder joint in the beginning of tension; (c) the failure of the solder joints after tension.

The illustrated crack propagation path significantly differs from the fracture in the stress-free model of solder joint with thin IMC layer in Fig. 7.15 a). This can be attributed to the concentration of residual stress at the corners of solder/ Cu_6Sn_5 interfaces where the crack initiated. This notable difference in crack propagation path was evidently resulted by the residual stress within the model,

since the stress distribution was the only difference in these two models.

Fig. 7.17 demonstrates the crack propagation path in the stressed solder joints with thick interfacial IMC layers. Before the tension, the residual stress distributed homogeneously within the majority of the solder matrix with an average value of 40 MPa, as illustrated in Fig. 7.17 a). When the tension displacement was applied, the crack initiated along the solder/ Cu_6Sn_5 interface where the solder matrix was seriously strained due to the different mechanical properties between solder and Cu_6Sn_5 layer. The overall stress distribution within the solder joint after failure is shown in Fig. 7.17 b).

It is notable that the fracture path within the stressed solder joint with thick IMC layer is similar to that in the stress-free solder joint in Fig. 7.15 b), which can be ascribed to similar stress distribution during tension. It is obvious that the residual stress within the solder matrix distributed evenly before the beginning of the tension in the stressed model. For the stress-free model, a similarly homogeneous distribution of stress can also be resulted from the applied tension load in the beginning of the tension due to the limited amount of the bulk solder. Hence, the crack propagated along a similar path within the pre-stressed and stress-free models.

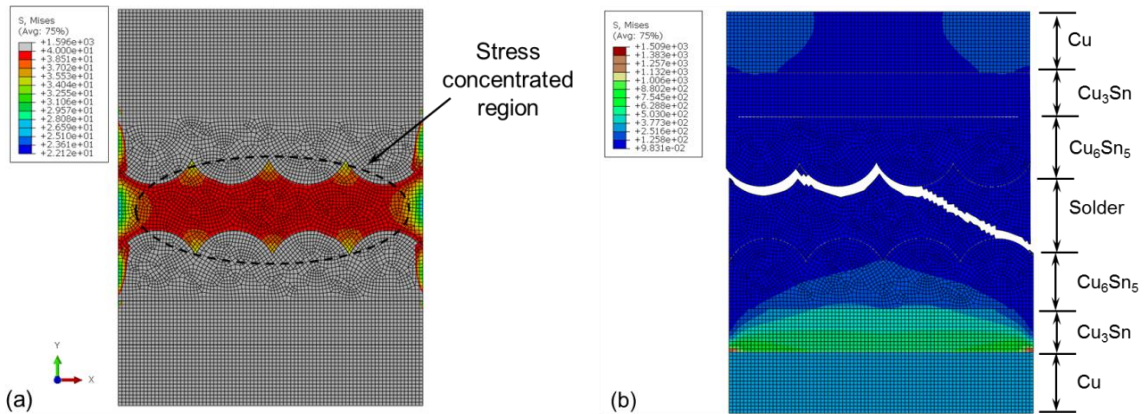


Fig. 7.17 The crack propagation path in the stressed Sn99Cu1/Cu solder joint with thick interfacial IMC layers: (a) the stress distribution within the solder matrix before tension; (b) the failure of the solder joint after tension.

7.4.3 Effect of microstructure on the fracture behaviour

Fig. 7.9 in section 7.2.4 illustrates the finite element models with the grain boundaries. The effects of microstructure on the fracture behaviour of solder joints were then investigated by applying the displacement on the upper Cu part in the model with the bottom Cu fixed.

The fracture path within the model with grain boundaries is illustrated in Fig. 7.18 a). It is shown that the crack propagated diagonally through the bulk solder, which is generally similar to the fracture in stress-free model in Fig. 7.15 a). However, it is also notable that the crack developed along the solder grain boundaries during the course of propagation due to the lower fracture strength. This is consistent with the experimental observation that the solder joint failed along the grain boundaries when heterogeneous particles congregated along the grain boundaries within solder matrix [32, 285].

For the model with grain boundaries and thick interfacial IMC layers, the crack propagation

path in Fig. 7.18 b) is quite similar to the fracture in the model without grain boundaries in Fig. 7.15 b). This could be ascribed to the limited number of grain boundaries along the potential fracture propagation path within the solder matrix in tension. As the discussion presented earlier, the stress within solder matrix can easily exceed the fracture strength of the bulk solder during tension because of the limited amount of solder in the middle. During the propagation of the crack in solder matrix, the solder joint fractured through the solder grains as the grain boundaries are generally orthogonal to the crack propagation path.

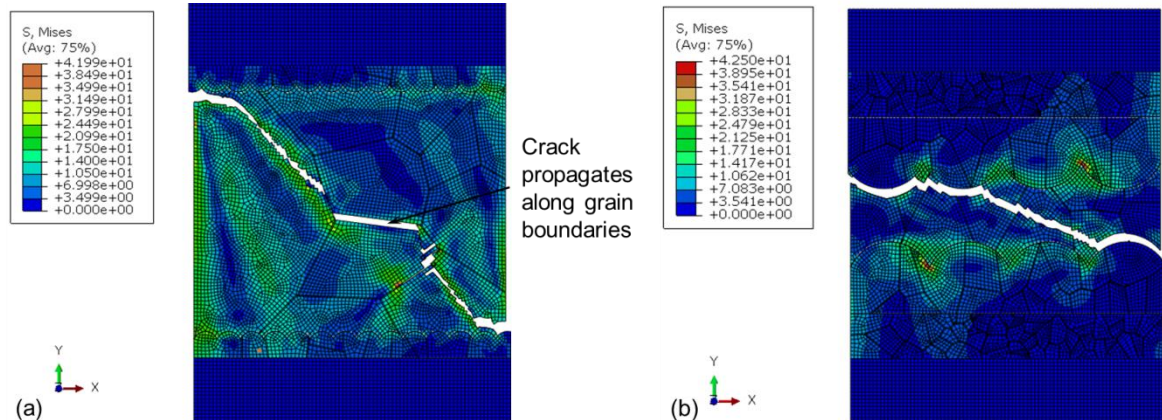


Fig. 7.18 Crack propagation path within the models for the solder joint (a) with thin and (b) thick interfacial IMC layers.

7.4.4 The combined effect of microstructure and residual stress

In actual solder joints, the growth of interfacial IMC layers is intrinsically accompanied by the residual stress and microstructural evolution. Therefore, the effect of residual stress and grain boundaries was incorporated in one model to simulate the combined effects of these two on the fracture behaviour of solder joints.

The modelling results are illustrated in Fig. 7.19. It can be observed that due to the concentrated residual stress at the corners of the solder/ Cu_6Sn_5 interface, the crack in the model of solder joints with thin IMC layer initiated from the two corners, as illustrated in Fig. 7.19 a). During the course of crack propagation, the grain boundaries of solder joint facilitated the development of cracks, so the fracture path within the bulk solder was slightly altered in comparison to the modelling results in Fig. 7.16.

In comparison to the fracture path in Fig. 7.15 a), Fig. 7.16 c) and Fig. 7.18 a), it can be found that the fracture path within the model with combined stress and grain boundaries was altered by both the stress and grain boundaries. The stress concentration at the two corners of the solder/ Cu_6Sn_5 interface served as the crack initiation sites, while the grain boundaries in bulk solder slightly modified the development of the crack.

Fig. 7.19 b) illustrates the cracks within the model of solder joints with thick interfacial IMC layers. It is clear that the cracks initiated and propagated within the interfacial Cu_6Sn_5 and Cu_3Sn layers, while the solder matrix remained intact. However, the modelling results in the original model in Fig. 7.15 b), the stressed model in Fig. 7.17 b) and the model with grain boundaries in Fig. 7.18

b) show that the solder joint fractured from the bulk solder when it is under tension. The comparison indicates that neither the residual stress nor the grain boundaries can initiate the crack within the interfacial IMC layers individually. The observed fracture within the interfacial IMC layers in literatures [286, 287] is probably due to the combined contribution from both the residual stress and the low adhesion strength of grain boundaries.

The distribution of the residual stress in Fig. 7.7 reveals that the residual stress rose significantly at the heterogeneous interfaces, such as Cu/Cu_3Sn and $Cu_6Sn_5/solder$ interfaces, in the aging and cooling. During the increase in the residual stress within interfacial IMC layers, crack can be initiated at the grain boundaries within the Cu_3Sn and Cu_6Sn_5 layers once the residual stress exceeded the fracture strength of IMC layers. Consequently, the crack can propagate within the interfacial IMC layers due to the low resistance to crack propagation within IMCs [138].

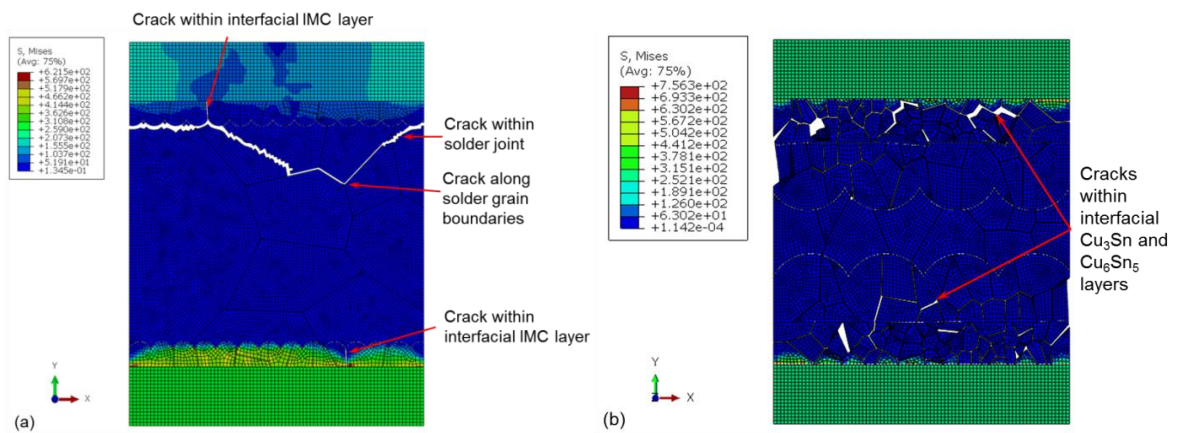


Fig. 7.19 The crack initiation and propagation in the models of solder joint with both residual stress and grain boundaries: (a) the model of solder joint with thin interfacial IMC layer; (b) the model with thick IMC layer.

7.5 Discussions

The fracture paths in different finite element models in section 7.4 are summarized in Table 7.6 with the comparison to experimental works in literatures. From the modelling results, the crack initiated and propagated only in the bulk solder in all the studied models for solder joints with thin interfacial IMC layer, despite the various loads applied in the model.

Furthermore, it was also demonstrated that the stress concentration region within solder matrix can serve as the crack initiation sites within solder matrix. And, the induced grain boundaries within solder matrix can facilitate the propagation of cracks, altering the crack propagation path in solder joints. The modelling results are generally consistent with the experimental observation that cracks normally develop within bulk solder in solder joints with thin IMC layer.

However, the stress-free models of solder joints with thick interfacial IMC layers failed from both the solder/ Cu_6Sn_5 interface and the solder matrix. The difference in the fracture paths of the two original models indicates that the thickness and morphology of interfacial IMC layers can alter the crack propagation path significantly.

For the model with both residual stress and microstructural factors, the crack propagation path in the model with thick interfacial IMC layers agrees well with the experimental observation. The comparison of fracture paths from the models of solder joints after aging in Table 7.6 implies that the observed fracture within interfacial IMC layers in experiments should be ascribed to the combined contribution of the residual stress and the weakness of grain boundaries. The sole influence of residual stress or microstructural defect cannot initiate the cracks within interfacial IMC layers.

Table 7.6 Summary of the fracture path in different finite element models and the comparison with experimental observation

	Before aging	After aging
Original models	Bulk solder	Solder/ Cu_6Sn_5 interface+ Bulk solder
Model with residual stress	Bulk solder	Solder/ Cu_6Sn_5 interface+ Bulk solder
Model with grain boundaries	Bulk solder	Solder/ Cu_6Sn_5 interface+ Bulk solder
Model with combined stress and grain boundaries	Bulk solder	Interfacial Cu_6Sn_5 , Cu_3Sn layers
Experimental observation	Bulk solder [175, 261, 262]	Interfacial Cu_6Sn_5 , Cu_3Sn layers [175, 261, 262]

In a real solder joint, the residual stress could be induced during the thermal experience, such as reflowing and aging, due to the incompatible CTEs in different parts in solder joints. The volume shrinkage induced by the growth of interfacial IMC layers in aging can also contribute significantly to the increase in the stress within interfacial IMC layers. Though the residual stress could be compensated by the creep/stress relaxation in the bulk solder and Cu, the stress could remain high within interfacial Cu_6Sn_5 and Cu_3Sn layers. For the solder joint with thin interfacial IMC layer under tension, the incompatible deformation between the bulk solder and interfacial IMC layers can lead to further increase in the concentrated stress at these heterogeneous interfaces. Therefore, cracks can be initiated. And the solder joint is then fractured diagonally under tension [261].

After aging, the residual stress within the solder joint increases with the growth of interfacial IMC layers due to the volume shrinkage induced by the growth of interfacial IMC layers. The adhesion strength of the grain boundaries in interfacial IMC layers could also deteriorate due to the aggregation of defects, such as voids and heterogeneous particles [288, 289]. Therefore, the residual stress that concentrates at the Cu/ Cu_3Sn interface could initiate cracks within interfacial Cu_3Sn layer even before the tensile test [290]. During the tensile test, the crack can further develop through the interfacial IMC layers, leading to brittle fracture of the solder joint.

7.6 Summary

In this chapter, the effects of microstructure, residual stress on the fracture behaviour of solder joints were investigated by modelling with progressively increased factors. From the presented modelling results and discussions, following conclusions can be reached:

1. In the model of the solder joint with thin IMC layer, the grain boundaries in the interfacial Cu_6Sn_5 layer had negligible effects on the fracture of solder joints while the solder grain boundaries can facilitate the crack propagation.
2. The thickness and morphology of interfacial IMC layers can alter the fracture path significantly, since the model with thin interfacial IMC layer fractured within solder matrix while the model with thick interfacial IMCs failed along the mixture of solder/ Cu_6Sn_5 interface and within solder matrix.
3. The residual stress normally concentrates at the heterogeneous interfaces, such as the Cu_3Sn/Cu interface and solder/ Cu_6Sn_5 interface, where the crack likely initiates.
4. The failure of interfacial IMC layers in solder joint under tension is resulted from the combined contribution of the residual stress and microstructural weakness, such as grain boundaries.

Chapter 8 Conclusions and future work

8.1 Main conclusions

Based on the presented experimental and modelling results in previous chapters, the main findings in this thesis are therefore summarized in this chapter. As each chapter is focused on individual research topics, and they are all correlated with others, the main conclusions for entire thesis can be drawn in the following sections.

8.1.1 Growth of IMCs at Sn99Cu1/Cu interface

The growth of interfacial IMC layers in both planar and perpendicular to the interdiffusion direction in Sn99Cu1/Cu solder joints was studied. During the aging at 175°C, the planar growth of interfacial Cu_6Sn_5 , Cu_3Sn layers was found to follow parabolic law with aging durations. The correlation can be expressed as $h_{IMC} = 0.27t^{1/2} + 465$, $h_{Cu_6Sn_5} = 0.16t^{1/2} + 4.1$ and $h_{Cu_3Sn} = 0.17t^{1/2}$, where t is the aging duration in hour, and h is the thickness of each IMC layer in μm .

Prior to aging, the interfacial Cu_6Sn_5 layer was identified, but the Cu_3Sn layer was not detected, which could be attributed to small amount of Cu_3Sn layer that was present, or the limited spatial resolution of the microscope and SEM utilised in the observation. After aging at 175°C for about 1006.5 hours, the thickness of both interfacial Cu_6Sn_5 and Cu_3Sn layers increased significantly, and the morphology of the IMC layer transformed from dendritic shape to layered structures after aging at 175°C for 1006.5 hours.

The growth of IMCs at the Sn99Cu1/Cu interface in perpendicular to the diffusion direction between solder and Cu was also investigated in this work. The protrusion of IMCs was found to follow parabolic law with aging duration, and it can be expressed as $y = 0.11\sqrt{t}$, where t is aging duration in *hour*, and y is the height of the perpendicular IMCs in μm .

The composition of the perpendicular IMCs was identified as Cu_3Sn at the beginning of the protrusion. During the perpendicular growth of IMCs, the composition of the IMCs at the top of the protrusion transformed from Cu_3Sn to Cu_6Sn_5 due to the decreasing concentration of Cu atoms with longer the diffusion distance in aging. It ultimately led to the double-layer structure of the protruded IMCs, with the outer Cu_6Sn_5 layer and inner Cu_3Sn . The formation sequence of these two types of IMCs was opposite to the planar growth of interfacial IMC layers within the solder joint.

Furthermore, the growth rate of the perpendicular IMCs was found to be much lower than the rate of planar growth due to longer diffusion distance. From the obtained parabolic correlations between the growth of IMCs and aging durations, it was concluded that both the planar and perpendicular growth of IMCs are diffusion-controlled processes.

8.1.2 Mechanical properties of Cu-Sn IMCs

The tensile fracture behaviours of both Cu_6Sn_5 and Cu_3Sn at the interface of Sn99Cu1/Cu solder joints were studied by cantilever bending tests on micro-pillars which were fabricated with FIB. SEM and EDX were employed to examine the micro pillars and the fracture surface of the pillar before and after the bending test. The fracture strength of the tested pillars was then estimated by finite element modelling.

When micro Cu_6Sn_5 pillars were subjected to the bending load applied by the indenter during cantilever bending tests, the pillars remained elastic before the fracture. After the test, both transgranular and intergranular fracture modes were identified according to the fracture surface of micro Cu_6Sn_5 pillars. The different fracture modes were primarily dependent on the microstructure of interfacial Cu_6Sn_5 layers and the number of grains involved at the bottom of the micro pillar. The tensile fracture strength and strain of Cu_6Sn_5 IMC were estimated to be approximately 1.3 GPa and 0.011, correspondingly. .

The micro Cu_3Sn pillars were also in elastic state until the fracture during cantilever bending test. From the fracture surface, intergranular fracture was the only failure mode in micro Cu_3Sn pillars. This could be resulted from the preferential crack propagation along the grain boundaries of the sub-micrometer Cu_3Sn grains at the bottom of the micro Cu_3Sn pillars. Based on modelling, the tensile fracture strength of Cu_3Sn were estimated to be 2.3GPa, and the corresponding fracture strain was approximately 0.017.

8.1.3 Collapse of solder joints

The collapse of solder joints induced by the growth of interfacial IMC layers after extended aging was investigated by surface profiling on specific designed specimens with white light interferometer. From the measurement, the reduction of joint height was about 1.2 μm after aging at 175°C for 1132 hours. The decrease in joint height followed parabolic law with aging durations, which can be expressed as $\Delta h = -0.031 \times \sqrt{t}$ under the experimental conditions. The dimensional change coefficient (the ratio of change in joint height / the thickness of interfacial IMC layers) based on experimental measurements was found to be $\alpha_{\text{experiment}} = -0.114$. Based on the hypothesis that the Cu_6Sn_5 and Cu_3Sn are isotropic and dense structure, the theoretical reduction of joint height induced by the growth of interfacial IMC layers under experimental conditions was evaluated to be $\Delta h_{\text{total}} = -(0.04-0.004x) \sqrt{t}$, thereby the estimated theoretical dimensional change coefficient $\alpha_{\text{ideal}} = -0.147+0.0147x$. The theoretical calculation demonstrated an excellent accordance with the experimental results.

Modelling results also showed that the stress induced by the constrained dimensional change mainly concentrated on interfacial IMC layers, which was significantly higher than that in solder and Cu. The residual stress further led to the refinement of grains in the Cu substrate near the Cu_3Sn/Cu interface.

8.1.4 Residual stress

The residual stresses within Sn99Cu1/Cu solder joints were evaluated by nanoindentation tests on the interfacial Cu_6Sn_5 and Cu_3Sn layers as well as the adjacent solder and Cu substrate with nano Vickers indenter across the solder joints. The residual stresses within the different parts of the solder joints were then measured by correlating the increase/reduction of maximum force of the nanoindentation with the projected contact areas of the indents.

The experimental results indicated that the stress states of each interlayer at the solder/Cu interface varied with the location and the compositions: (1) The Cu substrate close to the Cu_3Sn/Cu interface was under compression with the average stress of 560 MPa at both the centre and the

edge due to the aging; (2) The average compression stress within bulk solder near the solder/ Cu_6Sn_5 interface was 70 MPa and 90 MPa at the centre and edge respectively; (3) The compression stress within interfacial Cu_6Sn_5 layer also increased about 4 GPa and 3 GPa at the centre and edge respectively after aging; (4) The interfacial Cu_3Sn layer was subject to a increasing tension stress of 1.7 GPa and 0.5 GPa at the centre and edge respectively.

The comparisons of stress-time curves of adjacent two parts in the solder joints were also made. The results indicate that: (1) There was no observable correlation between the $S-t$ curves from the solder and the adjacent interfacial Cu_6Sn_5 layer; (2) The stress evolution within Cu substrate and the interfacial Cu_3Sn layer at the centre of Sn99Cu1 solder joints followed the opposite trend due to the aging, which indicates the contraction of Cu_3Sn layer during its growth was mainly constrained by the adjacent Cu; (3) The stress state of the interfacial Cu_3Sn layer at the edge was mainly governed by the confinement of the interfacial Cu_6Sn_5 layer.

During the aging, both the thermal expansion and the growth of interfacial IMC layers could cause the increase of residual stresses within solder joints, while creep/stress relaxation and the growth of Sn whiskers can release the stress. The observed growth of Sn whiskers within the solder matrix near the solder/ Cu_6Sn_5 interface confirmed that the solder matrix was under compression during aging.

8.1.5 Modelling on fracture behaviour of solder joints

The effect of both microstructure and residual stress on the fracture behaviour of solder joints was investigated by introducing the residual stress and grain boundaries in finite element models with the combination of Matlab and Python scripting in Abaqus. It is found that: (1) In the model of solder joints before aging, the grain boundaries in the interfacial Cu_6Sn_5 layer had negligible effect on the fracture of solder joints while the grain boundaries within the solder matrix can facilitate the crack propagation; (2) The thickness and morphology of interfacial IMC layers can alter the fracture path within a solder joint. In the model with thin interfacial IMC layers, the crack initiated and propagated within the solder matrix. When the interfacial IMC layers were the major part in the model, the crack initiated and propagated both within the solder matrix and along the solder/ Cu_6Sn_5 interface; (3) Due to the volume shrinkage and the mismatch of CTEs, the residual stresses normally concentrated at the interface between heterogeneous interfaces, such as the Cu_3Sn/Cu and solder/ Cu_6Sn_5 interfaces, where the crack was likely to initiate; (4) From the finite element model considering the residual stresses and defects in microstructure, the failure of interfacial IMC layers in solder joints under tension was resulted from the combined contributions from both the residual stress and microstructural weakness, such as grain boundaries.

8.2 Contribution of the work

The thesis focused on the growth of IMCs, the fracture characteristics of IMCs and its effect on the reliability of solder joints. It can contribute to the contemporary knowledge on the reliability of solder joints from following aspects:

1. The investigation on the perpendicular growth of IMCs reported a new phenomenon of the growth of IMCs, It can enhance the current understanding on the growth mechanisms of IMCs at the solder/Cu interface.
2. The fracture characteristics of Cu_6Sn_5 and Cu_3Sn in solder joints can significantly facilitate the analysis on the mechanism of the degradation in the reliability of solder joints after service or aging. Furthermore, the methodology established in the thesis, the combination of FIB and nanoindentation, is a promising and versatile approach to test micro-scale or even sub-micrometre features.
3. The experimental results on the collapse of solder joint induced by the growth of interfacial IMC layer confirmed that the growth of IMCs is accompanied by volume shrinkage. It unveils the potential effect of the growth of IMCs on the dimensions of solder joints, which could be a vital issue in the electronic devices with high standard of alignment.
4. The evolution of residual stress at the solder/Cu interface can improve the fundamental understanding of the effect of the growth of IMCs on the reliability of solder joints after aging.
5. The modelling on the fracture behaviour provides a new approach to introduce microstructural factors in the modelling on solder joints. It can also be utilised to introduce anisotropy in finite element models.

8.3 Future work

Due to the limit time and available resource during this PhD study, it is not possible to cover all the areas in certain depth and details, therefore several areas of potential future research that are worth of further investigation can be summarised as follows.

8.2.1 Growth of IMCs

1. In order to further investigate the perpendicular growth of IMCs in solder joints, FIB could be utilized to section the specimen after aging for every 100 hours, so that the morphological evolution of the protrusion of IMCs can be monitored to understand the growth mechanism of perpendicular IMCs.
2. The perpendicular growth of IMCs is probably driven by the compressive stresses existing at the solder/substrate interface induced by the growth of interfacial IMC layers. The evolution of residual stresses beneath the perpendicular IMCs can be evaluated by XRD after aging, and subsequently correlated to the perpendicular growth of IMCs.
3. Both the planar growth and the protrusion of IMCs are probably correlated with the evolution of residual stress within solder joints in aging. The relationship between them is one of the crucial factors that can deteriorate the reliability of solder joints in service. Studies on this should be conducted for better understanding of the mechanisms of the degradation of solder joints.

8.2.2 Mechanical properties of IMCs

1. The effect of grain orientations on the fracture strength of interfacial IMCs could be investigated through FIB milling in combination with EBSD mapping, and mechanical tests with nanoindentation. As such, the grain orientations of the fabricated IMC pillars can be manipulated and tested, so that the mechanical tests can provide diverse mechanical responses of IMC pillars with different crystalline direction.
2. *In-situ* nanoindentation system can be employed to monitor the deformation and fracture behaviour of micro-pillar specimens during the tests. The test and observation can enhance the current understanding of the fracture mechanism of solder joints.
3. Various types of loads can be applied in the test on fabricated pillars to understand the fracture behaviour under complex stress status, such as cycling bending and impact loads. These tests can help better reflect the reliability of solder joints under the actual service conditions.
4. Other solder alloys, such as Sn-Ni, Sn-Zn and Au-Sn solder alloys, are also extensively used in electronic devices as the solder, in which the reliability of solder joints is crucial due to the potential harsh service conditions. The mechanical properties of the produced IMCs in these systems are also essential to the understanding of reliability issues in these solder joints.
5. The methodology established in the study (the combination of FIB and nanoindentation for mechanical tests on micro-scale features) is a promising technique that can enable the mechanical tests on various micro and even sub-micrometre features, such as Cu pillar bump in 3D packaging.

8.2.3 Collapse of solder joints

1. For more precise characterization of the collapse of solder joints after aging in future, the reference surface for the measurement should be inert, so that the effect of potential oxidation in prolonged aging may be eliminated.
2. The potential effect of the collapse of solder joint on the performance of electronic devices should be investigated. Though the amount of collapse of solder joints is not very significant, this small change in dimension can possibly lead to degradation of electronic devices which require high alignment accuracy, such as optoelectronic devices.
3. The collapse of solder joints due to the growth of interfacial IMC layers for different solder joint dimensions which can lead to deviations in heights of the solder joints on the same chip should be further investigated. This could result in significant residual stress within the bonded chip, which may even lead to the crack initiation in some extreme cases.

8.2.4 Residual stress in solder joints

1. The study on the residual stress within interfacial IMC layers demonstrated that the residual stress evolves with aging durations, which potentially influence the fracture behaviour of solder joints under external load. XRD and other stress/strain measurement techniques can

be considered and employed for further investigation on the evolution of residual stress within solder joints after aging, which can provide a more reliable and accurate estimation at different layers and locations. This could therefore provide more fundamental understanding as to the transition of crack initiation and propagation path within solder joints after prolonged aging durations.

2. The observed growth of Sn whiskers within the voids close to the solder/Cu interface is an interesting phenomenon. Further investigations on its growth and the correlation with stress evolution at the solder/Cu interface may help reveal the mechanism of the growth of Sn whiskers and the stress evolution within solder joints.

8.2.5 Modelling on the fracture behaviour of solder joints

1. 3D models can be considered for the construction of complex joint structures to elaborate the influence of microstructure and residual stress on the fracture behaviour of solder joints presenting further detailed comprehension on the effects of interfacial IMCs.
2. Other microstructural factors, such as Kirkendall voids, electromigration and thermal migration, can significantly redistribute the materials and stresses within the solder joints, which ultimately degrades the mechanical reliability of solder joints. Modelling can also be considered to incorporate such reliability elements and simulate the redistribution of materials and stresses in solder joints and further to uncover the effect of interfacial IMCs on the fracture behaviour.
3. The combination of programming (such as Matlab) and modelling with FEA software (such as Abaqus) is a promising technique to introduce anisotropy in finite element analysis, in particular, the modelling on the fracture behaviour of miniaturized joints in 3D packaging where only a few grains exist in the interconnects.

References

- [1] Y. Tian, "Electrodeposition of indium bumps for ultrafine pitch interconnections," Doctor of Philosophy, Wolfson School of Mechanical and Manufacturing Engineering, Loughborough University, 2010.
- [2] J. H. L. P. Yaofeng Sun, "Digital image correlation for solder joint fatigue reliability in microelectronics packages," *Microelectronics Reliability*, vol. 48, pp. 310-318, February 2008.
- [3] H.-T. Lee, M.-H. Chen, H.-M. Jao, and T.-L. Liao, "Influence of interfacial intermetallic compound on fracture behavior of solder joints," *Materials Science and Engineering: A*, vol. 358, pp. 134-141, 2003.
- [4] X. Ma, F. Wang, Y. Qian, and F. Yoshida, "Development of Cu–Sn intermetallic compound at Pb-free solder/Cu joint interface," *Materials Letters*, vol. 57, pp. 3361-3365, 2003.
- [5] Y. W. L. C. E. Ho, S. C. Yang, C. R. Kao, "Volume effect on the soldering reaction between SnAgCu solders and Ni " in *Proceedings of International Symposium on Advanced Packaging Materials: Processes, Properties and Interfaces, 2005*, Irvine, 2005, pp. 39-44.
- [6] A. M. F. C. Gemme, G. Gagliardia, M. Gilchriesec, P. Netchaeva, L. Rossia, E. Ruscinoa, F. Vernocchia, M. Varasib, "Study of indium bumps for the ATLAS pixel detector," *Nuclear Instruments and Methods in Physics Research Section A: Accelerators, Spectrometers, Detectors and Associated Equipment*, vol. 465, pp. 200-203, June 2001.
- [7] H. Huebner, S. Penka, B. Barchmann, M. Eigner, W. Gruber, M. Nobis, *et al.*, "Microcontacts with sub-30um pitch for 3D chip-on-chip integration," *Microelectronic Engineering*, vol. 83, pp. 2155-2162, 2006.
- [8] Y. Ping-Feng, L. Yi-Shao, S.-R. Jian, and C. Jiunn, "Mechanical Properties of Cu₆Sn₅, Cu₃Sn, and Ni₃Sn₄ Intermetallic Compounds Measured by Nanoindentation," in *8th International Conference on Electronic Packaging Technology*, Shanghai, China, 2007, pp. 1-5.
- [9] L. Jiang, H. Jiang, and N. Chawla, "The Effect of Crystallographic Orientation on the Mechanical Behavior of Cu₆Sn₅ by Micropillar Compression Testing," *Journal of Electronic Materials*, vol. 41, pp. 2083-2088, 2012.
- [10] Q. K. Zhang, J. Tan, and Z. F. Zhang, "Fracture behaviors and strength of Cu₆Sn₅ intermetallic compounds by indentation testing," *Journal of Applied Physics*, vol. 110, pp. 014502-4, 2011.
- [11] W. K. Choi, S. K. Kang, and D. Y. Shih, "A study of the effects of solder volume on the interfacial reactions in solder joints using the differential scanning calorimetry technique," *Journal of Electronic Materials*, vol. 31, pp. 1283-1291, 2002.
- [12] M. N. Islam, Y. C. Chan, M. J. Rizvi, and W. Jillek, "Investigations of interfacial reactions of Sn–Zn based and Sn–Ag–Cu lead-free solder alloys as replacement for Sn–Pb solder," *Journal of Alloys and Compounds*, vol. 400, pp. 136-144, 2005.

- [13] H. T. Lee and Y. H. Lee, "Adhesive strength and tensile fracture of Ni particle enhanced Sn–Ag composite solder joints," *Materials Science and Engineering: A*, vol. 419, pp. 172-180, 2006.
- [14] Y.-H. Lee and H.-T. Lee, "Shear strength and interfacial microstructure of Sn–Ag–xNi/Cu single shear lap solder joints," *Materials Science and Engineering: A*, vol. 444, pp. 75-83, 2007.
- [15] P.-C. Shih and K.-L. Lin, "Effect of microstructural evolution on electrical property of the Sn–Ag–Cu solder balls joined with Sn–Zn–Bi paste," *Journal of Materials Research*, vol. 20, pp. 2854-2865, 2005.
- [16] C. C. Lee, P. J. Wang, and J. S. Kim, "Are Intermetallics in Solder Joints Really Brittle?," in *Electronic Components and Technology Conference*, Reno, USA, 2007, pp. 648-652.
- [17] R. J. Fields, S. R. Low III, and G. K. Lucey Jr., "Physical and Mechanical Properties of Intermetallic Compounds Commonly Found in Solder Joints," presented at the Proceedings of TMS Symposium, Cincinnati, USA, 20-24 October, 1991.
- [18] E. A. Brandes and G. B. Brook, *Smithells Metals Reference Book*, 7th Edition ed. Oxford, U.K.: Butterworth-Heinemann, 1990.
- [19] L. Jiang, H. Jiang, and N. Chawla, "The Effect of Crystallographic Orientation on the Mechanical Behavior of Cu_6Sn_5 by Micropillar Compression Testing," *Journal of Electronic Materials*, vol. 41, pp. 2083-2088, 2012.
- [20] G.-Y. Jang, J.-W. Lee, and J.-G. Duh, "The nanoindentation characteristics of Cu_6Sn_5 , Cu_3Sn , and Ni_3Sn_4 intermetallic compounds in the solder bump," *Journal of Electronic Materials*, vol. 33, pp. 1103-1110, 2004.
- [21] R. J. Fields, S. R. Low III, and G. K. Lucey Jr., *The Metal Science of Joining*. Warrendale, USA: TMS, 1992.
- [22] P. J. Shang, Z. Q. Liu, D. X. Li, and J. K. Shang, "TEM Observations of the Growth of Intermetallic Compounds at the SnBi/Cu Interface," *Journal of Electronic Materials*, vol. 38, pp. 2579-2584, 2009.
- [23] S.-S. Ha, J.-K. Jang, S.-O. Ha, J.-W. Yoon, H.-J. Lee, J.-H. Joo, *et al.*, "Effect of multiple reflows on interfacial reaction and shear strength of Sn–Ag electroplated solder bumps for flip chip package," *Microelectronic Engineering*, vol. 87, pp. 517-521, 2010.
- [24] S. Jeong, J. Kim, and H. Lee, "Effect of cooling rate on growth of the intermetallic compound and fracture mode of near-eutectic Sn-Ag-Cu/Cu pad: Before and after aging," *Journal of Electronic Materials*, vol. 33, pp. 1530-1544, 2004.
- [25] K. N. Tu, F. Ku, and T. Y. Lee, "Morphological stability of solder reaction products in flip chip technology," *Journal of Electronic Materials*, vol. 30, pp. 1129-1132, 2001.
- [26] A. M. Gusak and K. N. Tu, "Kinetic theory of flux-driven ripening," *Physical Review B*, vol. 66, p. 115403, 2002.
- [27] J. Görlich, G. Schmitz, and K. N. Tu, "On the mechanism of the binary Cu/Sn solder reaction," *Applied Physics Letters*, vol. 86, p. 053106, 2005.
- [28] C.-W. Hwang, K.-S. Kim, and K. Suganuma, "Interfaces in lead-free soldering," *Journal of Electronic Materials*, vol. 32, pp. 1249-1256, 2003.

- [29] H. K. Kim, H. K. Liou, and K. N. Tu, "Three-dimensional morphology of a very rough interface formed in the soldering reaction between eutectic SnPb and Cu," *Applied physics letters*, vol. 66, pp. 2337-2339, 1995.
- [30] P. J. Shang, Z. Q. Liu, D. X. Li, and J. K. Shang, "Directional growth of Cu₃Sn at the reactive interface between eutectic SnBi solder and (1 0 0) single crystal Cu," *Scripta Materialia*, vol. 59, pp. 317-320, 2008.
- [31] S. Ahat, M. Sheng, and L. Luo, "Microstructure and shear strength evolution of SnAg/Cu surface mount solder joint during aging," *Journal of Electronic Materials*, vol. 30, pp. 1317-1322, 2001.
- [32] C. Zhiwen, A. Bing, W. Yiping, L. Changqing, and R. Parkin, "Influence of IMCs volume ratio in micro-scale solder joints on their mechanical integrity," in *62nd Electronic Components and Technology Conference (ECTC)*, San Diego, USA, 2012, pp. 710-716.
- [33] L. C. Tsao, "Evolution of nano-Ag₃Sn particle formation on Cu–Sn intermetallic compounds of Sn_{3.5}Ag_{0.5}Cu composite solder/Cu during soldering," *Journal of Alloys and Compounds*, vol. 509, pp. 2326-2333, 2011.
- [34] R.-W. Yang, Y.-W. Chang, W.-C. Sung, and C. Chen, "Precipitation of large Ag₃Sn intermetallic compounds in SnAg_{2.5} microbumps after multiple reflows in 3D-IC packaging," *Materials Chemistry and Physics*, vol. 134, pp. 340-344, 2012.
- [35] K. S. Kim, S. H. Huh, and K. Suganuma, "Effects of fourth alloying additive on microstructures and tensile properties of Sn–Ag–Cu alloy and joints with Cu," *Microelectronics Reliability*, vol. 43, pp. 259-267, 2003.
- [36] C. P. Huang, C. Chen, C. Y. Liu, S. S. Lin, and K. H. Chen, "Metallurgical reactions of Sn-3.5Ag solder with various thicknesses of electroplated Ni/Cu under bump metallization," *Journal of Materials Research*, vol. 20, pp. 2772-2779, 2005.
- [37] J. W. Jang, D. R. Frear, T. Y. Lee, and K. N. Tu, "Morphology of interfacial reaction between lead-free solders and electroless Ni-P under bump metallization," *Journal of Applied Physics*, vol. 88, pp. 6359-6363, 2000.
- [38] R. S. Sidhu, S. V. Madge, X. Deng, and N. Chawla, "On the nature of the interface between Ag₃Sn intermetallics and Sn in Sn-3.5Ag solder alloys," *Journal of Electronic Materials*, vol. 36, pp. 1615-1620, 2007.
- [39] F. Ochoa, X. Deng, and N. Chawla, "Effects of cooling rate on creep behavior of a Sn-3.5Ag alloy," *Journal of Electronic Materials*, vol. 33, pp. 1596-1607, 2004.
- [40] F. Ochoa, J. J. Williams, and N. Chawla, "The effects of cooling rate on microstructure and mechanical behavior of Sn-3.5Ag solder," *JOM*, vol. 55, pp. 56-60, 2003.
- [41] F. Ochoa, J. J. Williams, and N. Chawla, "Effects of cooling rate on the microstructure and tensile behavior of a Sn-3.5wt.%Ag solder," *Journal of Electronic Materials*, vol. 32, pp. 1414-1420, 2003.
- [42] F. L. Tan and C. P. Tso, "Cooling of mobile electronic devices using phase change materials," *Applied Thermal Engineering*, vol. 24, pp. 159-169, 2004.

- [43] Y. C. Chan, A. C. K. So, and J. K. L. Lai, "Growth kinetic studies of Cu–Sn intermetallic compound and its effect on shear strength of LCCC SMT solder joints," *Materials Science and Engineering: B*, vol. 55, pp. 5-13, 1998.
- [44] W. Peng, E. Monlevade, and M. E. Marques, "Effect of thermal aging on the interfacial structure of SnAgCu solder joints on Cu," *Microelectronics Reliability*, vol. 47, pp. 2161-2168, 2007.
- [45] S. Choi, J. P. Lucas, K. N. Subramanian, and T. R. Bieler, "Formation and growth of interfacial intermetallic layers in eutectic Sn-Ag solder and its composite solder joints," *Journal of Materials Science: Materials in Electronics*, vol. 11, pp. 497-502, 2000.
- [46] K. N. Tu and R. D. Thompson, "Kinetics of interfacial reaction in bimetallic Cu-Sn thin films," *Acta Metallurgica*, vol. 30, pp. 947-952, 1982.
- [47] Z. Kejun, R. Stierman, C. Tz-Cheng, D. Edwards, K. Ano, and K. N. Tu, "Kirkendall void formation in eutectic SnPb solder joints on bare Cu and its effect on joint reliability," *Journal of Applied Physics*, vol. 97, pp. 024508-024508-8, 2005.
- [48] M. Onishi and H. Fujibuchi, "Reaction-Diffusion in the Cu-Sn System," *Transactions of the Japan Institute of Metals*, vol. 16, pp. 539-547, 1975.
- [49] H. C. Bhedwar, K. K. Ray, S. D. Kulkarni, and V. Balasubramanian, "Kirkendall effect studies in copper-tin diffusion couples," *Scripta Metallurgica*, vol. 6, pp. 919-922, 1972.
- [50] C. Jiunn, L. Yi-Shao, C.-Y. Ren, and D.-J. Huang, "First-principles calculations of elastic properties of Cu_3Sn superstructure," *Applied Physics Letters*, vol. 92, pp. 081901-081901-3, 2008.
- [51] W.-m. Tang, A.-q. He, Q. Liu, and D. G. Ivey, "Solid state interfacial reactions in electrodeposited Cu/Sn couples," *Transactions of Nonferrous Metals Society of China*, vol. 20, pp. 90-96, 2010.
- [52] C. Yu, Y. Yang, H. Lu, and J. M. Chen, "Effects of Current Stressing on Formation and Evolution of Kirkendall Voids at Sn–3.5Ag/Cu Interface," *Journal of Electronic Materials*, vol. 39, pp. 1309-1314, 2010.
- [53] L. Zhang, S. B. Xue, G. Zeng, L. L. Gao, and H. Ye, "Interface reaction between SnAgCu/SnAgCuCe solders and Cu substrate subjected to thermal cycling and isothermal aging," *Journal of Alloys and Compounds*, vol. 510, pp. 38-45, 2012.
- [54] D. Kim, J.-h. Chang, J. Park, and J. Pak, "Formation and behavior of Kirkendall voids within intermetallic layers of solder joints," *Journal of Materials Science: Materials in Electronics*, vol. 22, pp. 703-716, 2011.
- [55] W. Choi and H. Lee, "Effect of soldering and aging time on interfacial microstructure and growth of intermetallic compounds between Sn-3.5Ag solder alloy and Cu substrate," *Journal of Electronic Materials*, vol. 29, pp. 1207-1213, 2000.
- [56] T. Y. Lee, K. N. Tu, and D. R. Frear, "Electromigration of eutectic SnPb and SnAg_{3.8}Cu_{0.7} flip chip solder bumps and under-bump metallization," *Journal of Applied Physics*, vol. 90, pp. 4502-4508, 2001.

- [57] P. J. Shang, L. Zhang, Z. Q. Liu, J. Tan, and J. K. Shang, "Ex situ observations of fast intermetallic growth on the surface of interfacial region between eutectic SnBi solder and Cu substrate during solid-state aging process," *Microelectronics Reliability*, vol. 53, pp. 899-905, 2013.
- [58] C.-m. Chen and C.-h. Chen, "Interfacial Reactions between Eutectic SnZn Solder and Bulk or Thin-Film Cu Substrates," *Journal of Electronic Materials*, vol. 36, pp. 1363-1371, 2007.
- [59] P. L. Tu, Y. C. Chan, and J. K. L. Lai, "Effect of intermetallic compounds on vibration fatigue of μ BGA solder joint," *IEEE Transactions on Advanced Packaging*, vol. 24, pp. 197-205, 2001.
- [60] K. E. Aasmundtveit, W. Kaiying, N. Hoivik, J. M. Graff, and A. Elfving, "Au-Sn SLID bonding: Fluxless bonding with high temperature stability to above 350 °c," in *Microelectronics and Packaging Conference, 2009. EMPC 2009. European*, 2009, pp. 1-6.
- [61] L. He, G. Salomonsen, W. Kaiying, K. E. Aasmundtveit, and N. Hoivik, "Wafer-Level Cu/Sn to Cu/Sn SLID-Bonded Interconnects With Increased Strength," *IEEE Transactions on Components, Packaging and Manufacturing Technology*, vol. 1, pp. 1350-1358, 2011.
- [62] T. A. Tollefsen, M. M. V. Taklo, K. E. Aasmundtveit, and A. Larsson, "Reliable HT electronic packaging-Optimization of a Au-Sn SLID joint," in *4th Electronic System-Integration Technology Conference (ESTC)*, Amsterdam, Netherlands, 2012, pp. 1-6.
- [63] T. A. Tollefsen, A. Larsson, O. M. Lovvik, and K. E. Aasmundtveit, "High Temperature Interconnect and Die Attach Technology: Au-Sn SLID Bonding," *IEEE Transactions on Components, Packaging and Manufacturing Technology*, vol. 3, pp. 904-914, 2013.
- [64] T. Tollefsen, A. Larsson, O. Løvvik, and K. Aasmundtveit, "Au-Sn SLID Bonding—Properties and Possibilities," *Metallurgical and Materials Transactions B*, vol. 43, pp. 397-405, 2012.
- [65] S. Kumar and J. Jung, "Mechanical and electronic properties of Ag₃Sn intermetallic compound in lead free solders using ab initio atomistic calculation," *Materials Science and Engineering: B*, vol. 178, pp. 10-21, 2013.
- [66] N. T. S. Lee, V. B. C. Tan, and K. M. Lim, "First-principles calculations of structural and mechanical properties of Cu₆Sn₅," *Applied Physics Letters*, vol. 88, pp. 031913-031913-3, 2006.
- [67] C. Jiunn, L. Yi-Shao, C.-Y. Ren, and D.-J. Huang, "First-principles calculations of elastic properties of Cu₃Sn superstructure," *Applied Physics Letters*, vol. 92, pp. 081901-081901-3, 2008.
- [68] F. X. Che and J. H. L. Pang, "Characterization of IMC layer and its effect on thermomechanical fatigue life of Sn–3.8Ag–0.7Cu solder joints," *Journal of Alloys and Compounds*, vol. 541, pp. 6-13, 2012.
- [69] L. Xu and J. H. L. Pang, "Nano-indentation characterization of Ni–Cu–Sn IMC layer subject to isothermal aging," *Thin Solid Films*, vol. 504, pp. 362-366, 2006.
- [70] B. Subrahmanyam, "Elastic moduli of some complicated binary alloy systems," *Transactions of the Japan Institute of Metals*, vol. 13, pp. 93-95, 1972.

- [71] P.-F. Yang, Y.-S. Lai, S.-R. Jian, J. Chen, and R.-S. Chen, "Nanoindentation identifications of mechanical properties of Cu₆Sn₅, Cu₃Sn, and Ni₃Sn₄ intermetallic compounds derived by diffusion couples," *Materials Science and Engineering: A*, vol. 485, pp. 305-310, 2008.
- [72] S. Choudhury and L. Ladani, "Grain Growth Orientation and Anisotropy in Cu₆Sn₅ Intermetallic: Nanoindentation and Electron Backscatter Diffraction Analysis," *Journal of Electronic Materials*, vol. 43, pp. 996-1004, 2014.
- [73] L. Jiang and N. Chawla, "Mechanical properties of Cu₆Sn₅ intermetallic by micropillar compression testing," *Scripta Materialia*, vol. 63, pp. 480-483, 2010.
- [74] Q. K. Zhang, J. Tan, and Z. F. Zhang, "Fracture behaviors and strength of Cu₆Sn₅ intermetallic compounds by indentation testing," *Journal of Applied Physics*, vol. 110, pp. 014502-014502-4, 2011.
- [75] D. Raabe, K. Miyake, and H. Takahara, "Processing, microstructure, and properties of ternary high-strength Cu–Cr–Ag in situ composites," *Materials Science and Engineering: A*, vol. 291, pp. 186-197, 2000.
- [76] M. Winter and J. O. Besenhard, "Electrochemical lithiation of tin and tin-based intermetallics and composites," *Electrochimica Acta*, vol. 45, pp. 31-50, 1999.
- [77] M.-H. Lu and K.-C. Hsieh, "Sn-Cu Intermetallic Grain Morphology Related to Sn Layer Thickness," *Journal of Electronic Materials*, vol. 36, pp. 1448-1454, 2007.
- [78] H. D. Blair, P. Tsung-Yu, and J. M. Nicholson, "Intermetallic compound growth on Ni, Au/Ni, and Pd/Ni substrates with Sn/Pb, Sn/Ag, and Sn solders [PWBs]," in *48th Electronic Components & Technology Conference*, Seattle, USA, 1998, pp. 259-267.
- [79] P. L. Tu, Y. C. Chan, and J. K. L. Lai, "Effect of intermetallic compounds on vibration fatigue of μ BGA solder joint," *Advanced Packaging, IEEE Transactions on*, vol. 24, pp. 197-205, 2001.
- [80] C. C. Li, Z. X. Zhu, M. H. Chen, and C. R. Kao, "Volume shrinkage induced by interfacial reactions in micro joints," in *International Symposium on Advanced Packaging Materials (APM)*, Irvine, USA, 2013, pp. 8-14.
- [81] C. C. Li, C. K. Chung, W. L. Shih, and C. R. Kao, "Volume Shrinkage Induced by Interfacial Reaction in Micro-Ni/Sn/Ni Joints," *Metallurgical and Materials Transactions A*, vol. 45, pp. 2343-2346, 2014.
- [82] C. Zhiwen, A. Bing, W. Yiping, L. Changqing, and R. Parkin, "Dimensional change in micro-scale solder joint induced by evolution of IMCs," in *13th International Conference on Electronic Packaging Technology and High Density Packaging (ICEPT-HDP)*, Guilin, China, 2012, pp. 1234-1239.
- [83] P. L. Tu, Y. C. Chan, K. C. Hung, and J. K. L. Lai, "Comparative study of micro-BGA reliability under bending stress," *IEEE Transactions on Advanced Packaging*, vol. 23, pp. 750-756, 2000.
- [84] J. Lau, D. Shangguan, T. Castello, R. Horsley, J. Smetana, N. Hoo, *et al.*, "Failure analysis of lead-free solder joints for high-density package " *Soldering & Surface Mount Technology*, vol. 16, pp. 69-76, 2004.

- [85] T. K.N, "Interdiffusion and reaction in bimetallic Cu-Sn thin films," *Acta Metallurgica*, vol. 21, pp. 347-354, 1973.
- [86] W. J. Choi, T. Y. Lee, K. N. Tu, N. Tamura, R. S. Celestre, A. A. MacDowell, *et al.*, "Tin whiskers studied by synchrotron radiation scanning X-ray micro-diffraction," *Acta Materialia*, vol. 51, pp. 6253-6261, 2003.
- [87] K. N. Tu, "Irreversible processes of spontaneous whisker growth in bimetallic Cu-Sn thin-film reactions," *Physical Review B*, vol. 49, pp. 2030-2034, 1994.
- [88] K. N. Tu and J. C. M. Li, "Spontaneous whisker growth on lead-free solder finishes," *Materials Science and Engineering: A*, vol. 409, pp. 131-139, 2005.
- [89] H. Y. Chuang, J. J. Yu, M. S. Kuo, H. M. Tong, and C. R. Kao, "Elimination of voids in reactions between Ni and Sn: A novel effect of silver," *Scripta Materialia*, vol. 66, pp. 171-174, 2012.
- [90] S.-Y. Chang, Y.-C. Huang, and Y.-M. Lin, "Mechanical property and fracture behavior characterizations of 96.5 Sn–3.0 Ag–0.5 Cu solder joints," *Journal of Alloys and Compounds*, vol. 490, pp. 508-514, 2010.
- [91] T. Kangasvieri, O. Nousiainen, J. Putaala, R. Rautioaho, and J. Vähäkangas, "Reliability and RF performance of BGA solder joints with plastic-core solder balls in LTCC/PWB assemblies," *Microelectronics Reliability*, vol. 46, pp. 1335-1347, 2006.
- [92] Y. Jee, J. Yu, and Y. Ko, "Effects of Zn addition on the drop reliability of Sn-3.5 Ag-xZn/Ni (P) solder joints," *Journal of Materials Research*, vol. 22, pp. 2776-2784, 2007.
- [93] C.-B. Lee, S.-B. Jung, Y.-E. Shin, and C.-C. Shur, "Effect of isothermal aging on ball shear strength in BGA joints with Sn-3.5 Ag-0.75 Cu solder," *Materials Transactions*, vol. 43, pp. 1858-1863, 2002.
- [94] B. Y. Wu, H. W. Zhong, Y. C. Chan, and M. O. Alam, "Degradation of Sn37Pb and Sn3.5Ag0.5Cu solder joints between Au/Ni (P)/Cu pads stressed with moderate current density," *Journal of Materials Science: Materials in Electronics*, vol. 17, pp. 943-950, 2006.
- [95] S. Yoon, C. Park, S. Hong, J. Moon, I. Park, and H. Chun, "Interfacial reaction and solder joint reliability of Pb-free solders in lead frame chip scale packages (LF-CSP)," *Journal of Electronic Materials*, vol. 29, pp. 1233-1240, 2000.
- [96] S.-H. Chae, X. Zhang, K.-H. Lu, H.-L. Chao, P. Ho, M. Ding, *et al.*, "Electromigration statistics and damage evolution for Pb-free solder joints with Cu and Ni UBM in plastic flip-chip packages," *Journal of Materials Science: Materials in Electronics*, vol. 18, pp. 247-258, 2007.
- [97] P. J. Withers, "Residual stress and its role in failure," *Reports on Progress in Physics*, vol. 70, pp. 2211-2264, 2007.
- [98] P. J. Withers and H. K. D. H. Bhadeshia, "Residual stress. Part 1-Measurement techniques," *Materials Science and Technology*, vol. 17, pp. 355-365, 2001.
- [99] J. G. Lee, F. Guo, S. Choi, K. N. Subramanian, T. R. Bieler, and J. P. Lucas, "Residual-mechanical behavior of thermomechanically fatigued Sn-Ag based solder joints," *Journal of Electronic Materials*, vol. 31, pp. 946-952, 2002.

- [100] H.-T. Lee and M.-H. Chen, "Influence of intermetallic compounds on the adhesive strength of solder joints," *Materials Science and Engineering: A*, vol. 333, pp. 24-34, 2002.
- [101] R. Edward Green, *Treatise on Materials Science and Technology: Ultrasonic Investigation of Mechanical Properties* New York: Academic Press, 1973.
- [102] A. Seiichi, "Magnetic Studies of Residual Stress in Iron and Steel Induced by Uniaxial Deformation," *Japanese Journal of Applied Physics*, vol. 16, p. 1161, 1977.
- [103] T. W. Clyne and S. C. Gill, "Residual Stresses in Thermal Spray Coatings and Their Effect on Interfacial Adhesion: A Review of Recent Work," *Journal of Thermal Spray Technology*, vol. 5, pp. 401-418, 1996.
- [104] J. Y. Song, J. Yu, and T. Y. Lee, "Effects of reactive diffusion on stress evolution in Cu–Sn films," *Scripta Materialia*, vol. 51, pp. 167-170, 2004.
- [105] P. S. Prevey, *X-ray diffraction residual stress techniques*: ASM International, 1986.
- [106] C. H. Ma, J. H. Huang, and H. Chen, "Residual stress measurement in textured thin film by grazing-incidence X-ray diffraction," *Thin Solid Films*, vol. 418, pp. 73-78, 2002.
- [107] S. Zhang, H. Xie, X. Zeng, and P. Hing, "Residual stress characterization of diamond-like carbon coatings by an X-ray diffraction method," *Surface and Coatings Technology*, vol. 122, pp. 219-224, 1999.
- [108] P. S. Prevey, "X-ray diffraction residual stress techniques," *ASM International, ASM Handbook.*, vol. 10, pp. 380-392, 1986.
- [109] M. F. Doerner and W. D. Nix, "A method for interpreting the data from depth-sensing indentation instruments," *Journal of Materials Research*, vol. 1, pp. 601-609, 1986.
- [110] G. M. Pharr and W. C. Oliver, "Measurement of thin film mechanical properties using nanoindentation," *Mrs Bulletin*, vol. 17, pp. 28-33, 1992.
- [111] T. Y. Tsui, W. C. Oliver, and G. M. Pharr, "Influences of stress on the measurement of mechanical properties using nanoindentation: Part I. Experimental studies in an aluminum alloy," *Journal of Materials Research*, vol. 11, pp. 752-759, 1996.
- [112] Y.-H. Lee and D. Kwon, "Measurement of residual-stress effect by nanoindentation on elastically strained (1 0 0) W," *Scripta Materialia*, vol. 49, pp. 459-465, 2003.
- [113] Z.-H. Xu and X. Li, "Influence of equi-biaxial residual stress on unloading behaviour of nanoindentation," *Acta Materialia*, vol. 53, pp. 1913-1919, 2005.
- [114] S. Suresh and A. E. Giannakopoulos, "A new method for estimating residual stresses by instrumented sharp indentation," *Acta Materialia*, vol. 46, pp. 5755-5767, 1998.
- [115] L.-n. Zhu, B.-s. Xu, H.-d. Wang, and C.-b. Wang, "Measurement of residual stress in quenched 1045 steel by the nanoindentation method," *Materials Characterization*, vol. 61, pp. 1359-1362, 2010.
- [116] Y.-H. Lee and D. Kwon, "Residual stresses in DLC/Si and Au/Si systems: Application of a stress-relaxation model to the nanoindentation technique," *Journal of materials research*, vol. 17, pp. 901-906, 2002.
- [117] T. Reinikainen, M. Poech, M. Krumm, and J. Kivilahti, "A Finite-Element and Experimental Analysis of Stress Distribution in Various Shear Tests for Solder Joints," *Journal of Electronic Packaging*, vol. 120, pp. 106-113, 1998.

- [118] S. Rzepka, M. A. Korhonen, E. Meusel, and C. Y. Li, "The Effect of Underfill and Underfill Delamination on the Thermal Stress in Flip-Chip Solder Joints," *Journal of Electronic Packaging*, vol. 120, pp. 342-348, 1998.
- [119] V. Sarihan, "Temperature Dependent Viscoplastic Simulation of Controlled Collapse Solder Joint Under Thermal Cycling," *Journal of Electronic Packaging*, vol. 115, pp. 16-21, 1993.
- [120] L. F. Coffin, "The effect of high vacuum on the low cycle fatigue law," *Metallurgical Transactions*, vol. 3, pp. 1777-1788, 1972.
- [121] H. D. Solomon and E. D. Tolksdorf, "Energy Approach to the Fatigue of 60/40 Solder: Part I—Influence of Temperature and Cycle Frequency," *Journal of Electronic Packaging*, vol. 117, pp. 130-135, 1995.
- [122] H. D. Solomon and E. D. Tolksdorf, "Energy Approach to the Fatigue of 60/40 Solder: Part II - Influence of Hold Time and Asymmetric Loading," *Journal of Electronic Packaging*, vol. 118, pp. 67-71, 1996.
- [123] J. Lau and H. Solomon, "Predicting Thermal and Mechanical Fatigue Lives from Isothermal Low Cycle Data," in *Solder Joint Reliability*, ed: Springer US, 1991, pp. 406-454.
- [124] J. H. Lau, *Solder Joint Reliability: Theory and Applications*: Springer US, 1991.
- [125] B. Wong and D. E. Helling, "A mechanistic model for solder joint failure prediction under thermal cycling," *Journal of Electronic Packaging*, vol. 112, pp. 104-109, 1990.
- [126] P. Yi-Hsin, "A fracture mechanics approach to thermal fatigue life prediction of solder joints," *IEEE Transactions on Components, Hybrids, and Manufacturing Technology*, vol. 15, pp. 559-570, 1992.
- [127] S. R. Bodner and Y. Partom, "Constitutive Equations for Elastic-Viscoplastic Strain-Hardening Materials," *Journal of Applied Mechanics*, vol. 42, pp. 385-389, 1975.
- [128] J. L. Chaboche, "Unified cyclic viscoplastic constitutive equations: development, capabilities, and thermodynamic framework," 1996.
- [129] D. R. Frear, S. N. Burchett, M. K. Neilsen, and J. J. Stephens, "Microstructurally Based Finite Element Simulation on Solder Joint Behaviour," *Soldering & Surface Mount Technology*, vol. 9, pp. 39-42, 2014/09/10 1997.
- [130] L. Kachanov, *Introduction to continuum damage mechanics*: Springer, 1986.
- [131] J. Lemaître, *A course on damage mechanics*: Springer, 1996.
- [132] C. L. Chow, F. Yang, and H. E. Fang, "Damage mechanics characterization on the fatigue behaviour of a solder joint material," *Proceedings of the Institution of Mechanical Engineers, Part C: Journal of Mechanical Engineering Science*, vol. 215, pp. 883-892, 2001.
- [133] Y. Wei, C. L. Chow, H. E. Fang, and M. K. Neilsen, "Characteristics of creep damage for 60 Sn-40 Pb solder material," *Journal of Electronic Packaging*, vol. 123, pp. 278-283, 2001.
- [134] H. E. Fang, C. L. Chow, and F. Yang, "A Method of Damage Mechanics Analysis for Solder Material," *Key Engineering Materials*, vol. 145-149, pp. 367-374, 1998.
- [135] S. H. Ju, B. I. Sandor, and M. E. Plesha, "Life prediction of solder joints by damage and fracture mechanics," *Journal of Electronic packaging*, vol. 118, pp. 193-200, 1996.

- [136] D. R. Frear, S. N. Burchett, M. K. Neilsen, and J. J. Stephens, "Microstructurally based finite element simulation of solder joint behaviour," *Soldering and Surface Mount Technology*, pp. 39-42, 1997.
- [137] Q. D. Yang, D. J. Shim, and S. M. Spearing, "A cohesive zone model for low cycle fatigue life prediction of solder joints," *Microelectronic Engineering*, vol. 75, pp. 85-95, 2004.
- [138] B. Balakrisnan, C. C. Chum, M. Li, Z. Chen, and T. Cahyadi, "Fracture toughness of Cu-Sn intermetallic thin films," *Journal of Electronic Materials*, vol. 32, pp. 166-171, 2003.
- [139] A. Syed, "Predicting solder joint reliability for thermal, power, and bend cycle within 25% accuracy," in *51st Electronic Components and Technology Conference*, Orlando, USA, 2001, pp. 255-263.
- [140] K. E. Yazzie, H. E. Fei, H. Jiang, and N. Chawla, "Rate-dependent behavior of Sn alloy–Cu couples: Effects of microstructure and composition on mechanical shock resistance," *Acta Materialia*, vol. 60, pp. 4336-4348, 2012.
- [141] S. Li, A. Abdel-Wahab, E. Demirci, and V. Silberschmidt, "Fracture process in cortical bone: X-FEM analysis of microstructured models," *International Journal of Fracture*, vol. 184, pp. 43-55, 2013.
- [142] S. W. R. Lee and S. Fubin, "Impact of IMC Thickness on Lead-free Solder Joint Reliability under Thermal Aging: Ball Shear Tests vs. Cold Bump Pull Tests," in *International Microsystems, Packaging, Assembly Conference Taiwan*, Taiwan, 2006, pp. 1-4.
- [143] J. H. L. Pang, T. H. Low, B. S. Xiong, X. Luhua, and C. C. Neo, "Thermal cycling aging effects on Sn–Ag–Cu solder joint microstructure, IMC and strength," *Thin Solid Films*, vol. 462–463, pp. 370-375, 2004.
- [144] J.-W. Yoon, S.-W. Kim, and S.-B. Jung, "IMC Growth and Shear Strength of Sn-Ag-Bi-In/Au/Ni/Cu BGA Joints During Aging," *Materials Transactions*, vol. 45, pp. 727-733, 2004.
- [145] Y. Liu and F. Sun, "Characterization of interfacial IMCs in low-Ag Sn–Ag–xCu–Bi–Ni solder joints," *Journal of Materials Science: Materials in Electronics*, vol. 24, pp. 290-294, 2013.
- [146] C. Chen, H.-Y. Hsiao, Y.-W. Chang, F. Ouyang, and K. N. Tu, "Thermomigration in solder joints," *Materials Science and Engineering: R: Reports*, vol. 73, pp. 85-100, 2012/10// 2012.
- [147] L. M. Lee, H. Haliman, and A. A. Mohamad, "Interfacial reaction of a Sn-3.0 Ag-0.5 Cu thin film during solder reflow," *Soldering & Surface Mount Technology*, vol. 25, pp. 15-23, 2013.
- [148] J.-M. Wang, K.-J. Wang, and J.-G. Duh, "Cu Substrates with Different Grain Sizes," *Journal of Electronic Materials*, vol. 40, pp. 1549-1555, 2011.
- [149] K. Yazzie, J. Topliff, and N. Chawla, "On the Asymmetric Growth Behavior of Intermetallic Compound Layers During Extended Reflow of Sn-Rich Alloy on Cu," *Metallurgical and Materials Transactions A*, vol. 43, pp. 3442-3446, 2012.
- [150] X. Li, F. Li, F. Guo, and Y. Shi, "Effect of Isothermal Aging and Thermal Cycling on Interfacial IMC Growth and Fracture Behavior of SnAgCu/Cu Joints," *Journal of Electronic Materials*, vol. 40, pp. 51-61, 2011.
- [151] Z. Huijing, Q. Lin, L. Hua, Z. Ning, and M. HaiTao, "The study of cooling process' effect on the growth of IMC at Sn-3.5Ag/Cu soldering interface," in *14th International Conference on Electronic Packaging Technology (ICEPT)*, Dalian, China, 2013, pp. 372-376.

- [152] H. Xiao, X. Y. Li, Y. X. Zhu, J. L. Yang, J. Chen, and F. Guo, "Intermetallic growth study on SnAgCu/Cu solder joint interface during thermal aging," *Journal of Materials Science: Materials in Electronics*, vol. 24, pp. 2527-2536, 2013.
- [153] T.-T. Luu, A. Duan, K. Aasmundtveit, and N. Hoivik, "Optimized Cu-Sn Wafer-Level Bonding Using Intermetallic Phase Characterization," *Journal of Electronic Materials*, vol. 42, pp. 3582-3592, 2013.
- [154] H. L. J. Pang, K. H. Tan, X. Q. Shi, and Z. P. Wang, "Microstructure and intermetallic growth effects on shear and fatigue strength of solder joints subjected to thermal cycling aging," *Materials Science and Engineering: A*, vol. 307, pp. 42-50, 2001.
- [155] P. Borgesen, Y. Liang, P. Kondos, D. W. Henderson, G. Servis, W. Ju, *et al.*, "Sporadic Degradation in Board Level Drop Reliability - Those Aren't All Kirkendall Voids!," in *57th Electronic Components and Technology Conference*, Reno, USA, 2007, pp. 136-146.
- [156] H. K. Kim and K. N. Tu, "Kinetic analysis of the soldering reaction between eutectic SnPb alloy and Cu accompanied by ripening," *Physical Review B*, vol. 53, pp. 16027-16034, 1996.
- [157] J. Feng and S. Xue, "Growth behaviors of intermetallic compound layers in Cu/Al joints brazed with Zn-22Al and Zn-22Al-0.05Ce filler metals," *Materials & Design*, vol. 51, pp. 907-915, 2013.
- [158] Z. Cooperation. (2014, 10 July). *Optical Profiler Basics*. Available: <http://www.zygo.com/?/met/profilers/opticalprofilersabout.htm>
- [159] J. C. Wyant and K. Creath, "Advances in interferometric optical profiling," *International Journal of Machine Tools and Manufacture*, vol. 32, pp. 5-10, 1992/4// 1992.
- [160] R. M. Carter, P. Morrall, R. R. J. Maier, B. J. S. Jones, S. McCulloch, and J. S. Barton, "Optical characterisation of RF sputter coated palladium thin films for hydrogen sensing," in *21st International Conference on Optical Fiber Sensors*, Ottawa, Canada, 2011, pp. 77535T-77535T-4.
- [161] S.-M. Kuo and K.-L. Lin, "The Hillock Formation in a Cu/Sn-9Zn/Cu Lamella upon Current Stressing," *Journal of Electronic Materials*, vol. 36, pp. 1378-1382, 2007.
- [162] T. Y. Lee, K. N. Tu, S. M. Kuo, and D. R. Frear, "Electromigration of eutectic SnPb solder interconnects for flip chip technology," *Journal of Applied Physics*, vol. 89, pp. 3189-3194, 2001.
- [163] C. Y. Liu, C. Chih, and K. N. Tu, "Electromigration in Sn-Pb solder strips as a function of alloy composition," *Journal of Applied Physics*, vol. 88, pp. 5703-5709, 2000.
- [164] Y. S. Kaganovskii, L. N. Paritskaya, V. V. Bogdanov, and A. O. Grengo, "Intermetallic phase formation during diffusion along a free surface," *Acta Materialia*, vol. 45, pp. 3927-3934, 1997.
- [165] P. J. Shang, Z. Q. Liu, X. Y. Pang, D. X. Li, and J. K. Shang, "Growth mechanisms of Cu₃Sn on polycrystalline and single crystalline Cu substrates," *Acta Materialia*, vol. 57, pp. 4697-4706, 2009.
- [166] J. F. Li, S. H. Mannan, M. P. Clode, D. C. Whalley, and D. A. Hutt, "Interfacial reactions between molten Sn-Bi-X solders and Cu substrates for liquid solder interconnects," *Acta Materialia*, vol. 54, pp. 2907-2922, 2006.

- [167] A. Paul, A. A. Kodentsov, and F. J. J. Van Loo, "Intermetallic growth and Kirkendall effect manifestations in Cu/Sn and Au/Sn diffusion couples," *Zeitschrift fuer Metallkunde/Materials Research and Advanced Techniques*, vol. 95, pp. 913-920, 2004.
- [168] M. Y. Tsai, S. C. Yang, Y. W. Wang, and C. R. Kao, "Grain growth sequence of Cu₃Sn in the Cu/Sn and Cu/Sn–Zn systems," *Journal of Alloys and Compounds*, vol. 494, pp. 123-127, 2010.
- [169] T. Laurila, V. Vuorinen, and J. K. Kivilahti, "Interfacial reactions between lead-free solders and common base materials," *Materials Science and Engineering: R: Reports*, vol. 49, pp. 1-60, 2005.
- [170] K. N. Tu and R. D. Thompson, "Kinetics of interfacial reaction in bimetallic Cu–Sn thin films," *Acta Metallurgica*, vol. 30, pp. 947-952, 1982.
- [171] B.-J. Lee, N. M. Hwang, and H. M. Lee, "Prediction of interface reaction products between Cu and various solder alloys by thermodynamic calculation," *Acta Materialia*, vol. 45, pp. 1867-1874, 1997.
- [172] R. A. Gagliano, G. Ghosh, and M. E. Fine, "Nucleation kinetics of Cu₆Sn₅ by reaction of molten tin with a copper substrate," *Journal of Electronic Materials*, vol. 31, pp. 1195-1202, 2002.
- [173] C.-C. Pan, C.-H. Yu, and K.-L. Lin, "The amorphous origin and the nucleation of intermetallic compounds formed at the interface during the soldering of Sn_{3.0}Ag_{0.5}Cu on a Cu substrate," *Applied Physics Letters*, vol. 93, pp. 061912-061912-3, 2008.
- [174] M. N. Harif and I. Ahmad, "Mechanical properties study of lead free solder joint material used in semiconductor packaging subjected to thermal condition," in *International Conference on Electronic Devices, Systems and Applications (ICEDSA)*, Kuala Lumpur, Malaysia, 2010, pp. 331-334.
- [175] M. He, Z. Chen, and G. Qi, "Mechanical strength of thermally aged Sn-3.5Ag/Ni-P solder joints," *Metallurgical and Materials Transactions A*, vol. 36, pp. 65-75, 2005.
- [176] J. Keller, D. Baither, U. Wilke, and G. Schmitz, "Mechanical properties of Pb-free SnAg solder joints," *Acta Materialia*, vol. 59, pp. 2731-2741, 2011.
- [177] M. Yang, M. Li, L. Wang, Y. Fu, J. Kim, and L. Weng, "Cu₆Sn₅ Morphology Transition and Its Effect on Mechanical Properties of Eutectic Sn-Ag Solder Joints," *Journal of Electronic Materials*, vol. 40, pp. 176-188, 2011.
- [178] D. R. Frear, S. N. Burchett, and H. S. Morgan, *Mechanics of Solder Alloy Interconnects*: Springer, 1994.
- [179] C. Wen-Hwa, C. Hsien-Chie, and Y. Ching-Feng, "On the mechanical properties of Cu₃Sn intermetallic compound through molecular dynamics simulation and nanoindentation testing," in *11th International Conference on Thermal, Mechanical & Multi-Physics Simulation, and Experiments in Microelectronics and Microsystems (EuroSimE)* Bordeaux, France, 2010, pp. 1-7.
- [180] R. R. Chromik, R. P. Vinci, S. L. Allen, and M. R. Notis, "Nanoindentation measurements on Cu–Sn and Ag–Sn intermetallics formed in Pb-free solder joints," *Journal of materials research*, vol. 18, pp. 2251-2261, 2003.

- [181] X. Deng, N. Chawla, K. K. Chawla, and M. Koopman, "Deformation behavior of (Cu, Ag)–Sn intermetallics by nanoindentation," *Acta Materialia*, vol. 52, pp. 4291-4303, 2004.
- [182] R. R. Chromik, R. P. Vinci, S. L. Allen, and M. R. Notis, "Measuring the mechanical properties of Pb-free solder and Sn-based intermetallics by nanoindentation," *JOM*, vol. 55, pp. 66-69, 2003.
- [183] L. Xu and J. L. Pang, "Nanoindentation on SnAgCu lead-free solder joints and analysis," *Journal of Electronic Materials*, vol. 35, pp. 2107-2115, 2006.
- [184] Y. Tian, C. Hang, C. Wang, S. Yang, and P. Lin, "Effects of bump size on deformation and fracture behavior of Sn_{3.0}Ag_{0.5}Cu/Cu solder joints during shear testing," *Materials Science and Engineering: A*, vol. 529, pp. 468-478, 2011.
- [185] S. Choi, J. G. Lee, F. Guo, T. R. Bieler, K. N. Subramanian, and J. P. Lucas, "Creep properties of Sn-Ag solder joints containing intermetallic particles," *JOM*, vol. 53, pp. 22-26, 2001.
- [186] S. Reyntjens and R. Puers, "A review of focused ion beam applications in microsystem technology," *Journal of Micromechanics and Microengineering*, vol. 11, p. 287, 2001.
- [187] A. Lugstein, B. Basnar, J. Smoliner, and E. Bertagnolli, "FIB processing of silicon in the nanoscale regime," *Applied Physics A*, vol. 76, pp. 545-548, 2003.
- [188] W. Zhong, F. Qin, T. An, and C. Liu, "Morphology and nanoindentation properties of intermetallic compounds in solder joints," in *12th International Conference on Electronic Packaging Technology and High Density Packaging (ICEPT-HDP)*, Shanghai, China, 2011, pp. 1-6.
- [189] W. Shualdi, B. Bais, I. Ahmad, G. Omar, and A. Isnin, "Nanoindentation characterization of Sn-Ag-Sb/Cu substrate IMC Layer subject to thermal aging," in *IEEE Regional Symposium on Micro and Nanoelectronics (RSM)*, Kota Kinabalu, Malaysia, 2011, pp. 220-223.
- [190] C. J. Wilson, A. Ormeggi, and M. Narbutovskih, "Fracture testing of silicon microcantilever beams," *Journal of Applied Physics*, vol. 79, pp. 2386-2393, 1996.
- [191] R. Ding, J. Gong, A. J. Wilkinson, and I. P. Jones, "Transmission electron microscopy of deformed Ti–6Al–4 V micro-cantilevers," *Philosophical Magazine*, vol. 92, pp. 3290-3314, 2014/05/09 2012.
- [192] L. A. Giannuzzi and F. A. Stevie, "A review of focused ion beam milling techniques for TEM specimen preparation," *Micron*, vol. 30, pp. 197-204, 1999.
- [193] H. Zhang, B. E. Schuster, Q. Wei, and K. T. Ramesh, "The design of accurate micro-compression experiments," *Scripta Materialia*, vol. 54, pp. 181-186, 2006.
- [194] Abaqus, "Abaqus Analysis User's Manual," vol. Abaqus 6.10 documentation, ed, 2010, pp. 24.1.1–2.
- [195] X. Deng, M. Koopman, N. Chawla, and K. K. Chawla, "Young's modulus of (Cu, Ag)–Sn intermetallics measured by nanoindentation," *Materials Science and Engineering: A*, vol. 364, pp. 240-243, 1/15/ 2004.
- [196] G. Simmons and H. Wang, *Single crystal elastic constants and calculated aggregate properties: a handbook*, 2 ed.: M.I.T. Press, 1971.

- [197] R. E. Pratt, E. I. Stromswold, and D. J. Quesnel, "Effect of solid-state intermetallic growth on the fracture toughness of Cu/63Sn-37Pb solder joints," *IEEE Transactions on Components, Packaging, and Manufacturing Technology, Part A*, vol. 19, pp. 134-141, 1996.
- [198] F. Ericson and J. Å. Schweitz, "Micromechanical fracture strength of siliconEricson," *Journal of Applied Physics*, vol. 68, p. 4, 1990.
- [199] V. T. Srikar and S. M. Spearing, "A critical review of microscale mechanical testing methods used in the design of microelectromechanical systems," *Experimental Mechanics*, vol. 43, pp. 238-247, 2003.
- [200] T. Y. Zhang, Y. J. Su, C. F. Qian, M. H. Zhao, and L. Q. Chen, "Microbridge testing of silicon nitride thin films deposited on silicon wafers," *Acta Materialia*, vol. 48, pp. 2843-2857, 2000.
- [201] C. J. Wilson and P. A. Beck, "Fracture testing of bulk silicon microcantilever beams subjected to a side load," *Journal of Microelectromechanical Systems*, vol. 5, pp. 142-150, 1996.
- [202] J. G. Teng, J. W. Zhang, and S. T. Smith, "Interfacial stresses in reinforced concrete beams bonded with a soffit plate: a finite element study," *Construction and Building Materials*, vol. 16, pp. 1-14, 2002.
- [203] W. A. Logsdon, P. K. Liaw, and M. A. Burke, "Fracture behavior of 63sn-37pb solder," *Engineering Fracture Mechanics*, vol. 36, pp. 183-218, 1990.
- [204] S. Canovic, T. Jonsson, and M. Halvarsson, "Grain contrast imaging in FIB and SEM," *Journal of Physics: Conference Series*, vol. 126, p. 012054, 2008.
- [205] C. A. Volkert and A. M. Minor, "Focused ion beam microscopy and micromachining," *MRS bulletin*, vol. 32, pp. 389-399, 2007.
- [206] J. E. Pope, *Rules of Thumb for Mechanical Engineers: A Manual of Quick, Accurate Solutions to Everyday Mechanical Engineering Problems*: Gulf Publishing Company, 1997.
- [207] M. Amagai, M. Watanabe, M. Omiya, K. Kishimoto, and T. Shibuya, "Mechanical characterization of Sn–Ag-based lead-free solders," *Microelectronics Reliability*, vol. 42, pp. 951-966, 2002.
- [208] T. An and F. Qin, "Intergranular cracking simulation of the intermetallic compound layer in solder joints," *Computational Materials Science*, vol. 79, pp. 1-14, 2013.
- [209] Q. K. Zhang, Q. S. Zhu, H. F. Zou, and Z. F. Zhang, "Fatigue fracture mechanisms of Cu/lead-free solders interfaces," *Materials Science and Engineering: A*, vol. 527, pp. 1367-1376, 2010.
- [210] Q. K. Zhang and Z. F. Zhang, "Fracture mechanism and strength-influencing factors of Cu/Sn–4Ag solder joints aged for different times," *Journal of Alloys and Compounds*, vol. 485, pp. 853-861, 2009.
- [211] Q. K. Zhang, H. F. Zou, and Z. F. Zhang, "Tensile and Fatigue Behaviors of Aged Cu/Sn–4Ag Solder Joints," *Journal of Electronic Materials*, vol. 38, pp. 852-859, 2009.

- [212] C. Y. Liu, K. N. Tu, T. T. Sheng, C. H. Tung, D. R. Frear, and P. Elenius, "Electron microscopy study of interfacial reaction between eutectic SnPb and Cu/Ni (V)/Al thin film metallization," *Journal of Applied Physics*, vol. 87, pp. 750-754, 2000.
- [213] X. Deng, R. S. Sidhu, P. Johnson, and N. Chawla, "Influence of reflow and thermal aging on the shear strength and fracture behavior of Sn-3.5Ag solder/Cu joints," *Metallurgical and Materials Transactions A*, vol. 36, pp. 55-64, 2005.
- [214] J. Y. Kim and J. Yu, "Effects of residual impurities in electroplated Cu on the Kirkendall void formation during soldering," *Applied Physics Letters*, vol. 92, p. 092109, 2008.
- [215] D. Q. Yu, L. Wang, C. M. L. Wu, and C. M. T. Law, "The formation of nano-Ag₃Sn particles on the intermetallic compounds during wetting reaction," *Journal of Alloys and Compounds*, vol. 389, pp. 153-158, 2005.
- [216] R. Pratt, E. Stromswold, and D. Quesnel, "Mode I fracture toughness testing of eutectic Sn-Pb solder joints," *Journal of Electronic Materials*, vol. 23, pp. 375-381, 1994.
- [217] T. Tamai, Y. Nabeta, S. Sawada, and Y. Hattori, "Property of Tin Oxide Film Formed on Tin-Plated Connector Contacts," in *56th IEEE Holm Conference on Electrical Contacts (HOLM)*, Charleston, USA, 2010, pp. 1-8.
- [218] R. Berriche, R. Lowry, and M. I. Rosenfield, "An oxidation study of Cu leadframes," in *Proceedings of International Symposium on Advanced Packaging Materials: Processes, Properties and Interfaces*, Braselton, USA, 1999, pp. 275-281.
- [219] H. Miley, "Copper oxide films," *Journal of the American Chemical Society*, vol. 59, pp. 2626-2629, 1937.
- [220] R. A. Schapery, "Thermal Expansion Coefficients of Composite Materials Based on Energy Principles," *Journal of Composite Materials*, vol. 2, pp. 380-404, 1968.
- [221] B. Wang, "Research on the Interfacial Reactions and Mechanical Property of Solder Joints with Micron Stand-Off Height," PhD, Material Processing Engineering, Huazhong University of Science and Technology, Wuhan, 2010.
- [222] X. Lin and L. Luo, "Void Evolution in Sub-100-Micron Sn-Ag Solder Bumps during Multi-reflow and Aging and its Effects on Bonding Reliability," *Journal of Electronic Materials*, vol. 37, pp. 307-313, 2008.
- [223] K. Zeng, R. Stierman, T.-C. Chiu, D. Edwards, K. Ano, and K. N. Tu, "Kirkendall void formation in eutectic SnPb solder joints on bare Cu and its effect on joint reliability," *Journal of Applied Physics*, vol. 97, p. 024508, 2005.
- [224] Y. W. Wang, Y. W. Lin, and C. R. Kao, "Kirkendall voids formation in the reaction between Ni-doped SnAg lead-free solders and different Cu substrates," *Microelectronics Reliability*, vol. 49, pp. 248-252, 2009.
- [225] C. Y. Liu, J. T. Chen, Y. C. Chuang, L. Ke, and S. J. Wang, "Electromigration-induced Kirkendall voids at the Cu/Cu₃Sn interface in flip-chip Cu/Sn/Cu joints," *Applied Physics Letters*, vol. 90, pp. 112114-112114-3, 2007.
- [226] X. Luhua and J. H. L. Pang, "Effect of intermetallic and Kirkendall voids growth on board level drop reliability for SnAgCu lead-free BGA solder joint," in *56th Electronic Components and Technology Conference*, San Diego, USA, 2006, p. 8 pp.

- [227] F. Gao, H. Nishikawa, and T. Takemoto, "Additive Effect of Kirkendall Void Formation in Sn-3.5Ag Solder Joints on Common Substrates," *Journal of Electronic Materials*, vol. 37, pp. 45-50, 2008.
- [228] A. Harasaki, J. Schmit, and J. C. Wyant, "Offset of Coherent Envelope Position Due to Phase Change on Reflection," *Applied Optics*, vol. 40, pp. 2102-2106, 2001.
- [229] K. N. Tu, "Interdiffusion and reaction in bimetallic Cu-Sn thin films," *Acta Metallurgica*, vol. 21, pp. 347-354, 1973.
- [230] Y. C. Chan, A. C. K. So, and J. K. L. Lai, "Growth kinetic studies of Cu-Sn intermetallic compound and its effect on shear strength of LCCC SMT solder joints," *Materials Science and Engineering B*, vol. 55, pp. 5-13, 8th April 2011 1998.
- [231] E. Blond and N. Richet, "Thermomechanical modelling of ion-conducting membrane for oxygen separation," *Journal of the European Ceramic Society*, vol. 28, pp. 793-801, 2008.
- [232] S. B. Adler, "Chemical Expansivity of Electrochemical Ceramics," *Journal of the American Ceramic Society*, vol. 84, pp. 2117-2119, 2001.
- [233] E. S. W. Poh, W. H. Zhu, X. R. Zhang, C. K. Wang, A. Y. S. Sun, and H. B. Tan, "Lead-free solder material characterization for thermo-mechanical modeling," in *International Conference on Thermal, Mechanical and Multi-Physics Simulation and Experiments in Microelectronics and Micro-Systems*, Freiburg im Breisgau, Germany, 2008, pp. 1-8.
- [234] M. S. Mirza, D. C. Barton, P. Church, and J. L. Sturges, "Ductile Fracture of Pure Copper : An Experimental and Numerical Study," *Journal de Physique IV France*, vol. 07, pp. C3-891-C3-896, 1997.
- [235] M. P. Phaniraj, D.-I. Kim, and Y. W. Cho, "Effect of grain boundary characteristics on the oxidation behavior of ferritic stainless steel," *Corrosion Science*, vol. 53, pp. 4124-4130, 2011.
- [236] H. Y. Chuang, T. L. Yang, M. S. Kuo, Y. J. Chen, J. J. Yu, C. C. Li, *et al.*, "Critical Concerns in Soldering Reactions Arising from Space Confinement in 3-D IC Packages," *IEEE Transactions on Device and Materials Reliability*, vol. 12, pp. 233-240, 2012.
- [237] M. T. Pérez-Prado, G. González-Doncel, O. A. Ruano, and T. R. McNelley, "Texture analysis of the transition from slip to grain boundary sliding in a discontinuously recrystallized superplastic aluminum alloy," *Acta Materialia*, vol. 49, pp. 2259-2268, 2001.
- [238] O. Engler and M.-Y. Huh, "Evolution of the cube texture in high purity aluminum capacitor foils by continuous recrystallization and subsequent grain growth," *Materials Science and Engineering: A*, vol. 271, pp. 371-381, 1999.
- [239] Q. Xiao, H. J. Bailey, and W. D. Armstrong, "Aging Effects on Microstructure and Tensile Property of Sn3.9Ag0.6Cu Solder Alloy," *Journal of Electronic Packaging*, vol. 126, pp. 208-212, 2004.
- [240] G. T. T. Sheng, C. F. Hu, W. J. Choi, K. N. Tu, Y. Y. Bong, and L. Nguyen, "Tin whiskers studied by focused ion beam imaging and transmission electron microscopy," *Journal of Applied Physics*, vol. 92, pp. 64-69, 2002.

- [241] L. Ma, F. Guo, G. Xu, X. Wang, H. He, and H. Zhao, "Investigation of Stress Evolution Induced by Electromigration in Sn-Ag-Cu Solder Joints Based on an X-Ray Diffraction Technique," *Journal of Electronic Materials*, vol. 41, pp. 425-430, 2012.
- [242] G. Robert Humfeld and D. A. Dillard, "Residual Stress Development in Adhesive Joints Subjected to Thermal Cycling," *The Journal of Adhesion*, vol. 65, pp. 277-306, 2014/09/01 1998.
- [243] S. Carlsson and P. L. Larsson, "On the determination of residual stress and strain fields by sharp indentation testing.: Part I: theoretical and numerical analysis," *Acta Materialia*, vol. 49, pp. 2179-2191, 2001.
- [244] S. Carlsson and P. L. Larsson, "On the determination of residual stress and strain fields by sharp indentation testing.: Part II: experimental investigation," *Acta Materialia*, vol. 49, pp. 2193-2203, 2001.
- [245] K. O. Kese, Z. C. Li, and B. Bergman, "Influence of residual stress on elastic modulus and hardness of soda-lime glass measured by nanoindentation," *Journal of materials research*, vol. 19, pp. 3109-3119, 2004.
- [246] A. Bolshakov, W. C. Oliver, and G. M. Pharr, "Influences of stress on the measurement of mechanical properties using nanoindentation: Part II. Finite element simulations," *Journal of Materials Research*, vol. 11, pp. 760-768, 1996.
- [247] K. W. McElhane, J. J. Vlassak, and W. D. Nix, "Determination of indenter tip geometry and indentation contact area for depth-sensing indentation experiments," *Journal of Materials Research*, vol. 13, pp. 1300-1306, 1998.
- [248] C. A. Taylor, M. F. Wayne, and W. K. S. Chiu, "Residual stress measurement in thin carbon films by Raman spectroscopy and nanoindentation," *Thin Solid Films*, vol. 429, pp. 190-200, 2003.
- [249] J. M. Antunes, A. Cavaleiro, L. F. Menezes, M. I. Simões, and J. V. Fernandes, "Ultra-microhardness testing procedure with Vickers indenter," *Surface and Coatings Technology*, vol. 149, pp. 27-35, 2002.
- [250] W. C. Oliver and G. M. Pharr, "An improved technique for determining hardness and elastic modulus using load and displacement sensing indentation experiments," *Journal of materials research*, vol. 7, pp. 1564-1583, 1992.
- [251] X. Li and B. Bhushan, "A review of nanoindentation continuous stiffness measurement technique and its applications," *Materials Characterization*, vol. 48, pp. 11-36, 2002.
- [252] H. Czichos, T. Saito, and L. E. Smith, *Springer handbook of metrology and testing*: Springer, 2011.
- [253] M. D. Thouless, J. Gupta, and J. M. E. Harper, "Stress development and relaxation in copper films during thermal cycling," *Journal of materials research*, vol. 8, pp. 1845-1852, 1993.
- [254] J. Pan, B. J. Toleno, T. C. Chou, and W. J. Dee, "The effect of reflow profile on SnPb and SnAgCu solder joint shear strength," *Soldering & Surface Mount Technology*, vol. 18, pp. 48-56, 2014/09/02 2006.

- [255] S. G. Jadhav, T. R. Bieler, K. N. Subramanian, and J. P. Lucas, "Stress relaxation behavior of composite and eutectic Sn-Ag solder joints," *Journal of Electronic Materials*, vol. 30, pp. 1197-1205, 2001.
- [256] H. Mei Jin and P. Wu, "Coefficient of thermal expansion for solder alloys based on cluster expansion method," *Journal of Materials Chemistry*, vol. 12, pp. 1090-1093, 2002.
- [257] J. L. F. Guo, J. P. Lucas, K. N. Subramanian, T. R. Bieler, "Creep Properties of Eutectic Sn-3.5Ag Solder Joints Reinforced with Mechanically Incorporated Ni Particles," *Journal of Electronic Materials*, vol. 30, pp. 1222-1227, September 2001.
- [258] B. Cai, Q. P. Kong, P. Cui, L. Lu, and K. Lu, "Creep behavior of cold-rolled nanocrystalline pure copper," *Scripta Materialia*, vol. 45, pp. 1407-1413, 2001.
- [259] B. Z. Lee and D. N. Lee, "Spontaneous growth mechanism of tin whiskers," *Acta Materialia*, vol. 46, pp. 3701-3714, 1998.
- [260] M. L. Huang, C. M. L. Wu, J. K. L. Lai, and Y. C. Chan, "Microstructural evolution of a lead-free solder alloy Sn-Bi-Ag-Cu prepared by mechanical alloying during thermal shock and aging," *Journal of Electronic Materials*, vol. 29, pp. 1021-1026, 2000.
- [261] Z. Chen, M. He, A. Kumar, and G. J. Qi, "Effect of Interfacial Reaction on the Tensile Strength of Sn-3.5Ag/Ni-P and Sn-37Pb/Ni-P Solder Joints," *Journal of Electronic Materials*, vol. 36, pp. 17-25, 2007.
- [262] N. Zhang, Y. Shi, Z. Xia, Y. Lei, F. Guo, and X. Li, "Comparison of Impact Toughness and Fracture Morphologies Between Pb-Containing and Pb-Free Solder Joints Subject to the Charpy Impact Test," *Journal of Electronic Materials*, vol. 37, pp. 1631-1639, 2008.
- [263] J. P. Lucas, F. Guo, J. McDougall, T. R. Bieler, K. N. Subramanian, and J. K. Park, "Creep deformation behavior in eutectic Sn-Ag solder joints using a novel mapping technique," *Journal of Electronic Materials*, vol. 28, pp. 1270-1275, 1999.
- [264] N. N. Guo, J. Y. Zhang, P. M. Cheng, G. Liu, and J. Sun, "Room temperature creep behavior of free-standing Cu films with bimodal grain size distribution," *Scripta Materialia*, vol. 68, pp. 849-852, 2013.
- [265] Z. Jiang, X. Liu, G. Li, Q. Jiang, and J. Lian, "Strain rate sensitivity of a nanocrystalline Cu synthesized by electric brush plating," *Applied Physics Letters*, vol. 88, pp. 143115-143115-3, 2006.
- [266] C. Zhiwen, A. Bing, W. Yiping, L. Changqing, and R. Parkin, "An investigation of the influence of intermetallic compounds on compressive creep of SAC305/copper solder joints by modeling," in *International Symposium on Advanced Packaging Materials (APM)*, Xiamen, China, 2011, pp. 322-329.
- [267] K. Newman, "BGA brittle fracture - alternative solder joint integrity test methods," in *55th Electronic Components and Technology Conference*, Lake Buena Vista, USA, 2005, pp. 1194-1201.
- [268] S. Fubin, S. W. R. Lee, K. Newman, B. Sykes, and S. Clark, "Brittle Failure Mechanism of SnAgCu and SnPb Solder Balls during High Speed Ball Shear and Cold Ball Pull Tests," in *57th Electronic Components and Technology Conference*, Reno, USA, 2007, pp. 364-372.

- [269] G. Peng, L. Jian, L. Yongping, and W. Guichen, "Drop performance research of silver content on the SnAgCu based lead-free solder of joint level," in *14th International Conference on Electronic Packaging Technology (ICEPT)*, Dalian, USA, 2013, pp. 809-813.
- [270] D. Suh, D. W. Kim, P. Liu, H. Kim, J. A. Weninger, C. M. Kumar, *et al.*, "Effects of Ag content on fracture resistance of Sn–Ag–Cu lead-free solders under high-strain rate conditions," *Materials Science and Engineering: A*, vol. 460–461, pp. 595-603, 2007.
- [271] W. H. Müller, K. Weinberg, and T. Böhme, "On the effect of Kirkendall voids on solder joint reliability," *PAMM*, vol. 7, pp. 4030035-4030036, 2007.
- [272] J. Yu and J. Y. Kim, "Effects of residual S on Kirkendall void formation at Cu/Sn–3.5Ag solder joints," *Acta Materialia*, vol. 56, pp. 5514-5523, 2008.
- [273] R. Kretz, "Interpretation of the Shape of Mineral Grains in Metamorphic Rocks," *Journal of Petrology*, vol. 7, pp. 68-94, 1966.
- [274] A. U. Telang, T. R. Bieler, J. P. Lucas, K. N. Subramanian, L. P. Lehman, Y. Xing, *et al.*, "Grain-boundary character and grain growth in bulk tin and bulk lead-free solder alloys," *Journal of Electronic Materials*, vol. 33, pp. 1412-1423, 2004.
- [275] S. Kang, D. Leonard, D.-Y. Shih, L. Gignac, D. W. Henderson, S. Cho, *et al.*, "Interfacial reactions of Sn-Ag-Cu solders modified by minor Zn alloying addition," *Journal of Electronic Materials*, vol. 35, pp. 479-485, 2006.
- [276] H. F. Zou, H. J. Yang, and Z. F. Zhang, "A study on the orientation relationship between the scallop-type Cu₆Sn₅ grains and (0 1 1) Cu substrate using electron backscattered diffraction," *Journal of Applied Physics*, vol. 106, pp. 113512-113512-3, 2009.
- [277] T.-C. Liu, C. Chen, K.-J. Chiu, H.-W. Lin, and J.-C. Kuo, "Novel EBSD preparation method for Cu/Sn microbumps using a focused ion beam," *Materials Characterization*, vol. 74, pp. 42-48, 2012.
- [278] W. Liu, Y. Tian, C. Wang, X. Wang, and R. Liu, "Morphologies and grain orientations of Cu–Sn intermetallic compounds in Sn_{3.0}Ag_{0.5}Cu/Cu solder joints," *Materials Letters*, vol. 86, pp. 157-160, 2012.
- [279] D. Systèmes, "Abaqus 6.12 documentation collection," ed, 2012.
- [280] F. Farukh, E. Demirci, M. Acar, B. Pourdeyhimi, and V. Silberschmidt, "Meso-scale deformation and damage in thermally bonded nonwovens," *Journal of Materials Science*, vol. 48, pp. 2334-2345, 2013.
- [281] K. S. Kim, S. H. Huh, and K. Sukanuma, "Effects of intermetallic compounds on properties of Sn–Ag–Cu lead-free soldered joints," *Journal of Alloys and Compounds*, vol. 352, pp. 226-236, 2003.
- [282] S. Ahat, L. Du, M. Sheng, L. Luo, W. Kempe, and J. Freytag, "Effect of aging on the microstructure and shear strength of SnPbAg/Ni-P/Cu and SnAg/Ni-P/Cu solder joints," *Journal of Electronic Materials*, vol. 29, pp. 1105-1109, 2000.
- [283] H. F. Zou and Z. F. Zhang, "Effects of aging time, strain rate and solder thickness on interfacial fracture behaviors of Sn–3Cu/Cu single crystal joints," *Microelectronic Engineering*, vol. 87, pp. 601-609, 2010.

- [284] M. S. Mirza, D. C. Barton, P. Church, and J. L. Sturges, "Ductile fracture of pure copper: An experimental and numerical study," *Le Journal de Physique IV*, vol. 7, pp. C3-891, 1997.
- [285] Y. Ding, C. Wang, L. Mingyu, and B. Han-Sur, "Aging effects on fracture behavior of 63Sn37Pb eutectic solder during tensile tests under the SEM," *Materials Science and Engineering: A*, vol. 384, pp. 314-323, 2004.
- [286] S. Fubin and S. W. R. Lee, "Investigation of IMC thickness effect on the lead-free solder ball attachment strength: comparison between ball shear test and cold bump pull test results," in *56th Electronic Components and Technology Conference*, San Diego, USA, 2006, pp. 1196-1203.
- [287] S. Fubin, S. W. R. Lee, K. Newman, B. Sykes, and S. Clark, "High-Speed Solder Ball Shear and Pull Tests vs. Board Level Mechanical Drop Tests: Correlation of Failure Mode and Loading Speed," in *57th Electronic Components and Technology Conference*, Reno, USA, 2007, pp. 1504-1513.
- [288] Z. Chen, B. An, Y. Wu, C. Liu, and R. Parkin, "Influence of IMCs volume ratio in micro-scale solder joints on their mechanical integrity," presented at the 62nd Electronic Components and Technology Conference, San Diego, USA, 2012.
- [289] M. Zequn, M. Ahmad, M. Hu, and G. Ramakrishna, "Kirkendall voids at Cu/solder interface and their effects on solder joint reliability," in *55th Electronic Components and Technology Conference*, Lake Buena Vista, USA, 2005, pp. 415-420 Vol. 1.
- [290] R. Labie, W. Ruythooren, and J. Van Humbeeck, "Solid state diffusion in Cu–Sn and Ni–Sn diffusion couples with flip-chip scale dimensions," *Intermetallics*, vol. 15, pp. 396-403, 2007.

Appendices 1- Code for post-processing

```
#Derive the average stress-strain curves from modelling results
```

```
from miscUtils import sorted
from random import *
from abaqusConstants import *
def ys_distribution():
    import section
import regionToolset
import part
import material
import odbMaterial
import assembly
import step
import interaction
import load
import mesh
import job
import sketch
import visualization
import connectorBehavior

nodes1=[#labels of the first line of nodes]
nodes2=[#labels of the second line of nodes]

path1=session.Path('Cu6Sn5-1-9micron-1',NODE_LIST,'PART-1-1',nodes1)
path2=session.Path('Cu6Sn5-1-9micron-2',NODE_LIST,'PART-1-1',nodes2)

session.XYDataFromPath('Cu6Sn5-1-9micron-1', path1, includeIntersections=False,
shape=UNDEFORMED, labelType=TRUE_DISTANCE)
session.XYDataFromPath('Cu6Sn5-1-9micron-2', path2, includeIntersections=False,
shape=UNDEFORMED, labelType=TRUE_DISTANCE)
#session.XYDataFromPath(name='XYData-'+str(ii), path=pth, includeIntersections=True,
shape=UNDEFORMED, labelType=TRUE_DISTANCE)
```

```
m=59-2
```

```
for i in xrange(1,m):
```

```
    nodes=[]
```

```
    for n in xrange(0,len(nodes1)):
```

```
        nodes.append(nodes1[n]+i*(nodes2[n]-nodes1[n])
```

```
    path=session.Path('Cu6Sn5-1-9micron-'+str(i+1),NODE_LIST,'PART-1-1',nodes)
```

```
    session.XYDataFromPath('Cu6Sn5-1-9micron-'+str(i+1), path,  
includeIntersections=False, shape=UNDEFORMED, labelType=TRUE_DISTANCE)
```

Appendices 2- Code for creating grain boundaries

```
%Matlab code for generating arbitrary grain boundaries
```

```
Xmin=-0.025
```

```
Xmax=0.025
```

```
Ymin=-0.018
```

```
Ymax=0.018
```

```
Coordinates=zeros(10,2)
```

```
for i=1:10
```

```
    Coordinates(i,1)=Xmin + (Xmax-Xmin).*rand(1,1)
```

```
    Coordinates(i,2)=Ymin + (Ymax-Ymin).*rand(1,1)
```

```
end
```

```
[VX, VY] = voronoi(Coordinates(:,1),Coordinates(:,2));
```

```
h = plot(VX,VY,'-b',Coordinates(:,1),Coordinates(:,2),'.r');
```

```
set(h(1:end-1),'xliminclud','off','yliminclud','off');
```

Appendices 3- Code for importing grain boundaries

```
# Import the grain boundaries from Matlab into the models in Abaqus

from miscUtils import sorted
from random import *
from abaqusConstants import *
def ys_distribution():
    import section
import regionToolset
import part
import material
import odbMaterial
import assembly
import step
import interaction
import load
import mesh
import job
import sketch
import visualization
import connectorBehavior

# get the coordinates of the matrix
VX=[#data points from matlab]
VY=[#data points from matlab]

m=len(VX)
n=len(VY)
Cu3Sn=mdb.models['Model 1-6-weeks'].ConstrainedSketch('Cu3Sn-sketch',0.001)
for i in xrange(0,len(VX)/2):
    Cu3Sn.Line((VX[i],VY[i]),(VX[i+len(VX)/2],VY[i+len(VX)/2]))
```